Università degli Studi di Torino
Doctoral School of the University of Torino
PhD Programme in Chemical and Materials Sciences XXXV Cycle

ZrO_2/CeO_2-based catalysts: understanding their structural and chemical role towards CO_2 valorisation reactions

Davide Salusso

Supervisor:
Prof. Silvia Bordiga

Università degli Studi di Torino

Doctoral School of the University of Torino

PhD Programme in Chemical and Materials Sciences XXXV cycle

ZrO_2/CeO_2-based catalysts: understanding their structural and chemical role towards CO_2 valorisation reactions

Candidate: **Davide Salusso**

Supervisor: Prof. **Silvia Bordiga**

Jury Members: Prof. **Maria Cristina Paganini**
Università degli studi di Torino
Dipartimento di Chimica

Prof. **Paolo Ghigna**
Università degli Studi di Pavia
Dipartimento di Chimica

Prof. **Anatoly Frenkel**
Stony Brook University
Department of Materials Science and Chemical Engineering

Head of the Doctoral School: Prof. Alberto Rizzuti
PhD Programme Coordinator: Prof. Bartolome Civalleri

Torino, 2022

Table of Contents

1 Introduction 7

1.1 CO_2: Excess of everything is bad 7

1.2 CO_2 as a C1 raw source 9

1.3 High energy reactions 9

1.3.1 Secondary works on high energy reactions catalysts. 12

1.4 Low energy reactions 14

2 Materials and methods 28

2.1 Materials 28

2.2 Methods 29

2.2.1 Specific surface area. 29

2.2.2 Powder X-Ray Diffraction 30

2.2.3 Fourier Transform Infrared spectroscopy (FTIR) 31

2.2.4 UV-Vis Spectroscopy 34

2.2.5 X-ray Photoelectron Spectroscopy (XPS) 34

2.2.6 X-Ray Absorption Fine Structure (XAFS) 36

2.2.7 Multivariate Curve Resolution – Alternating Least Squares (MCR-ALS) 41

3 ZrO_2 doped with aliovalent elements (Ce, Zn, Ga): the need for a structural understanding of guest atom nature 46

3.1 Catalytic properties 46

3.2 $CeZrO_x$: understanding solid solution long- and short-range ordering ... 47

3.2.1 Average structural and electronic properties 48

3.2.2 Zr/Ce local structure 49

3.2.3 Deducing Ce-Zr short range ordering 53
3.3 Zn-doped ZrO_2: comprehension of Zn local environment 55
3.3.1 Powder X-Ray Diffraction (PXRD) 55
3.3.2 X-Ray Absorption Spectroscopy 56
3.3.3 ZnZr(X) : ZnO domain size 63
3.4 ZnO clusters stability in ZnZr-X catalysts 65
3.4.1 *Ex situ* XAS 65
3.4.2 *Ex situ* and *In situ* PXRD 68
3.5 Zn-doped ZrO_2 : catalyst deactivation after catalytic tests 71
3.5.1 *Ex situ* XAS 71
3.6 $GaZrO_x$: from oxides clusters to the solid solution scenario 72
3.6.1 Catalyst average structure and electronic properties: PXRD and UV-Vis spectroscopy 72
3.6.2 *In situ* XAFS: Ga local coordination 74
3.6.3 Short range disorder: the price for solid solution formation 80
3.7 $ZnZrO_x$ stabilisation through Ce-doping: $ZnCeZrO_x$ 80
3.7.1 *In situ* experiment description 81
3.7.2 In-situ PXRD/XAS: catalyst activation 82
3.7.3 Ce surface reduction: *in-situ* near ambient pressure NEXAFS 86
3.7.4 Ce_xZn_y alloy evolution under reaction-like conditions 88
3.7.5 $ZnCeZrO_x$: simple rationalization of a complex system 89
3.8 Conclusions 90

4 CO_2-to-Dimethilcarbonate reaction over ZrO_2: liquid vs gas phase mechanism 97

4.1 Liquid phase reaction 97

4.1.1 Adsorption of pure reagents/products 97

4.1.2 Reactivity of mixed methanol-CO_2 102

4.1.3 Liquid phase reaction: mechanism dependence with reaction temperature 106

4.2 Gas phase reaction 107

4.2.1 ZrO_2 in-situ activation 107

4.2.2 Methanol adsorption over ZrO_2 at 30°C 108

4.2.3 Carbon dioxide adsorption over ZrO_2 at 30°C and 150°C 110

4.2.4 Dimethilcarbonate adsorption/desorption at room temperature 114

4.2.5 Reactivity of CO_2/CH_3OH over ZrO_2 116

4.2.6 Gas phase reaction: the role of methanol concentration 122

4.3 Conclusions 123

4.4 CeO_2 Frustrated Lewis Pair improving CO_2 and CH_3OH conversion to Monomethylcarbonate 125

4.4.1 CeO_2 preparation and basic characterization 125

4.4.2 CH_3OH and CO_2 activation over Ce^{3+}/V_O and FLP 129

4.4.3 Conclusions 136

5 Aknowledments 143

6 Appendix : list of published articles during the thesis 144

6.1 A : Ticali P., Salusso D., Catal. Sci. Technol., 2021,11, 1249 144

6.2 B : Salusso et al., J. Phys. Chem. C 2021, 125, 40, 22249–22261 164

6.3 C : Ramirez A., et al., JACS Au 2021, 1, 10, 1719–1732..... 177

6.4 D : Ruzzi et al., Applied Catalysis A, General 635 (2022) 118568 191

6.5 E : Barreau M. et al., Materials Today Chemistry 26 (2022) 101011.... 203

6.6 F : Surface species in direct liquid phase synthesis of dimethyl carbonate from methanol and CO2: an MCR-ALS augmented ATR-IR study. Signorile et al., 2022 213

1 Introduction

1.1 CO_2: Excess of everything is bad

"Excess of everything is bad". This old proverb should remind to everyone, scientists and not, that CO_2 itself is not a problem. If we look at the CO_2 atmospheric concentration in the past hundreds of thousands of years, it is immediately clear as its concentration oscillated between 280 and 170 ppm, leading to warmer and colder ages, respectively.[1] The relation between CO_2 concentration and the planet average temperature, is a direct consequence of the molecule chemical configuration. CO_2 belongs to the greenhouse gases family containing all the molecules (e.g. H_2O, CH_4, N_2O, O_3) able to absorb and emit energy in the thermal infrared range.[1–3] This particular property occurs thanks to the molecule (non-symmetrical) electrical charges distribution during its vibration. This means that the concentration of CO_2 in the atmosphere, summed with the one of the other greenhouse gases, controls the amount of IR thermal radiation emitted by our planet after sun irradiation. Therefore, coming back to the proverb, the presence of CO_2 in our atmosphere is mandatory for having a planet with average temperature above 0°C however, having an excess of CO_2 is not a good thing. In the last centuries, the level of CO_2 increased to more than 400 ppm, inducing a constant increase of our planet average temperature.[1] It is then clear than we are not crucifying carbon dioxide, but rather its excess in our atmosphere.

For understanding the origin of CO_2 atmospheric excess, we should quickly analyse CO_2 natural cycle. With a rapid balance it can be found as ground and sea life emit 439 and 332 Gt/y of CO_2, respectively compensated with an absorption rate of 450 and 338 Gt/y, making the average CO_2 cycle positive with an absorption of 17 Gt/y. However, considering in this delicate balance the anthropogenic emissions changes completely the equation outcome. Since the industrial revolution ($XVIII^{th}$ century) our CO_2 emissions increased due to energy and food production, industries, cement,

and wastes, until reaching the current 37.8 Gt/y, causing a 50% increase of CO_2 atmospheric concentration (from 280 to 421 ppm).[4,5]

Until nowadays we considered CO_2 as a waste and atmosphere was used as dump with unlimited space. Nevertheless, as in the last century we learned to recycle wastes such as glass, plastic and paper to prevent landfill saturation and primary sources depletion, it is now time to consider CO_2 recycling as a serious option to reduce its atmospheric concentration and avoid draining our non-renewable sources (e.g. fossil fuels and coals).[6–8]

In the panorama of CO_2 emissions reduction strategies, Carbon Capture Storage (CCS) and Utilisation (CCU) technologies are potential short and long-term solutions.[4,7–12] A synergic development of these two strategies implies the collaboration between researchers and industrial partners from different field i.e., from capture and reaction plant design to chemical research or market perspective economic analysis. This synergy is the heart of the COZMOS project where I was actively involved during my PhD thesis.♣ The project started on May 2019 and will last until 2023. It unifies the efforts from several universities and research centres e.g., University of Turin, University of Oslo (UiO), CNRS Lyon, KAUST, ICC and University of Sheffield and companies e.g., SINTEF, TOPSOE, Linde, Tata-steel and Tüpras (see link for more detailed information♣) aiming to directly convert CO_2 to C_3 fuels and chemical building blocks.

As it will be described withing the thesis, I was actively involved in the project for the catalyst's structural characterization.

♣ https://www.aspire2050.eu/cozmos

1.2 CO_2 as a C1 raw source

Life Cycle Analysis of our industrial activities showed as we were, mostly involuntary, already absorbing roughly 0.23 Gt/y of CO_2 to our own profit for example for fertilizers production (57%), enhanced oil recovery (34%) and food/beverages production (9%).[4] Nevertheless, it is clear as this is not enough to balance our current emission (37.8 Gt/y).[5] Indeed, the International Energy Agency (IEA) estimated as a minimum of 3 Gt/y of CO_2 should be absorbed without any associated emissions, this being a crucial point for a CO_2 correct balance.[4] When considering any CCU or CCS technology, the amount of CO_2 that is stored/converted should imply that less CO_2 is emitted during the process, leading to a global positive balance. This concept is then the heart of new generation catalysts development, aiming to reduce CO_2 recycle reaction activation energy.[6,8,10] Depending on the final molecule targeted by CCU the required energy will vary, dividing the catalytic processes in: I) low energy and II) high energy processes, depending on the CO_2 carbon atom final oxidation state, easily identifiable by the increase of C/O ratio (1:2 in CO_2). Production of carbonates (-OCOO-), carbamates (-HN-COO-), and urea ($CO(NH_2)_2$) are then considered low energy processes whilst conversion of CO_2 to methanol (CH_3OH), methane (CH_4), formaldehyde (CH_2O), olefins (C_nH_{2n}) and saturated hydrocarbons (C_nH_{2n+2}) are high energy processes.[10,13,14]

This energetic definition also describes the chapters division of this thesis where the role of ZrO_2 and CeO_2 based catalyst for high energy and a low energy process is studied.

1.3 High energy reactions

High energy process mostly exploits CO_2 reduction with the use of H_2 to obtain CH_3OH, formaldehyde, methane, hydrocarbons, and olefines.[13,14] The possibility of obtaining high energy chemicals and fuels is opening to these reactions an impressive market. Indeed, according to the IEA the use of CO_2 to produce fuels could in principle reduced CO_2 emissions in the order >5Gt/y.[4] Nevertheless, this must imply

the use of green hydrogen[♣] i.e., hydrogen produced without emitting CO_2 (from fossil fuels combining CCS or by water electrolysis using electricity from renewable sources). To obtain hydrocarbons and olefines the COZMOS project aimed to develop a tandem catalyst like the one represented in Figure 1 consisting of two components: an oxidic part aiming to hydrogenate CO_2 to methanol and an acid zeolite/zeotype for direct conversion of methanol to olefins and hydrocarbons.[12,15–18]

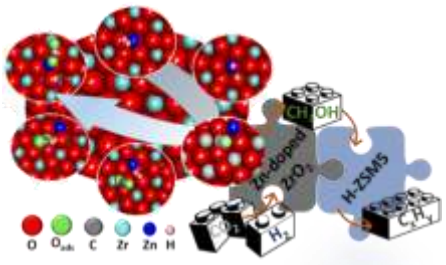

Figure 1 Pictorial representation of a tandem catalysts studied within this thesis where the oxidic catalyst (Zn-doped ZrO_2) and the acidic zeolite (H-ZSM5) are represented.

By mixing the two catalysts a cascade reaction gives access to the direct conversion of CO_2 to hydrocarbons. However, this requires compromising temperature and pressure for the equilibrium of the two reactions i.e., the former requiring low temperatures/high pressures whilst high temperatures enhance methanol dehydration and C-C coupling in the zeolite.[19] In this contest the scope of the thesis chapter dedicated to high energy reaction focuses on the structural understanding of the

[♣] The original IEA document refers to low carbon hydrogen, considering then both blue hydrogen (from fossil fuels combining CCS) and green hydrogen (water electrolysis using electricity from renewable sources). The former implies a massive use of CCS and at some point, we should recycle all the stored CO_2, likely by combining it with H_2 for high energy processes. Since using blue hydrogen either implies a secondary CO_2 recycling circle or CO_2 (unsustainable) long-term storage, I have preferred to keep in the text the concept of using only green hydrogen.

oxidic catalyst component prepared and tested by several partners of the project (i.e. UiO, SINTEF, ICC, TOPSOE and KAUST). As it can be seen from the yearly published articles, 10% of the growing scientific interest for CO_2 hydrogenation is related to ZrO_2 based catalysts.

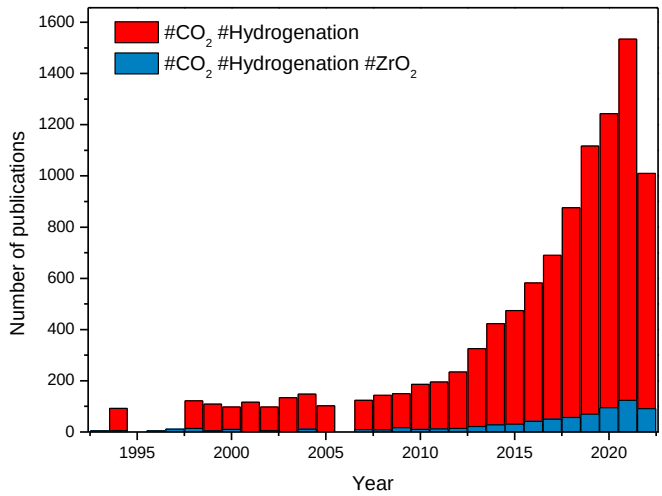

Figure 2 Yearly published articles related to CO_2 hydrogenation (red bars) and CO_2 hydrogenation ZrO_2 (blue bars). Citation Report graphic source: https://www.webofscience.com

The common denominator of these studies is about finding of the right guest atom and its concentration leading to the higher catalytic activity. Most of the studies are applying a systematic try-and-error approach screening several elements in different proportion without deeply investigating the fundamental drivers impacting the catalytic performance.[20] The high activity of aliovalent element doped ZrO_2 is attributed to the generation of stoichiometric oxygen vacancies to improve CO_2 and H_2 activation through carbonates and hydrides formation, respectively.[20] Since the chemical reactants/catalysts interactions occurs at a local level it means that they depend on the catalyst local structure. In the case of well-ordered crystals, there is no distinction between average and local structure, which is not the case when local

distortions cause deviations between local and average structure.[21] With the observation of a single-phase powder X-Ray diffractogram, doped-ZrO_2 is usually defined as a solid solution, hence implying the guest atom replacing Zr in its unit cell position. Nevertheless, diffractograms simplicity should not be automatically reflected to structure simplicity. Its Rietveld refinement in reciprocal space determines a global view of the catalyst structure however, only local probes can unveil the catalyst local structure, ultimately defining its catalytic behaviour.

Powder X-Ray Diffraction combined with Hard-X-Ray Absorption Spectroscopy (XAS) were then applied to determine the local electronic state, coordination and structure between guest atom and host matrix. Indeed, we investigated the origin of the catalytic differences between ZrO_2 doped with Ce, Zn and Ga. Even though the two catalysts presented the same crystallographic phases, measuring the XAS K-edges of all the elements (Zr, Ce, Zn and Ga) gave a complete view of the local structure in the investigated catalysts. The short-range ordering of the three catalysts presented formation of domains of different size which influenced dramatically the catalytic properties.

1.3.1 Secondary works on high energy reactions catalysts.

I would like to mention that during the thesis I worked also on other catalysts for CO_2 hydrogenation where the active site for CO_2 and H_2 activation was a metal sites grafted (PdZn alloy) over ZrO_2 and $CeZrO_x$ or included (Ni) in a CeO_2 lattice. The first catalyst was studied within the COZMOS project for direct conversion of CO_2 to propane. They were prepared and tested by UiO, CNR Lyon and KAUST whist I was actively involved in the XAS characterization of the PdZn alloy. The second catalyst ($NiCeO_x$) was instead part of an external collaboration built during the thesis with Dr. Spyros Zafeiratos from the ICPEES institute (Strasbourg, France). The catalyst was prepared and fully studied by Dr. Zafeiratos group for CO_2 conversion to methane and I had the opportunity to contribute to some NEXAFS measurements. I believe that my contribution to these topics was not intense as the efforts spent for

characterization of the oxides aforementioned. For this reason, there is not a chapter dedicated to these samples within the thesis. However, the work on these catalysts led to three publication which I reported in Appendix C, D and E for sake of clarity.

1.4 Low energy reactions

As aforementioned, in low energy reactions C/O ratio does not change hence CO_2 reactivity does not require a redox process.[13] This is the key point making these reactions market appetible and ready for the short-term implementation.[22] Indeed, all the high energy process discussed in the previous paragraph imply the massive use of green H_2, slowing down their short-term application. Contrarily, CO_2 conversion to organic carbonates by reaction with alcohol is an interesting H_2-free chemistry which could represent an immediate boost to CCU. Dimethyl carbonate (DMC) is the simplest carbonate with an increasing market as fuel additive, mild methylating agent and Li-ion batteries electrolyte.[13,23–28] Nevertheless, DMC is currently produced through the three reactions reported below, all implying toxic reagents and/or environmental unfriendly process.[23]

I) $COCl_2 + 2CH_3OH \rightarrow CH_3O(CO)OCH_3 + 2HCl$

II) $2CH_3OH + CO + ½\ O_2 \rightarrow CH_3O(CO)OCH_3 + H_2O$

III) $(CH_3O)_2SO_4 + Na_2CO_3 \rightarrow CH_3O(CO)OCH_3 + Na_2SO_4$

However, CO_2 can be used for direct production of DMC through the reaction with two molecules of methanol reported below.

IV) $CO_2 + 2CH_3OH \rightarrow CH_3O(CO)OCH_3 + H_2O$

Even though $300kt_{CO2}/y$ would be avoided with CO_2-based DMC, currently the reaction has a low efficiency, limiting its real-scale application.[29] Many homogenous catalysts have been proposed however, the separation simplicity, low cost, and negligible toxicity of (heterogenous) metal oxide catalysts make then optimal prototype systems for industrially-relevant applications.[25] However, the reaction yield is rarely higher than 10% (in absence of a sacrificial dehydrating agent), due to the high amount of water, causing catalysts deactivation. The conversion should increase at least to 20% to perform environmentally better than the conventional processes.[30] It is then of outmost importance to understand the catalyst reaction

mechanism for a rational design of new generation catalysts. The first investigated catalysts were ZrO_2 and CeO_2 with almost 100% selectivity but conversion lower than 5%. Even though the first reaction mechanism was proposed by Bell and coworkers[31] for ZrO_2, most of the recent research (Figure 3) is devoted to CeO_2, particularly to the role of oxygen vacancies towards CO_2 activation.

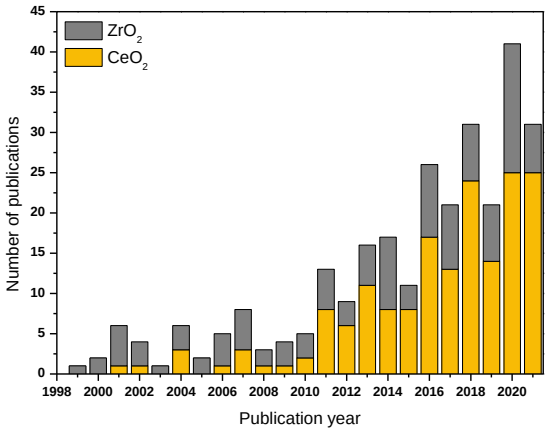

Figure 3 Publications/year distribution related to DMC production from CO_2 and CH_3OH over CeO_2 and ZrO_2 catalysts. Citation Report graphic source: https://www.webofscience.com/ (accessed Apr 28, 2022).

ZrO_2. Through a careful discussion of the surface chemistry of CO_2 and methanol dosed from gas phase, Bell and coworkers proposed a reaction mechanism involving the reaction of a methoxide species with CO_2 bent over a Zr-O Lewis Pair to form monomethylcarbonate (MMC) as reaction intermediate.[32] The last methylation occurs then through an electron donor-acceptor behaviour between methanol and Zr-O Lewis sites. Even though this mechanism followed a very precise analysis of the methoxide and carboxylates IR bands evolution, the complex band evolution might have hidden spectral components heavily overlapped with carbonates and MMC main vibrations. Moreover, working in a condensed phase does not completely reproduce DMC synthesis over oxides since it is usually carried out in liquid phase.[25]

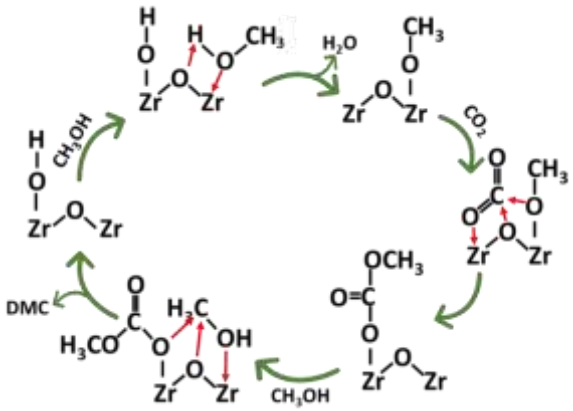

Figure 4 Proposed reaction mechanism of CO_2 and CH_3OH conversion over ZrO_2 catalyst.[31]

Aiming to characterize the surface species involved in the CO_2-to-DMC conversion reaction under realistic conditions we have studied the reaction over ZrO_2 in liquid phase by ATR-IR spectroscopy at temperatures ranging from 10 to 70°C. For a complete understanding of the band kinetic evolution the collected datasets were analysed with MCR-ALS.[33–35] Lastly the same spectra analysis approach was applied to the gas phase reaction repeating the experiment reported by Bell and coworkers,[31] unveiling the presence of spectral components previously not deconvolved.

CeO_2. CeO_2 and its solid solutions with Zr are the oxidic catalysts of major interest for DMC production (Figure 3). Particular attention has been recently dedicated to the role of oxygen vacancies (V_O) which have been proposed to contribute to the CO_2 activation through formation of a bidentate carbonate.[36] Indeed, the presence of the V_O increases charge delocalization over Ce^{4+}/Zr^{4+} improving the interaction with CO_2. Particularly, Liu and co-workers showed as in $CeZrO_x$ catalyst Ce^{3+} has an active role for CO_2 activation.[36]

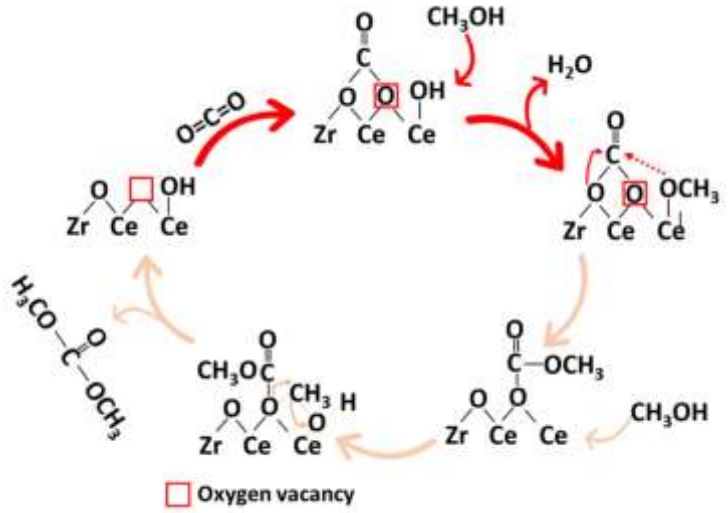

Figure 5 Reaction mechanism of CO_2 and CH_3OH conversion over $CeZrO_2$ catalyst. Darker arrows indicate the new mechanism part involving V_O whilst lighter arrows indicate the mechanism part unchanged respect to the first mechanism proposed by Bell et al.[31]

Their proposed mechanism (Figure 5) implies CO_2/Ce^{3+} redox interaction for a non-redox reaction which is however, not clearly discussed within their manuscript.[36] Moreover, the mechanism was proposed after an operando-FTIR experiment where carbonates bands were superficially assigned without considering the most recent demonstration of all the possible different carbonates vibrating at similar frequencies.[37] Furthermore, it was not considered as Aresta and co-workers reported CeO_2 catalyst deactivation caused by Ce^{3+} formation.[38,39] It is then evident as the proposed mechanism cannot completely describe the CO_2-to-DMC conversion over Ce^{3+}-rich catalyst. To remove the variable related to working with a solid solution i.e., clustering (see Chapter 3 results and discussion) or acidity/basicity differences induced by the guest atom, we have studied CO_2 and CH_3OH adsorption over 4 pure CeO_2 samples with different degree of defectivity and Ce^{3+} content by FT-IR, UV-Vis and XPS. Carbonates assignment was done after a careful analysis of $^{12}CO_2/^{13}CO_2$ IR band shifts whilst Ce^{3+}/CO_2 interaction was studied by Ce(3d) and

O(1s) XPS and UV-Vis spectra. It is noteworthy as the sample with lower Ce^{3+} concentration was not active towards MMC formation (evaluated by FT-IR bands formation) whilst the one with the highest Ce^{3+} content (≈35%) led to formation of Frustrated Lewis Pair (described below) giving access to a more complex and complete reaction mechanism.

Frustrated Lewis Pair (FLP). A FLP, reported in Figure 6 for clarity, consists of a Lewis acid (LA) and a Lewis base (LB) with bulky ligands that prevent these species from neutralizing each other.[40–42]

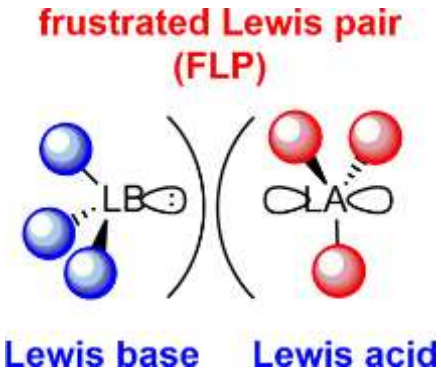

Figure 6 Pictorial representation of a Frustrated Lewis Pair reproduced from Stephan manuscript.[42]

Historically discovered in 1923 and firstly named in 2010,[43] FLP were firstly limited to homogeneous catalysis but extended recently to heterogeneous catalysis.[40,41,44–46] In particular, CeO_2 has been shown to form FLPs between two adjacent Ce^{3+} (LA) and an O_2- (LB) separated by an oxygen vacancy at a distance of ~4Å.[47,48] This particular condition was shown to occur only when surface Ce^{3+} concentration (>30%) ensured clustering of Ce^{3+}-V_O-Ce^{3+} over CeO_2 (101) planes.[49] CeO_2 FLPs improved reactivity of alkenes and alkynes, syngas and recently CO_2 .[47,48,50–52] In the latter case CO_2 activation over heterogeneous catalysts proceed via acid-base interaction with catalyst surface inducing bending of CO_2 double bond and making the C atom more electrophilic.[53] Considering CeO_2 FLPs, Zhang et al. predicted CO_2

activation through the formation of a bidentate carbonate ascribing to its formation the improved CO_2 conversion towards olefins and cyclic carbonates.[52] Nevertheless, the mechanism on how the FLP site activates CO_2 remains unclear. Indeed, FLP presence and activity is very difficult to be observed since it mainly consists of missing oxygens on a catalysts surface well known for its oxygen storage and mobility properties.[54] For this reason, associating improved CO_2 conversion at high temperature over Ce^{3+}-rich CeO_2 to FLP is not straightforward. The MMC formation if then a perfect a case study to disclose details on CO_2/FLP since it implies CO_2 whole incorporation in a new molecule ($CH_3O(CO_2)$-) at a moderate temperature (≈150°C) which prevents CeO_2 oxygen mobility i.e., reducing surface-to-bulk FLP mobility.

References

(1) Rockström, J.; W. Steffen; K. Noone; Å. Persson; F. S. Chapin; E. F. Lambin; T. M. Lenton; M. Scheffer; C. Folke; H. J. Schellnhuber; B. Nykvist; C. A. de Wit; T. Hughes; S. van der Leeuw; H. Rodhe; S. Sörlin; P. K. Snyder; R. Costanza; U. Svedin; M. Falkenmark; L. Karlberg; R. W. Corell; V. J. Fabry; J. Hansen; B. Walker; D. Liverman; K. Richardson; P. Crutzen; J. A. Foley. A Safe Operation Space for Humanity. *Nature* **2009**, *461* (September), 472–475.

(2) Cassia, R.; Nocioni, M.; Correa-Aragunde, N.; Lamattina, L. Climate Change and the Impact of Greenhouse Gasses: CO2 and NO, Friends and Foes of Plant Oxidative Stress. *Front. Plant Sci.* **2018**, *9* (March), 1–11. https://doi.org/10.3389/fpls.2018.00273.

(3) IPCC. Climate Change 2001. Synthesis Report. IPCC Third Assessment Report (TAR). *Ipcc* **2001**, 409.

(4) Putting CO 2 to Use. **2019**, No. September.

(5) Crippa, M.; Oreggioni, G.; Guizzardi, D.; Muntean, M.; Schaaf, E.; Lo Vullo, E.; Solazzo, E.; Monforti-Ferrario, F.; Olivier, J. G. .; Vignati, E. *Fossil CO2 and GHG Emissions of All World Countries - 2019 Report Publications Office of the EU*; 2019. https://doi.org/10.2760/687800.

(6) Aresta, M. *Carbon Dioxide as a Chemical Feedstock*; Prof. Dr. Michele Aresta, Ed.; Wiley-VCH Verlag GmbH & Co. KGaA.

(7) Royal Society. The Potential and Limitations of Using Carbon Dioxide. **2017**, 1–11.

(8) Aresta, M.; Dibenedetto, A.; Angelini, A. Catalysis for the Valorization of Exhaust Carbon : From CO2 to Chemicals, Materials, and Fuels.

Technological Use of CO2. *Chem. Rev.* **2014**, 1–18. https://doi.org/10.1002/9781119951438.eibc2257.

(9) Co, U. *Carbon Capture and Utilisation in the Green Economy*.

(10) Aresta, M.; Dibenedetto, A.; Angelini, A. The Changing Paradigm in CO_2 Utilization. *J. CO2 Util.* **2013**, *3–4*, 65–73. https://doi.org/10.1016/j.jcou.2013.08.001.

(11) Tabanelli, T.; Bonincontro, D.; Albonetti, S.; Cavani, F. *Conversion of CO 2 to Valuable Chemicals : Organic Carbonate as Green Candidates for the Replacement of Noxious Reactants*, 1st ed.; Elsevier B.V., 2019; Vol. 178. https://doi.org/10.1016/B978-0-444-64127-4.00007-0.

(12) Zhou, W.; Cheng, K.; Kang, J.; Zhou, C.; Subramanian, V.; Zhang, Q.; Wang, Y. New Horizon in C1 Chemistry: Breaking the Selectivity Limitation in Transformation of Syngas and Hydrogenation of CO_2 into Hydrocarbon Chemicals and Fuels. *Chem. Soc. Rev.* **2019**, *48* (12), 3193–3228. https://doi.org/10.1039/C8CS00502H.

(13) Sakakura, T.; Choi, J. C.; Yasuda, H. Transformation of Carbon Dioxide. *Chem. Rev.* **2007**, *107* (6), 2365–2387. https://doi.org/10.1021/cr068357u.

(14) Saeidi, S.; Amin, N. A. S.; Rahimpour, M. R. Hydrogenation of CO2 to Value-Added Products - A Review and Potential Future Developments. *J. CO2 Util.* **2014**, *5*, 66–81. https://doi.org/10.1016/j.jcou.2013.12.005.

(15) Wang, S.; Zhang, L.; Zhang, W.; Wang, P.; Qin, Z.; Yan, W.; Dong, M.; Li, J.; Wang, J.; He, L.; Olsbye, U.; Fan, W. Selective Conversion of CO_2 into Propene and Butene. *Chem* **2020**, *6* (12), 3344–3363. https://doi.org/10.1016/j.chempr.2020.09.025.

(16) Liu, X.; Zhou, W.; Yang, Y.; Cheng, K.; Kang, J.; Zhang, L.; Zhang, G.; Min,

X.; Zhang, Q.; Wang, Y. Design of Efficient Bifunctional Catalysts for Direct Conversion of Syngas into Lower Olefins: Via Methanol/Dimethyl Ether Intermediates. *Chem. Sci.* **2018**, *9* (20), 4708–4718. https://doi.org/10.1039/c8sc01597j.

(17) Cheng, K.; Gu, B.; Liu, X.; Kang, J.; Zhang, Q.; Wang, Y. Direct and Highly Selective Conversion of Synthesis Gas into Lower Olefins : Design of a Bifunctional Catalyst Combining Methanol Synthesis and Carbon – Carbon Coupling. **2016**, 4725–4728. https://doi.org/10.1002/anie.201601208.

(18) Cheng, K.; Zhou, W.; Kang, J.; He, S.; Shi, S.; Zhang, Q.; Pan, Y.; Wen, W.; Wang, Y. Bifunctional Catalysts for One-Step Conversion of Syngas into Aromatics with Excellent Selectivity and Stability. *Chem* **2017**, *3* (2), 334–347. https://doi.org/10.1016/j.chempr.2017.05.007.

(19) Thomas, W. J.; Portalski, S. . Thermodynamic in Methanol Synthesis. *Ind. Eng. Chem. Res.* **1958**, *50* (June), 967–970.

(20) Dang, S.; Gao, P.; Liu, Z.; Chen, X.; Yang, C.; Wang, H.; Zhong, L.; Li, S.; Sun, Y. Role of Zirconium in Direct CO2 Hydrogenation to Lower Olefins on Oxide/Zeolite Bifunctional Catalysts. *J. Catal.* **2018**, *364*, 382–393. https://doi.org/10.1016/j.jcat.2018.06.010.

(21) Takeshi, E.; Billinge, S. J. L. *Underneath the Bragg Peaks: Structural Analysis of Complex Materials*; 2012; Vol. 16.

(22) Chauvy, R.; Meunier, N.; Thomas, D.; De Weireld, G. Selecting Emerging CO2 Utilization Products for Short- to Mid-Term Deployment. *Appl. Energy* **2019**, *236* (December 2018), 662–680. https://doi.org/10.1016/j.apenergy.2018.11.096.

(23) Delledonne, D.; Rivetti, F.; Romano, U. Developments in the Production and Application of Dimethylcarbonate. **2001**, *221*, 241–251.

(24) Aricò, F.; Tundo, P. Dimethyl Carbonate as a Modern Green Reagent and Solvent. *Russ. Chem. Rev.* **2010**, *79* (6), 479–489. https://doi.org/10.1070/rc2010v079n06abeh004113.

(25) Keller, N.; Rebmann, G.; Keller, V. Catalysts , Mechanisms and Industrial Processes for the Dimethylcarbonate Synthesis. **2010**, *317*, 1–18. https://doi.org/10.1016/j.molcata.2009.10.027.

(26) Tamboli, A. H.; Chaugule, A. A.; Kim, H. Catalytic Developments in the Direct Dimethyl Carbonate Synthesis from Carbon Dioxide and Methanol. *Chem. Eng. J.* **2017**, *323*, 530–544. https://doi.org/10.1016/j.cej.2017.04.112.

(27) Assabumrungrat, S. Techno-Economic Evaluation of Different CO 2 -Based Processes for Dimethyl Carbonate Production. *Chem. Eng. Res. Des.* **2014**, 1–15. https://doi.org/10.1016/j.cherd.2014.07.013.

(28) Azapagic, A.; Cue, R. M. Carbon Capture , Storage and Utilisation Technologies : A Critical Analysis and Comparison of Their Life Cycle Environmental Impacts. **2015**, *9*, 82–102. https://doi.org/10.1016/j.jcou.2014.12.001.

(29) Otto, A.; Grube, T.; Schiebahn, S.; Stolten, D. Closing the Loop: Captured CO2 as a Feedstock in the Chemical Industry. *Energy Environ. Sci.* **2015**, *8* (11), 3283–3297. https://doi.org/10.1039/c5ee02591e.

(30) Garcia-Herrero, I.; Cuéllar-Franca, R. M.; Enríquez-Gutiérrez, V. M.; Alvarez-Guerra, M.; Irabien, A.; Azapagic, A. Environmental Assessment of Dimethyl Carbonate Production: Comparison of a Novel Electrosynthesis Route Utilizing CO2 with a Commercial Oxidative Carbonylation Process. *ACS Sustain. Chem. Eng.* **2016**, *4* (4), 2088–2097. https://doi.org/10.1021/acssuschemeng.5b01515.

(31) Jung, K. T.; Bell, A. T. An *in Situ* Infrared Study of Dimethyl Carbonate

Synthesis from Carbon Dioxide and Methanol over Zirconia. *J. Catal.* **2001**, *347*, 339–347. https://doi.org/10.1006/jcat.2001.3411.

(32) Zhao, S. Y.; Wang, S. P.; Zhao, Y. J.; Ma, X. Bin. An *in Situ* Infrared Study of Dimethyl Carbonate Synthesis from Carbon Dioxide and Methanol over Well-Shaped CeO2. *Chinese Chem. Lett.* **2017**, *28* (1), 65–69. https://doi.org/10.1016/j.cclet.2016.06.003.

(33) Jaumot, J.; Gargallo, R.; De Juan, A.; Tauler, R. A Graphical User-Friendly Interface for MCR-ALS: A New Tool for Multivariate Curve Resolution in MATLAB. *Chemom. Intell. Lab. Syst.* **2005**, *76* (1), 101–110. https://doi.org/10.1016/j.chemolab.2004.12.007.

(34) Ruckebusch, C.; Blanchet, L. Multivariate Curve Resolution: A Review of Advanced and Tailored Applications and Challenges. *Anal. Chim. Acta* **2013**, *765*, 28–36. https://doi.org/10.1016/j.aca.2012.12.028.

(35) Alcaráz, M. R.; Schwaighofer, A.; Goicoechea, H.; Lendl, B. Application of MCR-ALS to Reveal Intermediate Conformations in the Thermally Induced α-β Transition of Poly-L-Lysine Monitored by FT-IR Spectroscopy. *Spectrochim. Acta - Part A Mol. Biomol. Spectrosc.* **2017**, *185* (May 2017), 304–309. https://doi.org/10.1016/j.saa.2017.05.005.

(36) Liu, B.; Li, C.; Zhang, G.; Yao, X.; Chuang, S. S. C.; Li, Z. Oxygen Vacancy Promoting Dimethyl Carbonate Synthesis from CO2 and Methanol over Zr-Doped CeO2 Nanorods. *ACS Catal.* **2018**, *8* (11), 10446–10456. https://doi.org/10.1021/acscatal.8b00415.

(37) Vayssilov, G. N.; Mihaylov, M.; Petkov, P. S.; Hadjiivanov, K. I.; Neyman, K. M. Reassignment of the Vibrational Spectra of Carbonates , Formates , and Related Surface Species on Ceria : A Combined Density Functional and Infrared Spectroscopy Investigation. *J. Phys. Chem. C* **2011**, *115* (47), 23435–

23454.

(38) Aresta, M.; Dibenedetto, A.; Pastore, C.; Cuocci, C.; Aresta, B.; Cometa, S.; De Giglio, E. Cerium(IV)Oxide Modification by Inclusion of a Hetero-Atom: A Strategy for Producing Efficient and Robust Nano-Catalysts for Methanol Carboxylation. *Catal. Today* **2008**, *137* (1), 125–131. https://doi.org/10.1016/j.cattod.2008.04.043.

(39) Aresta, M.; Dibenedetto, A.; Pastore, C.; Angelini, A.; Aresta, B.; Pápai, I. Influence of Al2O3 on the Performance of CeO2 Used as Catalyst in the Direct Carboxylation of Methanol to Dimethylcarbonate and the Elucidation of the Reaction Mechanism. *J. Catal.* **2010**, *269* (1), 44–52. https://doi.org/10.1016/j.jcat.2009.10.014.

(40) Stephan, D. W. Frustrated Lewis Pairs: From Concept to Catalysis. *Acc. Chem. Res.* **2015**, *48* (2), 306–316. https://doi.org/10.1021/ar500375j.

(41) Stephan, D. W.; Erker, G. Frustrated Lewis Pairs: Metal-Free Hydrogen Activation and More. *Angew. Chemie - Int. Ed.* **2010**, *49* (1), 46–76. https://doi.org/10.1002/anie.200903708.

(42) Stephan, D. W. Frustrated Lewis Pairs. *J. Am. Chem. Soc.* **2015**, *137* (32), 10018–10032. https://doi.org/10.1021/jacs.5b06794.

(43) McCahill, J. S. J.; Welch, G. C.; Stephan, D. W. Reactivity of "Frustrated Lewis Pairs": Three-Component Reactions of Phosphines, a Borane, and Olefins. *Angew. Chemie* **2007**, *119* (26), 5056–5059. https://doi.org/10.1002/ange.200701215.

(44) Stephan, D. W.; Erker, G. Frustrated Lewis Pair Chemistry: Development and Perspectives. *Angew. Chemie - Int. Ed.* **2015**, *54* (22), 6400–6441. https://doi.org/10.1002/anie.201409800.

(45) Pérez, M.; Mahdi, T.; Hounjet, L. J.; Stephan, D. W. Electrophilic Phosphonium Cations Catalyze Hydroarylation and Hydrothiolation of Olefins. *Chem. Commun.* **2015**, *51* (56), 11301–11304. https://doi.org/10.1039/c5cc03572d.

(46) Stephan, D. W. The Broadening Reach of Frustrated Lewis Pair Chemistry. *Science (80-.).* **2016**, *354* (6317). https://doi.org/10.1126/science.aaf7229.

(47) Zhang, S.; Huang, Z. Q.; Ma, Y.; Gao, W.; Li, J.; Cao, F.; Li, L.; Chang, C. R.; Qu, Y. Solid Frustrated-Lewis-Pair Catalysts Constructed by Regulations on Surface Defects of Porous Nanorods of CeO2. *Nat. Commun.* **2017**, *8* (May), 1–11. https://doi.org/10.1038/ncomms15266.

(48) Huang, Z. Q.; Liu, L. P.; Qi, S.; Zhang, S.; Qu, Y.; Chang, C. R. Understanding All-Solid Frustrated-Lewis-Pair Sites on CeO2 from Theoretical Perspectives. *ACS Catal.* **2018**, *8* (1), 546–554. https://doi.org/10.1021/acscatal.7b02732.

(49) Nolan, M.; Parker, S. C.; Watson, G. W. The Electronic Structure of Oxygen Vacancy Defects at the Low Index Surfaces of Ceria. *Surf. Sci.* **2005**, *595* (1–3), 223–232. https://doi.org/10.1016/j.susc.2005.08.015.

(50) Huang, Z. Q.; Li, T. H.; Yang, B.; Chang, C. R. Role of Surface Frustrated Lewis Pairs on Reduced CeO2(110) in Direct Conversion of Syngas. *Chinese J. Catal.* **2020**, *41* (12), 1906–1915. https://doi.org/10.1016/S1872-2067(20)63627-0.

(51) Lim, C. H.; Holder, A. M.; Hynes, J. T.; Musgrave, C. B. Roles of the Lewis Acid and Base in the Chemical Reduction of CO 2 Catalyzed by Frustrated Lewis Pairs. *Inorg. Chem.* **2013**, *52* (17), 10062–10066. https://doi.org/10.1021/ic4013729.

(52) Zhang, S.; Xia, Z.; Zou, Y.; Cao, F.; Liu, Y.; Ma, Y.; Qu, Y. Interfacial

Frustrated Lewis Pairs of CeO2 Activate CO2 for Selective Tandem Transformation of Olefins and CO2 into Cyclic Carbonates. *J. Am. Chem. Soc.* **2019**, *141* (29), 11353–11357. https://doi.org/10.1021/jacs.9b03217.

(53) Borges, M.; Ø, J. J. Ø. C.; Olcina, J. G.; Hu, L.; Cornu, D.; Huang, R.; Stoian, D.; Urakawa, A. CO2 Activation over Catalytic Surfaces. *ChemPhysChem* **2017**, *18*, 3135–3141. https://doi.org/10.1002/cphc.201700782.

(54) Montini, T.; Melchionna, M.; Monai, M.; Fornasiero, P. Fundamentals and Catalytic Applications of CeO2-Based Materials. *Chem. Rev.* **2016**, *116* (10), 5987–6041. https://doi.org/10.1021/acs.chemrev.5b00603.

2 Materials and methods

2.1 Materials

All the samples described in Chapter 3 were characterized as received from one of the COZMOS partner. Most of the reported data were measured from one of the partners as well. When catalytic results were not available, literature data are reported for sake of comparison.

Zn-doped ZrO_2 samples described in Chapter 3 have been characterized as received from the University of Oslo (Norway). Briefly, catalysts were prepared by coprecipitation of $Zn(NO_3)_2$ and ZrN_2O_7 salts as described elsewhere.[1] Catalysts will be referred to as ZnZr(X) where "X" indicates Zn wt% evaluated by either ICP or EDX analysis. Pure ZrO_2 related to these samples was prepared with the same synthesis strategy without Zn salts.

Ga-doped ZrO_2 was prepared at the ICC Institute following the published receipt.[2] Ga content was evaluated by EDX analysis.

$ZnCeZrO_x$ catalyst described in Chapter 3.7 was prepared by ICC following the published receipt.[3] Zn and Ce contents were determined by ICP analysis.

Zeolites/Zeotypes. Even though the core of the studies withing this thesis were the employed oxides materials, few details on the reported zeolites and zeotypes employed for the reported catalytic test should be reported. **H-ZSM5 and SAPO-34** were commercial catalysts purchased by Zeolyts and ACS materials, respectively. Their characterization is fully described in the published manuscript reported in Appendix A.[1] **H-SSZ-13** was prepared by ICC following a receipt which is currently under publication. **H-RUB-13** was prepared by ICC partner as described in the respective published manuscript.[3]

ZrO_2 described in Chapter 4 was prepared by sol-gel synthesis according to the literature.[4]

CeO_2 catalysts reported in Chapter 4 were prepared by microwave (MW)-assisted sol-gel synthesis adapted from a conventional protocol.[5] As shown in Figure 7, microwaves were chosen as a heat source since they allow to rapidly obtain a homogenous temperature in the reactor cell, implying fast and reproducible synthesis with the formation of small crystallites due to high nucleation/low growth rates.

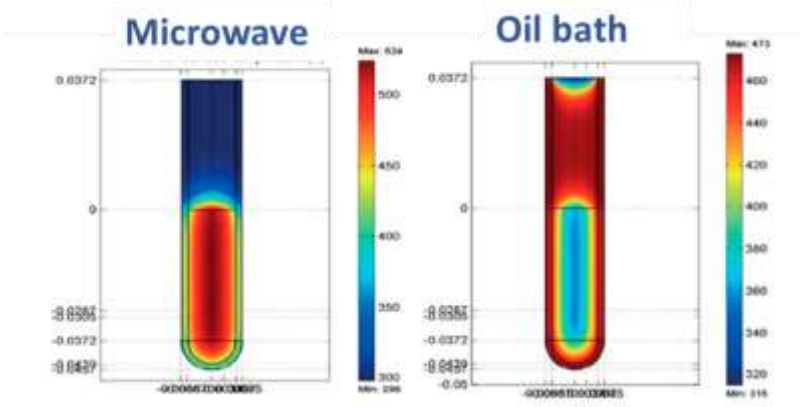

Figure 7 Thermal profile of a glass vial heated in a conventional oil bath and in a microwave reactor. The figure is reproduced from Zhu et al.[6]

The obtained CeO_2 powder was then divided into two batches, **MW(100)** and **MW(650)**, which were calcined under air for 8 h at 100 °C and 650 °C, respectively. Reference material was also prepared by conventional sol-gel synthesis and calcined at 650°C for 8h (**conv(650)**). [5]

2.2 Methods

2.2.1 Specific surface area.

Since the work of the thesis is dedicated to the catalysts characterization rather than the improvement of a synthesis strategy, the specific surface area (SSA) is used as valuable information to verify if a series of samples presented a comparable surface area hence excluding it from influencing the catalysts different properties. The SSAs

were determined by applying the Brunauer–Emmett–Teller (BET) method to the adsorption/desorption isotherms of N_2 at 77K obtained with a Micromeritics ASAP 2020 physisorption analyzer.[7]

2.2.2 Powder X-Ray Diffraction

Powder X-Ray diffraction (PXRD) patterns were collected to investigate the average structural properties of the catalysts i.e., phase composition and lattice parameters. In-situ PXRD measurements were particularly useful to follow the unit cell volume variation during thermal treatments.

The Laboratory PXRD patterns were collected at room temperature (RT) with a PW3050/60 X'Pert PRO MPD diffractometer (PANalytical) in the Bragg–Brentano geometry using either a flat glass sample holder or a spinning zero-noise Si holder. Patterns from the Cu $K\alpha_{1,2}$ X-ray source were recorded from 10 to 90° 2θ with a step size of 0.0167° and an integration time of 40 s. The Rietveld refinement method implemented in the FullProf software package[8] was used to extract phase abundances, lattice parameters and peak shapes following the procedure described in the manuscript reported in appendix.[1]

Ex situ Synchrotron PXRD patterns were recorded in transmission mode at BM31 beamline (ESRF) in Debye-Scherrer configuration employing monochromatic radiation (λ~0.270Å). Debye-Scherrer cones were collected from a CCD camera and were further integrated to obtain the reported line graphs. Samples were contained in a quartz capillary (Ø=0.5 mm). In-situ PXRD patterns were measured in the same capillary by flowing a 50 mL/min H_2:He flow (1:2) whilst heat was provided by a heat blower.

Unit cell volume variation with temperature was extracted from the in-situ PXRD pattern by using FullProf implemented sequential mode.

2.2.3 Fourier Transform Infrared spectroscopy (FTIR)

FTIR is an important technique to study catalyst surfaces adsorption properties. Indeed, the vibrational spectra of adsorbed molecules such as CO, CO_2, and CH_3OH gave important information on the catalysts' defectivity, oxidation state, and reactivity. In the case of ***ex situ*** **experiments** the sample was pressed to form a self-standing pellet of ≈10 cm^2 placed in a gold envelope. The envelope was then placed in a home-made cell equipped with KBr windows and suitable for thermal treatments under high vacuum (5E-04mbar) or gas environment (O_2/H_2). After the activation process (see below) the cell was mounted on the FT-IR instrument where a dedicated glass line allowed the dosing of controlled pressures/volume of specific molecules.

Ce^{3+}. FTIR spectra of the sample as prepared or as activated (see activation procedure hereafter) are already very informative. Indeed, as it will be discussed within Chapter 4, the presence of Ce^{3+} can be already qualitatively determined from the presence of a band at 2127 cm^{-1} in the sample spectra prior to the adsorption of any molecule. Indeed, this band is related to the $^2F_{5/2} \rightarrow {}^2F_{7/2}$ electronic adsorption which is present only in Ce^{3+}($[Xe]4f^15d^06s^0$) and absent in Ce^{4+} ($[Xe]4f^05d^06s^0$).[9,10]

CO. Carbon monoxide is employed since decades as simple accessible probe molecule to investigate the chemical nature of surface sites.[11,12] Once CO interacts with metal/ions sites on the catalyst surface, depending on the cation ionic potential, the predominant charge withdrawing direction can be divided into CO-to-cation or cation-to-CO, defining the interaction as σ-donation or π-backdonation, respectively. The former depletes charge density from CO slightly antibonding level, increasing its bond strength and causing a hypsochromic shift from the ideal CO stretching vibration (2143 cm^{-1}), whilst the latter fills CO strongly antibonding levels, weakening the triple bond and inducing a bathochromic shift. Typically, for cationic sites σ-donation prevails, for metallic sites π-backdonation prevails, thus causing bathochromic and hypsochromic, respectively, of the stretching vibration of adsorbed CO. As a consequence, CO adsorption allows to determine whether: a)

strong and weak Lewis acid sites (Ce^{4+} and Zr^{4+}),[13,14] are still present over the catalyst surface after grafting and reduction treatments (bands shifted to lower wavenumbers) and b) if Ce^{3+} is present on the surface from a typical band shifted around 2130 cm^{-1}.

CO adsorption experiments were carried out with an ad-hoc cell equipped with KBr windows allowing to cool the pellet temperature down to liquid nitrogen temperature (nominal 100K).

The adsorption of **CO_2** and **CH_3OH** is discussed within the text.

Activation. Before IR measurements, catalysts generally underwent an activation meant to clean the surface and to leave an oxidised/reduced state. In both cases, the followed protocol consisted on: i) outgassing and heating the catalyst at 5°C/min from RT to 150°C under vacuum, ii) heating from 150°C to 400°C (5°C/min) under static 100 mbar O_2 for CeO_2 (to prevent CeO_2 self-reduction) and under vacuum (5E-04 mbar) for ZrO_2 , iii) holding at 400°C for 30' under O_2 atmosphere, iv) cooling under O_2 until 150°C and then evacuating. In the case of reduced CeO_2 (MW(100)-red) the sample was kept at 150°C under H_2 for 30' then cooled to RT under vacuum (5E-04 mbar).

Operando IR experiments. Operando IR experiments were performed using FTIR in the case of gas-phase experiments and in ATR-IR mode for liquid-phase experiments. ATR-IR set-up description can be found in the submitted manuscript reported in the Appendix F. Gas phase experiments were conducted to study CO_2/CH_3OH alone and coupled adsorption/desorption kinetics on ZrO_2 surface. ZrO_2 sample was pressed into a self-standing pellet of ~10 mg mass and ~100 mm^2 area which was placed into a commercial water-cooled cell heatable stainless steel cell (Aabspec) suitable for thermal treatments (RT-400°C) under gas flow mounted in a Bruker Invenio spectrometer. Input gas flow was connected to the set-up reported in Figure 8 whilst the output stream was connected to a Mass Spectrometer.

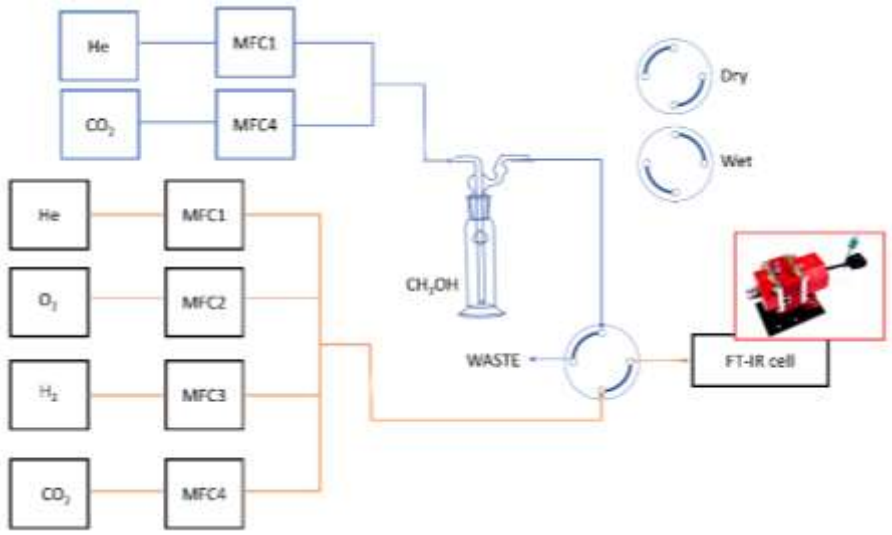

Figure 8 Scheme of the reaction set-up employed for operando IR. The employed 4-way valve is represented in both configurations allowing to send either dry or wet gases to the FT-IR cell.

A constant flow of 40 mL/min of all the employed gases was kept constant through the experiments. Prior CO_2/CH_3OH adsorption, desorption or reaction the catalyst underwent an activation procedure consistent into heating from RT to 400°C under an He:O_2 flow (50:50) and by holding the temperature at 400°C for 60'. After the activation the sample was cooled to RT or 150°C under He flow. CO_2 (99.999%) was provided through a Brookhaven mass-flowmeter whilst CH_3OH flow was obtained by flowing He through a gas-liquid bubbler filled with CH_3OH and kept at constant temperature. CH_3OH concentration in the bubbler output was calculated using the equation below.

$$F_{v,out} = F_{c,in} * \frac{P_v}{P_{head}.P_v}$$

The output vapour flow ($F_{v,out}$) is calculated in function of the incoming carrier flow ($F_{c,in}$), the liquid vapour pressure (P_v) which is temperature dependent (Figure 9) and

the bubbler head pressure (P_{head}) which is assumed to be equal to the ambient pressure.

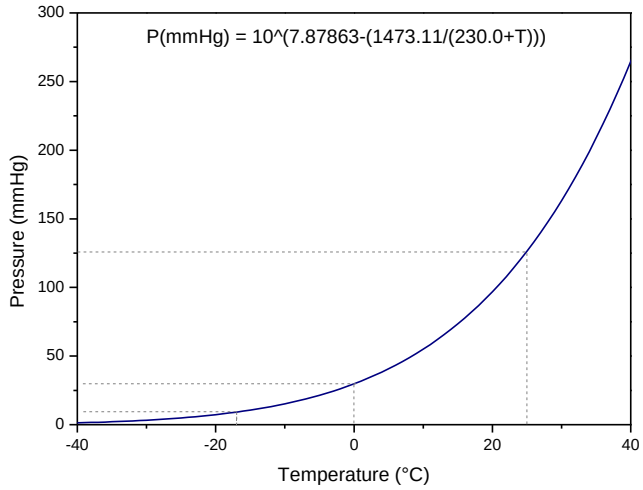

Figure 9 Graph reporting methanol vapour pressure relation with temperature. Source Langest's Handbook of Chemistry 10th ed.

2.2.4 UV-Vis Spectroscopy

UV-Vis spectra gave information on the catalyst's average electronic properties. Diffuse Reflectance UV-Vis spectra of CeO_2 samples described in CHAPTER 4.4 were collected in a Varian Cary 5000 spectrophotometer, equipped with an integrating sphere with an inner surface coated by Spectralon®(the same material used as white reference). The powders were placed in a quartz bulb cell, allowing thermal treatments. Pre-treatments and CO_2 interaction were performed in the same way as for the IR measurements. DR-UV-Vis spectra for Ga/Zn/Ce-ZrO_2 samples described in CHAPTER 3 were recorded on pellets with Avantes optic fibers.

2.2.5 X-ray Photoelectron Spectroscopy (XPS)

X-Ray Photoelectron Spectroscopy (XPS) is based on the measurement of the photoelectrons emitted after the absorption of an incoming photon. A dual anode X-Ray source (Al K_α) causes the emission of photoelectrons in the 0-1000 eV binding

energy range whilst an analyzer allows photoelectron energy discrimination, particularly in the Ce(3d) (870-980 eV), O(1s)(520-540 eV) and C(1s)(280-290 eV) energy regions. Quasi *in situ* X-Ray Photoelectron Spectroscopy (XPS) measurements were carried out at ICPEES (Strasbourg) in the laboratory of Dr. Spyros Zafeiratos. The ultrahigh vacuum (UHV) spectrometer was equipped with a variable pressure reactor allowing thermal/gas treatments of the catalyst in controlled atmosphere and consequent transfer to the XPS analysis chamber without exposing it to air. All the details concerning the measurement and the following data analysis are described in the manuscript under submission reported in the Appendix G.

Beam damage of as-prepared MW(100) (see Chapter 3) was evaluated for I) beam exposure during time and II) sample heating under vacuum. Considering dual anode beam damage (Figure 10a,b) we observed as by collecting spectra with 5min/scan (Figure 10a) the $Ce^{4+/3+}$ regions begin to vary after 30'. The first scan (5') presented Ce^{3+} abundance of 11% whilst averaging the 6 spectra in Figure 10a led to Ce^{3+}≈14%. Since there is not a considerable difference between the two spectra and fit results, we proceeded by collecting spectra with 30' time/scan for 330', observing as Ce^{3+} concentration increased to 15% after 60' of exposure while the sample temperature increased to 25°C. Eventually, Ce^{3+} concentration increased up to 25% after 330' exposure and temperature grew up to 35°C. On the contrary, catalyst damage induced by temperature under UHV (Figure 10b,c) showed a drastic increase of Ce^{3+} concentration already at 150°C, reaching values >45% at 400°C. These results showed as: I) dual anode exposure increased Ce^{3+} abundance of 4% in the first 60' and II) heating under vacuum had a stronger effect on Ce^{3+} oxidation state. Since at 50°C we observed 27% Ce^{3+} and after 330' of sample exposure to dual anode its temperature/Ce^{3+} reached 32°C/23%, we can conclude that heating from the X-Ray beam caused most of the damage from its exposure. To minimize the beam exposure effect on Ce(3d) region and following the evidence in Figure 10a, we then measured this region as the first one limiting the measurement to 30' time/scan.

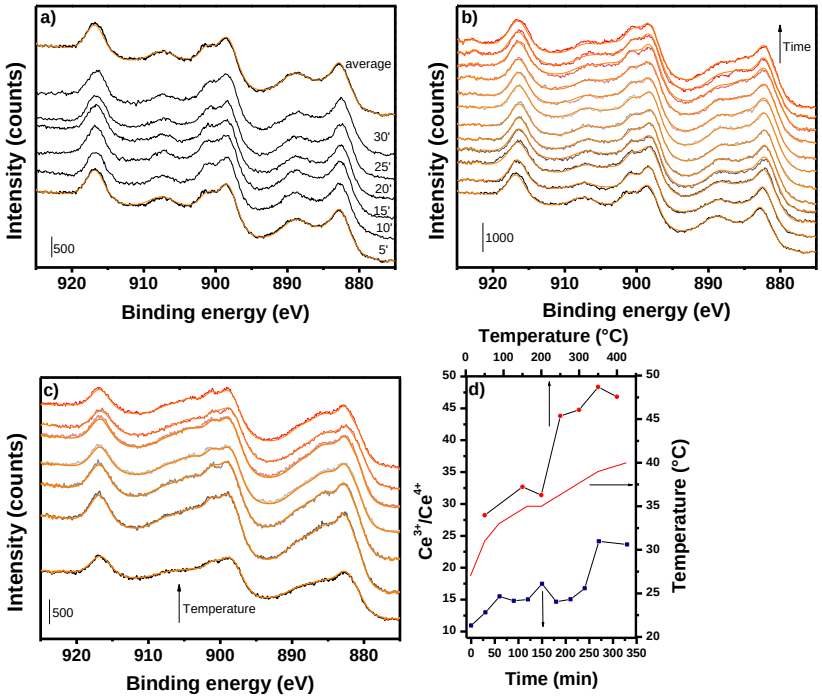

Figure 10 XPS experimental data and best fit curves (orange lines) collected : a) with 5' time/scan for 30' exposure to dual anode beam, b) with 30' time/scan for 330' exposure to dual anode beam (time increases from black to red line) and c) with 30' time/scan during heating under UHV (temperature increases from black to red line). d) Ce^{+3}/Ce^{+4}concentration evaluated by best-fit curves during the time and temperature measurements. Samples stage temperature profile evolution during time experiment is reported with red line.

2.2.6 X-Ray Absorption Fine Structure (XAFS)

XAFS is a well-known technique referring to the X-Ray absorption properties of an atom core-level. Particularly at energies lower and higher than the core-level binding energy the absorption probability is modulated by the absorber chemical and physical state. This makes XAFS an element selective technique sensitive to little concentration of the absorber. The XAFS spectrum is usually divided into two regions: I) x-ray absorption near edge (XANES) region, containing information on

the formal oxidation state and local geometry (tetrahedral, octahedral, etc.) and II) extended x-ray absorption fine structure (EXAFS) which is employed to determine structural information on the absorber environment (e.g., distances and coordination number with surrounding atoms). Multi-edge fit is a well-known approach to determine local disorder in alloys and oxides.[ref] Nevertheless, this approach is rarely employed in the catalysis community where catalysts are often claimed to be homogenous solid solutions by simple PXRD and single edge-fit, employing the determined structure to predict catalyst behaviour such as reaction mechanisms. Since the knowledge of the catalyst local structure is extremely important for these types of studies, this thesis aims to employ the multi-edge fit approach to the limit of its interpretability. However, as discussed in the thesis, often the catalyst presented such a high degree of disorder to imply the use of single edge-fit applied to all the measured sample edges. Zn, Zr and Ce K-edges were all recorded in transmission mode during several beamtimes at ESRF (BM31 and BM23 beamlines) and SOLEIL (Rock Beamline) synchrotrons, hence the experimental details are well reported in the Appendix.[1,15]

Ga K-edge spectra were recorded in fluorescence mode to discard to the contribution of Hf $L_{2,1}$-edges which were always present since Hf is a natural dopant of Zr. Spectra were energy aligned to the respective metal despite for Ce K-edge which was aligned to a reference CeO_2 sample provided by Sigma Aldrich (>99%). Energy alignment, background subtraction and edge-jump normalization were conducted with the Athena software from the Demeter package.[16] FT-EXAFS fit was conducted with the Artemis software from the same package. EXAFS fit procedure (fully described in the published manuscript reported in Appendix B[15]) was applied to extract scattering paths coordination numbers and radial distances. Concerning the fit of data collected during thermal treatments, the thermal Debye-Waller factors were modelled using the Einstein model as described in Appendix B.[15]

Hf as an internal reference. Hf is a natural dopant of Zr salts which is not-easily separate from ZrO_2 hence its concentration was evaluated by ICP analysis.[17,18] Hf participates neither to the CO_2 hydrogenation reaction nor in ZrO_2 tetragonal polymorph stabilization. Since its presence can be considered stable and constant during the whole reaction process, it can be used as an internal reference. By taking 3 ZnZr(X) samples (Figure 11a) normalized at the Zn K-edge we can observe as there is variation of Hf L_3-edge jump. This becomes clearer by normalizing the spectra at the Hf edge (Figure 11b) where Zn K-edge jump is observed to increase with Zn concentration. Indeed, by considering the latter normalization, we expressed Zn edge jump in function of Zn concentration obtaining the calibration line in Figure 11c. Since the same Zr salt precursor was used to prepare all the ZnZr(X) samples discussed in the thesis, this calibration line was used to evaluate the amount of Zn in samples with unknown concentrations and which available amount was too little to perform elemental analysis (e.g., ICP).

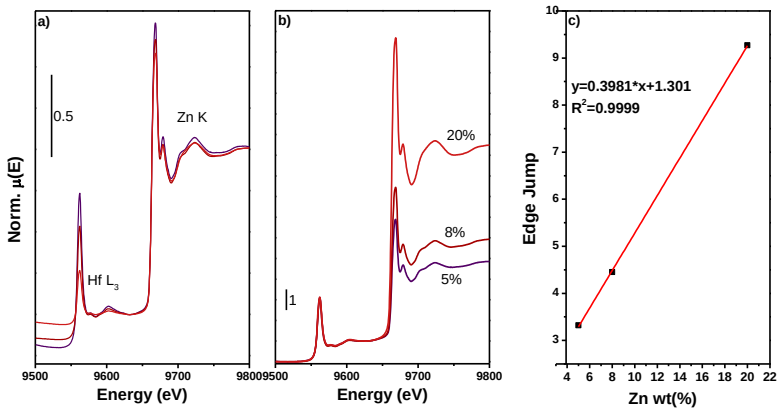

Figure 11 Zn K-edge and Hf L_3-edge energy regions for ZnZr(X) samples normalized at a) Zn K-edge and b) Hf L_3-edge. c) Zn concentration calibration line.

Ga K-edge XANES fit. Following the available literature[19,20] Ga K-edge XANES were fitted with pseudo-Voight (PV) (1) and arctangent function (2)

$$f(x) = \frac{A}{[1 + M(x - x_0)^2/\beta^2]\exp\{(1 - M)[(ln2)(x - x_0)^2/\beta^2]\}}$$

(1) Employed pseudo-Voight function where A, β, x0 and M are the curve height, full width half maximum, peak position and Lorentzian contribution ratio, respectively.

$$g(x) = B\left\{\left(\frac{1}{\pi}\right) arctan\left(\frac{x - x_0'}{\Gamma/2}\right) + (1/2)\right\}$$

(2) Employed arctangent function where B, Γ and x0' are the curve height, full width half maximum and inflection point, respectively.

For fitting Ga K-edge spectra 2 PV and 2 arctan functions were used to describe Ga tetrahedral (Td) and octahedral (Oh) coordination, respectively. M was fixed to 0.2 after its optimization through fitting Ga_2O_3 XANES as reference (Ga_2O_3 XANES fit results

	Tetrahedral				Octahedral			
	x0 (eV)	β (eV)	Γ (eV)	%	x0 (eV)	β (eV)	Γ (eV)	%
Ga2O3	10373.5	3.8	2.6	49	10376.7	4.1	1.2	51

) trying to maintain β, Γ, x0, x0' parameters for each couple included in their range found in literature (Table 1).[19,20] "A" was not constrained whilst B was fixed to 0.5 since spectra edge-jump was normalized to 1. Ga(Td) : Ga(Oh) ratio was quantitatively evaluated from the peak area ratio. The ratio obtained from Ga_2O_3 (as close as possible to 1) was used as feedback for evaluating the goodness of fit.

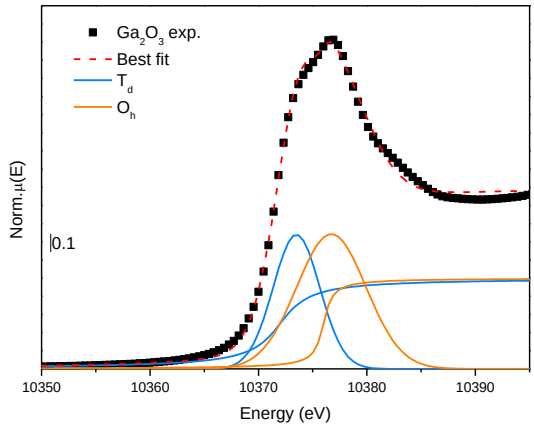

Figure 12 Ga_2O_3 XANES experimental spectra (squares) and best fit (dashed red line). Ga T_d and O_h pseudo Voight/arctan components are reported with blue and orange lines, respectively.

Table 1 Ga_2O_3 XANES fit results

	Tetrahedral				Octahedral			
	x0 (eV)	β (eV)	Γ (eV)	%	x0 (eV)	β (eV)	Γ (eV)	%
Ga_2O_3	10373.5	3.8	2.6	49	10376.7	4.1	1.2	51

Multi-edge approach. To have a complete description of the investigated catalysts a "multi-edge" approach was necessary. Indeed, XAFS spectra were measured not only for the guest element but also for the host matrix under the same conditions, allowing an improved parametrization of EXAFS fitting and a more complete description of the structure of the catalyst. For some specific elements such as Ce, we explored both K- and M_5-edges, which are in the hard and soft x-ray regions, respectively. The sensitivity of the two regions to bulk and surface properties gave access to important details of $Ce^{+3/+4}$ redox behaviour.

2.2.7 Multivariate Curve Resolution – Alternating Least Squares (MCR-ALS)

MCR-ALS is a powerful method to deconvolute a series of overlapping spectra presenting a significant variance. Briefly, a matrix D(m x n) is deconvoluted into two matrices C(m x k) and S^T(k x n) according to the equation : $D = SC^T + E$.

Spectroscopically speaking, D is a matrix where the rows represent energy points and columns the spectra, S is the matrix of the pure spectral profiles, C (^{T} : transpose) contains rows of concentration profiles related to each spectrum in S and E is the error matrix. The final aim of MCR analysis is then to identify the spectral components source of the variation observed in the dataset whilst the ALS procedure perform an alternated optimization of concentration and spectral profile at each cycle. It is then clear as this is a powerful chemometric approach to identify and quantify pure spectral components without possessing reference spectra of those components.

MCR requires an initial estimation of the number of components in the system. This it is done by Singular Value Decomposition (SVD) which describes the data into orthogonal vectors (e.g., linearly independent) helping the determination of the data matrix rank. This is probably the most complex and physically difficult task in the MCR process and has been carefully described in literature.[21] In all the reported MCR-ALS data the rank determination did not follow such a rigorous procedure as reported by Martini et al. [21] The elbow in the scree plot between variance and the component number was used to differentiate meaningful components from the data noise. This “non-golden rule” often leads to an ambiguous ranking assignment. Implicit assumption and “good practice” were then considered in support to the number of components determination. Another important step of MCR analysis is the rational application of constraints such as non-negativity and closure, which employment strongly depended on the dataset origin.

Indeed, MCR-ALS was applied to both XAS and FT-IR data in order to extract the pure spectral components and their concentration profiles. The main difference between the two datasets is on the applied constraints i.e., whilst non-negativity is applied to both XAS and FTIR spectral and concentration, closure is applied only to XAS data since in FTIR, due to different extinction coefficient of the formed species (e.g., carbonates, methoxides), closure is no longer valid.

References

(1) Ticali, P.; Salusso, D.; Ahmad, R.; Ahoba-Sam, C.; Ramirez, A.; Shterk, G.; Lomachenko, K. A.; Borfecchia, E.; Morandi, S.; Cavallo, L.; Gascon, J.; Bordiga, S.; Olsbye, U. CO 2 Hydrogenation to Methanol and Hydrocarbons over Bifunctional Zn-Doped ZrO 2 /Zeolite Catalysts. *Catal. Sci. Technol.* **2021**. https://doi.org/10.1039/D0CY01550D.

(2) Zhang, P.; Ma, L.; Meng, F.; Wang, L.; Zhang, R.; Yang, G.; Li, Z. Boosting CO2 Hydrogenation Performance for Light Olefin Synthesis over GaZrOx Combined with SAPO-34. *Appl. Catal. B Environ.* **2022**, *305* (December 2021), 121042. https://doi.org/10.1016/j.apcatb.2021.121042.

(3) Wang, S.; Zhang, L.; Zhang, W.; Wang, P.; Qin, Z.; Yan, W.; Dong, M.; Li, J.; Wang, J.; He, L.; Olsbye, U.; Fan, W. Selective Conversion of CO_2 into Propene and Butene. *Chem* **2020**, *6* (12), 3344–3363. https://doi.org/10.1016/j.chempr.2020.09.025.

(4) Gionco, C.; Paganini, M. C.; Giamello, E.; Sacco, O.; Vaiano, V.; Sannino, D. Rare Earth Oxides in Zirconium Dioxide: How to Turn a Wide Band Gap Metal Oxide into a Visible Light Active Photocatalyst. *J. Energy Chem.* **2017**, *26* (2), 270–276. https://doi.org/10.1016/j.jechem.2016.07.006.

(5) Manzoli, M.; Menegazzo, F.; Signoretto, M.; Cruciani, G.; Pinna, F. Effects of Synthetic Parameters on the Catalytic Performance of Au/CeO2 for Furfural Oxidative Esterification. *J. Catal.* **2015**, *330*, 465–473. https://doi.org/10.1016/j.jcat.2015.07.030.

(6) Zhu, Y. J.; Chen, F. Microwave-Assisted Preparation of Inorganic Nanostructures in Liquid Phase. *Chem. Rev.* **2014**, *114* (12), 6462–6555. https://doi.org/10.1021/cr400366s.

(7) Brunauer, S.; Emmett, P. H.; Teller, E. Adsorption of Gases in Multimolecular

Layers. *J. Am. Chem. Soc.* **1938**, *60* (2), 309–319. https://doi.org/10.1021/ja01269a023.

(8) Rodríguez-Carvajal, J. Recent Developments of the Program Fullprof. *Newsl. Comm. Powder Diffr. IUCr* **2001**, *26* (International Union of Crystallography), 12–19.

(9) Bozon-Verduraz, F.; Bensalem, A. IR Studies of Cerium Dioxide: Influence of Impurities and Defects. *J. Chem. Soc. Faraday Trans.* **1994**, *90* (4), 653–657. https://doi.org/10.1039/FT9949000653.

(10) Binet, C.; Badri, A.; Lavalley, J. C. A Spectroscopic Characterization of the Reduction of Ceria from Electronic Transitions of Intrinsic Point Defects. *J. Phys. Chem.* **1994**, *98* (25), 6392–6398. https://doi.org/10.1021/j100076a025.

(11) Hadjiivanov, K. I.; Vayssilov, G. N. Characterization of Oxide Surfaces and Zeolites by Carbon Monoxide as an IR Probe Molecule. *Adv. Catal.* **2002**, *47*, 307–511. https://doi.org/10.1016/S0360-0564(02)47008-3.

(12) Zecchina, A.; Scarano, D.; Bordiga, S.; Ricchiardi, G.; Spoto, G.; Geobaldo, F. IR Studies of CO and NO Adsorbed on Well Characterized Oxide Single Microcrystals. *Catal. Today* **1996**, *27* (3–4), 403–435. https://doi.org/10.1016/0920-5861(95)00202-2.

(13) Pokrovski, K.; Jung, K. T.; Bell, A. T. Investigation of CO and CO2 Adsorption on Tetragonal and Monoclinic Zirconia. *Langmuir* **2001**, *17* (14), 4297–4303. https://doi.org/10.1021/la001723z.

(14) Li, C.; Sakata, Y.; Arai, T.; Domen, K.; Maruya, K. Carbon Monoxide and Carbon Dioxide Adsorption on Cerium Oxide Studied by Fourier- Transform Infrared Spectroscopy. **1989**, *85* (4), 929–943.

(15) Salusso, D.; Borfecchia, E.; Bordiga, S. Combining X-Ray Diffraction and X-

Ray Absorption Spectroscopy to Unveil Zn Local Environment in Zn-Doped ZrO2Catalysts. *J. Phys. Chem. C* **2021**, *125* (40), 22249–22261. https://doi.org/10.1021/acs.jpcc.1c06202.

(16) Ravel, B.; Newville, M. ATHENA , ARTEMIS , HEPHAESTUS : Data Analysis for X-Ray Absorption Spectroscopy Using IFEFFIT. *J. Synchrotron Radiat.* **2005**, 537–541. https://doi.org/10.1107/S0909049505012719.

(17) Chertihin, G. V.; Andrews, L. Reactions of Laser Ablated Titanium, Zirconium, and Hafnium Atoms with Oxygen Molecules in Condensing Argon. *J. Phys. Chem.* **1995**, *99* (17), 6356–6366. https://doi.org/10.1021/j100017a015.

(18) Zheng, W.; Bowen, K. H.; Li, J.; Dąbkowska, I.; Gutowski, M. Electronic Structure Differences in ZrO 2 vs HfO 2. *J. Phys. Chem. A* **2005**, *109* (50), 11521–11525. https://doi.org/10.1021/jp053593e.

(19) Akatsuka, M.; Yoshida, T.; Yamamoto, N.; Yamamoto, M.; Ogawa, S.; Yagi, S. XAFS Analysis for Quantification of the Gallium Coordinations in Al2O3-Supported Ga2O3 Photocatalysts. *J. Phys. Conf. Ser.* **2016**, *712* (1), 3–7. https://doi.org/10.1088/1742-6596/712/1/012056.

(20) Nishi, K.; Shimizu, K. I.; Takamatsu, M.; Yoshida, H.; Satsuma, A.; Tanaka, T.; Yoshida, S.; Hattori, T. Deconvolution Analysis of Ga K-Edge XANES for Quantification of Gallium Coordinations in Oxide Environments. *J. Phys. Chem. B* **1998**, *102* (50), 10190–10195. https://doi.org/10.1021/jp982704p.

(21) Martini, A.; Borfecchia, E. Spectral Decomposition of X-Ray Absorption Spectroscopy Datasets: Methods and Applications. *Crystals* **2020**, *10* (8), 1–46. https://doi.org/10.3390/cryst10080664.

3 ZrO_2 doped with aliovalent elements (Ce, Zn, Ga): the need for a structural understanding of guest atom nature

3.1 Catalytic properties

The scientific community and particularly the COZMOS project are investigating doped ZrO_2 catalysts for their CO_2 hydrogenation properties.[1,2] M-doped ZrO_2 (M : Zn, Ce, Ga) catalysts showed interesting results concerning selective CO_2 hydrogenation to methanol with respect to pure ZrO_2 (Figure 13a) without implying the use of rare earth or noble elements e.g., Pt, Pd and Ni.[2–4] The catalysts' selectivity to methanol is exploited for increasing CO_2 conversion (<10%). Indeed, the oxides are physically mixed with an acid zeolite/zeotype (e.g. H-ZSM5, SAPO-34/18, H-SSZ13, etc.) which can directly convert methanol into hydrocarbons improving the global CO_2 conversion (Figure 13b).[5–11] As reported in Figure 13, whilst $ZnZrO_x$ and $GaZrO_x$ presented similar properties for CO_2-to-methanol conversion, once mixed with the acid zeolite $GaZrO_x$ outperform $ZnZrO_x$ and $CeZrO_x$ for both CO_2 conversion and propane selectivity.

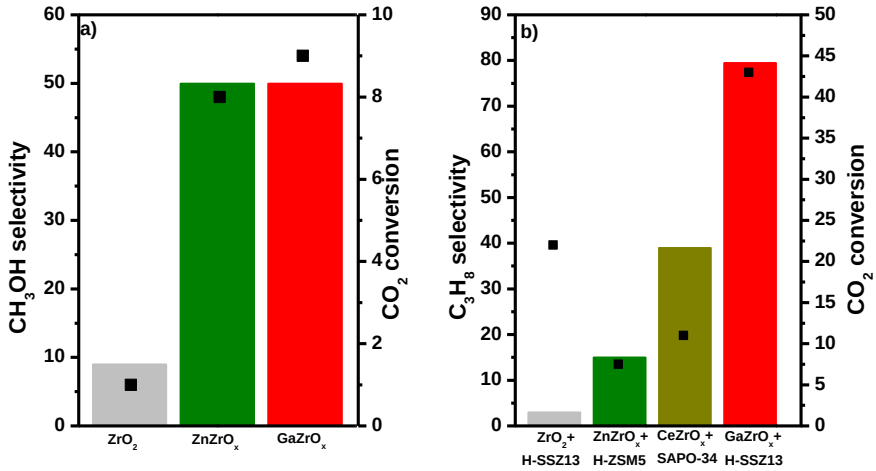

Figure 13 CH_3OH/Propane selectivity (bars) and CO_2 conversion (squares) properties of ZrO_2, $ZnZrO_x$,[7] $CeZrO_x$,[11] and $GaZrO_x$ [12] catalysts a) alone and b) physically mixed with acid zeolites.

Most of the reported studies focus on finding the best oxide/zeolite combination however, without providing a complete understanding of the oxidic catalyst structure.[6,9,10] The results reported in this chapter focuses on the structural comprehension of $ZnZrO_x$ and $GaZrO_x$ catalysts through PXRD and FT-EXAFS analysis. $CeZrO_x$ is used as an additional case study to support the obtained results.

3.2 $CeZrO_x$: understanding solid solution long- and short-range ordering

When describing ZrO_2 solid solutions, a typical example consists in CeO_2-ZrO_2 mixtures, which are well known catalysts widely employed because of their oxygen storage capacity and oxygen vacancies content.[13] The catalysts properties are very sensitive to the material local structure, making literature rich of their structural description using diffraction and FT-EXAFS.[14–16] Three major cases can be distinguished: A) CeO_2 and ZrO_2 are not well mixed forming nanoaggregates of different dimensions interacting only at their interface (Figure 14 left) (long-ordered domain type), B) CeO_2 and ZrO_2 are mixed on the long-range but a partial un-mixing remains at short range (Figure 14 middle) (shortly ordered domain type) and C) CeO_2 and ZrO_2 are perfectly mixed forming an ideal solid solution (Figure 14 right).

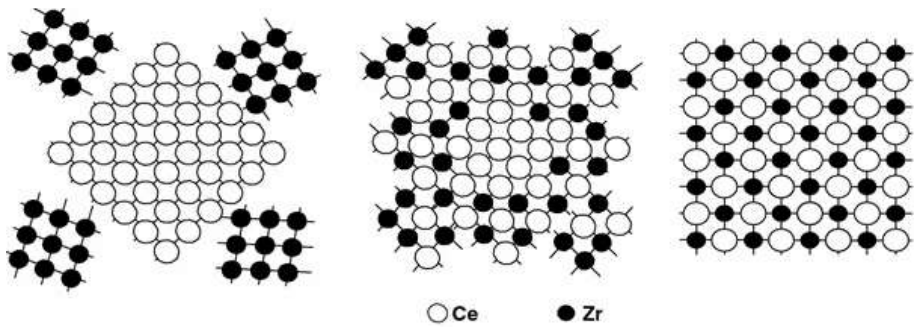

Figure 14 Pictorial representation of different solid solution scenario (from left to right): mixture of nanoscale oxides, partial local ordering, and perfect solid solution. Figure reproduced from Nagai et al.[14]

3.2.1 Average structural and electronic properties

Techniques such as PXRD and UV-Vis spectroscopy (Figure 15) probe the catalyst average structural and electronic properties, hence giving a macroscopic description of the catalyst. For example, in case of a commercial $CeZrO_4$ (Ce:Zr ratio of 58:42, full description of the catalyst reported in Appendix D)[4] PXRD pattern reported in Figure 15 shows a tetragonal ($P4_2/nmc$) average structure distinguished from the cubic CeO_2 Fm-3m from the presence of the (102) reflection. Indeed in the tetragonal polymorph the oxygen atoms are displaced along the [001] direction generating a modulation and inducing reflections of (odd odd even) type.[17] This polymorph is usually observed for $CeZrO_x$ catalysts and is often associated to the presence of oxygen vacancies introduced by Ce^{4+} and Zr^{4+} having different ionic radii (0.97 vs 0.84 Å)[18] hence causing expulsion of some oxygens during lattice relaxation. $CeZrO_4$ UV-Vis spectrum (Figure 15b) presents an absorption band different from ZrO_2 and CeO_2. Indeed, none of the two references band gap is observed in the catalysts and a broad absorption band is observed centred around 450 nm, usually associated to a Ce^{3+}-Ce^{4+} charge transfer,[19] suggesting the absence of clustering of one of the two oxides.

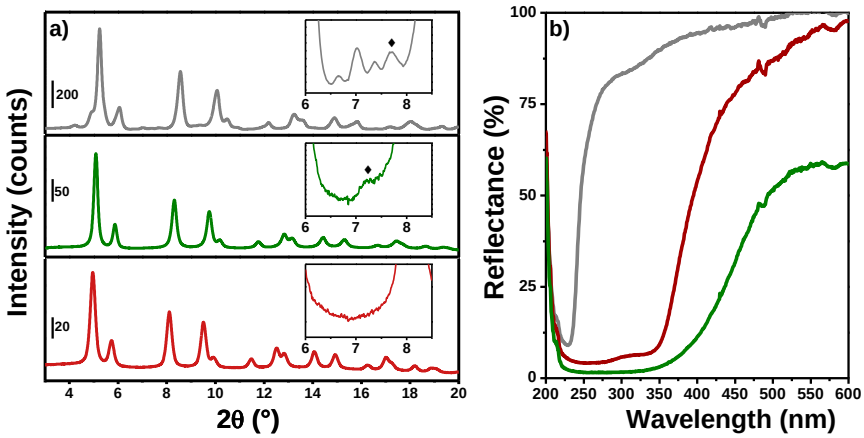

Figure 15 a) PXRD pattern ($\lambda \approx 0.27$Å) and b) UV-Vis spectra of ZrO_2 (gray lines), CeO_2 (red lines) and $CeZrO_4$ (green lines). (102) tetragonal reflection is indicated with a diamond in the insets in part a).

3.2.2 Zr/Ce local structure

From a local perspective, Zr K-edge XANES spectra (Figure 16a) presented a 1s→4p pre-edge related to non-centrosymmetric Zr-O coordination e.g., the ZrO_8 double tetrahedra coordination of the tetragonal polymorph.[20] On the contrary Ce K-edge XANES spectra is comparable with CeO_2 (cubic symmetry) with edge position shifted to lower energy (Figure 16b), highlighting the presence of Ce^{3+} already observed by UV-Vis spectroscopy (Figure 15b). A disordered Zr and Ce local environment is suggested from a first qualitative inspection of the phase-uncorrected FT-EXAFS regions which first and second shells intensities are dampened respect to the reference oxides. The first coordination shells position is comparable to the Zr-O and Ce-O from reference oxides whilst the second shells were initially assigned with a direct comparison with the pure oxides Zr-Zr and Ce-Ce intense shells positions.

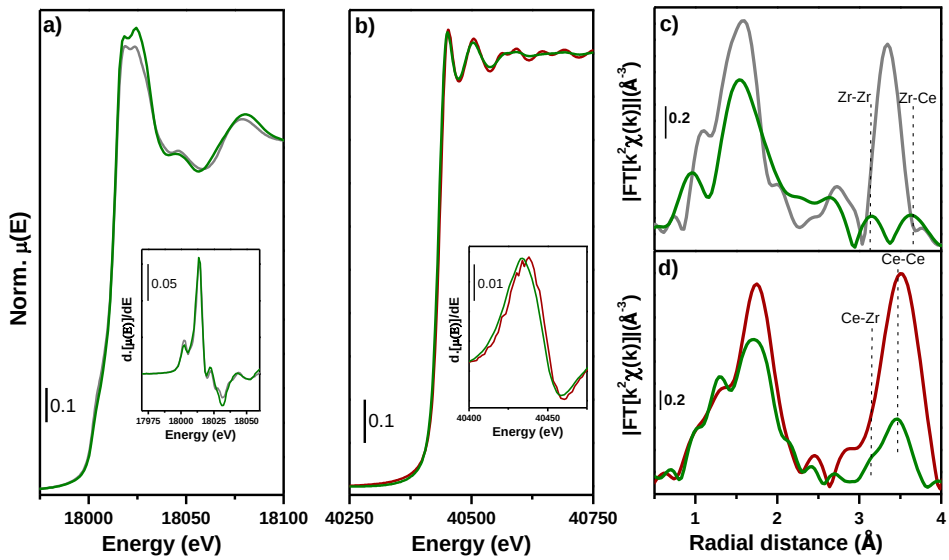

Figure 16 ZrO_2 (gray lines), CeO_2 (red lines) and $CeZrO_4$ (green lines) a,c) Zr K-edge a) XANES and c) phase uncorrected FT-EXAFS spectra (extracted in the 2-12 $Å^{-1}$ range) and b,d) Ce K-edge b) XANES and d) phase uncorrected FT-EXAFS (extracted in the 2-15 $Å^{-1}$ range) spectra. Detail of Zr K- and Ce K-edge XANES first derivative are shown in insets in panel (a) and (b) respectively.

To deep into Ce and Zr local structure we attempted a double edge fit where Ce-Zr and Zr-Ce radial distances and mean square displacements were constrained to the same values, accordingly to the potential presence of Zr-O-Ce chemical bond. Tetragonal ZrO_2 ($P4_2/nmc$) and cubic CeO_2 ($Fm\text{-}3m$) were used as input structures. Zr-Ce and Ce-Zr coordination number were instead constrained to Ce:Zr ratio evaluated by EDX analysis i.e., Ce = 4.8. The obtained results reported in

Table 2 consisted of physical values. However, whilst the fit well describes the experimental spectra at Ce K-edge (Figure 17 red panel), the same does not occur at Zr K-edge (Figure 17 blue panel), indicating as the employed $CeZrO_4$ solid solution model might not fully describe Zr local environment. Ce K-edge XANES (Figure 16 b) did not present any pre-edge fingerprints stemming from a CeO_8 non-centrosymmetricity hence we considered the local Ce-O cubic symmetry. Ce first coordination shell was then described with 8 equidistant oxygen atoms (Ce-O) which evaluated radial distance is well comparable with PXRD results (

Table 2). The second coordination shell was fit considering Ce-Ce and Ce-Zr scattering paths, both with same initial radial distance taken from PXRD refinement (≈3.72 Å) and correlated CN i.e., Ce-Zr CN : X and Ce-Ce : 12-X where X : number of Zr atoms as Ce next nearest neighbours (NNN) fixed according to Ce:Zr ratio evaluated by EDX. The evaluated radial distances unveiled a R(Ce-Zr) comparable with PXRD results and a R(Ce-Ce) closer to pure CeO_2 values (3.79 vs 3.84 Å) hence confirming the assignment hypothesized in Figure 16d. Following the local coordination evaluated from Zr K-edge XANES pre-edge, its FT-EXAFS first coordination shell was fit considering a double tetrahedra coordination with four closer ($Zr\text{-}O_I$) and four farther ($Zr\text{-}O_{II}$) oxygen atoms. On the contrary the second shell was described considering a Zr-Zr scattering path with independent radial distances and MSD, and a Zr-Ce path constrained to the Ce-Zr one. Interestingly, by considering the obtained Zr-Zr and Ce-Ce radial distances we noticed as their average (3.725 ± 0.043 Å) corresponds to the distance evaluated by PXRD (≈3.726 Å), highlighting the difference between a local and an average probe. However, whilst the fit well describes the experimental spectra at Ce K-edge (Figure 17 red panel), the same does not occur at Zr K-edge (Figure 17 blue panel), indicating as the employed $CeZrO_4$ solid solution model might not fully describe Zr local environment.

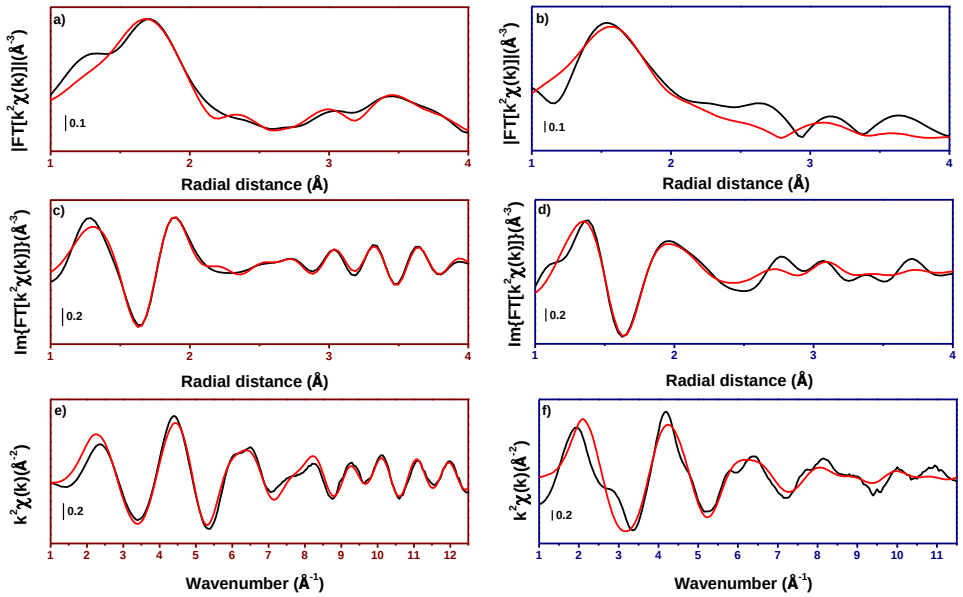

Figure 17 Ce K-edge (red panels) and Zr K-edge (blue panel) experimental (black lines) and best fit (red lines) of e,f) EXAFS and FT-EXAFS a,b) magnitude and c,d) imaginary part. Ce and Zr K-edges FT-EXAFS was extracted in the 3-12.4 and 3-11.4 $Å^{-1}$ k-range respectively. EXAFS fit was conducted in the 1-4 Å R-range at both edges.

Table 2 Radial distances (R), coordination number (CN) and Debye Waller factors (σ^2) obtained from $CeZrO_4$ PXRD Rietveld Refinement and Ce K- and Zr K-edges FT-EXAFS fitting. Fixed CN are indicated with *. Unphysical values are indicated with **bold** characters. SA : Sigma Aldrich. [a] Determined by PXRD refinement. [b] Determined by FT-EXAFS fit.

Sample	**Scatt. Path**	**R(Å)[a]**	**R(Å)[b]**	**CN**	**σ^2 (Å^2)**
$CeZrO_4$	Ce - O	2.28271	2.304±0.014	8	0.0111±0.0008
	Ce – Ce	3.7265	3.798±0.013	3±2	0.0063±0.0009
	Ce – Zr		3.744±0.013	9±2	0.016±0.003
	Zr – O_I	2.28271	2.12±0.05	4	0.008±0.003
	Zr - -O_{II}		2.26±0.09	4	0.012±0.010
	Zr – Zr	3.7265	3.667±0.041	9±2	0.017±0.005
	Zr - Ce		3.73±0.03	3±2	0.016±0.003

3.2.3 Deducing Ce-Zr short range ordering

Considering a perfect structural mixing between Ce and Zr the same radial distances and MSD should be obtained for common scattering path, as observed for example in CeZr clusters in UiO-66 catalysts.[21] From a mathematical viewpoint this result was achieved however, with an important misfit at the Zr K-edge second shell. Indeed, the difference between best fit and experimental data suggested as from Zr viewpoint at least one scattering component was missing in the second shell. Nevertheless, with the available data we did not try to model the local disorder to describe the missing scattering path. It is well reported as $CeZrO_x$ solid solution local structure (domain type vs solid solution) strongly depends on the synthesis strategy.[16] In the ideal solid solutions scenario (Figure 14 right), Zr second shell should be almost equal to Ce one (Ce:Zr≈1:1) whilst in scenario A (Figure 14 left), it should present an intense Zr-Zr component related to ZrO_2. The obtained lack of fit cannot

discard the formation of a perfect solid solution however, they clearly confirmed as the employed $CeZrO_4$ model does not describe Zr local environment. We then hypothesize as this particular sample might be located in the case scenario B (Figure 14 centre) where one of the cation (Ce) presents an higher degree of short range ordering respect to the other one (Zr).

3.3 Zn-doped ZrO_2: comprehension of Zn local environment

3.3.1 Powder X-Ray Diffraction (PXRD)

ZnZr(X) (X : Zn wt%) PXRD patterns (Figure 18) contain the same Bragg reflections, despite a series of extra peaks in the ZnZr(30) sample associated with a hexagonal ZnO extra phase. The tetragonal polymorph, further confirmed also from the Zr K-edge XAS analysis (vide infra), was used for Rietveld refinement of ZnZr(X) PXRD patterns (Figure 18) to extract lattice parameters, crystallite size, and phase composition. h-ZnO ($P6_3mc$) phase[22] was added to refine the extra reflections in the ZnZr(30) pattern. The effective Zn doping in the ZrO_2 structure can be simply verified by refined lattice parameters and the so-calculated unit cell volume. As the Zn^{2+} ionic radius (0.60 Å) is smaller than the Zr^{4+} one (0.84 Å), higher Zn loading consistently translates into a smaller unit cell volume (Figure 18d). It should be noteworthy as the unit cell volume evolution respect to Zn concentration does not respect the Vegard's Law which states a linear dependence between lattice expansion and guest atom concentration.[23] It should be stressed as this is only a qualitative interpretation of the unit cell volume behaviour. Indeed, to better understand ZnO solubility in ZrO_2, their binary phase diagram should be discussed. Unfortunately, as far as we could search into the literature, we did not find such diagram. Moreover, we should also expect as the ZnZr(X) tetragonal polymorph might be a metastable phase, suggesting that am hypothetical phase diagram might not be respected as well.

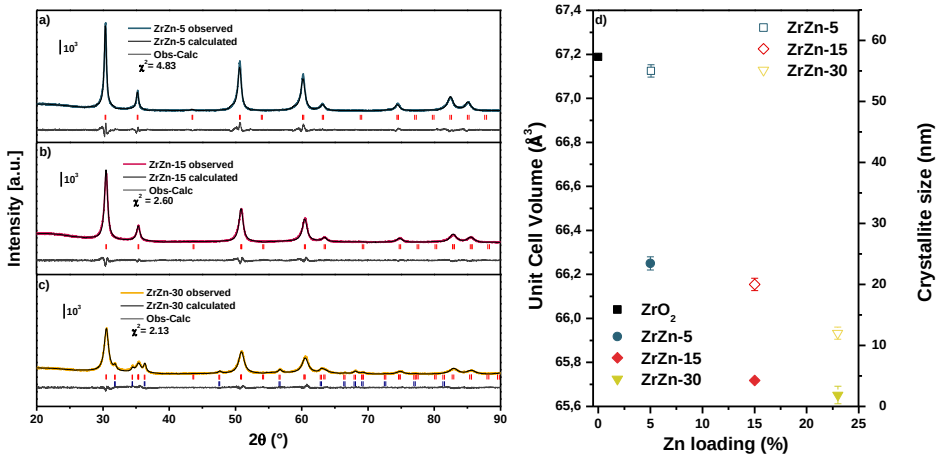

Figure 18 a,b,c) Laboratory PXRD (λ ≈ 1.54 Å) patterns measured for the three ZnZr(X) samples in transmission mode using glass capillary sample holder (Ø=0.5mm). Diffractograms for ZnZr(5)(blue curve), ZnZr(15) (red curve) and ZnZr(30) (yellow curve) are reported together with the corresponding refined curves (dark grey) and difference functions (light grey) between observed and calculated curves. t-ZrO_2 was used as the input structure for the refinement. t-ZrO_2 and h-ZnO Bragg reflections are indicated by red and blue vertical sticks, respectively. d) Unit cell volume (full symbols) and crystallite size (empty symbols) obtained from refined lattice parameters and peak shape, respectively, for ZnZr(5) (blue square), ZnZr(15) (red diamond) and ZnZr(30) (yellow triangles).

3.3.2 X-Ray Absorption Spectroscopy

Zr K-edge. XAS spectra of the three samples measured at RT in He atmosphere are reported in Figure 19, together with those of monoclinic and tetragonal ZrO_2 polymorphs, as references. Edge position, B/B' white-line peak split, and pre-edge shoulder "A" confirm the presence of ZrO_2 tetragonal polymorph. The latter one, more visible in the spectra first derivative, stems from a 1s→4d transition, characteristic of t-ZrO_2 where Zr coordinates 8 O atom in a non-centrosymmetric double tetrahedra configuration leaving open space for the presence of an oxygen

vacancy.[20] Moreover, Zr local geometry distortion increases with the Zn loading, as highlighted by the higher main edge FWHM (Figure 19)

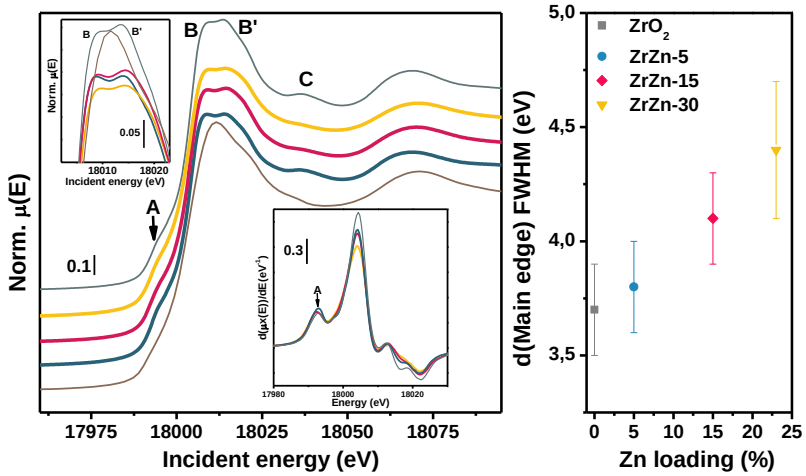

Figure 19 a) Stacked representation of Zr K-edge XANES measured at RT (He atmosphere) for the three ZnZr(X) samples. ZnZr(5) (blue), ZnZr(15) (yellow) and ZnZr(30) (red) are represented together with reference tetragonal (grey) and monoclinic (brown) ZrO_2 polymorphs. Top left inset: non-stacked detail of the white-line peak. Bottom right inset: XANES first derivative enhancing the pre-edge feature related to the 1s→4d transition. b) Main Edge FWHM for reference ZrO_2 and ZnZr(X) samples.

Phase-uncorrected Zr K-edge FT-EXAFS are reported in Figure 20a,b. The three spectra presented similar features: I) a first Zr-O shell located at 1.5 Å comparable between all the samples and substantially equivalent to that observed for the t-ZrO_2 model compound and II) a second shell at 3.2 Å associated to Zr-Zr scattering contribution which intensity is lower than reference ZrO_2 and is progressively abated as Zn concentration increases. Considering the presence of Zn as Zr Next Nearest Neighbour (NNN), Zr-Zr and Zr-Zn scattering contributions (Figure 20c) presented an imaginary component in complete antiphase, relating Zr second shell intensity loss with the increasing presence of Zn as NNN.

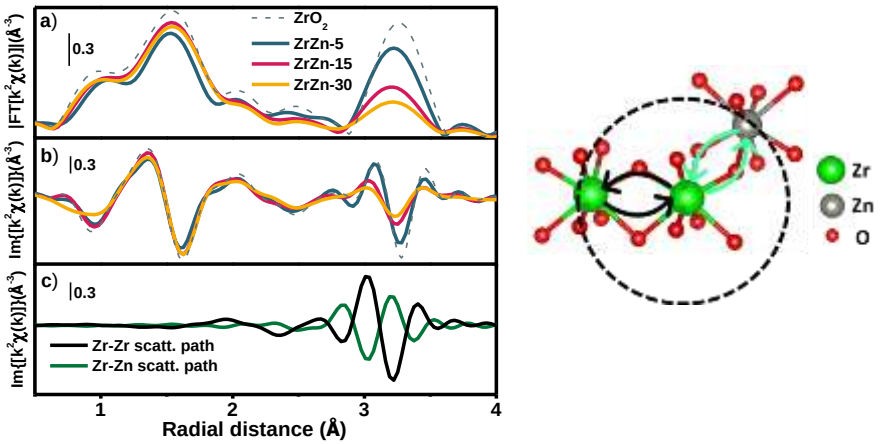

Figure 20 a) Magnitude and b) imaginary parts of k^2-weighted phase-uncorrected FT-EXAFS extracted in the k-range 2.5-12.0 $Å^{-1}$ for ZnZr(5) (blue), ZnZr(15) (red), ZnZr(30) (yellow) and reference t-ZrO_2 (dashed grey). c) Imaginary part of the individual Zr-Zr (black) and Zr-Zn (green) scattering paths generated by FEFF6 optimized after the fit of ZnZr(30). Left : sketched structural model describing Zr-Zr/Zn second coordination shell scattering paths.

To verify Zn role to the second shell dampening, EXAFS fits were conducted using tetragonal ZrO_2 model considering the presence of a Zr-Zn scattering path in second shell as sketched in the model in Figure 20. Even though the detailed fit procedure can be found in the published manuscript reported in the appendix,[24] the key parametrization of the fitting came from the description of Zn weight percentage. Since ARTHEMIS cannot handle non-integer occupancies, Zn was considered by replacing one of the 12 Zr atoms surrounding the absorber Zr by Zn and estimating Zr-Zr and Zr-Zn coordination number (CN) as 12-Zn and Zn, respectively, where Zn is a variable related to the number of Zn atoms as Zr NNN. To strengthen the fitting model, the same "Zn" variable was also considered in the Zr-O CN since every Zn^{2+} should introduce an V_O. The whole procedure, led to the best-fit curves reported Figure 21. A good agreement was observed for both magnitude and imaginary part of the FT-EXAFS spectra when comparing experimental and calculated curves.

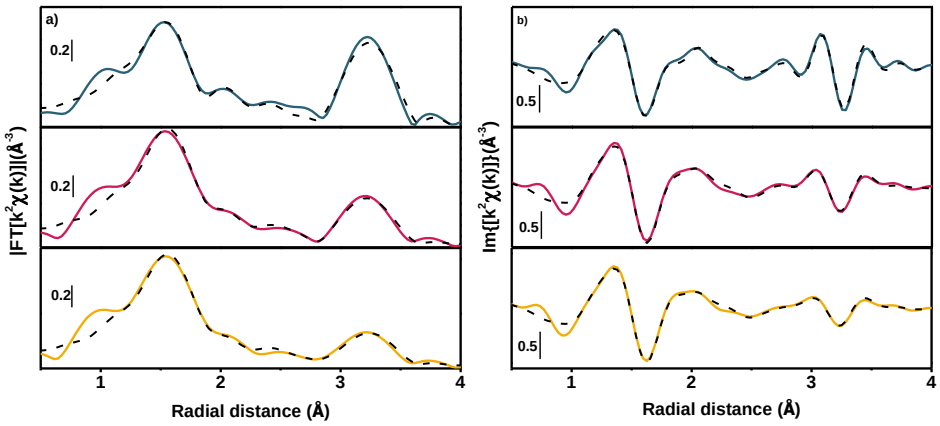

Figure 21 Experimental (coloured lines) and best fit (dashed grey lines) a) magnitude and b) imaginary parts of the k^2-weighted, phase-uncorrected FT-EXAFS spectra for ZnZr(5) (blue), ZnZr(15) (red) and ZnZr(30) (yellow).

Zn K-edge. The solid solution scenario, observed from Zr FT-EXAFS fitting, should be reproduced also from Zn K-edge viewpoint, measured quasi-simultaneously with the Zr K-edge ones. The spectra of the three ZnZr(X) samples are reported in Figure 22, together with Zn K-edge XANES spectra of h-ZnO and Zn metal foil references. Edge position reflected the presence of Zn^{2+} whilst white-line shape is no-longer comparable with h-ZnO one. Indeed, whilst the latter presents two clear spectral features indicated with letters A and B in Figure 22a related to 1s→4pπ and 1s→4pσ transitions, the former presented a single broader white-line which could be interpreted as deriving from a 1s→4pσ transition with reduced long range ordering. Noteworthy, A and B fingerprints are more evident in ZnZr(30) sample most probably due to the presence of segregated h-ZnO observed by PXRD. A fruitful information was derived from a straight comparison of Zr and Zn FT-EXAFS. Indeed, in the solid solution scenario, both should present a similar second shell related to the Zr-Zn and Zn-Zr scattering paths. Nevertheless, it was clearly observed as whilst the two edges presented comparable first coordination shell, Zn second shell was located at a (phase uncorrected) radial distance comparable to h-ZnO.

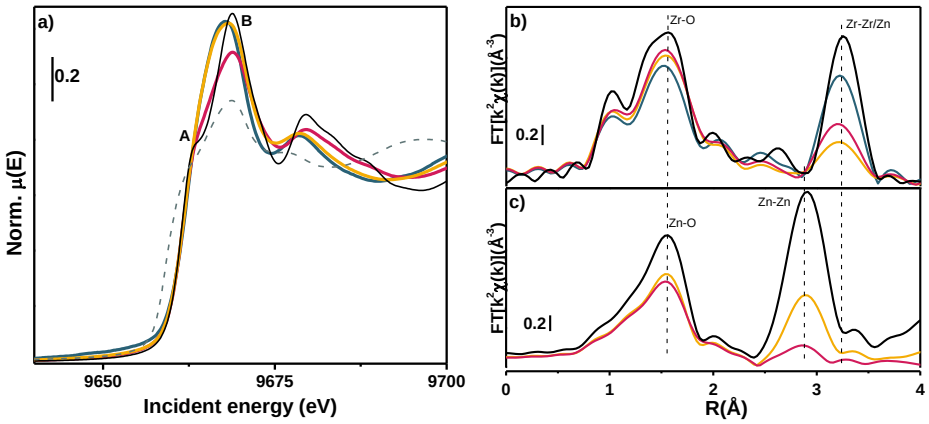

Figure 22 a) Zn K-edge XANES (main panel) and b) Zr and c) Zn K-edges phase-uncorrected k^2-weighted FT-EXAFS (inset) transformed in the 2-12 $Å^{-1}$ k-range measured at RT (He atmosphere), for the three ZnZr(X) samples. Spectra of ZnZr(5) (blue), ZnZr(15) (yellow) and ZnZr(30) (red) are shown together with those of reference h-ZnO (black) and Zn metal foil (dashed-grey). FT-EXAFS of ZnZr(5) is missing due to the low absorber concentration. FT-EXAFS spectra of reference ZrO_2 and h-ZnO are reported with black lines in parts b) and c), respectively.

Following this observation, the first Zn K-edge FT-EXAFS fit was conducted on ZnZr(15) by using hexagonal ZnO as input structure leading to a good data/fit agreement (

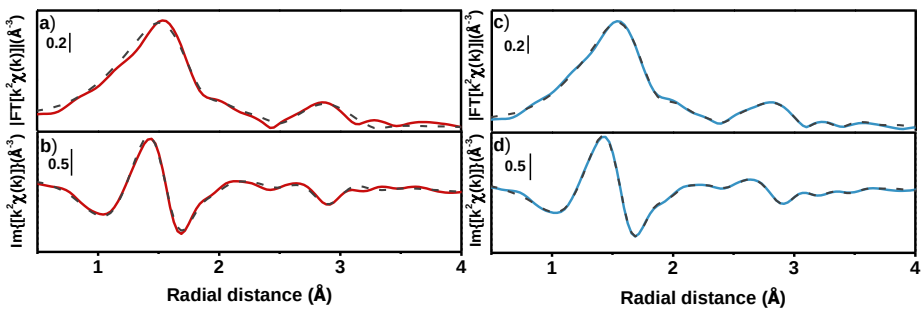

Figure 23a,b). Two details were observed: I) Zn-Zn shell intensity was lower than h-ZnO one, indicating a reduced Zn-Zn CN and II) a bump located at higher radial distances was not described. Even though this feature could be simply related to a

FT artifact, its radial position is qualitatively close to Zr second shell suggesting that it could be associated to a Zn-Zr scattering path.

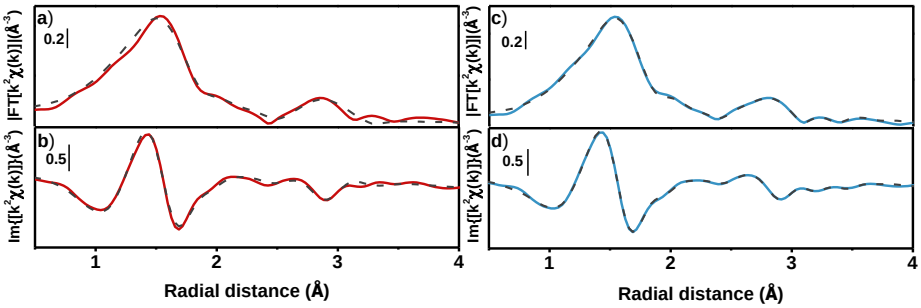

Figure 23 Experimental (solid coloured line) and best fit (dashed grey line) (a, c) magnitude and (b, d) imaginary parts for k^2-weighted FT-EXAFS of ZnZr(15) using (a, b) h-ZnO and (c, d) h-ZnO/ZrO_2 (Figure 20) as the input structure.

To discriminate the origin of this feature, XAFS spectra of ZnZr(15) at Zr and Zn K-edges were analysed under catalysts activation (Figure 24a,c).Whilst ZnZr(15) Zr and Zn K-edges of ZnZr(15) catalyst did not change upon the activation procedure described in the materials and methods, phase-uncorrected FT-EXAFS at Zn K-edge recorded during thermal activation in Figure 24a,c showed a constant decrease of the first and second shell intensity related to the increase in DW factors. However, the second shell presents a non-trivial dynamic involving the two components in the second shell. Indeed, the one at higher radial distances shifts to lower values until it convolutes with the Zn-Zn one at high temperature. After having discarded once more the simple h-ZnO model which did not describe the second shell dynamic (see Salusso et al.[24] for further details), we attempted to use the model sketched in Figure 25 for fitting the *in situ* data.

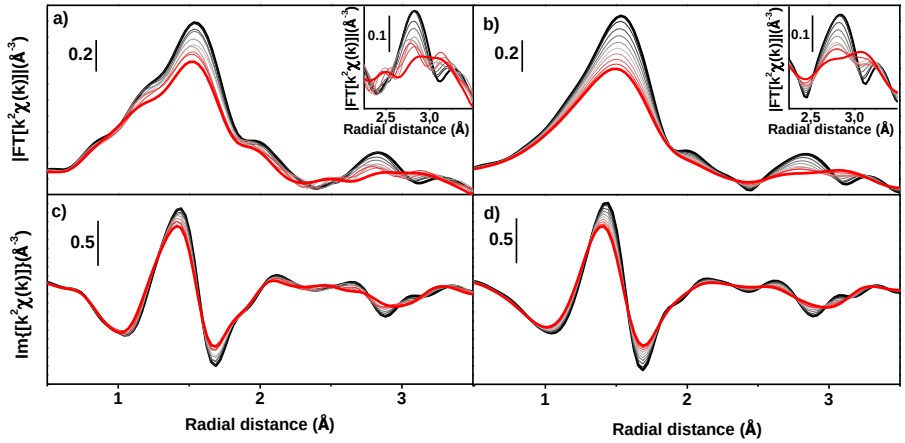

Figure 24 Zn K-edge a, c) Experimental and b, d) best fit of a, b) magnitude and c, d) imaginary parts of k^2-weighted FT-EXAFS of ZnZr(15) measured at increasing temperatures (black to red lines) in the RT-400 °C range under H_2 gas flow. A magnification of the second-shell region is reported in the insets. Fits are performed in the k-range 2-12 $Å^{-1}$ and R-range 1.0-4.0 Å.

Particularly, with this structural description we tried to integrate the results from both edges. Indeed, the average Zn atoms presents a non-trivial second shell composed by: I) a scattering contribution with Zn ($Zn\text{-}Zn_I$) located in ZnO bulk, II) scattering from a Zn atom bonded to Zr ($Zn\text{-}Zn_{II}$) and III) a direct scattering from Zr (Zn-Zr), previously observed from Zr K-edge. Using this structural description and by describing the thermal Debye Waller factor with the Einstein model we were able to well describe both first and second shell dynamics. This model was then used to fit also the data at RT under He, allowing a complete description of the component in second shell at higher radial distances.

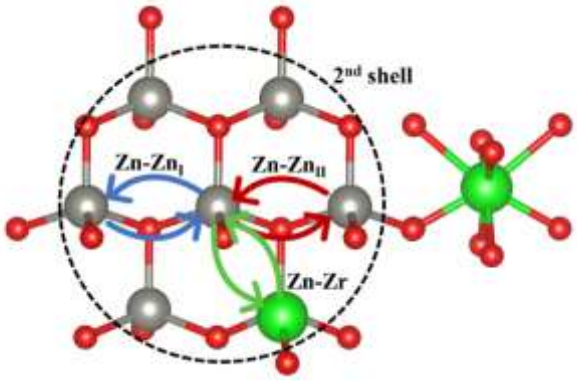

Figure 25 Pictorial representation of the scattering paths contributing in the second-shell region of Zn K-edge EXAFS, describing ZnO nanoclusters chemically bonded to the ZrO_2 matrix. Zn, Zr and O atoms are represented by grey, green and red spheres, respectively. 2nd shell is indicated by dashed circle while Zn-Zn$_I$, Zn-Zn$_{II}$ and Zn-Zr scattering paths are represented by blue, red and green arrows, respectively. As this is only a representative illustration, Zr is represented in both tetrahedral and double-tetrahedral coordination.

3.3.3 ZnZr(X) : ZnO domain size

We then conclude as ZnZr(X) catalysts can be described with the solid solution scenario A (Figure 14 left) i.e., long-range ordered domain type, consisting of nanosized ZnO-like domains embedded and chemically bonded in a ZrO_2 matrix. This view, pictorially represented in Figure 25 and Figure 26, explains I) the presence of Zr-Zn scattering path observed from Zr K-edge and the observed Zn underestimation. In fact, from Zr K-edge we evaluate only the surface of the ZnO cluster, the bigger the cluster the higher the underestimation. II) Zn K-edge second shell predominantly resembling ZnO, III) ZnO cluster surface being affected by the bond with Zr and IV) at the ZnO/ZrO_2 the most of V_O will be generated, explaining the increase of Zr local disorder at higher Zn loading observed from Zr XANES main edge FWHM.

Interestingly, the dimension of ZnO cluster (under the hypothesis of a spherical shape) was evaluated using the Greegor and Lytle equation to be among 11 Å (Figure 26). Moreover, this type of description supported a qualitative interpretation of Zn K-edge recorded under reaction conditions. Indeed, after activation the catalyst was subjected to a high-pressure stream (15 bar) of CO_2 and H_2 at 300°C. However, even if almost any variations were observed at both edges, Zn K-edge FT-EXAFS presented some subtle (but not negligible) variations in the second shell, particularly in the region where scattering paths from ZnO and ZrO_2 interface have been observed, suggesting as the interface between the two oxides might be the catalyst part active for CO_2 hydrogenation.

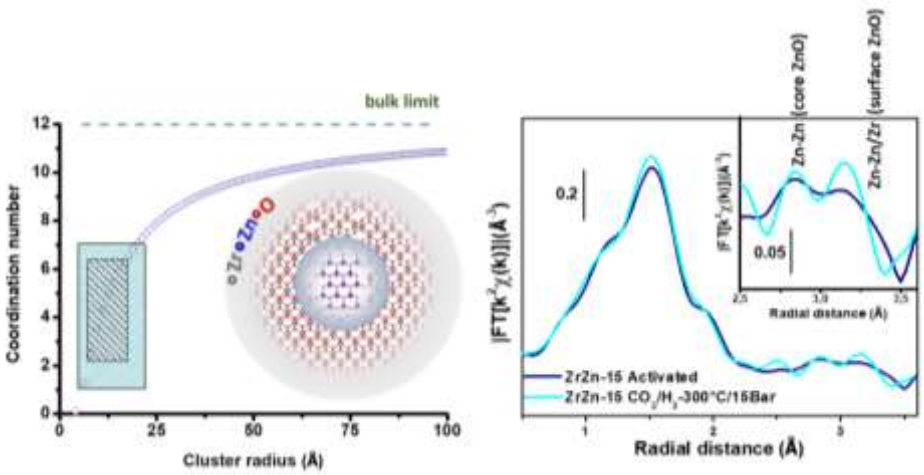

Figure 26 a) Relation between coordination number and cluster radius evaluated using the Greegor and Lytle equation within the spherical approximation. Zn-Zn distance found by EXAFS fit was used as shortest atomic distance. Outer and inner boxes indicate the area where CN extracted from fit of RT and under activation data are located, respectively. Dashed line indicates the coordination number bulk limit (12). b) Experimental magnitude part of k^2-weighted phase uncorrected FT-EXAFS of ZnZr(15) measured before (dark blue) and after (light blue) *in situ* reaction under CO_2/H_2 flux at 300°C, 15 bar. Insets showing detail of the R-space range where Zn-

Zn_I and Zn-Zn_{II}/Zr scattering contributions occur. In this R-space range, small modifications are observed upon exposure to the reaction feed for both the catalysts. Spectra were Fourier-transformed in the k-range 2-12 $Å^{-1}$.

3.4 ZnO clusters stability in ZnZr-X catalysts

After having described ZnZr(X) catalysts as consisting of ZnO nanoclusters in a ZrO_2 matrix, we decided to investigate how this structural configuration would affect the catalyst stability. Two new samples (ZnZr(10) and ZnZr(20)) were prepared and analysed by in -situ PXRD under H_2 activation to study the catalyst structural stability up to 600°C and by *ex situ* XAS after H_2 activation at different temperatures. Importantly, none of the two samples presented segregated h-ZnO reflections, therefore we could compare their Zn K-edge with the one of ZnZr(5)♣.

3.4.1 *Ex situ* XAS

Considering Zn present as ZnO nanoclusters, Zn K-edge XANES spectra in Figure 27a indicate that ZnO clusters are prevalently formed along the in-plane direction of the hexagonal lattice. As Zn concentration in the catalysts increases, a decrease of white-line intensity is observed, unveiling a lower unoccupied states density. Following Lee et al., ZnO particles of smaller diameters are expected to have larger surface-to-bulk atoms ratio which enhances near conduction band minimum surface states. Less unoccupied states are then associated to lower surface/bulk ratio, hence to larger ZnO clusters in ZnZr(X) catalysts. At energies slightly below the Zn K-edge, it can be observed the presence of Hf L_3-edge, a natural contaminant of ZrO_2. Even though it was showed that Hf has neither structural nor catalytic role,[7] it could actually be exploited as catalyst internal reference for direct quantification of Zn wt(%). In fact, while Hf abundance is the same in each catalyst since they share the same Zr precursor salt, Hf : Zn ratio changes with Zn loadings. By normalizing Zn

♣ZnZr(5) was measured as pellet during the same beamtime together with ZnZr(10/20). Unfortunately, ZnZr(15) was not available anymore to repeat the measurement in pellet.

K-edge spectra to the Hf L_3-edge we observe as Zn edge-jump becomes more pronounced as the Zn concentration increases. The values extracted after this normalization were used to build a Zn wt(%)/edge jump correlation line (Figure 27b).

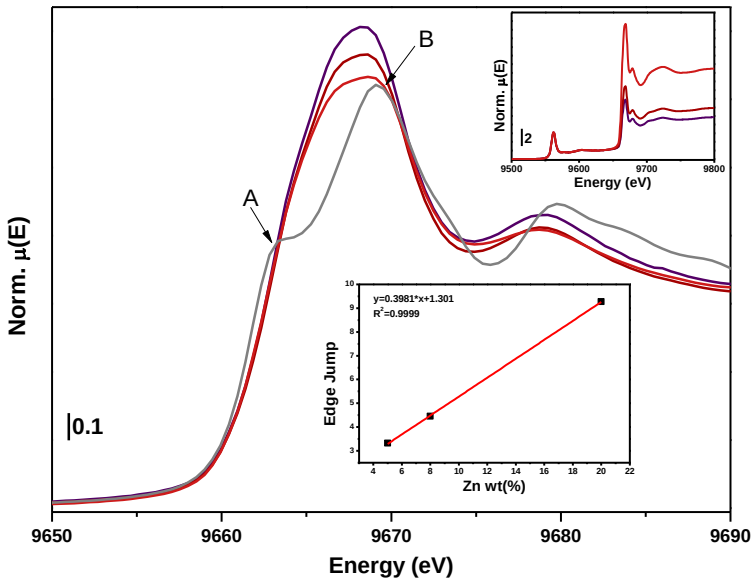

Figure 27 Zn K-edge (main panel) and Hf L_3-edge (top inset) normalized XANES spectra for ZnZr(5) (purple line), ZnZr(10) (dark red line), ZnZr(15) (red line) and ZnO (grey line). Zn wt(%) calibration curve is reported in the bottom inset.

This observation becomes useful when considering spectra with unknown Zn concentration i.e., ZnZr(20) (Figure 28) and ZnZr(10) after thermal treatments in H_2 at 550 and 700°C, namely ZnZr(20)_550, ZnZr(20)_700 and ZnZr(10)_700.♣ Hf : Zn ratio decreases as the reduction treatment temperature increases, suggesting a Zn concentration drop in the catalysts after reduction (Figure 28a). Indeed, by using

♣ For sake of brevity all the results for ZnZr(10) are not reported but they will be part of a manuscript in preparation.

these results we calculated that in ZnZr(20)_550 and _700 Zn wt(%) decreased to 13 and 3.7% whilst in ZnZr(10)_700 it dropped to 0.3%. Together with the decrease of Zn concentration, after H_2 treatment Zn K-edge 1s→$4p_{\sigma/\pi}$ transitions becomes more structured. In particular in ZnZr(20)_550 (Figure 28a) B component qualitatively increases whilst in ZnZr(20)_700 both A,B transitions are more defined and less intense, suggesting that ZnO cluster dimension first decreases with the loss of Zn concentration, while it subsequently increase at higher treatment temperatures. The same behaviour is observed for ZnZr(10) and for both catalysts it is more evident from Zn K-edge FT-EXAFS analysis. Indeed, whilst the first shell, related to Zn-O_{ZnO} ('ZnO': scattering paths from ZnO phase) does not change, the second shell intensity, previously defined as originating from a complex contribution of Zn-Zn_{ZnO}, Zn-Zn_{int} and Zn-Zr_{int} scattering paths ('int': ZnO/ZrO_2 interface), increases after treatment at 700°C/H_2 (Figure 28b).[24] Since the second shell intensity is directly dependent on the Zn-Zn_{ZnO} coordination number and it was previously used to estimate the ZnO cluster dimension, the rise of its intensity is direct evidence of ZnO cluster radius expansion.

Parallel to Zn, Zr K-edge (Figure 28c) gives a direct information on the matrix local structure and indirect hints on ZnO clusters. Zr XANES 1s→4p pre-edge and white-line B/B' splitting can be used to identify the tetragonal polymorph. Moreover, Zn-Zr scattering path was observed in Zr EXAFS second shell since the antiphase configuration between Zr-Zr_{ZrO2} and Zr-Zn_{int} paths caused a drop of its intensity. With the decrease of Zn abundance, Zr second shell is restored confirming a decrease of ZnO/ZrO_2 interface.

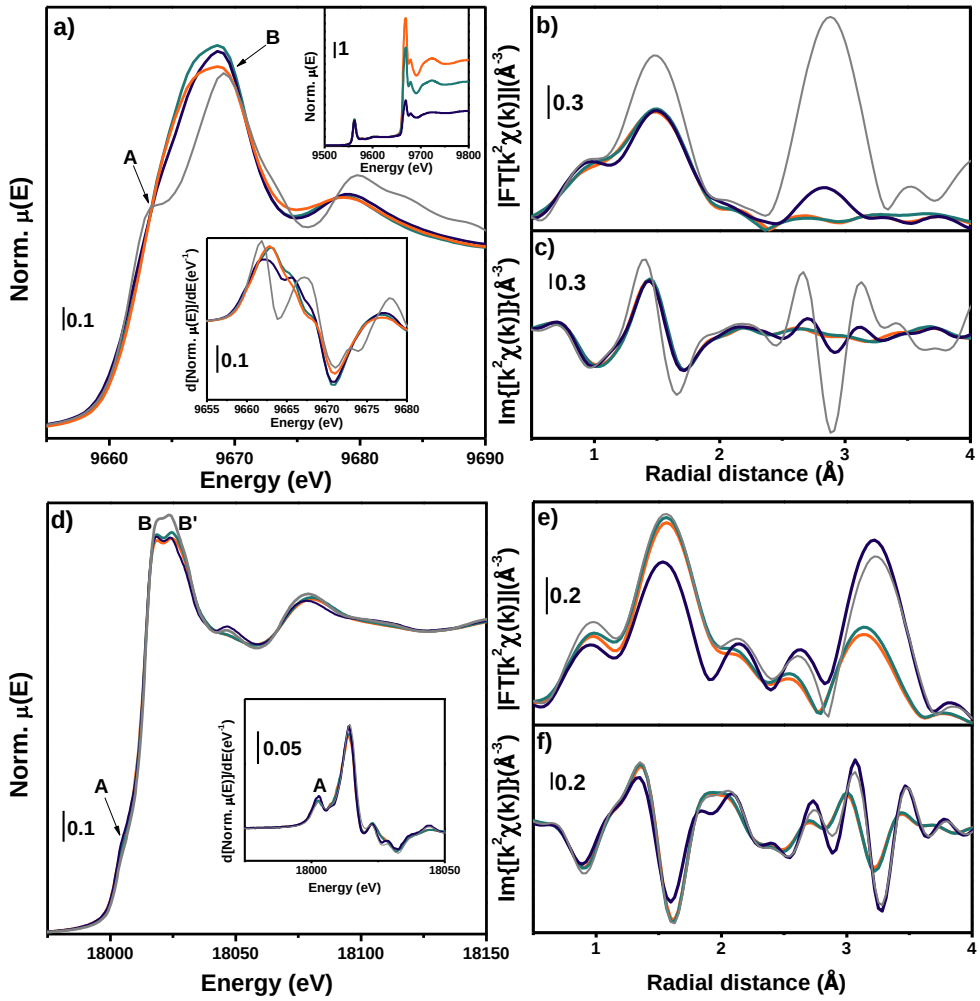

Figure 28 XANES (a, d) and k^2-weighted FT-EXAFS magnitude (b, e) and imaginary (c, f) parts for Zn (a, b, c) and Zr (d, e, f) K-edges of ZnZr(20) as prepared (orange line), ZnZr(20)_550 (green line) and ZnZr(20)_ 700 (blue line). FT-EXAFS have been extracted in the 2.3-10.4 $Å^{-1}$ k-space range. h-ZnO and t-ZrO_2 reference spectra are reported in grey. Hf L_3-edge are showed in the top inset in (a). XANES first derivative are reported in bottom insets in panels (a, d).

3.4.2 *Ex situ* and *In situ* PXRD

Ex situ PXRD data collected on the same samples (Figure 29a) showed the appearance of monoclinic reflections after H_2 treatment, suggesting a slight decrease

in the fraction of ZrO_2 tetragonal polymorph in favour of the monoclinic one. Moreover, H_2 reduction caused a shift to lower angles of t-ZrO_2 reflections unveiling an increase of the average unit cell volume. Indeed, the volume was showed to be inversely proportional to Zn concentration,[24] hence here confirming the Zn loss during H_2 reduction.

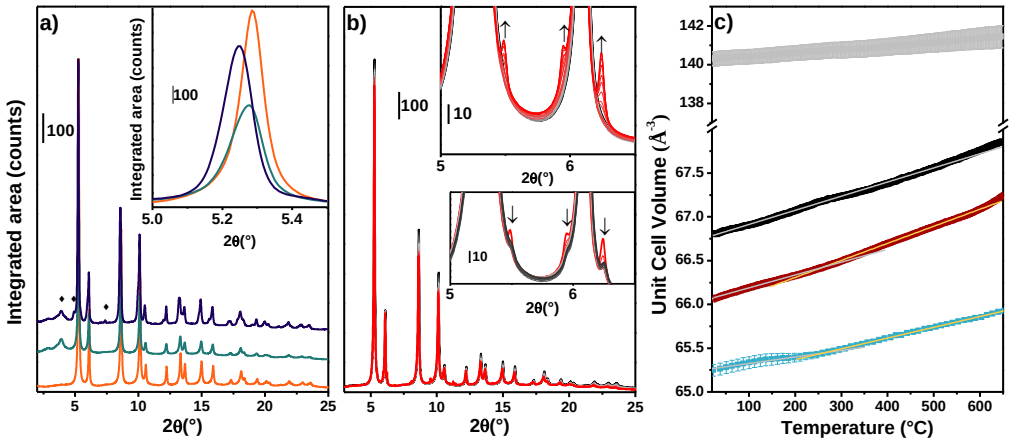

Figure 29 a) Stacked *ex situ* PXRD of ZnZn(20) (orange line), ZrZn(20)_550 (green line) and ZrZn(20)_700 (blue line). Main monoclinic Bragg reflections are indicated with diamonds. Detail of t-ZrO_2 (110) reflection is showed in the inset. b) ZnZr(20) PXRD pattern collected during H_2-TPR experiment. Temperature increases from RT (black line) to 650°C (red line). Detail of ZnO reflections during heating and cooling (temperature decreases from red to black line), indicated with arrows, are reported in the top and bottom insets, respectively. (c) Unit cell volume thermal evolution for reference t-ZrO_2 (black line) and m-ZrO_2 (grey line), ZnZr(10) (red line) and ZnZr(20) (light blue line). Linearity regions are showed with coloured lines.

To understand the Zn loss dynamic, *in situ* PXRD pattern for pure ZrO_2 and ZnZr(10)/20 catalysts have been then measured from RT to 650°C under H_2/He stream. RT-PXRD patterns indicate that the presence of Zn stabilized the tetragonal polymorph in ZnZr(20) catalysts (Figure 29b) decreasing its unit cell volume (Figure 29c). However, a clear difference was observed in the unit cell volume thermal

behaviour between pure ZrO_2 and ZnZr(10/20). In fact, as showed Figure 29c, whilst pure ZrO_2 behaves linearly until 500°C, ZnZr(10) and ZnZr(20) presented two regions of linear behaviour with distinct slopes. The first region (grey line Figure 29c) can be associated to unit cell thermal expansion while the steeper second one (yellow line Figure 29c) begins for both catalysts around 250 °C. The Zn loss highlighted by XAS could indeed be the reason for different unit cell expansion i.e., by decreasing Zn content the unit cell volume grows more rapidly since $R(Zn^{2+}) < R(Zr^{4+})$.[18] Moreover, at T > 600°C h-ZnO reflections started to be observed for ZnZr(20) catalyst (Figure 29b, inset), confirming as showed by XAS, that the Zn loss is accompanied by an increase in the average dimension of ZnO clusters, in which the residual Zn is organized. Our data suggest that such aggregation phenomenon gradually proceeds as temperature increases, until the characteristic h-ZnO reflections become visible by PXRD. Interestingly, h-ZnO reflections were not observed in RT *ex situ* diffractograms (Figure 29a). In the ZrZn-20 case we observe as during cooling under H_2 h-ZnO reflections intensity decreases (Figure 29b) suggesting that at lower temperatures ZnO dimension decreases to a certain extent, with a partial recover of ZnO cluster nanosizing.

Considering the results reported above we can conclude that the thermal stability of ZnZr(X) catalysts is strongly affected by ZnO domain-ordering. Indeed, as sketched in Figure 30, at high temperature ZnO cluster dimensions increase, facilitating Zn sublimation, and thus leading to the observed decrease in Zn concentration. Globally, this affects catalyst activity by i) reducing ZrO_2 tetragonal polymorph stability, which is more active than the monoclinic one and ii) lowering ZnO/ZrO_2 interface, the catalyst site active towards CO_2 hydrogenation. With the decreasing of the temperature, nanosized ZnO clusters are partially recovered however, with a substantial reduction in the total Zn concentration and larger cluster size with respect to the as-prepared catalysts.

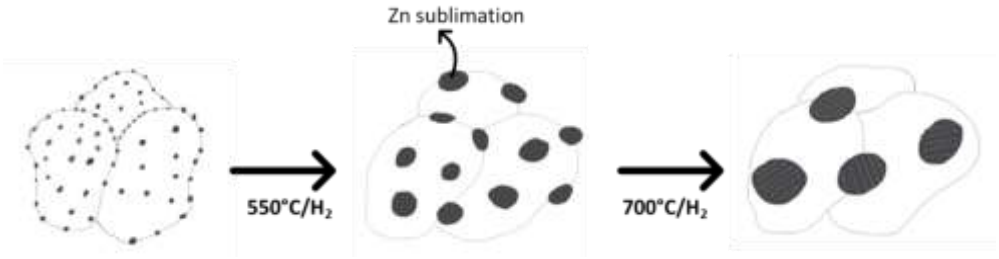

Figure 30 Proposed scheme for Zn loss dynamics in ZnZr(X) catalysts during H_2 activation.

3.5 Zn-doped ZrO_2 : catalyst deactivation after catalytic tests

3.5.1 *Ex situ* XAS

After having observed as Zn stability in ZnZr(X) catalysts is related to the formation of ZnO clusters which increases Zn volatility under H_2 at high temperatures, we measured *ex situ* Zn K-edge spectra of ZnZr(10) catalysts before (F-ZnZr(10)) and after (S-ZnZr(10)) catalytic test with (ZnZr(10)/S18) and without SAPO-18. Zn K-edge XANES spectra shows that Zn overall maintains the nanostructured ZnO-profile typically observed in these catalysts. In addition, a slight decrease of white-line intensity is observed in the spent catalysts (Figure 31a), associated to an increase of ZnO clusters dimensions. Even though ZnO clusters size increase is associated to a reduction of the total Zn concentration, as observed from Hf L_3-edge (Figure 31b,c), the lost Zn does not appear to diffuse in SAPO-18, as indicated by the absence of any additional spectral feature, possibly associated to Zn ions exchanged into the zeotype.

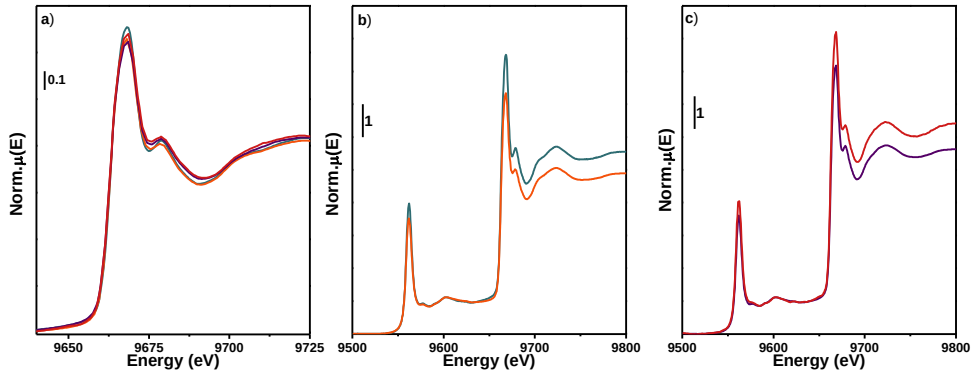

Figure 31 Zn K-edge XANES spectra for a) samples F-ZnZr(10) (blue line), F-ZnZr(10)/S18 (red line), S- ZnZr(10)/S18 (purple line), S-ZnZr(10) (orange line) and b) reference ZnO (grey line) and Zn(10%)Al_2O_3 (brown line). Hf L_3-edge XANES spectra for a) F-ZnZr(10) (blue line) and S-ZnZr(10) (orange line) and b) F-ZnZr(10)/S18 (red line) and S-ZnZr(10)/S18 (purple line).

3.6 $GaZrO_x$: from oxides clusters to the solid solution scenario

3.6.1 Catalyst average structure and electronic properties: PXRD and UV-Vis spectroscopy

Considering the solid solution scenario reported in Figure *14*, ZnZr(X) catalysts can described with the scenario A, which explains the parallel presence of ZnO nanoclusters in contact with a ZrO_2 matrix. This analysis was then applied to Ga-doped ZrO_2 catalyst which presented improved catalytic properties for CO_2 hydrogenation respect to ZnZr(X).[12] After reviewing literature results on different Ga concentrations (see Fend et al.[25]), GaZr(21) (21 wt% Ga loading) was chosen as case study sample. Considering PXRD pattern (Figure 32c) the same results reported for ZnZr(X) catalysts can be observed : I) tetragonal polymorph is stabilized respect to the monoclinic one, present in pure ZrO_2 prepared with the same synthesis strategy (Figure 32a) and II) the unit cell volume decreases as observed from the Bragg peak shift to lower angles. The t-ZrO_2 (102) reflection, quite visible in ZnZr(10) (Figure 32b), is not detected in GaZr(21) probably due to peak broadening induced by

crystallite size. Indeed, the tetragonal polymorph is confirmed from the Zr K-edge 1s→4p pre-edge peak.

To further investigate electronic properties of these catalysts, UV-Vis spectra in Figure 32d,e were measured and compared with those of the respective reference oxides i.e., ZnO, ZrO_2 and Ga_2O_3. ZnZr(X) spectra reflect the mixed oxides scenario. Indeed, ZnZr(5/10/15) spectra can be qualitatively described as a combination of reference ZrO_2 and ZnO. At higher Zn loadings, the series presented a band gap redshift towards ZnO one, likely be related to the quantum confinement reduction,[26] i.e., the smaller the ZnO cluster, the more blueshifted is the band gap, in agreement with larger ZnO cluster observed by XAS at higher Zn concentration (see Section 3.4.1). On the contrary GaZr(21) spectra reflects electronic properties not-identifiable by single ZrO_2 and Ga_2O_3, as observed for $CeZrO_4$ (Figure *15*b) suggesting an improved Ga dispersion in ZrO_2 lattice.

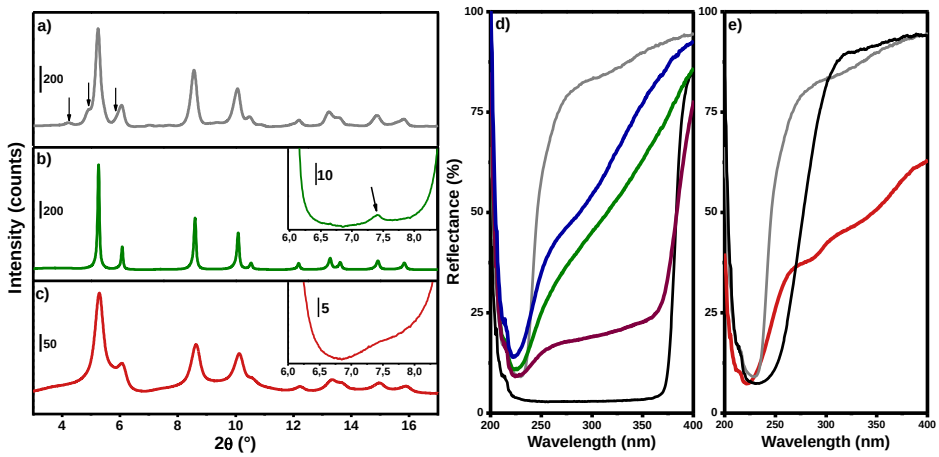

Figure 32 PXRD pattern (λ ≈ 0.27Å) for a) ZrO_2 (arrows indicate monoclinic reflections), b) ZnZr(10) and c) GaZr(21). t(102) Bragg peak is showed in the insets and indicated by an arrow. UV-Vis spectra for d) ZrO_2 (grey line), ZnZr(5) (blue line), ZnZr(10) (green line), ZnZr(15) (purple line) and ZnO (black line) and e) ZrO_2 (grey line), GaZr(21) (red line) and Ga_2O_3 (black line).

3.6.2 *In situ* XAFS: Ga local coordination

As discussed in the previous sections, ZnZr(10) Zn K-edge XANES spectra can be described considering a broadening of ZnO $1s \rightarrow 4p_{\pi}$ and $1s \rightarrow 4p_{\sigma}$ transitions. Using the same type of qualitative description, Ga K-edge XANES from reference beta-Ga_2O_3 (Sigma Aldrich >99%) (Figure 33a) is described with two components, associated to Ga with tetrahedral (T_d) and octahedral (O_h) coordination, respectively, showed in Figure 33d. GaZr(21) XANES spectra collected at RT (Figure 33a) consists of a single broad white-line which position suggests an higher abundance of T_d fraction. Moreover, after H_2 activation we observed an important decrease in the white-line intensity parallel to a slight shift of the edge position to lower energies. T_d/O_h ratio, evaluated with the fit procedure described in Chapter 2.2.6, showed as the as prepared sample contained already ≈74% of Ga(T_d) which increased to ≈78% after H_2 activation, relating the white-line intensity loss and the energy shift to a variation of T_d/O_h ratio (Figure 33a,b). If we consider Ga replacing Zr in ZrO_2 unit cell, Ga(T_d) might adapt easily to ZrO_8 double tetrahedral geometry respect to Ga(O_h), by introducing oxygen vacancies around Zr hence stabilizing the tetragonal polymorph. Indeed, only ≈26% of Ga has octahedral coordination, which could convert to the tetrahedral one by losing a pair of oxygen atoms during H_2 activation.

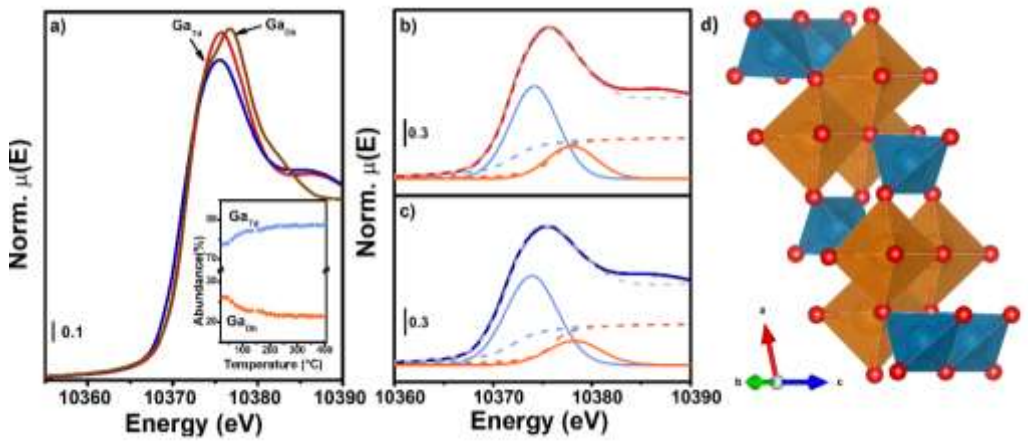

Figure 33 a) Ga K-edge XANES spectra at RT (red line) and 400°C (blue line) under H_2. Reference Ga_2O_3 is shown with brown line. Ga T_d (light blue squares) and O_h (orange squares) concentration evolution during H_2 thermal reduction is reported in the inset. Experimental (solid red line) and best fit (dashed grey line) Ga K-edge XANES measured at b) RT and c) 400°C with employed Pseudo Voigt (solid line) and Arctangent (dashed lines) functions to describe Ga T_d (light blue lines) and O_h (orange lines) components. d) Beta-Ga_2O_3 structure is reported on the right side with T_d and O_h polyhedral showed in blue and orange, respectively.

GaZr(21) Ga/Zr K-edges FT-EXAFS reported in Figure 34a,b gives an important information on Ga local geometry. Similarly, to ZnZr(10) sample, reported in Figure 34a,c for clarity, Zr K-edge second shell is abated due to Zr-Ga scattering paths having an imaginary component in antiphase respect to Zr-Zr. Differently from ZnZr(10), Zn FT-EXAFS first and second shell was likely ascribed to ZnO-like coordination, Ga K-edge presented a different scenario. Indeed, Ga K-edge first and second shell are not comparable to those of Ga_2O_3 suggesting the potential absence of Ga_2O_3 clustering.

The so observed Ga geometry improved the catalyst stability. Indeed, *ex situ* Ga K-edge XANES spectra collected on a spent catalyst after 14h of catalytic tests (Figure 34d) showed as ratio between Ga K- and Hf L_2-edges XANES spectra were almost

not modified after exposure to reaction conditions for long-time, highlighting as loss of Ga does not occur as instead observed for ZnZr(X) catalysts, reinforcing the hypothesis that Ga might be chemically inserted in ZrO_2 lattice.

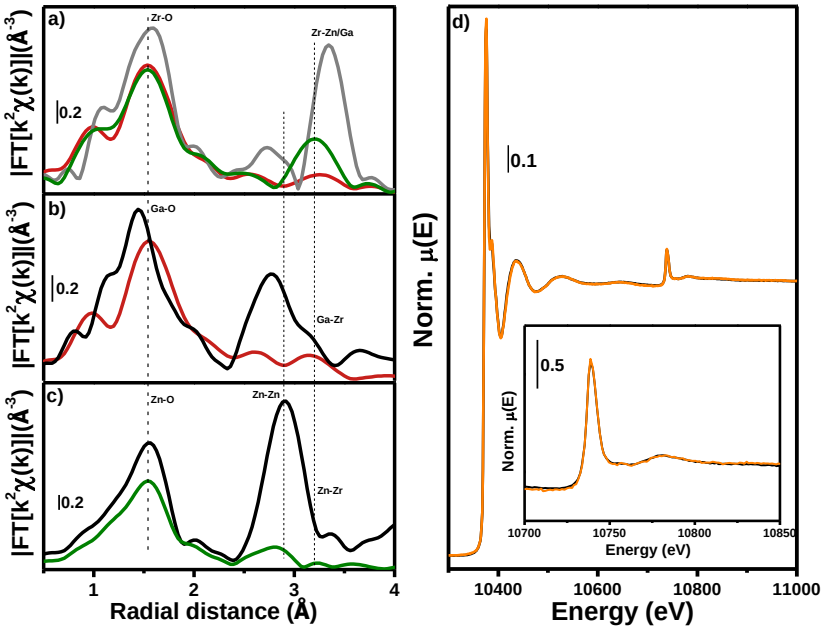

Figure 34 a,b,c) Magnitude of k^2-weighted phase-uncorrected FT-EXAFS for ZnZr(10) (green line) and GaZr(21) (red line) catalysts and ZrO_2 (grey line), Ga_2O_3 (black line) and ZnO (black line) extracted at a) Zr K-edge, b) Ga K-edge and c) Zn K-edge. d) Ga K-edge (main panel) and detail of Hf L_2 (inset) XANES spectra for F-GaZr(21) (black line) and S-GaZr(21) (orange line).

To further investigate Ga/Zr local environment, a double edge fit of the two edges FT-EXAFSs was conducted considering tetragonal ZrO_2 as input structure. Ga and Zr first coordination shell showed the presence of two cation-oxygen scattering paths from both edges viewpoint. Zr-$O_{I/II}$ scattering paths are associated to the double tetrahedra coordination, and their CN was related to the Ga content through a stoichiometric relation implying the formation of an V_O every 2 Ga atoms. The Ga content was constrained to 6 according to the total Ga evaluated by ICP analysis. As

sketched in Figure 35, Ga-O SS paths was described with 4 closer oxygens in tetrahedral (T_d) coordination (Ga-O_{Td}) and 6 farther oxygens in octahedral (O_h) coordination (Ga-O_{Oh}). The two scattering paths coordination number was weighted to the tetrahedral/octahedral above evaluated from XANES fit (≈74%) (Figure 33).

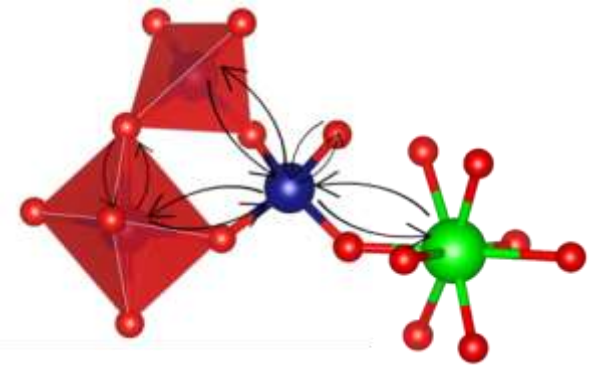

Figure 35 Proposed structural model for Ga local coordination. Scattering paths are indicated with arrows.

Unit cell parameters evaluated by PXRD Rietveld Refinement led to estimate the average the Zr/Ga-$O_{I/II}$ distances reported in Table *3*. Whilst PXRD gave an information on average distances, first shell FT-EXAFS fit provided a local information. By comparing Ga-O-Zr average radial distance with PXRD results (see equations below) we noticed as Ga-O_{Td}/Zr-O_I and Ga-O_{Oh}/Zr-O_{II} can be averaged to describe Ga_{Td}-O-Zr(O_{II}) ($\bar{R}_{\text{FT-EXAFS}}$: 1.98 Å vs R_{PXRD} : 2.05Å) and Ga_{Oh}-O-Zr(O_{II}) ($\bar{R}_{\text{FT-EXAFS}}$: 2.35 Å vs R_{PXRD} : 2.36Å) chemical bonds, respectively.

$$\frac{1.86(Ga - O_{Td}) + 2.09(Zr - O_I)}{2} = 1.98 \pm 0.04\text{Å} \approx 2.05\text{Å}(PXRD)$$

$$\frac{2.45(Ga - O_{Oh}) + 2.25(Zr - O_{II})}{2} = 2.35 \pm 0.11\text{Å} \approx 2.36\text{Å}(PXRD)$$

Zr second shell was described considering Zr-Ga and Zr-Zr SS paths with CN constrained to the Ga content, independent radial distances and Debye Waller

factors. Parallelly, Ga second shell presented a complex scenario: first of all, we considered a Ga-Zr scattering path with radial distance and Debye Waller factor constrained to the Zr-Ga one. Second, the structural model considered so far implied the presence of two Ga-Ga SS paths to describe both Ga in Td and Oh coordination, as done for the first coordination shell fit. The paths CN was weighted to the Ga content and to the Td/Oh ratio evaluated from Ga XANES fit (Table 3), independent radial distances were considered whilst since the same path is considered, the Debye Waller factor was fit to the same variable. The obtained results reported in Table 3 showed as the Zr-Ga/Ga-Zr SS paths presented comparable radial distance in line with PXRD result. At the same time Zr-Zr and Ga-Ga path resulted in longer and shorter distances respectively, in line with their ionic radii. Considering the latter path, it is noteworthy to notice that shorter and longer radial distances were evaluated for Ga-Ga_{Oh} and Ga-Ga_{Td} paths, in line with their difference in Ga_2O_3 (Ga-Ga_{Oh} ≈3.10Å vs Ga-Ga_{Td} ≈ 3.6Å). However, the evaluated Debye Waller factor presented a suspiciously large value (0.03$Å^2$) suggesting an high degree of structural disorder for these two paths. Moreover, the same comparison between radial distances evaluated by PXRD and FT-EXAFS done for first coordination shell can be applied to the second coordination shell. It is noteworthy to observe as the average distance evaluated by FT-EXAFS (see equation below) is closely comparable with PXRD results.

$$(3.49(Ga - Ga_{Td}) + 3.62(Ga - Ga_{Oh}) + 3.60(Ga - Zr) + 3.63(Zr - Zr))/4$$
$$= 3.59 \pm 0.12Å \approx 3.59Å(PXRD)$$

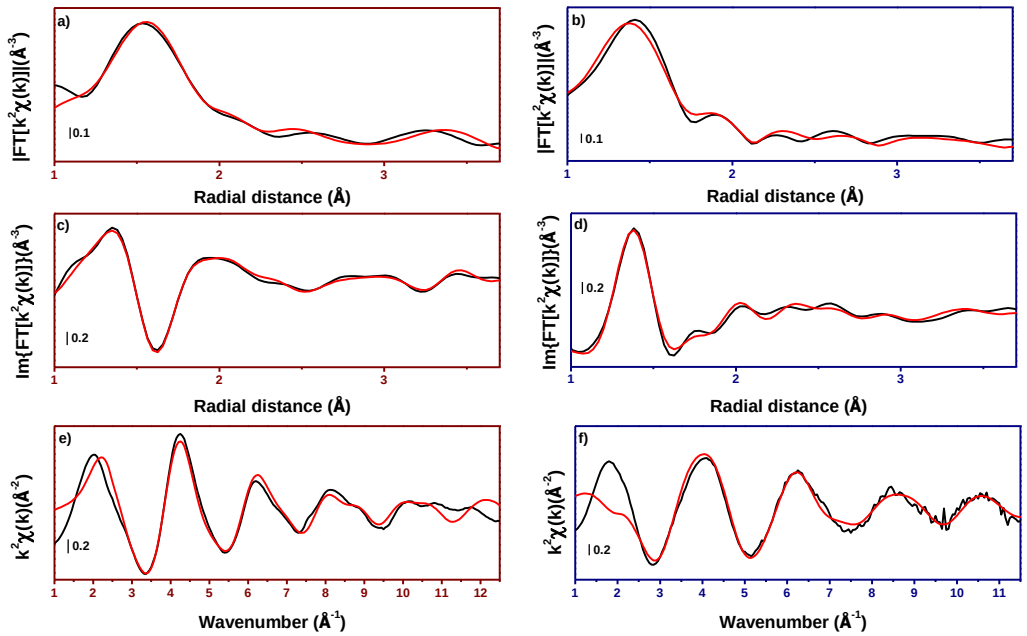

Figure 36 Zr K-edge (red panels) and Ga K-edge (blue panel) experimental (black lines) and best fit (red lines) of e,f) EXAFS and FT-EXAFS a,b) magnitude and c,d)imaginary components. Zr and Ga K-edges FT-EXAFS was extracted in the 2.3-11.4 $Å^{-1}$ k-range. EXAFS fit was conducted in the 1-3.7 Å R-range at both edges.

Table 3 GaZr(21) PXRD Rietveld refinement and FT-EXAFS fit results. R-factor = 0.011, employed 18 variables over 29 independent parameters. Ga K-edge: E_0 = -8± 5, Td=0.74, Ga=6. Zr K-edge : E_0 = -1.4±0.7 ,. [a] Determined from PXRD refinement. [b] Determined from FT-EXAFS fit.

Sample		**R(Å)[a]**	**R(Å)[b]**	**CN**	**σ^2 ($Å^2$)**
GaZr(21)	Ga-O_{Td}		1.86±0.04	4xT_d	0.004±0.003
	Ga-O_{Oh}		2.44±0.11	6x(1-Td)	0.004±0.003

	Ga-Ga_{Td}		3.5±0.3	GaxTd	**0.03±0.06**
	Ga-Ga_{Oh}		3.28±0.16	Gax(1-Td)	**0.03±0.06**
	Ga-Zr	3.5984	3.62±0.04	12-Ga	0.003±0.008
	Zr-O_I	2.0557	2.097±0.008	4-Ga/4	0.0074±0.0008
	Zr-O_{II}	2.3656	2.254±0.011	4-Ga/4	0.0031±0.0013
	Zr-Zr	3.5984	3.630±0.019	12-Ga	0.015±0.002
	Zr-Ga		3.60±0.04	Ga	0.023±0.008

3.6.3 Short range disorder: the price for solid solution formation

GaZr(21) was the last studied catalyst showing local ordering scenario completely different from $ZnZrO_x$ catalyst. The PXRD pattern presented tetragonal reflection however with abated intensities and broader FWHM respect to the other catalysts, indicating a smaller crystallite size hence a reduced long-range ordering. Moreover, the PXRD background presented an interesting modulation which will be object of future Total Scattering measurements for Pair Distribution Function extraction. Ga K-edge XANES indicates a high concentration of Ga T_d coordinated (≈74%). Ga content evaluated by ICP and its Td:Oh ratio were used as input parameters to conduct a double-edge fit of Zr and Ga FT-EXAFS spectra. The employed model considering Ga replacing Zr in its tetragonal unit cell, with Ga with either Td or Oh coordination well fit the experimental spectra. A high degree of disorder in the Ga-Ga coordination shell was observed, suggesting as this structural model could be only a preliminary description of this complex catalyst structure.

3.7 $ZnZrO_x$ stabilisation through Ce-doping: $ZnCeZrO_x$

To stabilize ZnZr(X) catalysts, ICC partner tried to include Zn in a Ce-doped ZrO_2 lattice.[27] The presence of Cerium should induce a volume expansion improving Zn

accommodation in ZrO_2 lattice. The obtained catalysts presented a single phase diffractogram ascribable to tetragonal ZrO_2 polymorph. The catalyst presented a stoichiometry of $Zn_{0.5}Ce_{0.2}Zr_{1.8}O_4$ evaluated by ICP-AES analysis and a surface area of 79.4 m^2/g. The catalyst catalytic properties were tested in combination with several zeolites (H-RUB-13, H-SAPO-34, H-ZSM-11 and H-ZSM-5) showing the highest CO_2 conversion (10.7%) and $C_2^=$-$C_4^=$ selectivity (83.4%) with H-RUB-13 at 350°C and 1MPa, which is an improvement respect to ZnZr(X) but lower then $GaZrO_x$.

To analyse the domain short range ordering stability of the catalyst, in-situ PXRD and XAS experiments were performed under activation and reaction conditions.

3.7.1 *In situ* experiment description

Quasi-simultaneous in-situ PXRD/XAS data were collected during the protocol described in Figure 37 at the BM31 beamline of the ESRF Synchrotron. The beamline set-up allows to switch between PXRD (λ=0.270Å) and the XAS monochromators with a total PXRD/XAS collection time of ≈5 minutes. Data were collected from a powder pressed in a capillary with diameter optimized depending on the measured K-edge (i.e. Zn, Zr and Ce). Due to capillary thickness, PXRD data were collected in parallel to XAS measurements at Zn K-edge, presenting the thinner capillary (Ø=0.5 mm) whilst Zr and Ce K-edge were collected by repeating the same experimental conditions without measuring the PXRD data on Ø=0.7 mm capillaries.

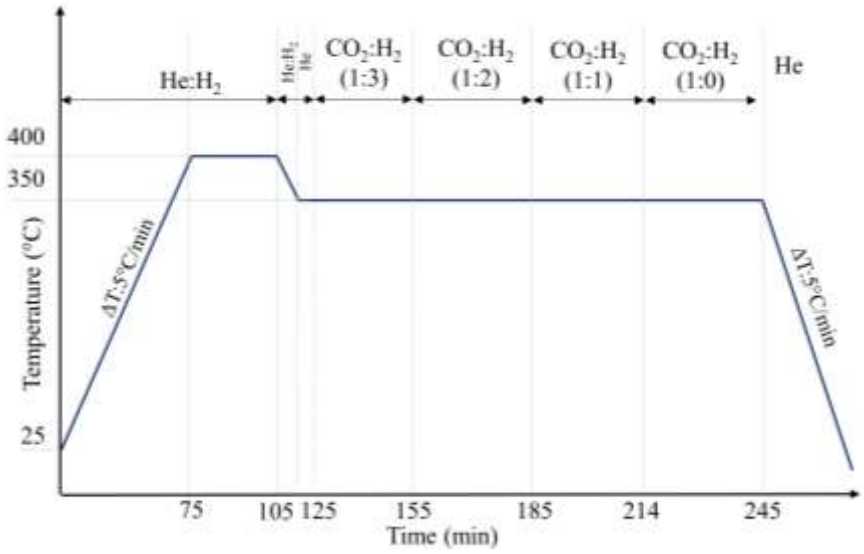

Figure 37 Activation/Reaction protocol employed for measuring quasi simultaneous in-situ PXRD/XAS data.

3.7.2 In-situ PXRD/XAS: catalyst activation

As for ZnZr(X) catalyst, the most relevant details on $ZnCeZrO_x$ (named ZCZ) structure were obtained during its activation under $He:H_2$ stream. The initial PXRD pattern collected at RT (Figure 38 a black line) presented t-ZrO_2 Bragg reflections, likely stabilized by Zn and Ce presence, with additional h-ZnO reflections (Figure 38 a arrows), highlighting the potential presence of long range ordered/segregated ZnO domains already in the as prepared catalyst. During thermal activation the catalyst structure is maintained i.e., no extra reflections were formed. However, important variations were observed in the t-ZrO_2 average unit cell volume and ZrO_2/ZnO relative concentration, reported in Figure 38b and c. Until 300°C the unit cell volume increases in line with reference ZrO_2 thermal expansion. However, at T>300°C the volume began to rise very rapidly until 400°C where it presented a decrease during the 30' holding, which will be rationalised hereafter. Parallelly, we noticed as the ZnO relative abundance increased respect to t-ZrO_2, in line with an increase of ZnO domains ordering observed for ZnZr(X) catalysts and explaining the

slope variation of unit cell expansion. It is noteworthy as the increase of ZnO content explains the peculiar evolution of the observed Bragg reflection some of which presented an intensity rise during heating (Figure 38a inset), in contradiction with the higher thermal Debye Waller contribution.

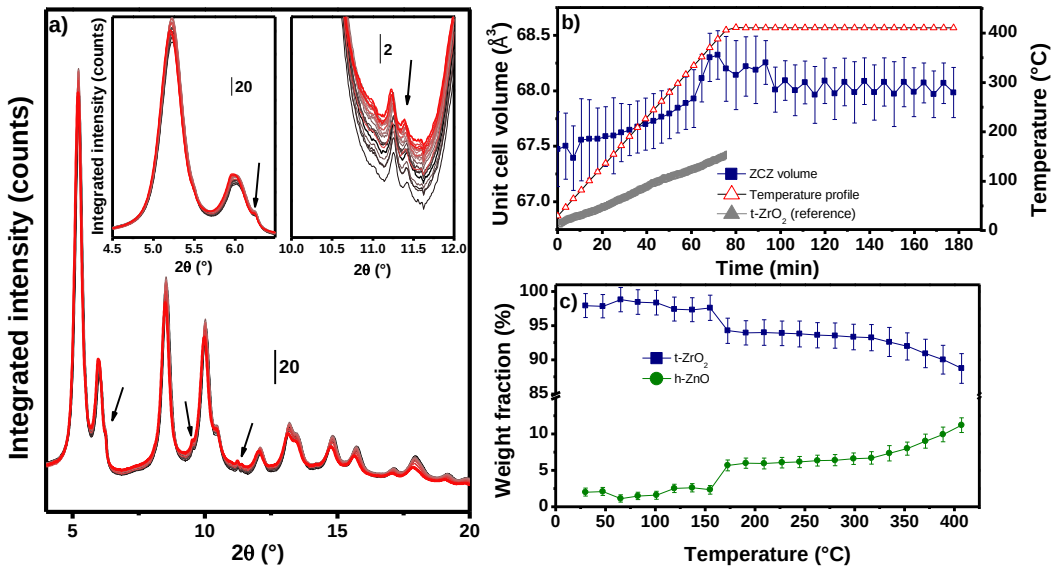

Figure 38 a) In-situ PXRD pattern ($\lambda \approx 0.27$Å) collected during catalyst activation under He:H_2 from RT (black line) to 400°C (red line). h-ZnO reflections are indicated with arrows. b) Unit cell volume and c) ZrO_2/ZnO relative abundances evaluated with Sequential Rietveld Refinement of the experimental diffractograms. Reference t-ZrO_2 unit cell volume expansion is reported with grey symbols for clarity.

Quasi-simultaneously to PXRD patterns we collected Zn K-edge spectra due to the employment of the thinner capillary (Ø=0.5 mm) whilst Zr and Ce k-edges were collected by following the same protocol reported in Figure 37, however, with thicker capillaries not allowing to collect also PXRD patterns.

The as prepared catalyst presented Zn, Zr and Ce K-edge XANES spectra (Figure 39 black lines) well ascribable to those previously observed for ZnZr(X) and $CeZrO_4$

catalysts (see Chapter 3.2). Zn K-edge (Figure 39 a) indicates a ZnO-like environment whilst Zr K-edge (Figure 39 b) highlighted the presence of the tetragonal polymorph from the 1s→4p pre-edge fingerprint of the ZrO_8 double tetrahedra coordination, both in line with the previous findings on ZnZr(5/10/15) catalysts. Differently from $CeZrO_4$ where some Ce^{3+} was already observed in the as-prepared catalyst, ZCZ Ce K-edge (Figure 39 c) presented a white-line shape and energy position indicating the presence of Ce^{4+} in a cubic CeO_2-like environment with Ce^{3+} concentration lower than the detection limit (<5%).

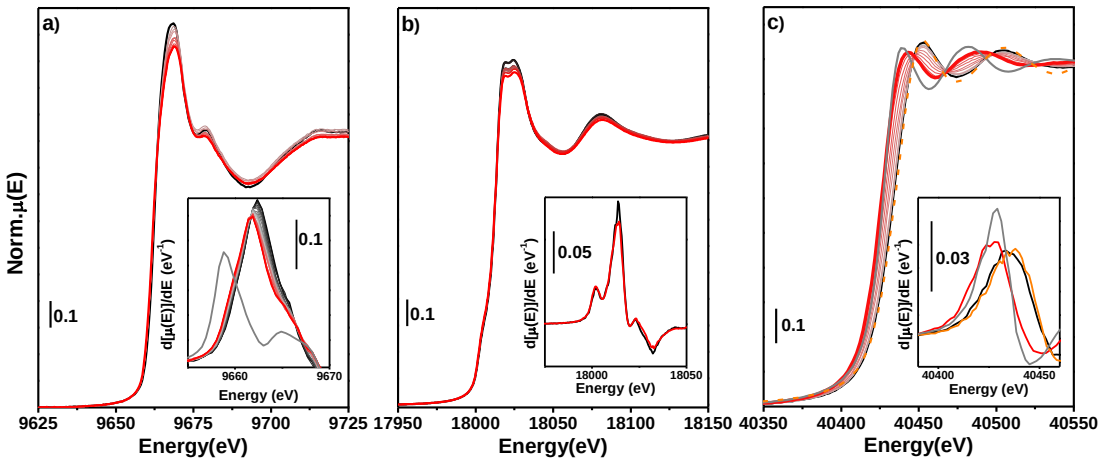

Figure 39 In-situ XANES spectra collected at a) Zn, b) Zr and c) Ce K-edges. Temperature increases from black to red line. Respective XANES first derivative is reported in the insets in every panel. Zn foil, $Ce(NO_3)_3$ and CeO_2 reference spectra are reported with grey and orange line, respectively.

As for ZnZr(X) catalysts, during activation no net variations were observed at Zr K-edge XANES spectra (Figure 39 b). Contrarily, at Zn K-edge we observed an important decrease of the white line intensity and a slight energy shift to lower energies of the rising edge, clearly visible in the spectra first derivative (Figure 39 a inset). The former spectral change, too large to be associated only to DW factor effect, could be related to an increase of ZnO domain size, as observed for ZnZr(X)

catalysts, in line with the rise of h-ZnO relative concentration extracted by PXRD Rietveld Refinement discussed in the previous paragraph (Figure 39 c). Furthermore, the spectra first derivative presented slight shift to lower energies with an additional weak contribution at energy position comparable with metallic Zn, indicating a potential $Zn^{2+} \rightarrow Zn^{\delta}$ ($2<\delta<0$) partial reduction. Parallelly, under the same conditions Ce K-edge (Figure 39 c) showed an important white-line and absorption edge shift to lower energies. Indeed, by comparing the collected spectra with CeO_2 and $Ce(NO_3)_3$ references (Figure 39 c) we noticed as ZCZ spectra collected at 400°C presented a shoulder in the rising edge at energies lower than Ce^{3+}. This is more visible in the XANES first derivative (Figure 39 c inset), suggesting the presence of Ce with oxidation state lower than Ce^{3+}.

To further investigate the electronic evolution of Ce states during the activation protocol, MCR-ALS routine was employed to extract the spectral component related to the final Cerium oxidation state. An unbiased MCR-ALS routine (not reported for brevity) led to two spectral components consisting in the two spectra collected at RT and 400°C respectively. Since we know that Ce has to go through the Ce^{3+} oxidation state before reaching the unknown final oxidation state, $Ce(NO_3)_3$ spectra was employed as reference component to extract the Ce^{3+} component i.e., 20 replicas of the spectra were reported after the experimental dataset. With this approach, the PCA allowed to extract the three components reported in Figure 40a. Considering the white-line/absorption edge energy position and post edge oscillation shape the spectra in red and green can be associated to those of Ce^{4+} and Ce^{3+} from CeO_2 and $Ce(NO_3)_3$ references, respectively. Contrarily the last spectrum (blue line) is not ascribable to any of the references and presented an energy position lower (>5eV) than Ce^{3+}. Ce metal foil XANES spectra could not be measured due to Ce(0) instability and reference Ce K-edge spectra for this oxidation state are rarely available in literature. Hence, we could not identify the oxidation state of the extracted component and from now on we will refer to it as $Ce^{\delta+}$. Nevertheless, the

obtained concentration profiles, reported in Figure 40b, unveiled an almost complete reduction of Ce^{4+} starting at 320°C with the formation of Ce^{3+} and $Ce^{\delta+}$, the latter becoming the most abundant component (≈60%) in the activated catalyst.

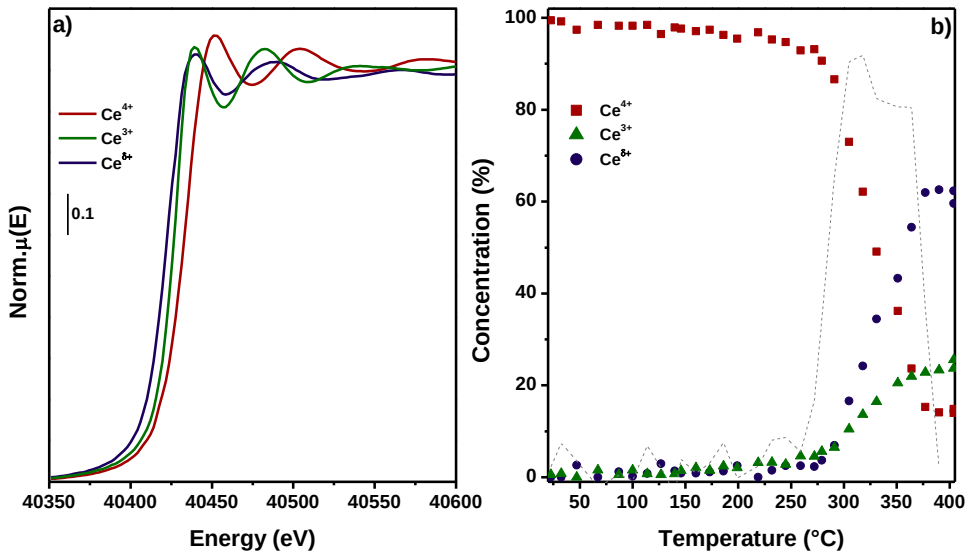

Figure 40 Ce K-edge XANES a) Spectra components and their respective b) concentration profile evolutions extracted from MCR-ALS routine. Ce^{4+} first derivative is reported with dashed grey line.

It is noteworthy as Ce and Zn reductions occurs parallelly, indicating a potential concerted reduction likely related to the formation of a Ce_xZn_y alloy further discussed with the FT-EXAFS analysis. Unfortunately, due to the low content of metallic Zn, an attempted MCR-ALS routine to Zn K-edge spectra (not reported for sake of brevity) did not allow to extract two meaningful components i.e., Zn^{2+} and Zn^0.

3.7.3 Ce surface reduction: *in-situ* near ambient pressure NEXAFS

Even though Ce K-edge spectra clearly showed the formation of strongly reduced $Ce^{\delta+}$ species on ZCZ catalyst, hard X-Ray measured in transmission mode are probing both bulk and surface of the catalysts, leaving uncertain Ce surface (i.e.,

reactive) oxidation state. For this reason, we decided to measure Ce M_5-edge NEXAFS spectra in Total Electron Yield (TEY) detection mode which reduced the X-Ray penetration depth to few nm enhancing the technique surface sensitivity. The measurement set-up available at APE-HE beamline allowed an almost complete reproduction of the hard X-Ray measurements however, limiting the maximum temperature to 375°C. Spectra collected during sample activation (RT-375°C/H_2:He 50 mL/min) are reported in Figure 41a. The results indicates a clear evolution from an initial spectrum at RT with shape and energy position, ascribable to Ce^{4+} (see CeO_2 reference in Figure 41b inset), to a final spectra at lower energy characterized by a double-edge fingerprint, comparable to Ce^{3+} reference spectra (see CeF_3 reference in Figure 41b inset).

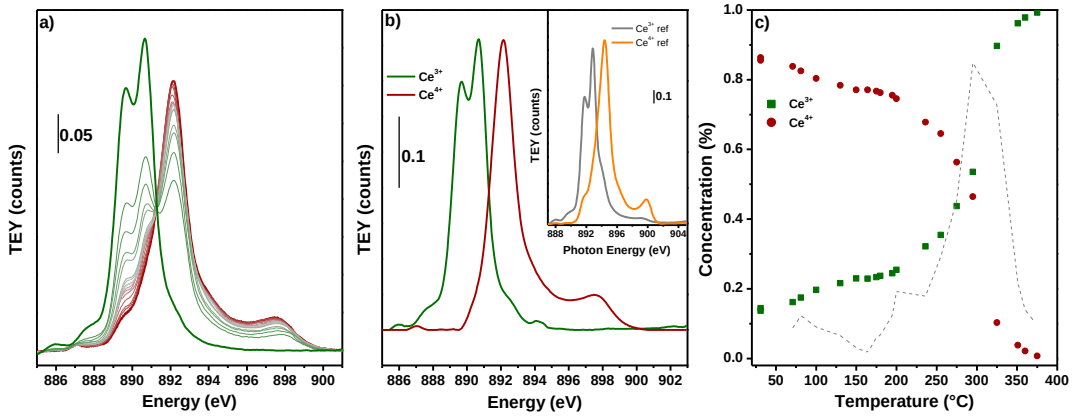

Figure 41 a) Experimental Ce M_5-edge collected under H_2:He (1:1 50 mL/min) stream from RT to 375°C. Temperature increases from red to green line. b) Concentration profile and c) spectra component extracted from MCR-ALS routine. Ce^{4+} first derivative is reported with dashed grey line. Reference CeO_2 (orange line) and CeF_3 (grey line) experimental spectra are reported in the inset in panel b).

Since Ce local environment affects the M_5-edge bands shape, particularly the feature at 898 eV, a linear combination fit using CeO_2/CeF_3 as references spectra was not possible. Contrarily, by applying an unbiased MCR-ALS routine i.e., without the use

of any reference spectra, we successfully extracted two spectra component reported in Figure 41b well comparable with $Ce^{4+/3+}$ references oxidation states (see Figure 41b inset). The components concentration profiles indicate a complete Ce^{4+}-to-Ce^{3+} reduction starting at 200°C and with a maximum variation at 300°C, both temperatures lower than what observed at Ce K-edge. It is noteworthy as Ce^{3+} and Ce^{0} have similar M_5-edge NEXAFS spectra, hence making their distinction almost impossible.[28] We should then consider as in the evaluated Ce^{3+} content, part of Ce might have oxidation state δ where $3<\delta<0$.

3.7.4 Ce_xZn_y alloy evolution under reaction-like conditions

To understand the behaviour of the ZCZ catalysts and particularly of the Ce_xZn_y alloy, Ce K-edge XANES and Ce M_5-edge NEXAFS spectra were collected under reaction-like conditions (350°C, CO_2:H_2:He 50 mL/min, 1 bar) varying the CO_2:H_2 ratio. From the spectra evolution reported in Figure 42 we immediately noticed a variation of their position and shape at both edges towards the reference Ce^{4+}. The collected spectra were analysed by MCR-ALS routine together with those measured during catalyst activation to completely describe the Ce species kinetic evolution with the extracted components discussed in the previous sections. The obtained Ce K-edge concentration profiles (Figure 42c) indicated as the presence of CO_2 causes a complete oxidation of Ce^{3+} to Ce^{4+} whilst $Ce^{\delta+}$ presented a higher stability, with a final Ce^{4+}/$Ce^{\delta+}$ concentration of ≈60/40%, respectively. Interestingly, the same behaviour was observed also at Ce M_5-edge (Figure 42d). We observed a Ce^{3+} oxidation to Ce^{4+} with the increase of CO_2 concentration, finishing with a final ratio under pure CO_2 comparable with the results obtained with hard X-ray.

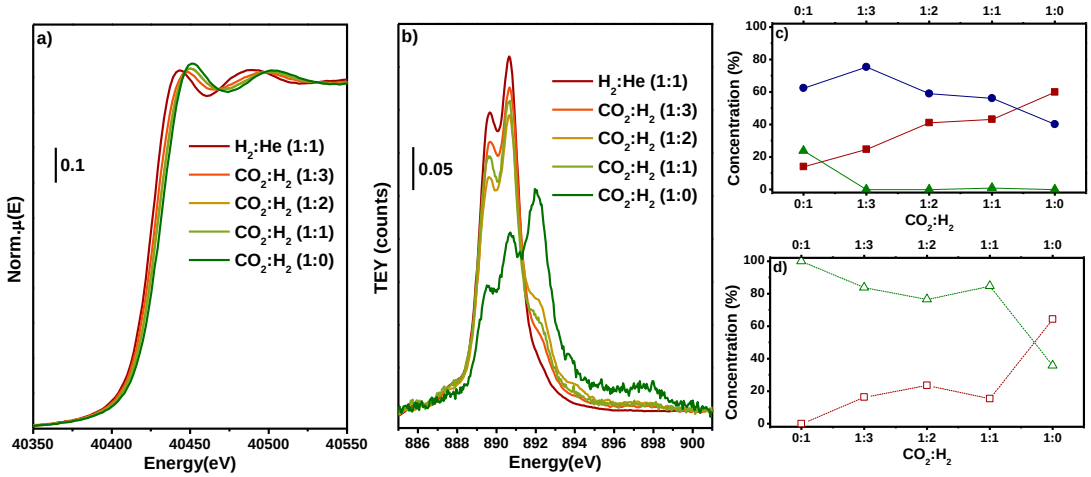

Figure 42 a) Ce K-edge XANES and b) M_5-edge NEXAFS spectra collected under 1 bar of different CO_2:H_2 ratio at 350°C. c,d) Ce^{4+} (squares), Ce^{3+}(triangles) and $Ce^{\delta+}$(circles) concentration profile extracted from MCR-ALS protocol applied to c) XANES (filled symbols) and d) NEXAFS (empty symbols) experimental spectra.

Since from hard X-Ray Ce^{3+} was observed to disappear completely with CO_2 presence in the feed, we can assume as the Ce^{3+} component observed by soft X-ray might be actually related to Ce(0), presenting a surface stability comparable with $Ce^{\delta+}$ observed in the catalyst bulk.

3.7.5 $ZnCeZrO_x$: simple rationalization of a complex system

The obtained results indicated as ZCZ catalyst presented a high degree of local structural complexity. The as prepared catalyst structure, sketched in Figure 43, consisted in a $CeZrO_x$ type 2 matrix with embedded ZnO domains larger than those previously observed for ZnZr(X) catalyst. Under reducing conditions (H_2, 400°C): I) ZnO domain size increases, influencing $CeZrO_x$ expansion linearity and II) Ce atoms are easily reduced first on the surface then in the bulk. The presence of a type 2 solid solution likely facilitates Ce migration at the highest temperatures (≈400°C) towards ZnO domains to form a Ce_xZn_y alloy on the domain surface, causing a drop of the unit cell volume and the Zr-Zr/Ce local radial distance. The formed Ce_xZn_y

presented a stability higher than Ce^{3+} under reaction like conditions i.e., in presence of CO_2, suggesting as this component might be the catalyst actual active part for CO_2 hydrogenation.

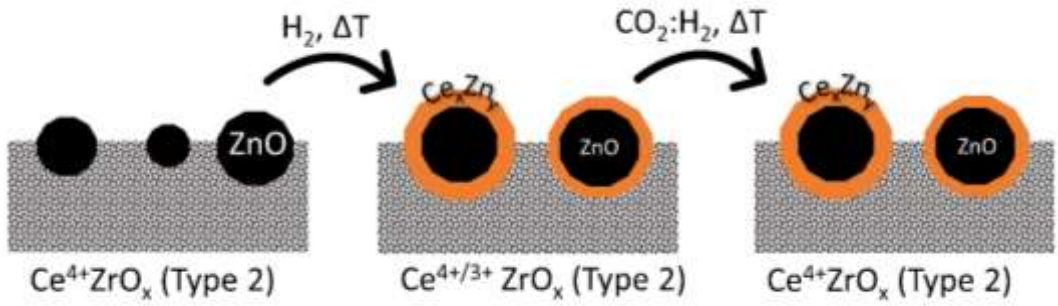

Figure 43 $ZnCeZrO_x$ structural evolution under activation and reaction conditions.

3.8 Conclusions

$ZnZrO_x$, $CeZrO_x$ and $GaZrO_x$ average structure was determined through Rietveld Refinement whilst guest atom/host matrix local structures were investigated by analysis of XANES and FT-EXAFS spectra collected at Zn K-, Ga K-, Zr K-, Ce K- and Hf $L_{3,2}$-edges. Even though the PXRD pattern (average structural probe) presented a single phase in all the three samples, it was observed particularly in the ZnZr(X) case where more data were available, as the unit cell volume did not change linearly with the guest atom concentration, hence not respecting the Vegard's law.[23] This is indeed a first indicator of the potential local order complexity respect to average structure reflected from PXRD patterns. Another indicator came from the UV-Vis (average electronic probe) spectra of the catalysts. Even if this technique is rarely employed for heterogenous catalysts characterization whilst more spread in photocatalysis, we here showed as it can be a powerful tool to verify if the sample presents new electronic properties (i.e., intimate guest atom/host matrix mixing) or it can be described with two different oxides (i.e., local domain ordering). Finally, analysis of XANES and FT-EXAFS spectra (i.e., local probes) unveiled as $ZnZrO_x$,

$CeZrO_x$ and $GaZrO_x$ can be referred to the three solid solution scenarios reported in Figure *14*. The conducted study showed as measuring both matrix and guest atom K-edges was fundamental to determine the local structure of the catalyst. It was observed as the average structure determined by PXRD was related to the long-range ordering of the matrix whilst the guest atom atom always presented a certain degree of local disorder. The guest atom dispersion respect to its clustering (domain ordering) is showed to drastically influence the catalyst properties. In term of activity, the guest atom dispersion increases the oxygen vacancies concentration hence improving the CO_2 conversion. On the contrary, it was observed as the guest atom clustering reduces the catalyst stability. Indeed, $GaZrO_x$ showed as Ga concentration did not change after reaction whilst $ZnZrO_x$ reported as the ZnO cluster dimension increased with a parallel decrease of the total Zn content. The detailed analysis on $Zn/CeZrO_x$ was used to understanding the peculiar behaviour of Zn-doped $CeZrO_x$. ZnO clustering was observed to occur also in this chase. However, during H_2 activation the presence of ZnO cluster to Ce atoms increased the reducibility of the latter at both bulk and surface scales. The Ce reducibility enhancement is ascribed to the formation of an intermetallic Ce_xZn_y compound presenting a high stability under reaction-like conditions. More detailed properties of this intermetallic and its role for CO_2 hydrogenation reaction will be object of future studies.

References

(1) Huang, J.; Li, W.; Wang, K.; Huang, J.; Liu, X.; Fu, D.; Li, Q.; Zhan, G. M XO Y-ZrO2 (M = Zn, Co, Cu) Solid Solutions Derived from Schiff Base-Bridged UiO-66 Composites as High-Performance Catalysts for CO2 Hydrogenation. *ACS Appl. Mater. Interfaces* **2019**, *11* (36), 33263–33272. https://doi.org/10.1021/acsami.9b11547.

(2) Dang, S.; Gao, P.; Liu, Z.; Chen, X.; Yang, C.; Wang, H.; Zhong, L.; Li, S.; Sun, Y. Role of Zirconium in Direct CO2 Hydrogenation to Lower Olefins on Oxide/Zeolite Bifunctional Catalysts. *J. Catal.* **2018**, *364*, 382–393. https://doi.org/10.1016/j.jcat.2018.06.010.

(3) Ramirez, A.; Ticali, P.; Salusso, D.; Cordero-Lanzac, T.; Ould-Chikh, S.; Ahoba-Sam, C.; Bugaev, A. L.; Borfecchia, E.; Morandi, S.; Signorile, M.; Bordiga, S.; Gascon, J.; Olsbye, U. Multifunctional Catalyst Combination for the Direct Conversion of CO 2 to Propane. *JACS Au* **2021**, *1* (10), 1719–1732. https://doi.org/10.1021/jacsau.1c00302.

(4) Ruzzi, P.; Salusso, D.; Baravaglio, M.; Szeto, K. C.; De Mallmann, A.; Jiménez, L. G.; Godard, C.; Benayad, A.; Morandi, S.; Bordiga, S.; Taoufik, M. Supported PdZn Nanoparticles for Selective CO2 Conversion, through the Grafting of a Heterobimetallic Complex on CeZrOx. *Appl. Catal. A Gen.* **2022**, *635* (November 2021). https://doi.org/10.1016/j.apcata.2022.118568.

(5) Ojelade, O. A.; Zaman, S. F. A Review on CO_2 Hydrogenation to Lower Olefins: Understanding the Structure-Property Relationships in Heterogeneous Catalytic Systems. *J. CO2 Util.* **2021**, *47* (January), 101506. https://doi.org/10.1016/j.jcou.2021.101506.

(6) Li, Z.; Qu, Y.; Wang, J.; Liu, H.; Li, M.; Miao, S.; Li, C. Highly Selective Conversion of Carbon Dioxide to Aromatics over Tandem Catalysts. *Joule*

2019, *3* (2), 570–583. https://doi.org/10.1016/j.joule.2018.10.027.

(7) Ticali, P.; Salusso, D.; Ahmad, R.; Ahoba-Sam, C.; Ramirez, A.; Shterk, G.; Lomachenko, K. A.; Borfecchia, E.; Morandi, S.; Cavallo, L.; Gascon, J.; Bordiga, S.; Olsbye, U. CO 2 Hydrogenation to Methanol and Hydrocarbons over Bifunctional Zn-Doped ZrO 2 /Zeolite Catalysts. *Catal. Sci. Technol.* **2021**. https://doi.org/10.1039/D0CY01550D.

(8) Liu, X.; Wang, M.; Yin, H.; Hu, J.; Cheng, K.; Kang, J.; Zhang, Q.; Wang, Y. Tandem Catalysis for Hydrogenation of CO and CO2 to Lower Ole Fi Ns with Bifunctional Catalysts Composed of Spinel Oxide and SAPO-34. **2020**. https://doi.org/10.1021/acscatal.0c01579.

(9) Kirilin, A. V.; Dewilde, J. F.; Santos, V.; Chojecki, A.; Scieranka, K.; Malek, A. Conversion of Synthesis Gas to Light Olefins: Impact of Hydrogenation Activity of Methanol Synthesis Catalyst on the Hybrid Process Selectivity over Cr-Zn and Cu-Zn with SAPO-34. *Ind. Eng. Chem. Res.* **2017**, *56* (45), 13392–13401. https://doi.org/10.1021/acs.iecr.7b02401.

(10) Li, Z.; Wang, J.; Qu, Y.; Liu, H.; Tang, C.; Miao, S.; Feng, Z.; An, H.; Li, C. Highly Selective Conversion of Carbon Dioxide to Lower Olefins. *ACS Catal.* **2017**, *7* (12), 8544–8548. https://doi.org/10.1021/acscatal.7b03251.

(11) Zhang, W.; Wang, S.; Guo, S.; Qin, Z.; Dong, M.; Wang, J.; Fan, W. Effective Conversion of CO 2 into Light Olefins along with Generation of Low Amounts of CO. *J. Catal.* **2022**, *413*, 923–933. https://doi.org/10.1016/j.jcat.2022.07.041.

(12) Sen, W.; Li, Z.; Pengfei, W.; Weiyong, Z.; Zhangfeng, Q.; Mei, D.; Jianguo, W.; Unni, O.; Weibin, F. Highly Selective Hydrogenation of CO2 to Propane. *NATCATAL-2*.

(13) Montini, T.; Melchionna, M.; Monai, M.; Fornasiero, P. Fundamentals and

Catalytic Applications of CeO2-Based Materials. *Chem. Rev.* **2016**, *116* (10), 5987–6041. https://doi.org/10.1021/acs.chemrev.5b00603.

(14) Nagai, Y.; Yamamoto, T.; Tanaka, T.; Yoshida, S.; Nonaka, T.; Okamoto, T.; Suda, A.; Sugiura, M. XAFS and XRD Analysis of Ceria-Zirconia Oxygen Storage Promoters for Automotive Catalysts. *Top. Catal.* **2008**, *47* (3–4), 137–147. https://doi.org/10.1007/s11244-007-9018-3.

(15) Nagai, Y.; Yamamoto, T.; Tanaka, T.; Nonaka, T.; Suda, A. Study on the Thermal Degradation of CeO2-ZrO2 Solid Solution by XAFS and XRD. *Phys. Scr. T* **2005**, *T115*, 664–666. https://doi.org/10.1238/Physica.Topical.115a00664.

(16) Vlaic, G.; Fornasiero, P.; Geremia, S.; Kašpar, J.; Graziani, M. Relationship between the Zirconia-Promoted Reduction in the Rh-Loaded Ce0.5Zr0.5O2 Mixed Oxide and the Zr-O Local Structure. *J. Catal.* **1997**, *168* (2), 386–392. https://doi.org/10.1006/jcat.1997.1644.

(17) Miyazawa, K.; Suzuki, K.; Sakuma, T. HREM Observation of Domain Boundaries in Tetragonal Zirconia. *Philos. Mag. B Phys. Condens. Matter; Stat. Mech. Electron. Opt. Magn. Prop.* **1993**, *67* (4), 595–599. https://doi.org/10.1080/13642819308207695.

(18) Shannon, B. Y. R. D.; H, M.; Baur, N. H.; Gibbs, O. H.; Eu, M.; Cu, V. Revised Effective Ionic Radii and Systematic Studies of Interatomie Distances in Halides and Chaleogenides. *Acta Crystallogr. Sect. A Found. Crystallogr.* **1976**, *32*, 751–767. https://doi.org/https://doi.org/10.1107/S0567739476001551.

(19) Schilling, C.; Hess, C. Real-Time Observation of the Defect Dynamics in Working Au/CeO2 Catalysts by Combined Operando Raman/UV-Vis Spectroscopy. *J. Phys. Chem. C* **2018**, *122* (5), 2909–2917.

https://doi.org/10.1021/acs.jpcc.8b00027.

(20) Li, P.; Chen, I. W.; Penner-Hahn, J. E. X-Ray-Absorption Studies of Zirconia Polymorphs. I. Characteristic Local Structures. *Phys. Rev. B* **1993**, *48* (14), 10063–10073. https://doi.org/10.1103/PhysRevB.48.10063.

(21) Lomachenko, K. A.; Jacobsen, J.; Bugaev, A. L.; Atzori, C.; Bonino, F.; Bordiga, S.; Stock, N.; Lamberti, C. Exact Stoichiometry of Ce x Zr 6-x Cornerstones in Mixed-Metal UiO-66 Metal-Organic Frameworks Revealed by Extended X-Ray Absorption Fine Structure Spectroscopy. *J. Am. Chem. Soc.* **2018**, *140* (50), 17379–17383. https://doi.org/10.1021/jacs.8b10343.

(22) Abrahams, S. C. and Bernstein, J. L. Remeasurement of the Structure of Hexagonal ZnO. *Acta Crystallogr. Sect. B Struct. Sci.* **1969**, *25*, 1233--1236. https://doi.org/10.1107/S0567740869003876.

(23) Kempter, C. P. Vegard's "Law." *Phys. Status Solidi* **1966**, *18* (2), K117–K118. https://doi.org/10.1002/pssb.19660180251.

(24) Salusso, D.; Borfecchia, E.; Bordiga, S. Combining X-Ray Diffraction and X-Ray Absorption Spectroscopy to Unveil Zn Local Environment in Zn-Doped ZrO2Catalysts. *J. Phys. Chem. C* **2021**, *125* (40), 22249–22261. https://doi.org/10.1021/acs.jpcc.1c06202.

(25) Feng, W. H.; Yu, M. M.; Wang, L. J.; Miao, Y. T.; Shakouri, M.; Ran, J.; Hu, Y.; Li, Z.; Huang, R.; Lu, Y. L.; Gao, D.; Wu, J. F. Insights into Bimetallic Oxide Synergy during Carbon Dioxide Hydrogenation to Methanol and Dimethyl Ether over GaZrOxOxide Catalysts. *ACS Catal.* **2021**, *11* (8), 4704–4711. https://doi.org/10.1021/acscatal.0c05410.

(26) Caetano, B. L.; Santilli, C. V.; Meneau, F.; Briois, V.; Pulcinelli, S. H. *In Situ* and Simultaneous UV-Vis/SAXS and UV-Vis/XAFS Time-Resolved Monitoring of ZnO Quantum Dots Formation and Growth. *J. Phys. Chem. C*

2011, *115* (11), 4404–4412. https://doi.org/10.1021/jp109585t.

(27) Wang, S.; Zhang, L.; Zhang, W.; Wang, P.; Qin, Z.; Yan, W.; Dong, M.; Li, J.; Wang, J.; He, L.; Olsbye, U.; Fan, W. Selective Conversion of CO_2 into Propene and Butene. *Chem* **2020**, *6* (12), 3344–3363. https://doi.org/10.1016/j.chempr.2020.09.025.

(28) Yağci, O. The M4, 5 Photo-Absorption Spectra of Cerium in Ce02 and Oxidation of Metallic Cerium. *J. Phys. C Solid State Phys.* **1986**, *19* (18), 3487–3495. https://doi.org/10.1088/0022-3719/19/18/020.

(29) Zelinska, O.; Conrad, M.; Harbrecht, B. Refinement of the Crystal Structure of Cerium Zinc (1:11), CeZn11. *Zeitschrift fur Krist. - New Cryst. Struct.* **2004**, *219* (1–4), 389–390. https://doi.org/10.1524/ncrs.2004.219.14.389.

4 CO_2-to-Dimethilcarbonate reaction over ZrO_2: liquid vs gas phase mechanism

4.1 Liquid phase reaction

In situ liquid phase IR experiments were conducted in multiple reflections ATR mode. All the experimental details are reported in materials and methods and in the Appendix F. Briefly, ZrO_2 catalyst was deposited over the crystal element (ZnSe) and pre-treated under cyclohexane at 70°C/60'. Background was collected after activation prior each measurement. As summarized in Figure 44, a methanol in cyclohexane solution (0.2 M) was mixed in a 1:1 ratio with CO_2-saturated cyclohexane and sent to the ZrO_2 catalyst at different temperatures (10,30,50 and 70°C).

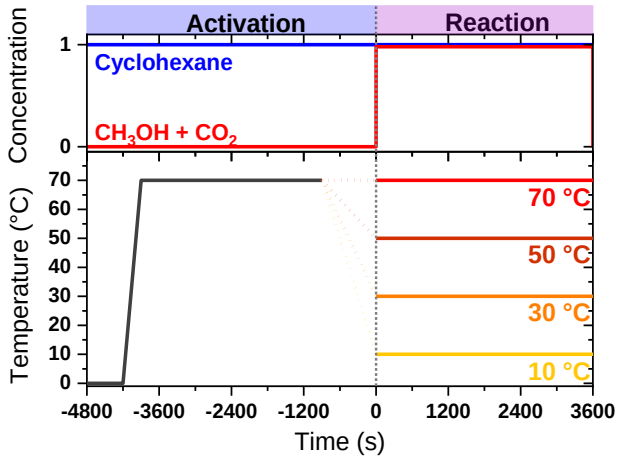

Figure 44 Schematic of the temperature/concentration profiles adopted in the in-situ ATR-IR experiments.

4.1.1 Adsorption of pure reagents/products

The *in situ* ATR-IR spectra related to the adsorption/desorption of methanol over ZrO_2 at 30 °C are presented in Figure 45a,b.

Three components were identified by Principal Component Analysis (PCA), leading to the spectral and concentration profiles in Figure 45c,d after MCR-ALS routine.

After a careful analysis of the spectra fingerprints and their time evolution we could identify component 1 as the spectrum of methanol solution, component 2 as weak physisorption of methanol with some surface sites of ZrO_2 and component 3 as linear and bridged methoxy groups coordinated to exposed Zr^{4+}.[1–3]

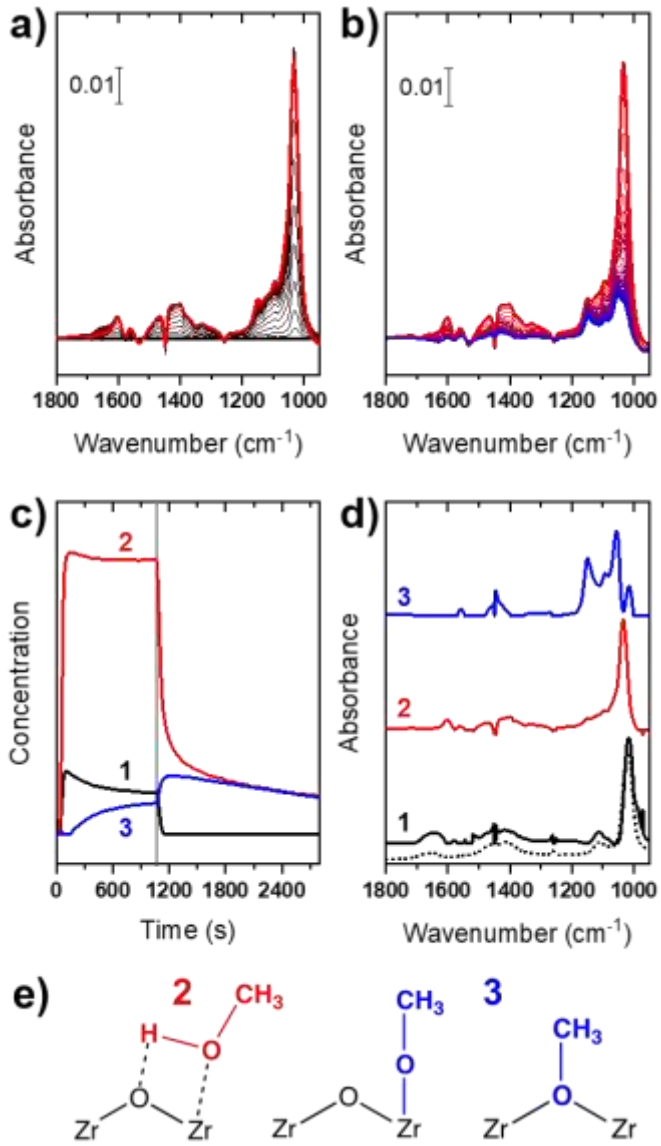

Figure 45 *In situ* ATR-IR spectra collected during a) adsorption of methanol on ZrO_2 (from a 0.2 M solution of methanol in cyclohexane, time evolution from black to red) at 30 °C and b) its desorption (by exposure to cyclohexane, time evolution from red to blue). c) Pure component spectra obtained by MCR-ALS (the ATR-IR spectrum of the bare 0.2 M solution of methanol in cyclohexane is shown as a dotted line). d) Corresponding concentration profiles as a function of time (the vertical grey

line represents the switch from the methanol solution to cyclohexane). e) Molecular structures of species associated to components 2 (weakly physisorbed methanol) and 3 (surface methoxide species); component 1 (liquid phase methanol) structure is omitted.

Considering adsorption of CO_2-saturated cyclohexane (Figure 46) we observed the formation of several signals in the carbonates vibration region. At maximum coverage (e.g. stable signal increase) four bands were distinguished at 1610, 1420, 1315 and 1040 cm^{-1} with an uncertainty on the second one being close to solvent phase poorly compensated signal. The same behavior is confirmed during desorption (Figure 46b), where the band at 1420 cm-1 showed a complete reversibility: this signal, typical of the bicarbonates-like ν(CO)sym mode. Conversely, the bands at 1610, 1315 and 1040 cm^{-1}, together with an additional component at 1530 cm -1 becoming evident at the lower CO_2 coverage, decreased during desorption and stabilized towards at the end of the experiment, finally yielding the pink spectrum labelled as 4 in Figure 46. These signals can be assigned to various families of carbonate-like species, most probably adsorbed mono- and bi-dentate carbonates. [4–7] A precise assignment of each band to a precise specific family of carbonates is not trivial due to the liquid phase environment, indeed as a much very heterogenous population of surfaces sites is expected as compared to gas-phase activated samples. Interestingly, bicarbonates fingerprint at 1225 cm^{-1} stemming from isolated δ(OH) was not observed, probably due to the liquid working conditions. However, we cannot exclude that the bicarbonates vibration might actually be related to another carbonate species different from gas phase adsorption.

MCR-ALS was attempted trying to isolate two spectral components. However, contrarily respect to gas-phase experiments, the procedure did not converge to meaningful spectra. In the following reactivity analysis we then considered the spectrum labelled 4 in Figure 46 as single component for surface carbonate.

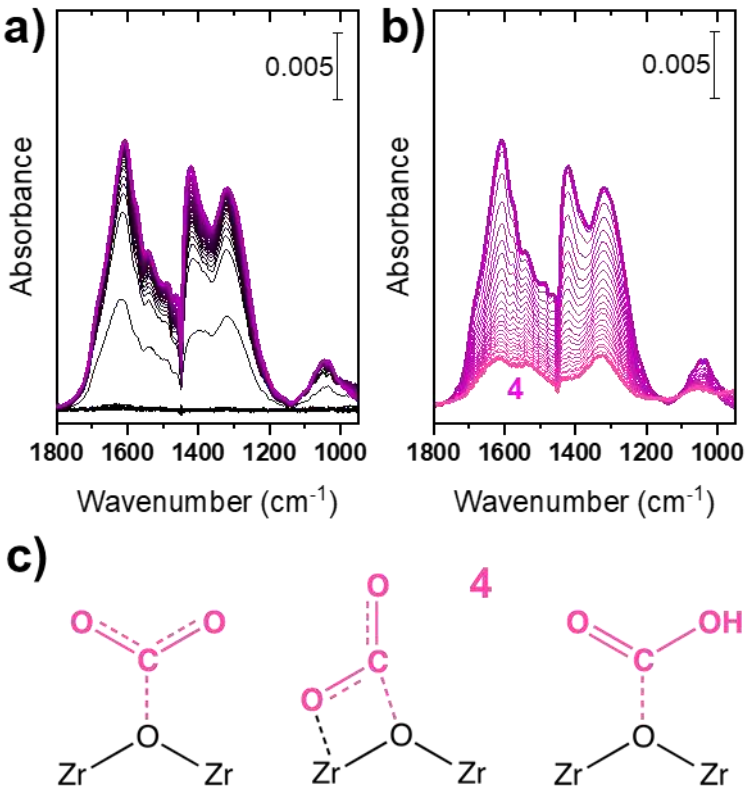

Figure 46 *In situ* ATR-IR spectra collected during a) adsorption of CO_2 on ZrO_2 (from CO_2-saturated cyclohexane, time evolution from black to violet) and b) desorption (cyclohexane, time evolution from violet to magenta) at 30 °C. c) Molecular structures of species associated to component 3 (from left to right: surface monodentate carbonate-like, bidentate carbonate-like and bicarbonate-like species).

Finally, the interaction of the reaction product (DMC) with ZrO_2 was studied, to evaluate the stability of the final product on the catalyst surface (Figure 47) We observed a reversible adsorption/desorption of DMC without presenting any decomposition to MMC. This could be related to either solvent-stabilization of DMC or to the non-completely active ZrO_2 surface due to the limited activation

temperature. Nevertheless, considering the reactivity experiments (see next session) showing some DMC production, we can discard the latter option.

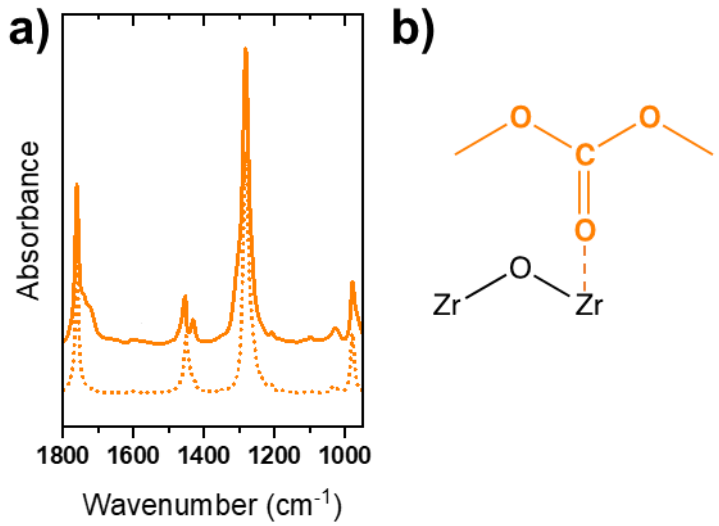

Figure 47 *In situ* ATR-IR spectrum of DMC adsorbed on ZrO_2 (from a 0.1 M solution of DMC in cyclohexane, after 30 min of contact, solid curve) at 30 °C. The spectrum of the bare 0.1 M solution of DMC in cyclohexane is reported for the sake of comparison (dotted line).

4.1.2 Reactivity of mixed methanol-CO_2

Figure 48 shows the *in situ* ATR-IR spectra collected during the simultaneous interaction of methanol and CO_2 on ZrO_2 at different temperatures.

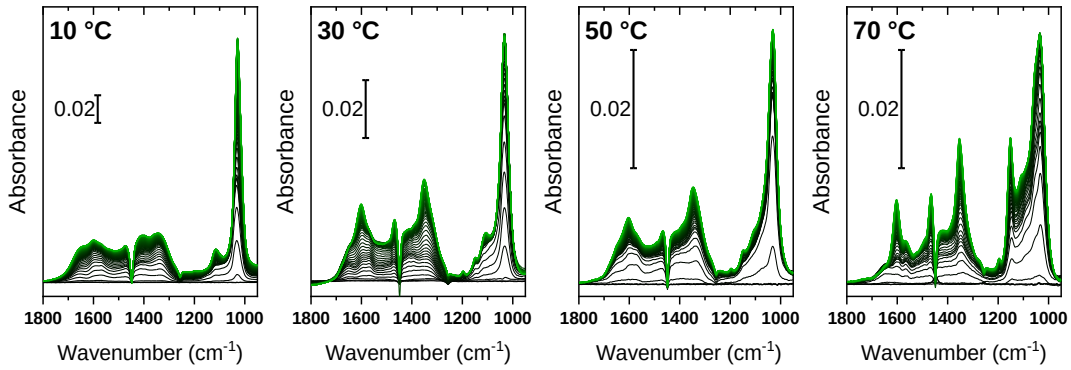

Figure 48 *In situ* ATR-IR spectra collected during the co-feeding of methanol and CO_2 (from a CO_2 saturated 0.1 M solution of methanol in cyclohexane) on ZrO_2 at different temperatures. Spectra were recorded for 1 h (time evolution from black to green).

A first qualitative analysis of the spectra shows as they are characterized by similar spectroscopic component but with lower intensity at higher temperature, in line with higher species desorption. Methanol and carbonates were well evident at each temperature whilst methoxides become more evident at higher temperatures, in line with lower methanol stability. The presence of triplet of bands at 1350, 1465 and 1600 cm^{-1} highlighted the formation of MMC as observed in the gas phase reaction. The dataset in Figure 48 were then analysed by MCR-ALS using methanol and carbonates as reference pure components. Since the same spectroscopic features were observed regardless of the reaction temperature, all data were merged in a single dataset and analyzed simultaneously, leading to the (re)optimized spectra of the pure components and their concentration profiles at each temperature are shown in Figure 49. An attempt to introduce the reaction product (DMC) as a sixth component was performed also in this case including 50 replicas of the spectrum of adsorbed DMC as shown in Figure 47. Nonetheless, inconsistent results were obtained on a chemical basis (not reported for sake of brevity).

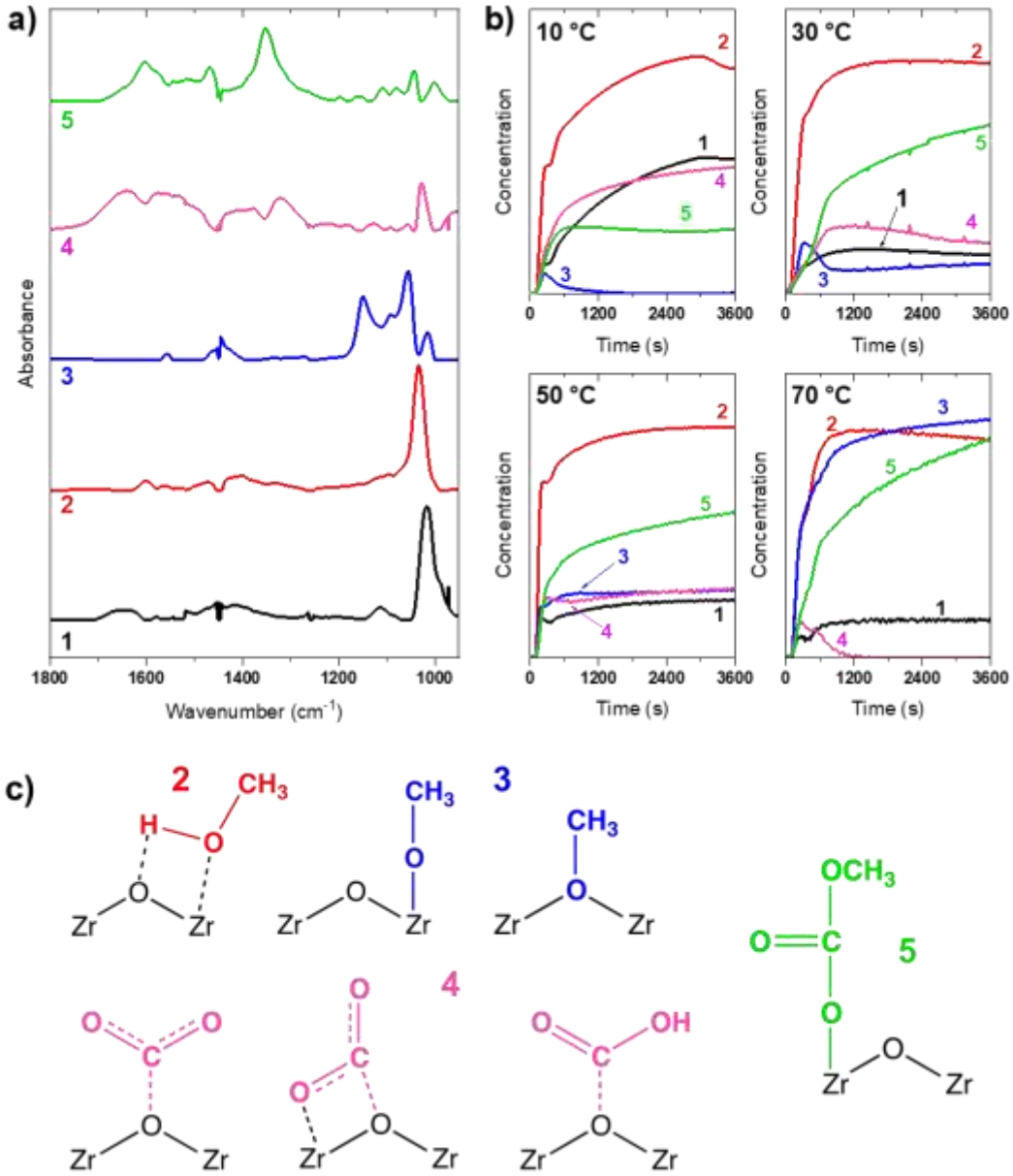

Figure 49 a) Spectra of pure components and b) their concentration profiles obtained from MCR-ALS for reactivity experiments conducted at different temperatures. c) Molecular structures of species associated to all components, including component **5** (i.e. surface MMC intermediate); component 1 (liquid phase methanol) structure is omitted.

Four of the five obtained spectra can be associated to those observed from the previous pure experiments: **1**, liquid phase methanol; **2**, molecular methanol adducts at ZrO_2 surface; **3**, surface methoxy groups and **4**, surface carbonates. Conversely, component **5** presents three main bands 1600, 1470 and 1350 cm^{-1}, ascribable to monomethyl carbonate (MMC) main vibrations.[7] Interestingly MMC is the CO_2-to-DMC reaction intermediate and its spectral component was completely extracted by the MCR-ALS routine.

The obtained results, summarized with the reaction mechanism in Figure 50, unveiled as ZrO_2 surface (**I**) is contacted with methanol and CO_2 solubilized in the working solvent, both surface carbonates and methoxide species are formed (**II**), and their respective ratio is strongly temperature dependent. At temperature $\leq$ 50°C, carbonates and methoxide species react together to form MMC (**III**), whilst at 70°C the reaction takes place between chemisorbed methoxide and gas-phase CO_2 (**III'**). The formation of MMC affects the equilibria determining the population of surface species (**IV**): in detail, the higher the temperature, the higher the concentration of MMC, at expenses of surface carbonates, that turns from the dominating surface specie at 10 °C to a closely nil concentration at 70 °C. Eventually, though not detected under the experimental conditions adopted in this study, the reaction of MMC with a second methanol molecule leads to the synthesis of DMC, that is desorbed from the surface as the final reaction product.

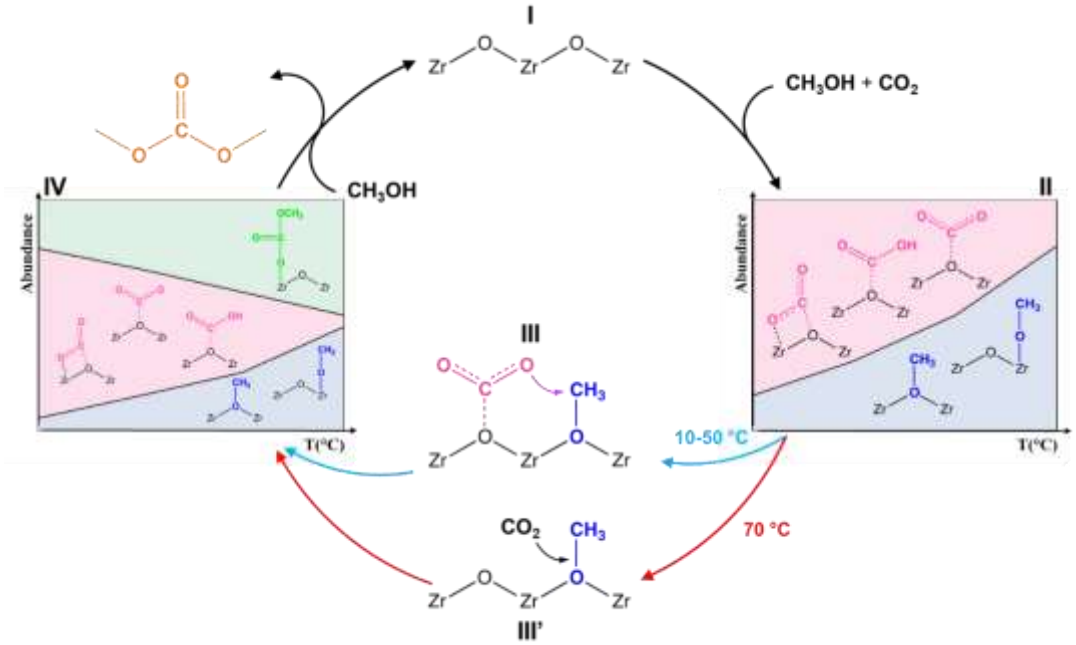

Figure 50 DMC formation reaction mechanism proposed for CO_2 and CH_3OH adsorbed over ZrO_2 at different temperatures. Abundance/Temperature diagrams (steps **II** and **IV**) are referred to the concentrations reported in Figure 49.

4.1.3 Liquid phase reaction: mechanism dependence with reaction temperature

The obtained results indicated as CO_2/CH_3OH activation strongly depend on temperature. Low temperatures (<30 °C), favoured the formation of stable carbonates by limiting methanol activation to its molecular physisorption, hence reducing monomethyl carbonate and preventing dimethyl carbonate (DMC) formation. On the contrary high temperatures (>50 °C), improved methanol dissociation thus forming reactive methoxide species at the expenses of the stability of carbonates, leading to an increase of MMC formation. Moreover, whilst the coexistence of carbonates and methoxide species at 10-50°C induces us to hypothesize the already known reaction mechanism involving an interaction between the two species, the abundance of methoxides at higher temperature together with the low levels of carbonates and the pronounced MMC formation suggested that the

interaction between methoxide and CO_2 could occur prior to carbonates formation. This observation may imply that DMC is produced through an alternative new reaction pathway involving a direct interaction between CO_2 and methoxide species preventing formation of stable carbonates and thus catalyst deactivation. It is noteworthy that for closing the catalytic cycle, DMC decomposition over ZrO_2 must be prevented prior to its desorption. This seems to be promoted by the liquid phase. Indeed, because, the liquid phase ATR-IR experiments demonstrated an increased stability of the DMC product at 50 and 70°C, allowing its further desorption at already 70°C. Conversely, gas phase experiments showed the rapid decomposition of DMC over ZrO2.

4.2 Gas phase reaction

4.2.1 ZrO_2 in-situ activation

All the measurements reported in the following sections were forerun by the activation procedure reported in Figure 51a aimed to prepare a clean catalyst surface. The activation consisted in the following four-step protocol : I) heating RT-150°C (5°C/min) under He (50 mL/min) (green line), II) heating 150-400°C under an He/O_2 mixture (50 mL/min 3:2 He:O_2) (red line), III) holding at 400°C for 60' under the same mixture (blue line) and IV) cooling to RT under He/O_2 and changing to pure He at 150°C. As reported in the spectra in Figure 51b, the employed protocol allowed to completely remove adsorbed water and organic pollutants however, without removing all the carbonates which would have required higher activation temperatures causing a potential (counterproductive) loss of surface area. More relevant is to observe as isolated hydroxyl groups are formed above 3500 cm^{-1} with the removal adsorbed water, indicated by the broad absorption band at ≈3300 cm^{-1}. After activation (blue line) two sharp hydroxyl bands are observed at 3677 and 3770 cm^{-1}, associated to tri-bridged and terminal Zr-OH groups. The bi-bridged hydroxyl groups are not observed, in line with the more abundant ZrO_2 monoclinic polymorph.[6] In the following results, the activated spectra has been subtracted from

the measured spectra in order to magnify the variations observed on the catalyst surface.

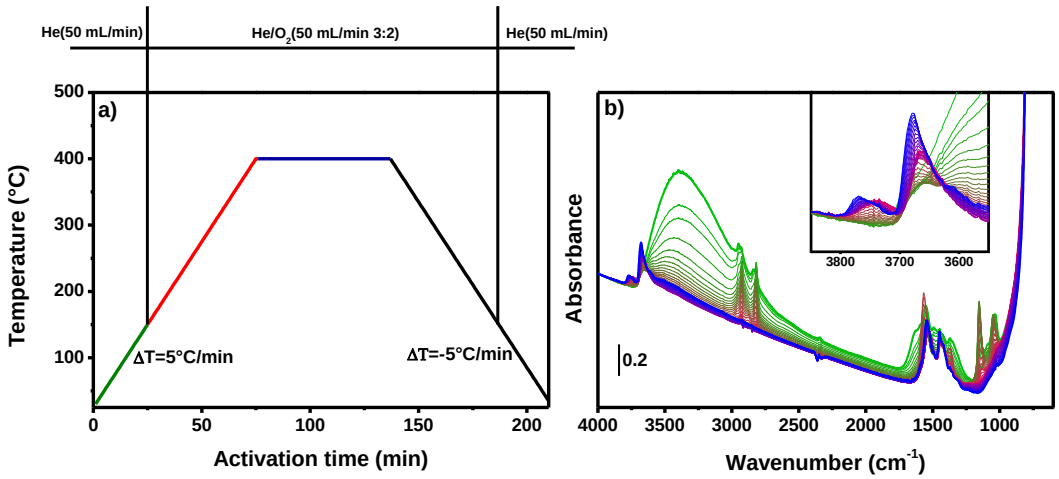

Figure 51 Activation procedure a) thermal/chemical ramp and b) spectra obtained during the activation. Colours in panel b) refers to the respective activation steps in panel a).

4.2.2 Methanol adsorption over ZrO_2 at 30°C

In-situ FT-IR spectra in Figure 52a shows a rapid adsorption of methanol over ZrO_2, forming physisorbed methanol, distinguishable from the P,Q and R branches in the 1100-1000 cm^{-1} range, followed by chemisorbed terminal methoxide at 1160 cm^{-1}. The spectra collected during desorption (Figure 52b) highlights as physisorbed methanol hides a methoxide component in the 1050-1100 cm^{-1} range (e.g. bi- or tri-bridged) which is stable during desorption. MCR-ALS analysis of the dataset showed the presence of the two spectral components reported in Figure 52c. The first component (Figure 52c black line) is comparable to methanol gas phase tabulated IR spectra (Met1). The second component (Figure 52c) presents two separated bands at 1161 and 1058 cm^{-1} identified as terminal and tri-bridged methoxide species, respectively (Met2). Even though the presence of these two components is well described in literature, the MCR-ALS analysis disclosed a clear view on their

adsorption kinetic behaviour. Indeed, the extracted concentration profiles reported in Figure 52d shows as the methanol physisorbed state rapidly covers ZrO_2 surface limiting the formation of reactive methoxide species. Contrarily, during desorption the methoxide species concentration increases parallel to a decrease of physisorbed component, suggesting as methanol concentration might play an important role in the methoxide accessibility.

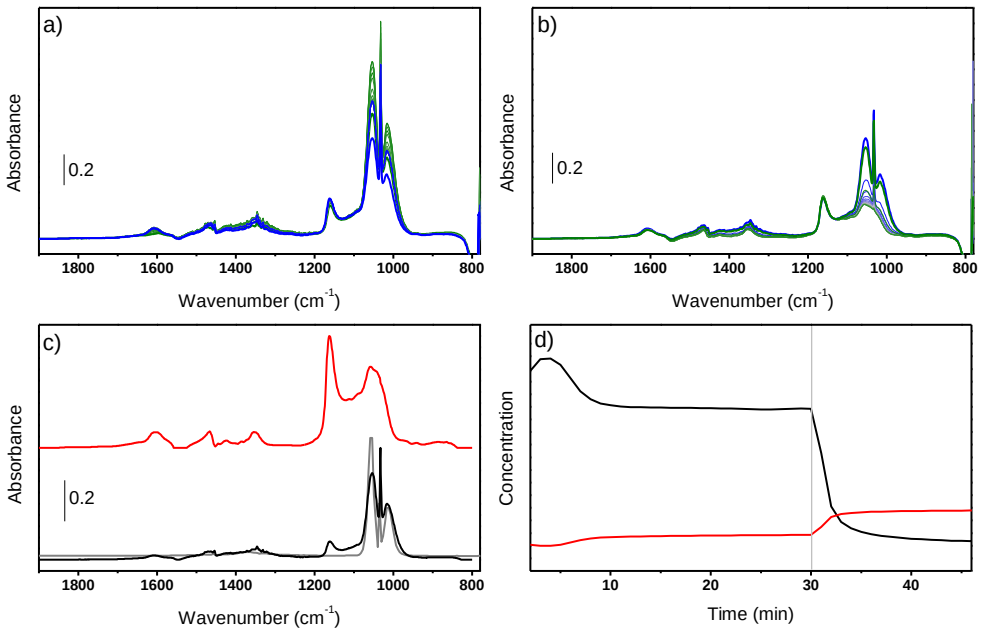

Figure 52 *In situ* FT-IR spectra collected during a) adsorption of methanol on ZrO_2 (15 mL/min He with 4% mol CH_3OH, time evolution from green to blue) at 30 °C and b) its desorption (by exposure to 15 mL/min of pure He, time evolution from blue to green). c) Pure component spectra obtained by MCR-ALS (FT-IR spectrum of pure CH_3OH taken from NIST webbook is shown with gray line). d) Corresponding concentration profiles as a function of time (the vertical gray line represents the switch from He/CH_3OH to He).

4.2.3 Carbon dioxide adsorption over ZrO_2 at 30°C and 150°C

FT-IR spectra in Figure 53a shows as CO_2 adsorption over ZrO_2 induces the formation of several bands between 1800 and 800 cm^{-1} which can all be associated to carbonates (CO_3) and bicarbonates (h-CO_3) species following the available literature. Nevertheless, since these species present convoluted broad bands, the CO_2 adsorption kinetic studies were often conducted following the evolution of a single isolated band. The MCR-ALS allowed to separate the two spectral components of carbonates and hydrogen-carbonates (h-CO_3) reported with pink and blue lines in Figure 53c. The assignment of h-CO_3 was relatively simple due to the presence of the characteristic δ(OH), $\nu(C{=}O)_{sym}$ and $\nu(C{=}O)_{asym}$ at 1221, 1425 and 1627 cm^{-1}, respectively, together with the consumption of Zr-OH groups parallel to the formation of h-CO_3 ν(OH) at 3617 cm^{-1} (Figure 53a inset). Contrarily the carbonates identification is less trivial. By considering the presence of two isolated bands at 1608 and 1330 cm^{-1}, we can assign them to a carbonate $\nu(OCO)_{asym}$ and $\nu(OCO)_{sym}$ vibrations. Moreover, their separation ($\Delta\nu \approx 280$ cm^{-1}) indicate the presence of either a bridged or tridentate carbonate. Since the specific identification of this carbonate will not be important for the further reaction analysis, we name this species t-CO_3 without referring to a specific carbonate but indicating a family of carbonates with coordination degree >2. Following the components concentration profiles in Figure 53d we observed as h-CO_3 species are rapidly adsorbed over ZrO_2 whilst t-CO_3 are not observed util the former species reached a plateau. When h-CO_3 reach its maximum concentration, their abundance started to decrease parallel to the increase of t-CO_3. This concentration kinetics shows as h-CO_3 formation is kinetically faster than t-CO_3 which on the contrary are thermodynamically more stable, in agreement with previous literature results. Indeed, during desorption, the t-CO_3 concentration continued to increase to the detriment of h-CO_3 decrease.

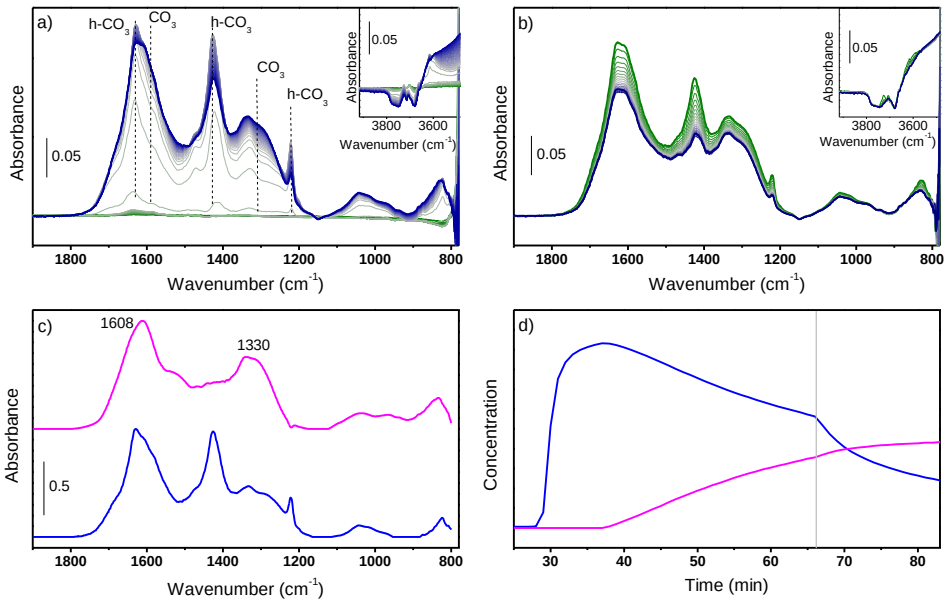

Figure 53 *In situ* FT-IR spectra collected during a) adsorption of CO_2 on ZrO_2 (50 mL/min He:CO_2 4:1, time evolution from green to blue) and b) desorption (50 mL/min He, time evolution from blue to green) at 30 °C. c) pure component spectra obtained by MCR-ALS. d) Corresponding concentration profiles as a function of time (the vertical gray line represents the switch from He/CO_2 to He).

This result suggests as CO_2 adsorption, hence its activation, might be promoted by hydroxyl groups through formation of h-CO_3 species which are then decomposed to more stable t-CO_3.

To improve the comprehension of CO_2 adsorption kinetic, the spectra in Figure 54a,b were collected at 150°C i.e., reaction-like temperature. The spectra measured during CO_2 adsorption in Figure 54a reported a higher degree of evolution and convolution complexity respect to those collected at 30°C (Figure 53a). h-CO_3 presence were identified from the fingerprint δ(OH) and $\nu(C{=}O)_{sym}$ vibrations at 1225 cm^{-1} and 1425 cm^{-1}, respectively. However, $\nu(C{=}O)_{asym}$ and ν(OH) were not identified, the former being too convoluted with other carbonates and the latter completely broadened from the high temperatures and covered by CO_2 overtones. 20 replicas of

the spectral components obtained at 30°C (Figure 53c) were then inserted at the end of the dataset for driving the SVD towards the probable components and parallelly optimizing the already found spectra. This approach led to find the three independent components reported in Figure 54c. Whilst the first component (Figure 54c blue line) is related to h-CO_3 species already found at 30°C, the other two components are associated to different carbonates. Among the two spectra we can recognize the already found t-CO_3 (pink line) whilst the second spectra (purple line) presented two components at 1536 and 1331 cm^{-1}. Considering the two bands as associated to $\nu(OCO)_{asym/sym}$ vibrations, their separation ($\Delta\nu \approx 205$ cm^{-1}) can be ascribed to a bidentate carbonate (b-CO_3). The high-temperature concentration profile unveiled as under reaction conditions h-CO_3 follows the same kinetic observed at 30°C whilst on the contrary b-CO_3 are formed more rapidly and are more stable than the former species. Moreover, t-CO_3 previously observed at 30°C are not observed during the whole adsorption/desorption cycle suggesting the higher stability of b-CO_3 at higher temperatures.

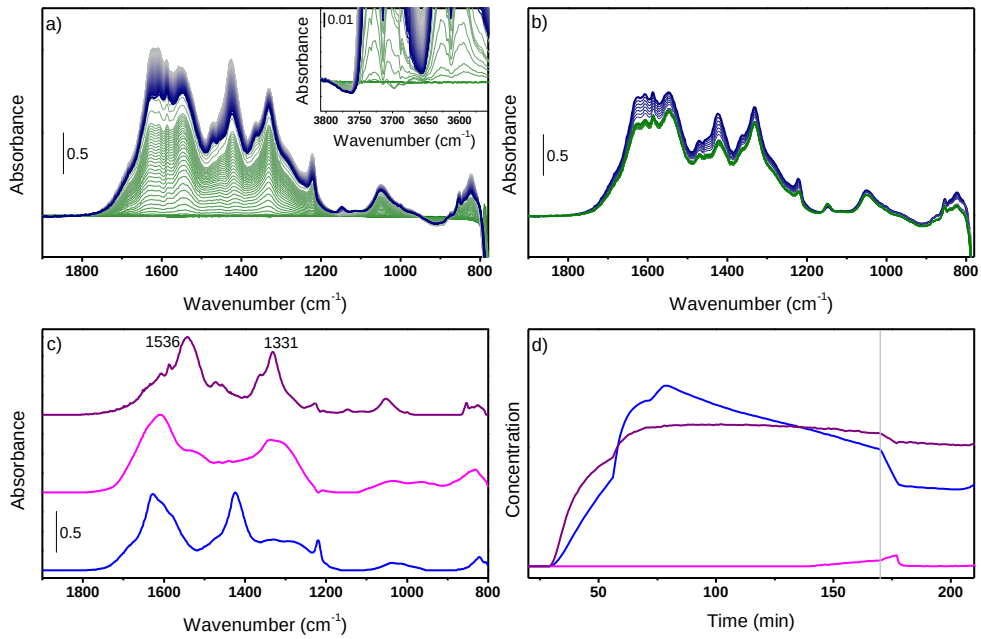

Figure 54 *In situ* FT-IR spectra collected during a) adsorption of CO_2 on ZrO_2 (50 mL/min He:CO_2 4:1, time evolution from green to blue) and b) desorption (50 mL/min He, time evolution from blue to green) at 150°C. c) pure component spectra obtained by MCR-ALS. d) Corresponding concentration profiles as a function of time (the vertical gray line represents the switch from He/CO_2 to He).

It seems unlikely that t-CO_3 component is formed only at high temperature whilst it is more probable that this species might be already formed at 30°C but being less intense and convoluted with b-CO_3. For this reason, the dataset collected at 30°C was re-analysed considering the three components optimized at 150°C as starting references, leading to the spectral components and concentration profiles in Figure 55b,c. No net variations were observed in the CO_3/h-CO_3 kinetics and spectral profile. Indeed, the concentration profiles (Figure 55c) show as t-CO_3 and b-CO_3 have similar kinetic highlighting, explaining why their spectra have never been deconvoluted. Through this deconvolution, the three t-CO_3, b-CO_3 and h-CO_3 components will be used in the further analysis.

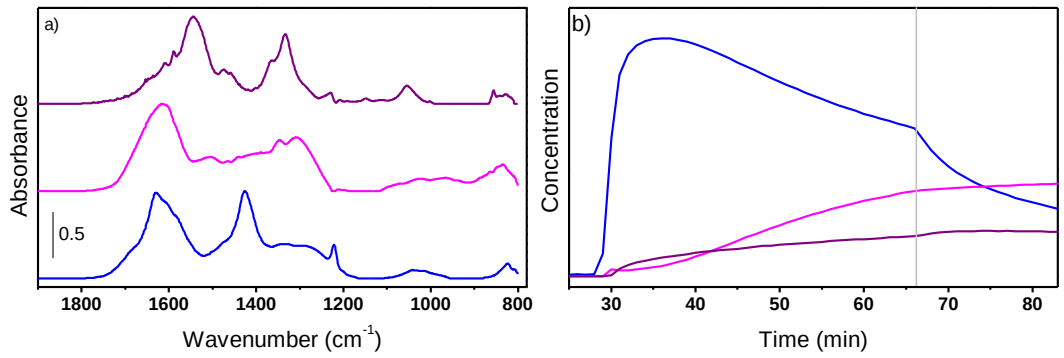

Figure 55 a) t-CO_3 spectra component extracted at 30°C (gray line) and weighted t-CO_3 (violet) and b-CO_3 (pink) extracted at 150°C. b) Pure component spectra obtained by MCR-ALS applied to the dataset in Figure 53a,b. d) Corresponding concentration profiles as a function of time (the vertical gray line represents the switch from He/CO_2 to He).

4.2.4 Dimethilcarbonate adsorption/desorption at room temperature

Due to its low vapor pressure, dimethilcarbonate (DMC) adsorption was investigated in static conditions following the same procedure described for RT-CO adsorption measurements i.e., a partial pressure of DMC was sent over a previously activated ZrO_2 pellet and spectra were collected during desorption of DMC partial pressure. Withing the formed wealth of bands in the spectra reported in Figure 56a we can distinguish DMC characteristic ν(C=O), $\delta(CH_3)_{asym}$ and $\nu(OCO)_{asym}$ vibrations at 1760, 1456 and 1291 cm^{-1}, respectively[8] and monomethylcarbonate $\nu(OCO)_{asym}$, $\delta(CH_3)_{asym}$ and $\nu(OCO)_{sym}$, vibrations at 1602, 1472 and 1361 cm^{-1}, respectively.[9] As already reported by Bell et al.[3] we observed a rapid DMC-to-MMC decomposition as soon as the former was adsorbed over ZrO_2 surface. Moreover, the formed MMC was stable over ZrO_2 since the main bands between 1300 and 1600 cm^{-1} were observed even after complete desorption of residual gas-phase components from the sample environment. Even if the obtained dataset contained a limited number of spectra (≈20), it presented a sufficient variance to apply MCR-ALS routine. Two

spectra components were extracted and to DMC and MMC, with a surprisingly clear deconvolution of their $\delta(CH_3)_{asym}$ vibration located at 1456 and 1472 cm^{-1}, respectively, which is usually not deconvoluted. On the contrary, MMC spectra presented extra features in the 1000-1200 cm^{-1} region, ascribable to methoxide vibrations. Indeed, DMC to MMC decomposition implies the formation of a methyl group which likely forms methoxide species. The use of methoxide spectra as references did not improve the deconvolution of those components (not reported for brevity). Nevertheless, as it will be discussed in the next session, the obtained MMC component was used as an initial guess further on optimized during the analysis of data collected under reaction conditions. The concentration profile reported in Figure 56c shows an increase of MMC concentration during DMC desorption, indicating a DMC-to-MMC decomposition. Nevertheless, the DMC desorption kinetic gave us access to clean reference spectra of DMC and MMC adsorbed on ZrO_2. More importantly, whilst DMC can be obtained as a stable specieMMC is unavailable as stable molecule according to its intermediate nature.

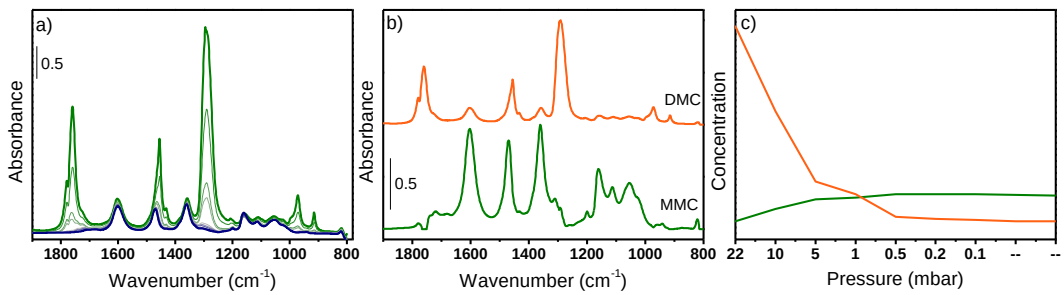

Figure 56 *Ex situ* FT-IR spectra collected during a) desorption of DMC on ZrO_2 (22 mbar, pressure evolution from green to blue) at RT. b) pure component spectra obtained by MCR-ALS. c) Corresponding concentration profiles as a function of pressure evolution.

4.2.5 Reactivity of CO_2/CH_3OH over ZrO_2

The spectra collected during adsorption of CO_2 carrying different CH_3OH over ZrO_2 are reported in Figure 57. Spectra were collected also during reactants desorption, but bare data are not reported for sake of brevity. This part of the datasets is however included in data analysis and discussed therein.

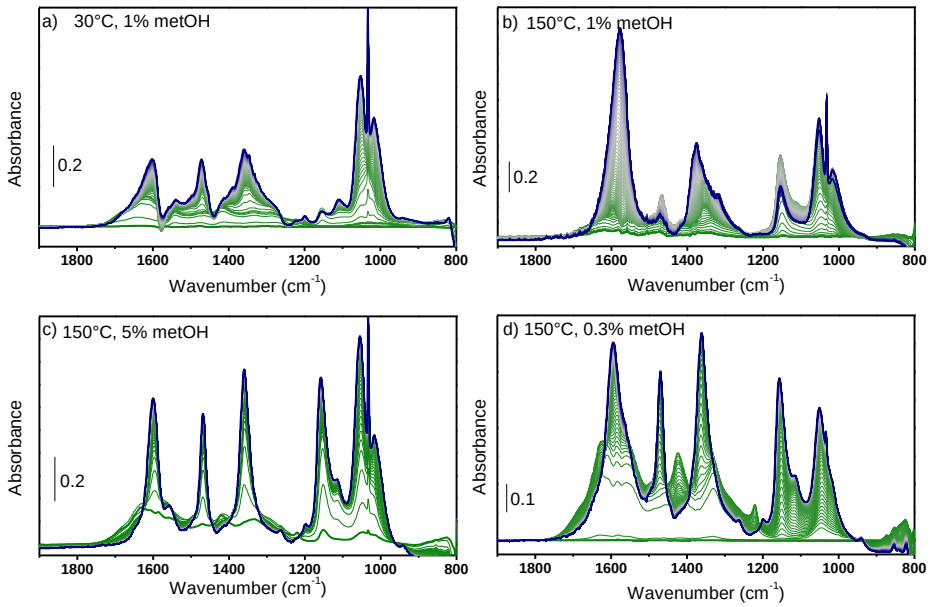

Figure 57 *In situ* FT-IR spectra collected during adsorption of CO_2/CH_3OH on ZrO_2 at a) 30°C and b,c,d) 150°C.

Since we observed as two different carbonates are observed at 30°C and 150°C, we first investigated their role in the reaction by investigating MMC and DMC formation at 30 and 150°C (Figure 57a,b). Afterwards, since liquid-phase experiments showed an important role of methoxide groups for CO_2 activation at higher temperatures, we have exploited the reaction with higher/lower methanol concentration in the reaction feed (Figure 57c,d). A first inspection of the recorded spectra unveiled the major presence of methanol and MMC fingerprints in the 1000-1100 cm^{-1} and 1300-1650 cm^{-1} ranges, reporting important differences when temperature and methanol concentrations are modified. For instance, by increasing

the temperature from 30°C to 150°C alters both MMC and methoxide groups behaviors. By fixing methanol concentration (1%), at higher temperatures methoxide formation is improved whilst MMC triplet presented a variation in relative intensity. Moreover, we noticed that varying methanol concentration led to: I) sharper MMC bands with higher methanol content (Figure 57c) or II) presence of extra bands parallel to almost absent gas phase methanol vibrations with lower methanol content (Figure 57d). Since the spectra presented similar components, the adsorption/desorption data were analyzed simultaneously by merging them one after another in a single dataset. From the recorded spectra, components from methanol, methoxide, bicarbonates, bi-/tri-bridged carbonates, methyl carbonate and dimethylcarbonate should be considered. For this reason, seven pure components were selected from the SVD analysis. However, since this high value of pure components might not lead to MCR-ALS converge, the seven spectral profiles reported in Figure 55b were repeated 50 times after the dataset. This approach allows to drive the SVD towards the reference components whilst parallelly also optimizes the pure component.

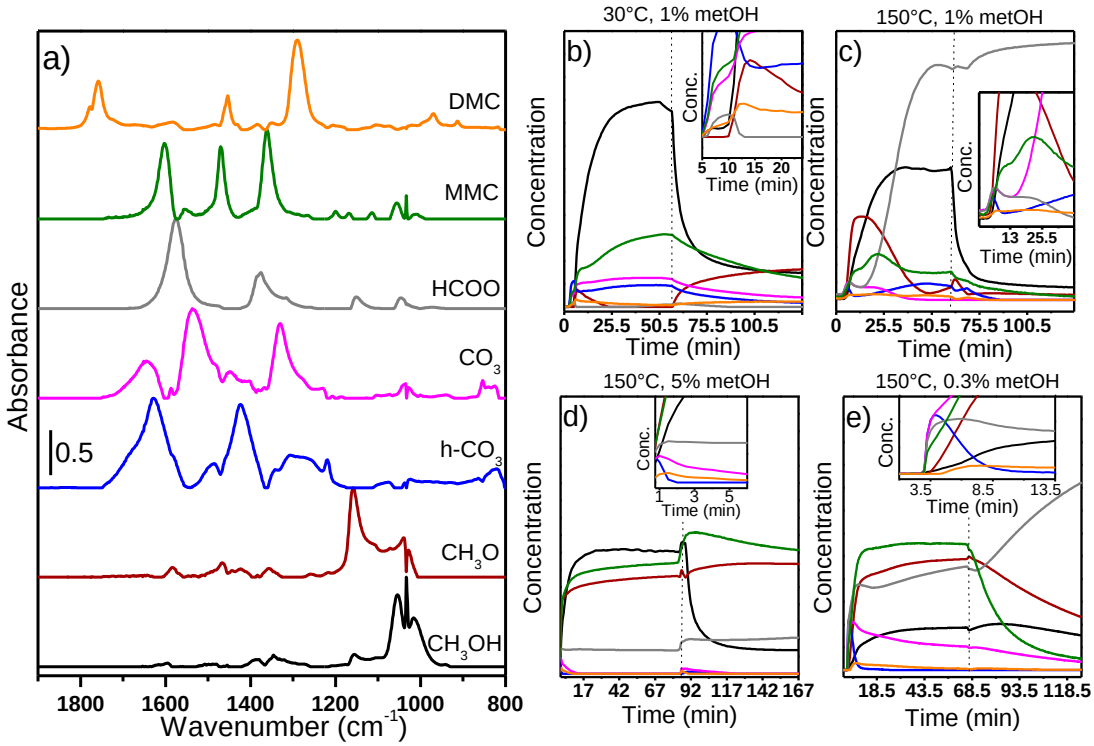

Figure 58 a) Spectra of pure components and b,c,d,e) their concentration profiles obtained from MCR-ALS for reactivity experiments conducted at a,b) different temperatures and c,d,e) methanol concentration.

Most of the (re)optimized spectral components reported in Figure 58a can be associated to those already observed during the pure experiments. Nevertheless, we observed the presence of a spectral component which resemble that derived from pure reagents adsorption (b-CO_3), however showing different bands position. Indeed, the spectra presented two sharp bands at 1375 and 1575 cm^{-1} which according to literature can be associate to formate (HCOO) $\nu(OCO)_{sym}$ and $\nu(OCO)_{asym}$.[10] Indeed, the presence of formate species was further confirmed from analysis of ν(CH) spectral region discussed in the next session. Contrarily the pink spectra, previously associated to carbonates, presented several bands which likely originated from the convolution of the t-CO_3 component with the pristine b-CO_3 one. Indeed, we can

identify two sharp bands at 1329 and 1534 cm^{-1} which for bands position and separation can be ascribed to $\nu(CO)_{sym/asym}$ of a bidentate carbonate. Two weaker central bands were also observed at 1401 and 1445 cm^{-1} and associated to the same vibration of a monodentate carbonate. Moreover, a broader band was observed at 1650 cm^{-1} which is likely related another bidentate carbonate ν(CO) vibration.[6] For sake of simplicity then identified this species as generic carbonates. The concentration profiles obtained in Figure 58 showed an important dependence of the formed species to the reaction temperature and even more to methanol concentration. Considering temperature as a variable, the first instants of reaction at 30°(Figure 58b inset) showed as h-CO_3 and CO_3 formation occurs before methoxide and remains constant through the whole adsorption. The concentration profile of the two components is very similar suggesting an important correlation of the two species during the reaction. Contrarily, at 150°C we clearly observed as whilst initially only CO_3 are formed and, after few minutes, they are decomposed to h-CO_3. At lower temperature methanol (black line) presence prevents methoxides (red line) formation, which are on the contrary quickly formed at higher temperatures. However, even at 150°C after few minutes methanol prevents methoxides production. Parallel to methoxide/methanol equilibrium, there is a clear competition between carbonates and methoxides as observed under liquid phase conditions (Figure 50), the former more stable at 30°C whilst the latter becoming more abundant at 150°C. Interestingly we observed a higher concentration of the reaction intermediate monomethyl carbonate (MMC, green line) at 30°C, where it presented an initial rapid growth followed by a slower growth after the first minutes of reaction, suggesting two different kinetic leading to MMC. Noteworthy, parallel to MMC initial rapid formation, a minor concentration increase was observed in DMC signal (orange line). At higher temperature the initial formation of MMC and (little) DMC, is followed by their concentration loss. Particularly, MMC decrease is accompanied with the rapid rise of formate component (not observed at 30°C) with parallel h-CO_3

formation and CH_3O concentration decrease. These results highlights as whilst at higher temperatures methanol desorption is favored improving methoxide formation, methoxide-loss and formats-rise have the same slope, suggesting a potential decomposition of the former to the latter, as already reported in literature to occur at 170°C.[11] Moreover, by comparing MMC and h-CO_3 slopes in the last reaction part, we observed as the presence of formates favors CO_3-to- h-CO_3 conversion causing a drop in MMC concentration. This is further confirmed by reactants desorption. At 30°C the lower methanol concentration allows the formation of extra methoxide species causing a slight increase of DMC concentration. On the contrary at 150°C formates showed high stability under desorption conditions, preventing an additional formation of all the other species.

By changing methanol concentration there is a particular relation between methanol and methoxide concentrations. With a CO_2:CH_3OH 5:1 ratio in the reaction feed we observed as the high accumulation of methanol does not completely prevent methoxides formation. A low concentration of formate species is observed, whilst MMC formation after a quick increase maintained a constant slight increase. Contrarily, as already discussed, by lowering the ratio to 25:1 (Figure 58d), CH_3O-species are formed before CH_3OH accumulation but are then decomposed to formate, which concentration rised preventing MMC formation. At minor methanol contents (83:1)(Figure 58e) its concentration grows less than the other components. The little surface accumulation of liquid methanol allows a rapid growth of methoxide. However, contrarily to the 25:1 experiment (Figure 58c), an methoxide concentration higher than methanol induces and equilibrium with the formed formate, preventing methoxide decomposition and maintaining MMC concentration. It is well observable as CO_3 formed at the beginning of adsorption are constantly consumed parallelly to formate growth, confirming the latter higher stability respect to the former. Interestingly during desorption, we can notice as at low methanol content methoxide are decomposed to formate, which concentration increases. By increasing methanol

concentrate during desorption the formate are stabilized (25:1 case) and eventually in minor concentration (5:1 case), allowing further methoxide formation and MMC increase.

To confirm formate presence, we qualitative analysed the ν(CH) spectral region of the collected spectra reported in Figure 59. Even though the spectra showed the presence of several convoluted bands, we could distinguish five bands ascribable to $\nu(CH)_{sym}$ and $\nu(CH)_{asym}$ of methoxide (2818 and 2923 cm^{-1}), methanol (2843 and 2949 cm^{-1}) and formate (2865 cm^{-1}), where the former component is more intense at 150°C/1% CH_3OH conditions and its intensity grows parallelly to methoxide vibration decrease. Both the observation are in line with the previous findings indicating formate production caused by methoxide decomposition.

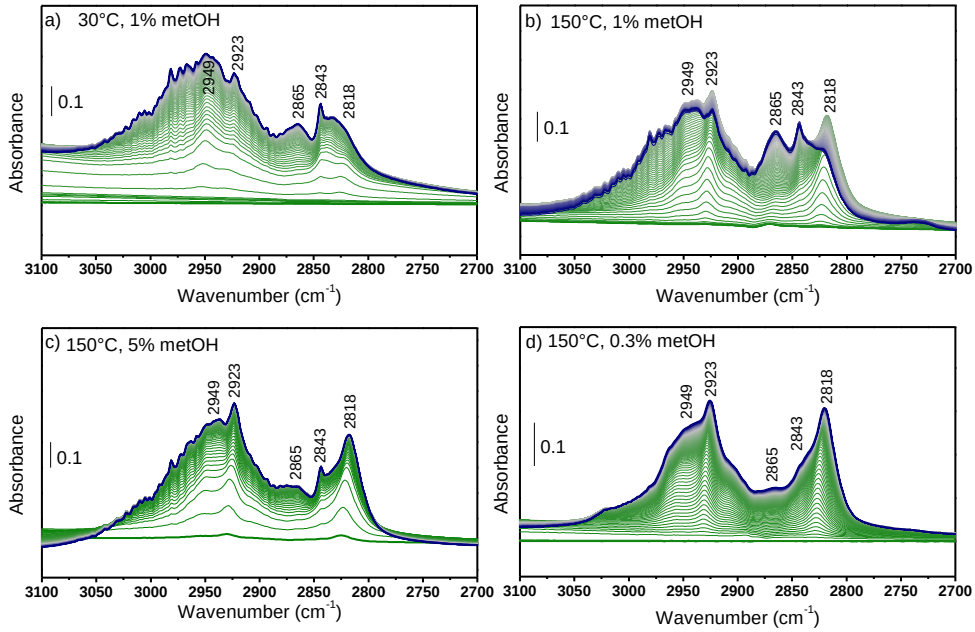

Figure 59 Detail of *in situ* FT-IR ν(CH) region spectra collected during adsorption of CO_2/CH_3OH on ZrO_2 at a) 30°C and b,c,d) 150°C. Reaction feed was set to 30 mL/min He with 25% CO_2 and X% CH_3OH, where X was a,b)1%, c)5% and d)0.3%. Time evolution goes from green to blue line.

4.2.6 Gas phase reaction: the role of methanol concentration

The study conducted in gas phase allowed us to work under temperature conditions closure to the reaction one (150°C). The results measured at 30°C and 150°C with the same methanol concentration (1%) indicated the same reaction mechanism already reported in literature and describe for the liquid phase reaction at T<50°C where carbonates and methoxide species react together to form MMC (step III Figure 60). Nevertheless, at high temperature in gas phase we observed a drop in MMC formation after ≈20 minutes caused by methoxide decomposition to formate. A complex interplay is observed between methoxide formation/decomposition and methanol concentration. Lower methanol concentrations improved an initial methoxide formation however, causing their decomposition to formate after few minutes. The decomposition process will be object of a future study however, we can hypothesize as it is caused by the abundant methoxide and water species, both products of methanol dissociation over Zr-OH, reacting together as reported below.

$$CH_3O\text{-}Zr + H_2O \rightarrow HCOO\text{-}Zr + H_2$$

Formate production reaches is maximum with 1% of methanol parallel to a complete detriment of MMC formation, confirming as the former species is not reactive towards the latter. By increasing methanol concentration to 5% we noticed an important improvement towards methoxide stabilization inducing a direct increase of MMC formation. It is noteworthy as under liquid phase reaction formate were not observed indicating as the liquid state (i.e., maximum methanol concentration) completely prevents methanol decomposition. At highest methanol contents, MMC formation was observed even though carbonates were not present, highlighting as MMC might be formed through a direct interaction between methoxide and gas phase CO_2 (step III' Figure 60), as hypothesized to occur for liquid phase reaction at 70°C.

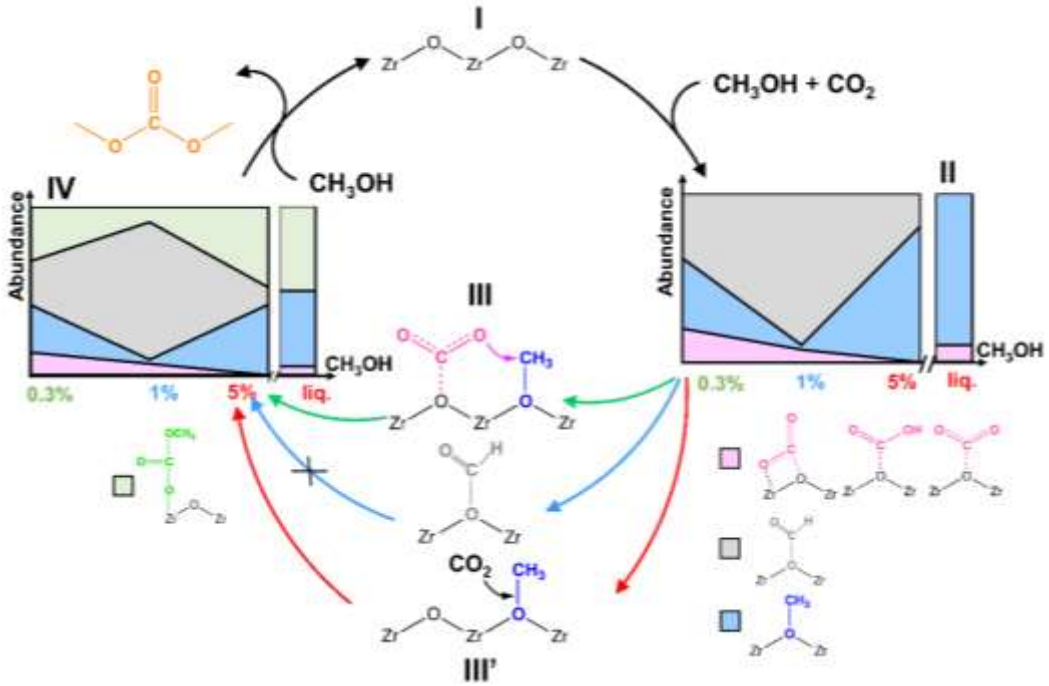

Figure 60 Proposed reaction mechanism for DMC formation at different methanol concentrations. Abundance/CH_3OH diagrams (steps **II** and **IV**) are referred to the concentrations (150°C) reported in Figure 58. Liquid (liq.) concentration are referred to the data collected at 70°C reported in Figure 49.

4.3 Conclusions

Within this study we successfully showed as MCR-ALS can be applied to deconvolute several spectra component formed under reaction conditions. Even though this approach cannot be considered as quantitative since absorption coefficients are not considered, the concentration profiles gave a valuable information of the involved species behaviour. Performing adsorption/desorption experiment of pure species prior the full reaction was employed to extract reference spectra, allowing to extract spectra component of reaction intermediate (i.e., MMC), otherwise inaccessible. Two mechanisms were identified indicating either a reaction between carbonates and methoxide species or a direct interaction between methoxide and gas phase CO_2. Higher temperatures shift the reaction towards the latter

mechanism. However, the total methanol concentration in the feed is observed a fundamental parameter to prevent methoxide decomposition to non-reactive formate.

4.4 CeO_2 Frustrated Lewis Pair improving CO_2 and CH_3OH conversion to Monomethylcarbonate

4.4.1 CeO_2 preparation and basic characterization

Frustrated Lewis Pair (FLP) formation over CeO_2 depends on the Ce^{3+} and oxygen vacancies surface concentration. Microwave assisted sol-gel synthesis was employed to prepare a crystalline CeO_2 sample with rough surface. The as prepared sample was further calcined at 100°C and named MW(100). To verify the role of microwave-induced defectivity, the same sample was calcined at 650°C (MW(650)) and at the same time a last sample was prepared by conventional sol-gel synthesis and calcined at 650°C (conv(650)). Powder X-Ray Diffraction (PXRD) pattern of the three samples presented Bragg peaks associated with the FCC CeO_2 phase. MW(650) presented an higher crystallite size and SSA respect to MW(100), indicating as the higher calcination temperature caused crystallites sintering whilst parallelly improving N_2 surface adsorption properties. Contrarily conv(650) presented bigger crystallites with lower surface area. Since FLP formation implies the Ce^{3+}/V_O clustering, surface-to-bulk oxygen mobility, a well-known phenomenon occurring in CeO_2 at mid-high temperatures, should be avoided. For this reason, for all the spectroscopic characterization MW(100) was further reduced at 150°C under H_2, to induce Ce^{3+} and V_O without inducing oxygen mobility.

Samples bulk defectivity was characterized with Raman spectroscopy exploiting the availability of two exiting lasers sources (514 and 325 nm). In particular, 514 nm source allows a more precise F_{2g} mode identification (position and FWHM) while the latter, being in resonance conditions, enhances defects signals. Conv(650) presented a single sharp band at 464 cm^{-1} associated to the Ce-O F_{2g} mode, confirming a pure/not-defective CeO_2 catalyst (Figure 61a). The band Full Width Half Maximum (FMHM) increased and its position redshifted in order MW(650) < MW(100) < MW(100)-red, in line with smaller and more defective particles with higher Ce^{3+}/V_O concentration. Moreover, I_{590}/I_{F2g} ratio, often reported as a defect-

meter and more clearly observed with UV-Raman spectra (Figure 61b), qualitatively showed as MW(100) the highest surface defectivity i.e., defectivity is reduced from calcination whilst conventional synthesis did not form any defects on the catalyst surface. Moreover, resonant-Raman (Figure 61b) clearly distinguished a band at 489 cm^{-1}, previously associated to Ce^{3+} in the second coordination sphere of an oxygen vacancy.[12] A quantitative evaluation of I_{590}/I_{F2g} and I_{489}/I_{F2g} is not possible due to the convoluted presence of quartz signals from the Raman cell, confirmed from the band at 808 cm^{-1}.

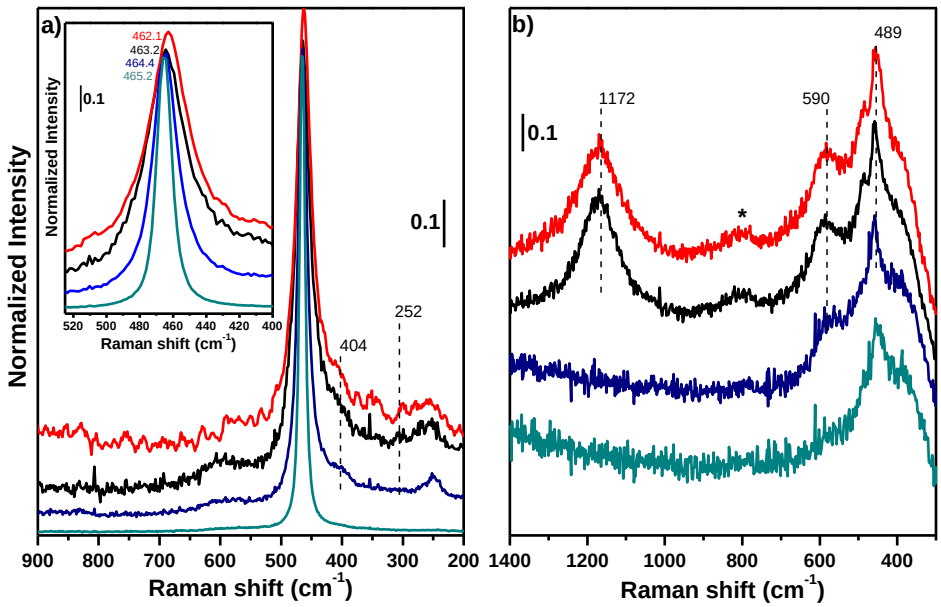

Figure 61 Stacked Raman spectra of conv(650) (dark cyan line), MW(650) (blue line), MW(100) (black line) and MW(100)-red (red line) measured with a) 514 nm and b) 325 nm laser. Detail of CeO_2. F_{2g} bands for the four catalysts and their Raman Shift position are reported in the inset in panel a. Quartz signal is showed with *.

To selectively quantify Ce^{3+} formed at the catalyst surface, XPS spectra were collected after CeO_2 oxidation and reduction at the same temperatures exploited in the previous measurements. After a careful evaluation of Ce^{3+} induced by beam

damage (see Materials and methods), we observed as 14% of Ce^{3+} was already present on MW(100) (Figure 62a) whilst Ce^{3+} increased to 35% after H_2 treatment (Figure 62c). Even if Ce^{3+}/Ce^{4+} ratio has been often evaluated also from O 1s spectra, other surface species observed by IR spectroscopy might contribute to this spectral region. We then described O 1s region considering two contributions: a first one at 529.7 eV related to lattice CeO_2 oxygen (O_L) and a second one at higher energy (≈531 eV), namely O^{β}, potentially originated by a complex convolution of all the other species i.e., $OH(Ce^{4+})$, $OH(Ce^{3+})$, $CO_3^{=}$ and O close to V_O (O_{Vo}).[13–15] Since *ex situ* IR spectra collected under the same activation conditions did not show an important variation in carbonates and hydroxyl species, we can associate the increase of O^{β} in MW(100)-red O1s spectra (Figure 62b) to a variation of oxygen electronic configuration i.e., an increase of surroundings V_O.

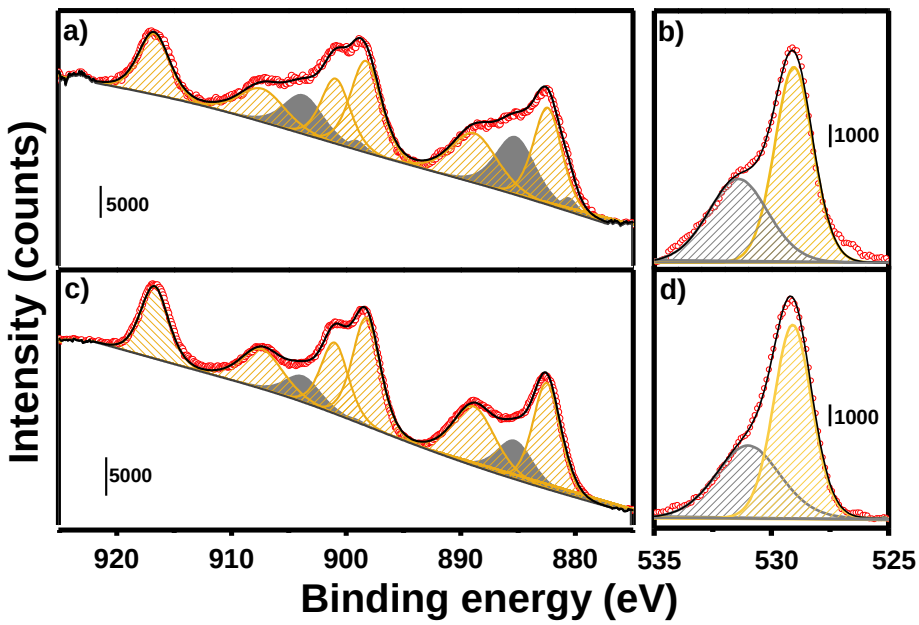

Figure 62 *Ex situ* a,c) Ce (3d) and b,d) O (1S) XPS experimental spectra (red circles) and best fit (black line) of c,d) MW(100) and a,b)MW(100)-red. Ce^{4+}/O_L and Ce^{3+}/O^{β} components are reported with yellow and grey bands.

Surface CO chemisorption at nominal 100 K was to qualitatively evaluate surface Ce^{3+} abundance. Briefly, bands at $\nu > 2147$ cm^{-1} are related to Ce^{4+} sites following the rule of thumb "the higher the wavenumber the more uncoordinated the site is". This simple principle, well verified in literature, confirmed as the surface defectivity decreases in order MW(100)<MW(650)<conv(650). Moreover, in the first catalysts bands at $\nu < 2147$ cm^{-1} becomes visible. Whilst the one around 2101 cm^{-1} observed in all the sample and associated to ^{13}CO, the band at 2131cm^{-1} is associated to CO-Ce^{3+} interaction.[16] Notably, in MW(100)-red, the Ce^{4+} bands is shifted to lower energies whilst the Ce^{3+} bands intensity increases, highlighting as the most defective Ce^{4+} sites are reduced to Ce^{3+}.

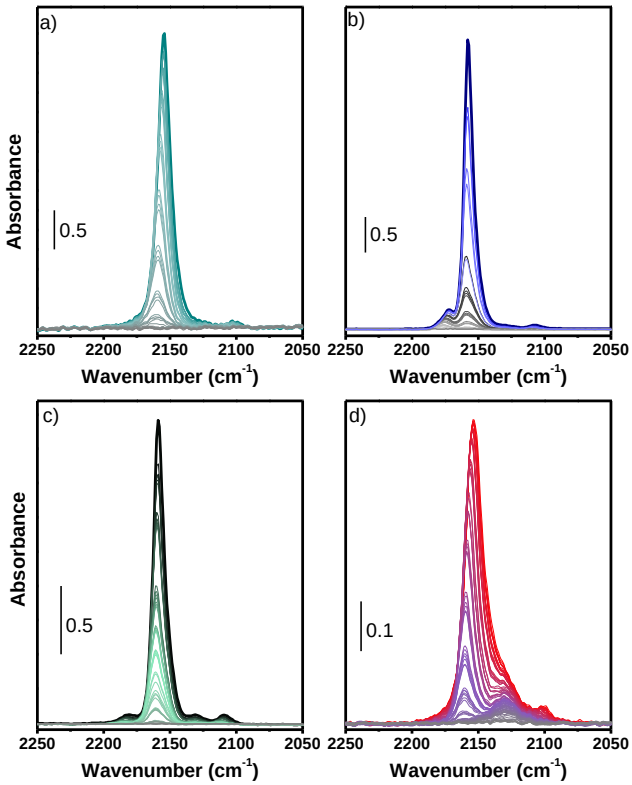

Figure 63 Difference FTIR spectra of CO increasing partial pressure (from gray to coloured line) at LNT over a) conv(650), b) MW(650), c) MW(100) and d) MW(100)-red.

4.4.2 CH_3OH and CO_2 activation over Ce^{3+}/V_O and FLP

Methanol and carbon dioxide absorption were employed to probe surface oxygen vacancies and to identify formed carbonates. After methanol adsorption (Figure 66a) over the CeO_2 samples, besides the formation of usual methoxide species (terminal, bi-bridged and tri-bridged), we observed a band at 1073 cm^{-1} over MW(100)-red sample (Figure 66a red line), associated to a methoxide group bridging two Ce^{3+} atom without interacting with the V_O (b'-OCH_3).[17] Indeed, CeO_2 reduction process is well known to cause a blueshift of b-OCH_3 ν(CO) due to different charge delocalization over the methoxide oxygen atom i.e., Ce^{3+} polarizes and delocalizes less than Ce^{4+}, causing an increase of C-O bond order and shifting ν(CO) to higher energies.[18] Moreover, MW(100)-red presented m-OCH_3/b-OCH_3 intensity ratio lower than the ideal one (2:1), contrarily respected from the other catalysts, unveiling a preferential reduction of (100) and (110) faces where b-OCH_3 are more stable, giving then access to FLP formation.[17] II) Ce^{3+} electronic transition at 2127 cm^{-1} was not modified by methanol adsorption suggesting (Figure 64a), as confirmed by XPS (vide infra), that b'-OCH_3 did not modify cerium oxidation state.

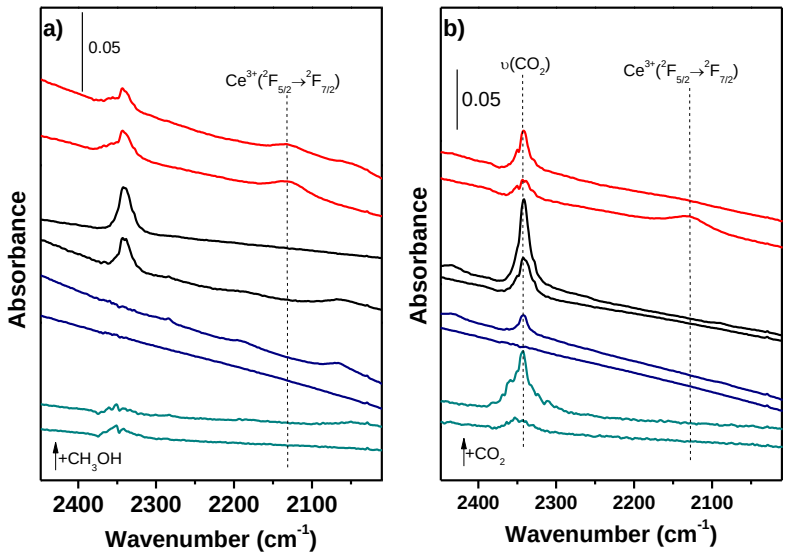

Figure 64 FT-IR spectra prior (lower) and after (higher) adsorption of a) CH_3OH (3 mbar) and b) CO_2 (100 mbar) at RT over conv(650) (dark cyan line), MW(650) (blue line), MW(100) (black line) and MW(100)-red (red line) catalysts.

To finely assign mono/bidentate/bridged carbonates/bicarbonates vibrations, we performed $^{13}CO_2$ adsorption (Figure 65) and compared the relative frequency shift ($\Delta^{13}C$) with recent literature.[19] Following Vaysillov and coworkers.[19] carbonates nomenclature, based on the number of cerium ions bounding each carbonates oxygen atom,$^{13}CO_2$ results (Figure 65) indicated as the formed carbonates can be restricted to four bidentate species sketched in Figure 66 for clarity.

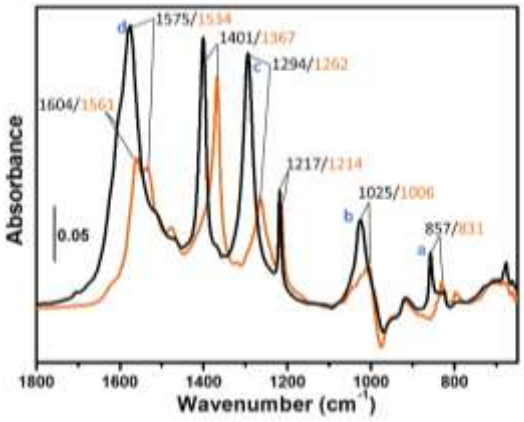

Band	Δ13	1.21	1.21'	1.2.1	1.2.1'
a	26	26	24	24	24
b	19	5	1	5	2
c	32	29	34	29	32
d	41	41	42	43	42

Figure 65 FTIR spectra of MW(100) after absorption of CO_2 (black line) and $^{13}CO_2$ (orange line). Main identified vibrations are indicated. Spectra are reported as difference by substracting the activated spectra. $\Delta^{13}C$ shifts of carbonates vibrations are reported in the table together with the relative shift of simulated carbonates from Vaysillov and coworkers.[19]

Noteworthy, we observed as on MW(100)-red catalysts CO_2 caused a I) consumption of Ce^{3+} electronic transition at 2127 cm^{-1} suggesting a Ce^{3+}/CO_2 electronic interaction (Figure 64b) and II) a higher carbonates-to-bicarbonates ratio respect to the other catalysts (Figure 66b) indicating, as rationalised hereafter, an increase of 1.21' carbonate associated to the higher Ce^{3+}/V_O content.

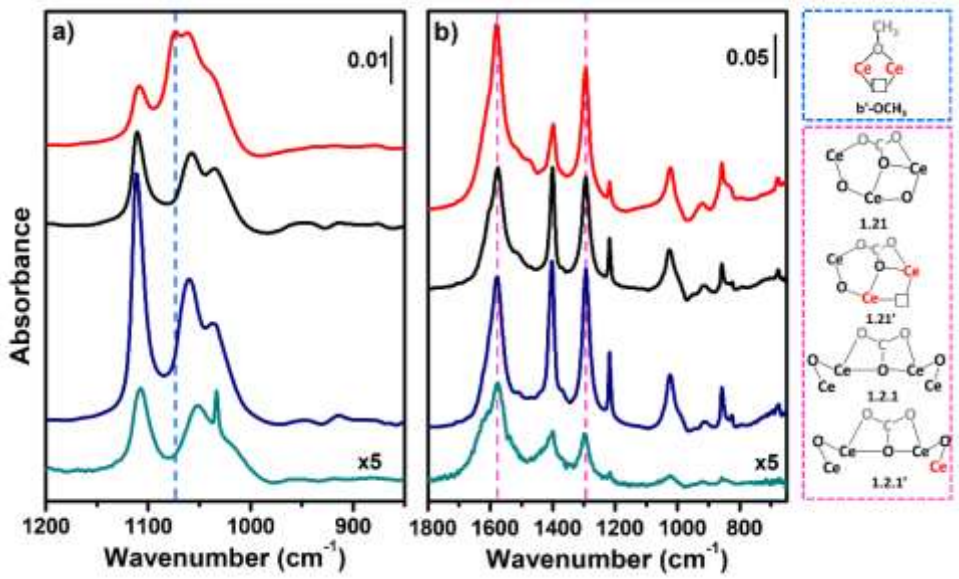

Figure 66 Difference FTIR spectra of a) 3 mbar methanol and b) 100 mbar CO_2 RT adsorption over conv(650) (dark cyan line), MW(650) (blue line), MW(100) (black line) and MW(100)-red (red line) catalysts. Sketched methoxide and carbonates species formed over CeO_2 are showed in blue and purple panels, respectively. CH_3OH and CO_2 atoms are showed in grey, Ce^{3+} in red and oxygen vacancy with black square. Carbonates nomenclature based on the number of cerium ions bounding each carbonates oxygen atom was taken from Vayssilov et al.[19] while apostrophe is here used to indicate carbonates considering Ce^{+3} presence. The spectrum of the material prior interaction with CH_3OH/CO_2 has been subtracted.

The hypothesized bidentate carbonate formed over a FLP should imply a sort of Ce^{3+}-to-CO_2 charge transfer. UV-Vis (Figure 67a) and XPS spectra of MW(100)-red (Figure 69) were measured before and after interaction with CO_2. We observed a decrease of: I) Ce^{3+}/Ce^{4+} CT (Figure 67a) and II) Ce^{3+}(3d) peaks (Figure 69b,e) after CO_2 adsorption at RT and 30°C/150°C, respectively. In addition, O1s XPS peaks (

Figure 67 b,c) showed as O_L and O^{β} signals did not undergo a considerable variation after CO_2 adsorption, suggesting as the latter did not modify O electronic

reconfiguration occurred after reduction (vide supra), signifying as the formed carbonate did not fill the V_O, as instead previously hypothesized.[20]

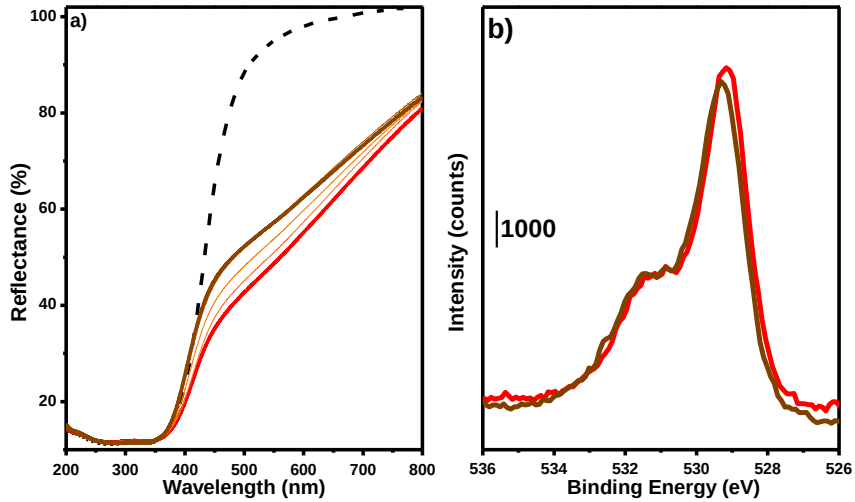

Figure 67 a) *Ex situ* UV-Vis spectra of MW(100)-red prior (red line) and after interaction with CO_2 atmosphere. The effect of increasing CO_2 partial pressure from 25 to 100 mbar is illustrated by the spectra from red to brown line. MW(100) is showed with dashed black line. b, c) XPS O 1S experimental spectra (red line), best fit curve (dashed black line), O_L (yellow curve), O^{β} (grey curve) and linear background (grey line) of MW(100)-red b) before and c) after interaction with 100 mbar of CO_2.

To verify the effective CO_2 and CH_3OH activation over FLP we exploited their reactivity to form monomethylcarbonate (MMC), the fundamental intermediate of dimethilcarbonate (DMC), by studying CO_2/CH_3OH chemical interaction with CeO_2 surface previously saturated with methoxide (CH_3O-CeO_2) or carbonates (CO_3-CeO_2) species, respectively. The presence of Ce^{3+} alone should indeed reduce MMC formation [21,22] whilst clustered Ce^{3+}/V_O forming a FLP should improve CO_2 reactivity. FTIR spectra in Figure 68a showed as CH_3OH adsorption over CO_3-CeO_2 caused a consumption of b-CO_3 and hCO_3 species in all the samples forming methoxide and

MMC species however without a considerable difference between the formed MMC bands intensity indicated with dashed lines in Figure 68a. Moreover, b'-OCH_3 have not been observed in MW(100)-red, suggesting that Ce^{3+} was already involved in the 1.21' carbonate formation.

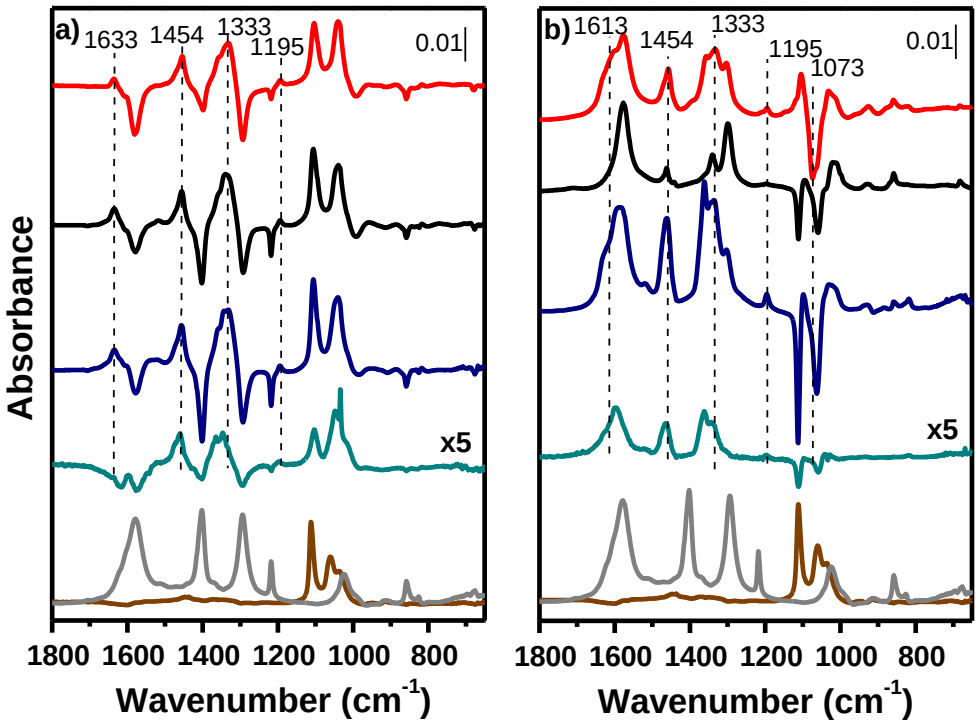

Figure 68 Difference FTIR spectra of conv(650) (light blue line), MW(650) (blue line), MW(100) (dark line) and MW(100)-red (red line) after a) CH_3OH (3 mbar) adsorption at RT over CeO_2 samples, previously reacted with CO_2 (100 mbar) at RT. Spectra of each CO_3-CeO_2 component have been substracted. b) CO_2 adsorption (100 mbar) at RT over catalysts previously reacted with 3 mbar of CH_3OH (CH_3O-CeO_2) at RT. Spectra of each CH_3O-CeO_2 component have been substracted. CH_3O-MW(650) (grey line) and CO_3-MW(650) (brown line) component are showed for clarity.

XPS spectra of CH_3OH adsorption over CO_3-MW(100)-red exploited at 30°C and 150°C (reaction temperature) in Figure 69°, showed a first decrease of Ce^{3+} bands after CO_2 adsorption followed by an increase upon interaction with CH_3OH. Whilst the former was described above and associated to Ce^{3+} partial reoxidation due to 1.21' carbonates formation, the latter can be associated either to methanol-induced Ce^{4+} reduction or MW(100) beam damage.[23–25]

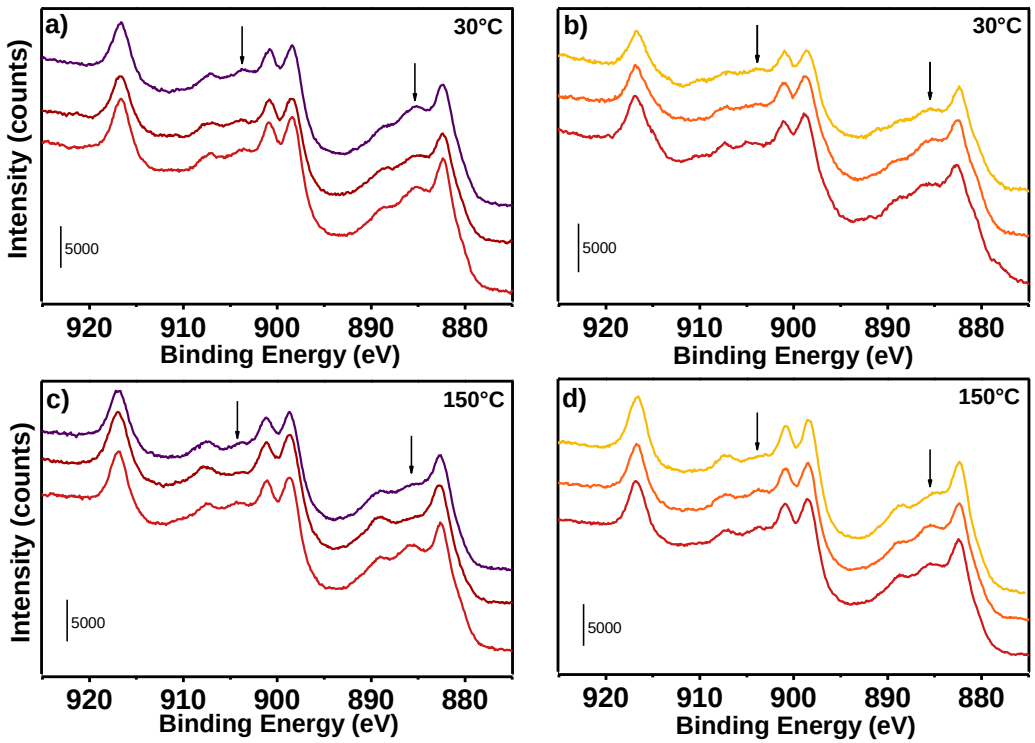

Figure 69 *Ex situ* Ce 3d XPS experimental spectra measured at 30°C and 150°C of MW(100)-red catalyst (red line) after : a,c) a first interaction with CO_2 (dark red line) followed by CH_3OH (purple line) or c,d) a first interaction with CH_3OH (orange line) followed by CO_2 (yellow line). Ce^{3+} most intense peaks are indicated with arrows.

Whilst the formed carbonates did not show particular differences in the reactivity with methanol, the reverse interaction i.e., CO_2 interacting with a surface with methoxide species, showed a different behaviour. Upon CO_2 adsorption over CH_3O-

CeO_2 samples (Figure 68b) we observed as methoxide species were consumed to form b-CO_3 and MMC. MMC was well formed over Ce^{3+}-free catalysts i.e., conv(650) and MW(650) whilst it was barely observed on MW(100) confirming as low Ce^{3+} content (≈14%) poisoned the reaction.[21–25] Following these results MW(100)-red with Ce^{3+}>30% should present an even lower MMC formation. Conversely we observed a qualitative higher concentration of MMC formed respect to MW(100) (Figure 68b) together with consumption of Ce^{+3} $^2F_{5/2}\rightarrow{}^2F_{7/2}$ electronic transition (not shown for brevity) and b'-OCH_3 species, both indirectly suggesting Ce^{3+} oxidation upon CO_2 adsorption at CH_3O-MW(100)-red. At the same time, Ce(3d) XPS spectra (Figure 69b,d) collected after CH_3OH and then CO_2 adsorption at 30°C and 150°C showed: I) a partial increase of Ce^{3+} bands after CH_3OH adsorption, again difficult to distinguish from beam damage effect and II) a Ce^{3+} partial consumption after subsequent CO_2 adsorption, confirming as Ce^{3+}/CO_2 interaction occurred even on a methoxide-reach CeO_2 surface at 30 and 150°C i.e., reaction-like temperature, since formation of b'-OCH_3 did not oxidise Ce^{3+} species

4.4.3 Conclusions

Microwave-induced defectivity in CeO_2 was characterized by FTIR, UV-VIS, Raman and XP spectroscopies. MW(100) reducibility was observed at 150°C under H_2 and confirmed by CH_3OH adsorption to be selectively limited to the (101) and (100) planes . Together with CO adsorption and Ce^{3+} quantification exploited by XPS, these results confirmed formation of Frustrated Lewis Pairs sketched in Figure 70. Ce^{3+} $^2F_{5/2}\rightarrow{}^2F_{7/2}$ electronic transition, together with Ce^{3+}/Ce^{4+} CT and Ce^{3+}(3d) XPS spectra were employed as fingerprints to observe as: I) Ce^{3+} was not oxidised upon CH_3OH adsorption through formation of a bridged-methoxide group (b'-OCH_3) which preserved Ce^{3+}/V_O (Figure 70) i.e., keeping the FLP site intact and II) CO_2 reoxidised Ce^{3+} without either filling the V_O or producing CO. Ce^{3+}/CO_2 electronic interaction must then occur through formation of a negatively charged carbonate allowing Ce^{3+}-to-CO_2 charge redistribution preventing V_O occupation (Figure 70). Even if by IR

measurements it was not possible to isolate a single carbonate between the four reported in Figure 67, coupling IR with UV-Vis and XPS results we observed as b-CO_3^{2-}/h-CO_3^{-} ratio increased parallel to Ce^{3+} content in the order MW(100)-red > MW(100) > MW(650) > conv (650). Considering then that I) only one of the four carbonates identified in Figure 67 implied $CO_3^{=}$ formed over Ce^{3+}/V_O, II) bidentate carbonates abundance increased with Ce^{3+} content, III) Ce^{3+} fingerprints i.e., IR 2127 cm^{-1} band, Ce^{3+}/Ce^{4+} UV-Vis CT and Ce^{3+}(3d) peaks have been consumed after CO_2 adsorption and IV) V_O/CO_2 interaction was not observed by O 1S spectra, we can hypothesize as the carbonate 1.21' concentration increased with Ce^{3+} content reaching the highest concentration over MW(100)-red. Indeed, this bidentate carbonate would allow Ce^{3+}-to-CO_2 charge redistribution without filling the oxygen vacancy and corresponds to the one predicted in case of CO_2 adsorbed over FLP sites (Figure 70). We here then showed as the high Ce^{3+} concentration (>30%), usually considered as detrimental for CO_2 conversion to DMC, allows CO_2 and CH_3OH activation over Frustrated Lewis Pair to 1.21' b-CO_3 and b'-OCH_3 species, respectively, making CO_2 C atom more electrophilic, hence more prone to react with methoxide O atom to form MMC (Figure 70).

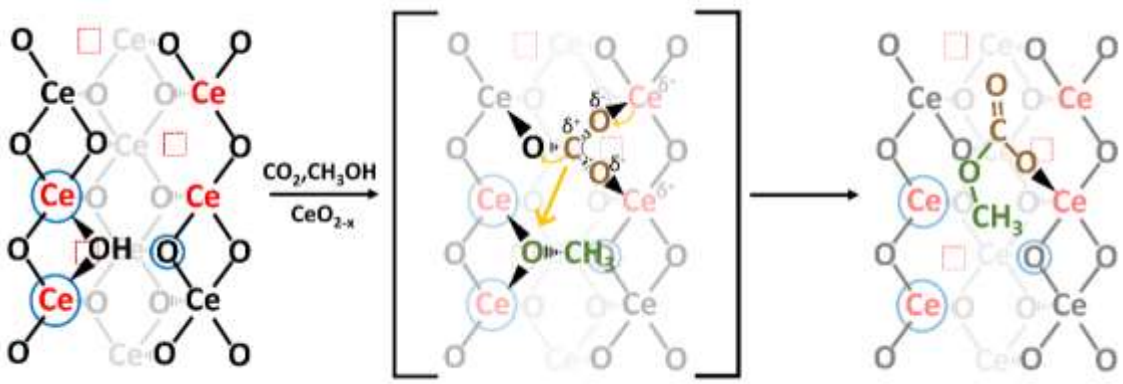

Figure 70 Sketched CO_2 (brown) and CH_3OH (green) reaction over CeO_2 surface with Ce^{4+} (black), Ce^{3+} (red), V_O (red squares) and FLP (blue circle) to form MMC.

References

(1) Daturi, M.; Binet, C.; Lavalley, J.; Sporken, R. Surface Investigation on CeZrO Compounds x -1-X2. *Phys. Chem. Chem. Phys.* **1999**, *1*, 5717–5724.

(2) Binet, C.; Daturi, M. Methanol as an IR Probe to Study the Reduction Process in Ceria-Zirconia Mixed Compounds. *Catal. Today* **2001**, *70* (1–3), 155–167. https://doi.org/10.1016/S0920-5861(01)00415-1.

(3) Jung, K. T.; Bell, A. T. An in Situ Infrared Study of Dimethyl Carbonate Synthesis from Carbon Dioxide and Methanol over Zirconia. *J. Catal.* **2001**, *347*, 339–347. https://doi.org/10.1006/jcat.2001.3411.

(4) Morterra, C.; Orio, L. Surface Characterization of Zirconium Oxide. II. The Interaction with Carbon Dioxide at Ambient Temperature. *Mater. Chem. Phys.* **1990**, *24* (3), 247–268. https://doi.org/10.1016/0254-0584(90)90089-S.

(5) Hertl, W. Surface Chemistry of Zirconia Polymorphs. *Langmuir* **1989**, *5* (1), 96–100. https://doi.org/10.1021/la00085a018.

(6) Pokrovski, K.; Jung, K. T.; Bell, A. T. Investigation of CO and CO2 Adsorption on Tetragonal and Monoclinic Zirconia. *Langmuir* **2001**, *17* (14), 4297–4303. https://doi.org/10.1021/la001723z.

(7) Taek Jung, K.; Bell, A. T. An *in Situ* Infrared Study of Dimethyl Carbonate Synthesis from Carbon Dioxide and Methanol over Zirconia. *J. Catal.* **2001**, *204* (2), 339–347. https://doi.org/10.1006/jcat.2001.3411.

(8) Katon, J. E.; Cohen, M. D. The Vibrational Spectra and Structure of Dimethyl Carbonate and Its Conformational Behavior. *Can. J. Chem.* **1975**, *53* (9), 1378–1386. https://doi.org/10.1139/v75-191.

(9) Behrendt, W.; Gattow, G.; Dräger, M. Über Chalkogenolate. LXI. Untersuchungen Über Halbester Der Kohlensäure. 1. Darstellung Und

Eigenschaften von Monomethyl- Und Monoäthylcarbonaten. *ZAAC - J. Inorg. Gen. Chem.* **1973**, *397* (3), 237–246. https://doi.org/10.1002/zaac.19733970303.

(10) Busca, G.; Lamotte, J.; Lavalley, J. ciaude; Lorenzelli, V. FT-IR Study of the Adsorption and Transformation of Formaldehyde on Oxide Surfaces. *J. Am. Chem. Soc.* **1987**, *109* (17), 5197–5202. https://doi.org/10.1021/ja00251a025.

(11) Ferrizz, R. M.; Wong, G. S.; Egami, T.; Vohs, J. M. Structure Sensitivity of the Reaction of Methanol on Ceria. *Langmuir* **2001**, *17* (8), 2464–2470. https://doi.org/10.1021/la001729o.

(12) Schilling, C.; Hofmann, A.; Hess, C.; Ganduglia-Pirovano, M. V. Raman Spectra of Polycrystalline CeO2: A Density Functional Theory Study. *J. Phys. Chem. C* **2017**, *121* (38), 20834–20849. https://doi.org/10.1021/acs.jpcc.7b06643.

(13) De Oliveira Jardim, E.; Rico-Francés, S.; Coloma, F.; Ramos-Fernández, E. V.; Silvestre-Albero, J.; Sepúlveda-Escribano, A. Superior Performance of Gold Supported on Doped CeO2 Catalystsfor the Preferential CO Oxidation (PROX). *Appl. Catal. A Gen.* **2014**, *487*, 119–129. https://doi.org/10.1016/j.apcata.2014.09.003.

(14) López, J. M.; Gilbank, A. L.; García, T.; Solsona, B.; Agouram, S.; Torrente-Murciano, L. The Prevalence of Surface Oxygen Vacancies over the Mobility of Bulk Oxygen in Nanostructured Ceria for the Total Toluene Oxidation. *Appl. Catal. B Environ.* **2015**, *174–175*, 403–412. https://doi.org/10.1016/j.apcatb.2015.03.017.

(15) Chen, A.; Yu, X.; Zhou, Y.; Miao, S.; Li, Y.; Kuld, S.; Sehested, J.; Liu, J.; Aoki, T.; Hong, S.; Camellone, M. F.; Fabris, S.; Ning, J.; Jin, C.; Yang, C.; Nefedov, A.; Wöll, C.; Wang, Y.; Shen, W. Structure of the Catalytically

Active Copper–Ceria Interfacial Perimeter. *Nat. Catal.* **2019**, *2* (4), 334–341. https://doi.org/10.1038/s41929-019-0226-6.

(16) Hadjiivanov, K. I.; Vayssilov, G. N. Characterization of Oxide Surfaces and Zeolites by Carbon Monoxide as an IR Probe Molecule. *Adv. Catal.* **2002**, *47*, 307–511. https://doi.org/10.1016/S0360-0564(02)47008-3.

(17) Badri, A.; Binet, C.; Lavalley, J. C. Use of Methanol as an IR Molecular Probe to Study the Surface of Polycrystalline Ceria. *J. Chem. Soc. - Faraday Trans.* **1997**, *93* (6), 1159–1168. https://doi.org/10.1039/a606628c.

(18) Siokou, A.; Nix, R. M. Interaction of Methanol with Well-Defined Ceria Surfaces: Reflection/Absorption Infrared Spectroscopy, X-Ray Photoelectron Spectroscopy, and Temperature-Programmed Desorption Study. *J. Phys. Chem. B* **1999**, *103* (33), 6984–6997. https://doi.org/10.1021/jp991127h.

(19) Vayssilov, G. N.; Mihaylov, M.; Petkov, P. S.; Hadjiivanov, K. I.; Neyman, K. M. Reassignment of the Vibrational Spectra of Carbonates , Formates , and Related Surface Species on Ceria : A Combined Density Functional and Infrared Spectroscopy Investigation. *J. Phys. Chem. C* **2011**, *115* (47), 23435–23454.

(20) Liu, B.; Li, C.; Zhang, G.; Yao, X.; Chuang, S. S. C.; Li, Z. Oxygen Vacancy Promoting Dimethyl Carbonate Synthesis from CO2 and Methanol over Zr-Doped CeO2 Nanorods. *ACS Catal.* **2018**, *8* (11), 10446–10456. https://doi.org/10.1021/acscatal.8b00415.

(21) Aresta, M.; Dibenedetto, A.; Pastore, C.; Cuocci, C.; Aresta, B.; Cometa, S.; De Giglio, E. Cerium(IV)Oxide Modification by Inclusion of a Hetero-Atom: A Strategy for Producing Efficient and Robust Nano-Catalysts for Methanol Carboxylation. *Catal. Today* **2008**, *137* (1), 125–131. https://doi.org/10.1016/j.cattod.2008.04.043.

(22) Aresta, M.; Dibenedetto, A.; Pastore, C.; Angelini, A.; Aresta, B.; Pápai, I. Influence of Al2O3 on the Performance of CeO2 Used as Catalyst in the Direct Carboxylation of Methanol to Dimethylcarbonate and the Elucidation of the Reaction Mechanism. *J. Catal.* **2010**, *269* (1), 44–52. https://doi.org/10.1016/j.jcat.2009.10.014.

(23) Mullins, D. R.; Robbins, M. D.; Zhou, J. Adsorption and Reaction of Methanol on Thin-Film Cerium Oxide. *Surf. Sci.* **2006**, *600* (7), 1547–1558. https://doi.org/10.1016/j.susc.2006.02.011.

(24) Beste, A.; Mullins, D. R.; Overbury, S. H.; Harrison, R. J. Adsorption and Dissociation of Methanol on the Fully Oxidized and Partially Reduced (1 1 1) Cerium Oxide Surface: Dependence on the Configuration of the Cerium 4f Electrons. *Surf. Sci.* **2008**, *602* (1), 162–175. https://doi.org/10.1016/j.susc.2007.10.024.

(25) Matolín, V.; Libra, J.; Škoda, M.; Tsud, N.; Prince, K. C.; Skála, T. Methanol Adsorption on a CeO2(1 1 1)/Cu(1 1 1) Thin Film Model Catalyst. *Surf. Sci.* **2009**, *603* (8), 1087–1092. https://doi.org/10.1016/j.susc.2009.02.010.

5 Aknowledments

The COZMOS project has received funding from the European Union's Horizon 2020 research and innovation programme under grant agreement 837733.

Acknowledgments to be written

6 Appendix : list of published articles during the thesis

6.1 A : Ticali P., Salusso D., Catal. Sci. Technol., 2021,11, 1249

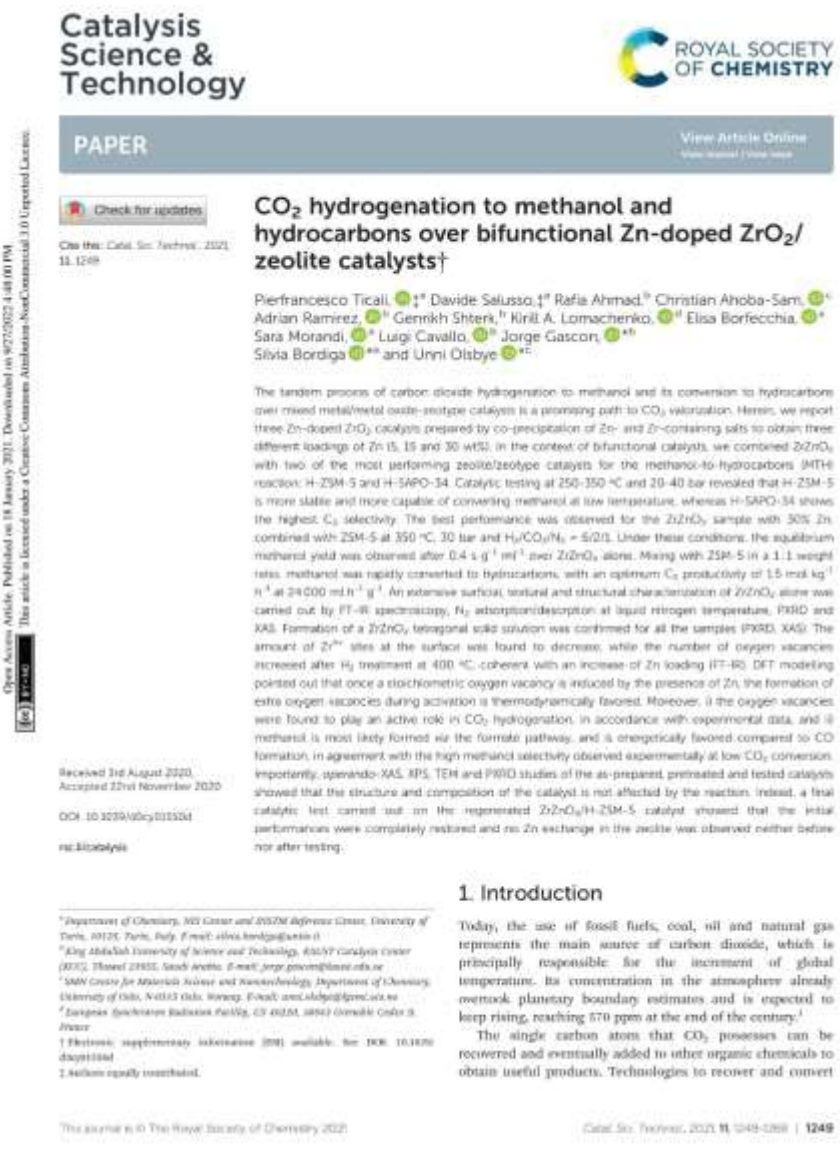

Catalysis Science & Technology

ROYAL SOCIETY OF CHEMISTRY

PAPER

View Article Online

Check for updates

Cite this: Catal. Sci. Technol., 2021, 11, 1249

CO_2 hydrogenation to methanol and hydrocarbons over bifunctional Zn-doped ZrO_2/zeolite catalysts†

Pierfrancesco Ticali, ‡[a] Davide Salusso, ‡[a] Rafia Ahmad,[b] Christian Ahoba-Sam, [c] Adrian Ramirez, [b] Genrikh Shterk,[b] Kirill A. Lomachenko, [d] Elisa Borfecchia, [e] Sara Morandi, [a] Luigi Cavallo, [b] Jorge Gascon, [b]*[b] Silvia Bordiga [a]*[a] and Unni Olsbye [c]*[c]

The tandem process of carbon dioxide hydrogenation to methanol and its conversion to hydrocarbons over mixed metal/metal oxide–zeotype catalysts is a promising path to CO_2 valorization. Herein, we report three Zn-doped ZrO_2 catalysts prepared by co-precipitation of Zn- and Zr-containing salts to obtain three different loadings of Zn (5, 15 and 30 wt%). In the context of bifunctional catalysts, we combined $ZrZnO_x$ with two of the most performing zeolite/zeotype catalysts for the methanol-to-hydrocarbons (MTH) reaction: H-ZSM-5 and H-SAPO-34. Catalytic testing at 250–350 °C and 20–40 bar revealed that H-ZSM-5 is more stable and more capable of converting methanol at low temperature, whereas H-SAPO-34 shows the highest C_5^+ selectivity. The best performance was observed for the $ZrZnO_x$ sample with 30% Zn combined with ZSM-5 at 350 °C, 30 bar and $H_2/CO_2/N_2$ = 5/2/1. Under these conditions, the equilibrium methanol yield was observed after 0.4 s g^{-1} ml^{-1} over $ZrZnO_x$ alone. Mixing with ZSM-5 in a 1:1 weight ratio, methanol was rapidly converted to hydrocarbons, with an optimum C_5^+ productivity of 1.5 mol kg^{-1} h^{-1} at 24 000 ml h^{-1} g^{-1}. An extensive surficial, textural and structural characterization of $ZrZnO_x$ alone was carried out by FT-IR spectroscopy, N_2 adsorption/desorption at liquid nitrogen temperature, PXRD and XAS. Formation of a $ZrZnO_x$ tetragonal solid solution was confirmed for all the samples (PXRD, XAS). The amount of Zr^{3+} sites at the surface was found to decrease, while the number of oxygen vacancies increased after H_2 treatment at 400 °C, coherent with an increase of Zn loading (FT-IR). DFT modelling pointed out that once a stoichiometric oxygen vacancy is induced by the presence of Zn, the formation of extra oxygen vacancies during activation is thermodynamically favored. Moreover, i) the oxygen vacancies were found to play an active role in CO_2 hydrogenation, in accordance with experimental data, and ii) methanol is most likely formed *via* the formate pathway, and is energetically favored compared to CO formation, in agreement with the high methanol selectivity observed experimentally at low CO_2 conversion. Importantly, operando-XAS, XPS, TEM and PXRD studies of the as-prepared, pretreated and tested catalysts showed that the structure and composition of the catalyst is not affected by the reaction. Indeed, a final catalytic test carried out on the regenerated $ZrZnO_x$/H-ZSM-5 catalyst showed that the initial performances were completely restored and no Zn exchange in the zeolite was observed neither before nor after testing.

Received 3rd August 2020,
Accepted 22nd November 2020

DOI: 10.1039/d0cy01552d

rsc.li/catalysis

1. Introduction

Today, the use of fossil fuels, coal, oil and natural gas represents the main source of carbon dioxide, which is principally responsible for the increment of global temperature. Its concentration in the atmosphere already overtook planetary boundary estimates and is expected to keep rising, reaching 570 ppm at the end of the century.[1]

The single carbon atoms that CO_2 possesses can be recovered and eventually added to other organic chemicals to obtain useful products. Technologies to recover and convert

[a] Department of Chemistry, NIS Center and INSTM Reference Center, University of Turin, 10125, Turin, Italy. E-mail: silvia.bordiga@unito.it
[b] King Abdullah University of Science and Technology, KAUST Catalysis Center (KCC), Thuwal 23955, Saudi Arabia. E-mail: jorge.gascon@kaust.edu.sa
[c] SMN Centre for Materials Science and Nanotechnology, Department of Chemistry, University of Oslo, N-0315 Oslo, Norway. E-mail: unni.olsbye@kjemi.uio.no
[d] European Synchrotron Radiation Facility, CS 40220, 38043 Grenoble Cedex 9, France
[e] Department of Physics and Geology, University of Perugia, Via A. Pascoli, I-06123 Perugia, Italy

† Electronic supplementary information (ESI) available. See DOI: 10.1039/d0cy01552d

‡ Authors equally contributed.

CO_2 have been known since the mid-19th century, however, only from the 1970s, CO_2 found its first industrial application in the synthesis of methanol from CO_2-enriched syngas (CO and H_2).[3] To date, CO_2 capture and utilization represents a promising route to control its emission while limiting fossil fuel extraction. Currently, biological, electrochemical and catalytic processes are all exploited for CO_2 valorization. Concerning the catalytic processes, carbon capture and storage (CCS) technologies[3] can be coupled with utilization of CO_2 as a feedstock in: i) low energy processes[4] such as production of urea, carbonates, carbamates and ii) high-energy processes where high-value chemicals (CH_4, HCOOH, and CH_3OH) are obtained.[5,6]

High-energy processes mostly exploit the capability of certain materials to reduce carbon dioxide to hydrocarbons and/or olefins. However, as CO_2 is the most oxidized form of carbon, it is located in a thermodynamic well, which makes its chemical reduction challenging,[5] such that high temperature and pressure are required, increasing the total cost of the process.

CO_2 reduction can be achieved by using H_2: both academic and industrial research efforts are today focused on using renewable sources of H_2 to reduce the environmental impact of these processes.[6,7] Hydrogenation is industrially exploited for the production of methanol, massively employed as a solvent, alternative fuel and feedstock for the chemical industry. To date, industrial-scale methanol production is still carried out from syngas over $Cu/ZnO/Al_2O_3$ catalysts developed by Imperial Chemical Industries (ICI).[8] Partial substitution of the feed with CO_2 causes a drastic catalyst selectivity decreases[6] due to the reverse water gas shift (RWGS) reaction (eqn (1)).

Another approach is to convert methanol to hydrocarbons in the same reaction batch. For this purpose, bifunctional catalysts play a key role in carbon dioxide hydrogenation and conversion to organic compounds, but the main challenge consists of compromising the catalyst performances, such as activity, selectivity and conversion, with the energy cost of the total reaction, *i.e.* low pressure and temperature (1 bar, <400 °C). The main reactions involved in this process are:

$$CO_2 + H_2 = CO + H_2O \text{ (RWGS)} \quad (1)$$

$$CO_2 + 3H_2 = CH_3OH + H_2O \quad (2)$$

$$CO + 2H_2 = CH_3OH \quad (3)$$

$$nCH_3OH \rightarrow C_nH_{2n} + nH_2O \quad (4)$$

Recently, several groups[9–14] investigated bifunctional catalysts obtained by combining a metal or metal oxide phase employed in CO_2 conversion to methanol with a selective zeolite/zeotype for the methanol-to-hydrocarbons process (MTH). However, the coexistence of two catalysts under the same reaction conditions is challenging. As a matter of fact, each catalyst should be the most appropriate for each reaction and, simultaneously, the two active phases must not poison each other, *e.g.* water production in the second step of the reaction may induce sintering of the catalyst dedicated to methanol synthesis.[15] Moreover, at high temperature, the possibility that the two materials undergo mutual interactions (*e.g.* inter-phase ion-exchange phenomena) altering their physico-chemical properties must be considered.[10]

Starting from the first step involved in CO_2 hydrogenation to methanol, it is important to compromise the thermodynamics of the reaction,[16] *i.e.* methanol formation at low temperature and high pressure. From a global point of view, low temperature favors methanol production on the first catalyst while high temperature enhances methanol dehydration and C–C coupling in the zeolite. With this respect, high temperature moves the equilibrium of the first catalyst towards the endothermic RWGS reaction (eqn (1)).

In recent years, different research studies[6,7,17–22] have been focused on using the same types of catalysts involved in the RWGS reaction but trying to promote: i) stabilization of intermediates for hydrogenation to methanol or other hydrocarbons instead of RWGS ones; ii) H_2 dissociation by heterolytic splitting; and iii) inhibition of the water poisoning effect, which hampers the catalytic hydrogenation activity.[23]

ZrO_2 has been investigated as a support material in many binary and ternary systems for CO/CO_2 hydrogenation to methanol.[23–29] IR and TPD studies over pristine zirconia conducted by Pokrovski *et al.*[30] showed that CO and CO_2 are mainly adsorbed as HCO^-, CO_3^{2-} and HCO_3^-, m/b-CO_3^{2-}, respectively. The CO_2 adsorption capacity increases with the strength of Zr^{4+} Lewis acid sites, O^{2-} Lewis basic sites and higher concentration and basicity of hydroxyl groups. However former studies showed that the main CO_2/ZrO_2 interaction occurs through the oxide basic sites;[30,31] in particular with the formation of bicarbonate b-HCO_3–Zr,[26] which following hydrogenation is promoted from the weak hydrophilic character of the support.[32] Recent NAP-XPS and IRAS studies by Li *et al.*[33] showed that the presence of hydroxyl groups on the ZrO_2 surface is essential for the bicarbonate species formation. Doping of ZrO_2 with an aliovalent cation (*e.g.* Zn^{2+}) induces the formation of oxygen vacancies (V_O) and, as a direct consequence, generates defects featured by coordinatively unsaturated Zr^{4+} sites (*cus*-Zr^{3+}) which can act as strong basic and acid sites respectively.[34]

Carbon mono- and di-oxide activation was reported to be facilitated by the presence of neighbouring *cus*-Zr^{4+} ion sites and V_O.[25,35–37] Thus, V_O enhance the Brønsted acidity of Zr–OH groups adjacent to *cus*-Zr^{3+} cations.[38] Between the potential dopants, Zn^{2+} has been investigated in the formation of $ZnZrO_x$ solid solutions. CO_2 adsorption and methanol selectivity are enhanced by the increase of basic sites[23,28,34] while H_2 activation is influenced by the synergy of Zn–Zr sites.[31] Therefore, the simultaneous presence of *cus*-sites, V_O and surface hydroxyl groups seems to be a key combination to improve CO_2 adsorption, activation and hydrogenation to methanol.

Hence, both Zn and ZrO_2 seem to promote several reactions related to environmental concerns. To date, a major fraction of recent works based on Zn–Zr systems deals with syngas conversion[14,30,37] whereas another fraction is devoted to Zn–Zr systems involved in CO_2 hydrogenation aiming for different products, such as methanol. In the case of Zn-doped ZrO_2 studied by Wang *et al.*,[31] CO_2 conversion increases up to 20% at high temperatures (>320 °C) while methanol selectivity drops to less than 30%. These findings highlight that operation at high temperature thermodynamically favors side reactions, such as RWGS.[10]

In another recent contribution, Li *et al.*[29] used a metal–organic approach to prepare the catalysts by means of a Schiff base, yielding a Zn-doped ZrO_2 solid solution (with a 1:1 ratio). This catalyst showed a methanol selectivity of 70% with 5.7% CO_2 conversion at 320 °C, $V(CO_2)/V(H_2)/V(N_2)$ = 24/72/4% and GHSV = 18 000 mL g^{-1} h^{-1}. XRD and TEM/EDS analysis confirmed the doping of Zn in the ZrO_2 system, without any segregated phases. DRIFT spectroscopy was employed to investigate the produced species after CO_2 hydrogenation, highlighting the formation of CH_xO species on the ZnO–ZrO_2 phase, confirming that methanol is one of the main products obtained by this class of catalysts.

As for the zeolite/zeotype material for a selective MTH process, in recent years many acidic catalysts have been proposed focusing on features, such as pore and channel dimensions or reaction intermediates; recalling some examples, H-ZSM-5 has been proven to favor $C_5^=$ alkenes.[13,19] Ongoing research efforts principally aim at: i) improving catalyst performance, *e.g.* by evaluating and optimizing Al dispersion in the zeolitic framework;[40,41] ii) reducing coke and aromatic species formation, by understanding the influence of pore and channel dimensions in the search for optimized zeolite/zeotypes; iii) pushing temperature and pressure to a thermodynamically-favored range.

The Zn–Zr binary oxide has been combined with H-SAPO-34/H-ZSM-5/H-SSZ-13 to exploit hydrocarbon synthesis from syngas.[13,38] Coupling a metal oxide for methanol production with a porous catalyst dedicated to MTH/MTO allows precise control of the elementary steps involved in the reaction (CO/CO_2 chemisorption, C–C coupling and C–C cleavage).[42] The weak hydrogenating nature of $ZnZrO_2$ allows selective hydrogenation of CO/CO_2 but not the eventual production of olefins/hydrocarbons.

More recent works started to investigate tandem catalysts (ZnO–ZrO_2/zeolite and zeotype) for CO_2 hydrogenation. Li *et al.*[14] studied a ZnO–ZrO_2 mixed metal oxide system, similar to those studied in this manuscript coupled with H-SAPO-34. A CO_2 conversion of 12.6% was found at 380 °C and 3600 mL g^{-1} h^{-1}, with 80% selectivity to $C_2^=$–$C_4^=$. According to their XRD and HAADF-STEM findings, the sample is a solid solution with no trace of segregated phases. By means of DRIFT spectroscopy, they studied the reaction products adsorbed on the surface of the catalyst, concluding that CH_xO species are generated on the oxidic ZnZrO phase and then transferred onto SAPO zeolite for lower olefins production. Similarly, Zhou *et al.* studied a ZnO–ZrO_2 solid solution in tandem with ZSM-5 zeolite and reported high selectivity towards aromatic products.[15]

Choosing what kind of zeolite/zeotype material should be used in this reaction is not straightforward. Park *et al.*[44] compared two systems: CuZnO–ZrO_2/H-ZSM-5 and CuZnO–ZrO_2/H-SAPO-34. They found that the hydrocarbon distribution is strictly related to the nature of the zeolite. However, the interplay between the two catalytic functions is still not fully understood.

In this work, we investigated the catalytic properties of bifunctional catalysts obtained by physically mixing three different Zn-doped ZrO_2 ($ZrZnO_x$) with MTH-active zeolite/zeotype catalysts, H-ZSM-5 and H-SAPO-34. As such, our contribution represents a side-by-side comparison of these two materials combined with $ZnZrO_x$.

Firstly, we thoroughly characterized the oxidic phase by infrared spectroscopy (IR), powder X-ray diffraction (PXRD), N_2 adsorption/desorption and density functional theory (DFT) modelling, ultimately aiming at understanding its role in CO_2 hydrogenation. Specifically, our integrated characterization approach targeted: i) the role of Zn in creating defects; ii) the detailed properties of Zn and Zr sites as revealed by IR of adsorbed CO; iii) the response of the catalyst to high-temperature treatment under model oxidative and reducing conditions. Experimental findings were corroborated by theoretical modelling, which were also used to explore different reaction pathways for CO_2 hydrogenation over $ZrZnO_x$.

Secondly, we studied both the oxidic phase alone and the combined systems by catalytic test runs under different conditions, space times and after regeneration. For all the investigated cases, we determined the CO_2 conversion as well as methanol and hydrocarbon product distributions, highlighting the role of Zn in influencing the catalytic properties of the investigated systems.

Finally, we employed *operando* X-ray absorption spectroscopy (XAS) at Zr and Zn K-edges to directly probe the local structure and electronic properties of the $ZrZnO_x$/ZSM-5 system before and after activation in H_2, as well as to assess its stability under reaction conditions, *i.e.* high temperature (300 °C) and pressure (10 bar) under a CO_2/H_2 feed.

In this work, we aim to give a significant contribution to the understanding of the oxygen vacancy formation and its role in the CO_2 hydrogenation pathway, elucidating the synergy between cations in $ZnZrO_x$ solid solutions. We also critically evaluated the relationship between experimental conditions (*i.e.* contact time) and catalyst activity towards value-added hydrocarbons at lower temperature than those usually reported in the literature.[15,16]

2. Experimental

2.1. Materials

Three Zn-containing ZrO_2 samples were prepared by co-precipitation starting from solutions of zirconium and zinc

inorganic salts following the recipe from Wang *et al.*[31] The samples were named ZrZn-*X*, where *X* is the Zn loading determined by ICP-AES analysis (*vide infra*) and reported in Table 1. The typical procedure for making sample ZrZn-30, taken as an example, was by mixing 0.6 g $Zn(NO_3)_2{\cdot}6H_2O$ and 2.15 g $ZrN_2O_7{\cdot}xH_2O$ in 100 ml of type 2 H_2O in a round bottom flask. The mixtures prepared for the three samples were then heated to 70 °C in an oil bath under reflux amidst stirring. 3.06 g $(NH_4)_2CO_3$ was dissolved in 100 ml of type 2 H_2O and then added to the warm precursor solutions dropwise: white precipitates immediately formed. The mixtures were further stirred at 70 °C for 2 h, cooled at ambient temperature, centrifuged and the precipitates were washed twice with type 2 H_2O. The wet powders were oven-dried at 110 °C and then calcined at 500 °C for 3 h.

Combined systems were obtained by mechanical mixing of the ZrZn-*X* catalysts with a commercial H-ZSM-5 zeolite with a mass ratio of 1:1. For comparison purposes, combined systems using commercial H-SAPO-34 were also prepared by the same mechanical mixing protocol. Commercial H-ZSM-5 and H-SAPO-34 characteristics are reported in the ESI.†

2.2. Methods

2.2.1. Chemical, textural and structural characterization of the ZrZn-*X* catalysts. Zirconium and zinc contents in the ZrZn-*X* specimens were determined using a Perkin Elmer Optima 7000 DV (Perkin Elmer, Norwalk, Connecticut, USA) inductively coupled plasma-atomic emission spectrometer (ICP-AES) equipped with a PEEK Mira Mist nebulizer, a cyclonic spray chamber and an Echelle monochromator. The wavelengths used for Zr and Zn determination were λ_{Zr} = 339.197 nm and λ_{Zn} = 213.857 nm. For the analyses, a pre-treatment of the samples was required. Acid digestion of the oxides was carried out using a Milestone MLS-1200 MEGA microwave laboratory unit (Milestone, Sorisole, Italy). Aliquots of 200 mg of each sample were transferred in tetrafluoromethoxyl (TFM) bombs and digested with 2 mL of hydrofluoric acid and 5 mL of *aqua regia* before the analysis. Four heating steps of 5 min each (250, 400, 600, and 250 W power, respectively), followed by a ventilation step of 25 min, were applied. Then 0.7 g of boric acid was added, and the bombs were further heated for 5 min at 250 W and again cooled by a ventilation step of 15 min. At the end of the full treatment, the samples appeared completely dissolved. The digested solutions were diluted to 20 mL with high purity water. Each sample was analysed in duplicate and each concentration value was averaged on the basis of three instrumental measurements. Blanks were simultaneously run. It is well-known that Hf, chemically similar to Zr, is a common natural contaminant in every Zr compound. For this reason, using λ_{Hf} = 277.336 nm the presence of Hf was determined to be less than 2 wt% for each sample, but there is no evidence about its influence on our results.

Specific surface areas (SSAs) and pore size distributions (PSDs) of the ZrZn-*X* samples were determined by applying the Brunauer–Emmett–Teller (BET) method and the DFT method, respectively, to the adsorption/desorption isotherms of N_2 at liquid nitrogen temperature obtained with a Micromeritics ASAP 2010 physisorption analyzer. PSDs were obtained applying the DFT method on cylindrical pores, using the Tarazona NLDFT approach. The adsorption/desorption isotherms were determined over a wide range of relative pressures ($10^{-6} < p/p_0 < 1$). All the samples underwent an activation step to remove physisorbed species from the surface while avoiding irreversible changes of the surface or the solid structure. Each sample was studied after outgassing under vacuum at 120 °C (heating ramp of 5 °C min^{-1}) for 5 h (residual pressure of 10^{-4} mbar).

Powder X-ray diffraction (PXRD) patterns of the as-prepared ZrZn-*X* catalysts were collected at room temperature (RT) using a glass capillary (ø = 0.3 mm) in a PW3050/60 X'Pert PRO MPD diffractometer from PANalytical working with the Bragg–Brentano geometry. Patterns from the Cu $K\alpha_{1,2}$ X-ray source were recorded from 10 to 90° 2θ with a step size of 0.0156° and an integration time of 150 s. The Rietveld refinement method implemented in the FullProf software package[47] was used to extract lattice parameters and average crystallite size from all the three samples. The PXRD patterns of ZrZn-30 alone and that physically mixed with the ZSM-5 zeolite recovered after catalytic tests (referred to as 'tested' in the following) were measured and refined following the same procedure mentioned above. We refer to the ESI† for the complete procedure description.

2.2.2. Spectroscopic characterization of the ZrZn-*X* catalysts. Absorption/transmission IR spectra were run on a Perkin-Elmer FTIR 2000 spectrophotometer equipped with a Hg–Cd–Te cryo-detector, working in the range of wavenumbers 7200–580 cm^{-1} at a resolution of 2 cm^{-1}. For IR analysis, the ZrZn-*X* powders were compressed in self-supporting discs (~20 mg cm^{-2}) and placed in IR cells suitable for different kinds of measurements. In particular, a commercial stainless steel cell (Aabspec), allowing thermal treatments *in situ* under vacuum or a controlled atmosphere and the simultaneous registration of spectra at temperatures up to 600 °C, was employed to study H_2 interaction at 400 °C on the pre-oxidized catalysts. IR measurements in hydrogen

Table 1 Chemical, textural and structural features of ZrZn-*X* catalysts. In order: Zn loading, specific surface area (SSA), pore volume, lattice parameter (*a* = *b*), and average crystallite size (*d*)

	ZrZn-5	ZrZn-15	ZrZn-30
Zn loading (wt%)	5	15	30
SSA ($m^2\ g^{-1}$)	47	46	37
DFT cumulative pore volume ($cm^3\ g^{-1}$)	0.24	0.21	0.49
Space group	$P4_2/nmc$	$P4_2/nmc$	$P4_2/nmc$
a (= *b*) (Å)	3.6049 ± 0.0008	3.58900 ± 0.00018	3.59440 ± 0.0008
c (Å)	5.0980 ± 0.0015	5.1020 ± 0.0005	5.082 ± 0.002
Crystallite size (nm)	55 ± 1	20 ± 1	12 ± 1

were performed to study the effect of the activation step used for the catalytic tests (*vide infra*).

In order to characterize the Lewis acid sites, *i.e.* Zn^{2+} and Zr^{4+}, at the surface of both pre-oxidized and pre-reduced samples, the catalysts were placed in a quartz IR cell, allowing thermal treatments and *ex situ* measurements of CO adsorption at liquid nitrogen temperature (LNT).

Before the IR measurements, the samples were outgassed under vacuum at 400 °C for 30 min and then oxidized or reduced. The oxidation pre-treatment was performed in dry oxygen (40 mbar) for 30 min at 400 °C. Finally, the samples were cooled to room temperature (RT) in O_2.

The reduction pre-treatment was performed in the same way using H_2. In this case, the hydrogen was outgassed at 400 °C and then the samples were cooled at RT under vacuum.

2.2.3. Molecular modelling of the ZrZn-*X* catalysts. Periodic cells were optimized with spin-polarized DFT calculations using the Vienna *ab initio* simulation package (VASP 5.4.4).[46,47] Projector augmented wave (PAW)[48] potentials were used to describe the core electrons with the generalized gradient approximation (GGA) using the PBE[51] functional including the Becke-Johnson damped D3 dispersion correction[52] as implemented in VASP. The Kohn–Sham one-electron wave functions were expanded by using a plane wave basis set with a kinetic energy cutoff of 450 eV. The Brillouin zone of the structures was sampled using the Γ point. An energy convergence criterion of 10^{-6} eV and a force convergence criterion of 0.05 eV $Å^{-1}$ were used.

The unit lattice vectors and atoms of tetragonal ZrO_2 were fully optimized in the beginning. We began the geometry optimization with the experimental lattice parameter values, which were optimized to $a = b = 3.646$ Å, and $c = 5.275$ Å. The most stable surface of the tetragonal ZrO_2 phase was simulated by a $2 \times 2 \times 1$ supercell model. To eliminate the artificial dipole moments within the slab model, we constructed a symmetric slab of at least 5 layers of Zr atoms. The slab was separated from its periodic image by 15 Å to avoid spurious interactions between the periodic slab models. The adsorption energy of the reactants and reaction intermediates was calculated as:

$$\Delta E[\text{adsorption}] = E[\text{adsorbate} + \text{surface}] - E[\text{adsorbate}] - E[\text{clean surface}]$$

2.2.4. Catalytic tests on the ZrZn-*X* catalysts and the combined ZrZn-*X*/zeolite systems. Catalytic tests were executed in a 16 channel Flowrence® from Avantium. 50 mg of the stand-alone MeOH catalyst (ZrZn-*X* samples) or 100 mg of the combined catalyst with a ZrZn-*X*/zeolite mass ratio of 1 : 1 in a mixed bed configuration was typically used. The attention was focused on the systems with H-ZSM-5 zeolite; however, for comparison purposes, combined systems with H-SAPO-34 were also tested and the results are reported in the ESI.† The gas feed composition was: 23 vol% of CO_2, 69 vol% of H_2 and 8 vol% of He as the internal standard. We typically aimed to have 12 000 ml h^{-1} g^{-1} per channel. One of the 16 channels was always used without a catalyst as the blank. Prior to feeding the reaction mixture, all the samples were reduced *in situ* with a pure H_2 atmosphere for 4 hours at 400 °C. The tubes were then pressurized to 30 bar using a membrane-based pressure controller. Regeneration tests were carried out *in situ* at atmospheric pressure and 600 °C with a 5% O_2 in N_2 stream for 6 hours. In some cases, the reacted gas was diluted with N_2 (20 mL min^{-1} per reactor) in the reactor outlet and automatically supplied for online gas chromatographic (GC) analysis.

The GC is an Agilent 7890B with two sample loops. After flushing the loops for 24 min, the content is injected. One sample loop goes to the TCD channel with 2 Hayesep pre-columns and MS5A, where He, H_2, CH_4 and CO are separated. Gases that have longer retention times than CO_2 on the Hayesep column (column 4 Hayesep Q 0.5 m G3591-80023) are back-flushed. Further separation of permanent gases is done on another Hayesep column (column 5 Hayesep Q 6 Ft G3591-80013) to separate CO_2 before going to MS5A. Another sample loop goes to an Innowax pre-column (5 m, 0.20 mm OD, 0.4 μm film); in the first 0.5 min of the method, the gases coming from the pre-column are sent to the Gaspro column (Gaspro 30 M, 0.32 mm OD) followed by FID. After 0.5 min, the valve is switched and gases are sent to the Innowax column (45 m, 0.2 mm OD, 0.4 μm) followed by FID. The Gaspro column separates C_1–C_4, paraffins and olefins, while the Innowax column separates oxygenates and aromatics.

Conversions, CO selectivity, MeOH selectivity, hydrocarbon distribution selectivity (CO free) and C_1 productivity are reported on the C_1 basis and are defined as follows:

$$\text{Conv}_{CO_2}(\%) = \frac{CO_{2\text{blk}}/He_{\text{blk}} - CO_{2\text{R}}/He_{\text{R}}}{CO_{2\text{blk}}/He_{\text{blk}}} \times 100$$

$$S_{CO}(\%) = \frac{\frac{C_{CO,R}}{C_{He,R}}}{\left(\frac{C_{CO_2,blk}}{C_{He,blk}} - \frac{C_{CO_2,R}}{C_{He,R}}\right)} \cdot 100$$

$$S_{MeOH}(\%) = \frac{\frac{C_{MeOH,R}}{C_{He,R}}}{\left(\frac{C_{CO_2,blk}}{C_{He,blk}} - \frac{C_{CO_2,R}}{C_{He,R}}\right)} \cdot 100$$

$$C_n \text{ Hydrocarbon Sel } (\%) = \frac{n \cdot (C_n)}{\sum n \cdot C_n} \times 100$$

$$\text{Product}_{C_1}\left(\text{mol } K_{gcat}^{-1} \text{ h}^{-1}\right) = \frac{\text{Yield } (C_1 + C_1^{=})/100 \cdot \text{GHSV}_{CO_2}}{22.4}$$

where Ci_{blk} and Ci_R are the concentrations determined by GC analysis in the blank and in the reactor outlet, respectively. Carbon balance closure was better than 2.5% in all cases.

2.2.5. XAS measurements on the combined ZrZn-*X*/ZSM-5 systems. Zn and Zr K-edge *operando* XAS experiments in transmission mode were performed at the Quick-XAS ROCK beamline[53] (Rocking Optics for Chemical Kinetics) of the French Synchrotron SOLEIL. A quasi-simultaneous scanning of Zr (17.7–19 keV) and Zn (9.3–10.7 keV) K-edges was possible thanks to the quick edge-jump feature of the ROCK beamline.[53] However, jumping between two absorption edges dictated to find a compromise between the sample thickness and the absorption length of both edges. Hard X-ray XAS allows monitoring with element-selectivity of the bulk properties of the combined systems and the ZrZn-*X*/zeolite interaction under *operando* conditions. For this purpose, around 5 mg of ZrZn-*X*: H-ZSM-5 = 1 : 1 physical mixture was mortar-grounded, sieved down to 40 μm and loaded in a quartz capillary reactor (ϕ = 1 mm). The capillary reactor was then connected to an appropriate gas-flow setup for the CO_2 hydrogenation reaction, supporting operation at high gas pressure. The temperature at the measurement position was controlled by a heat gun. The gas total flux was maintained constant (10 ml min^{-1}) during all the measurements. The measurement protocol for the three combined systems consisted of two main parts: 1. activation: heating (RT to 400 °C, 5 °C min^{-1}) at 1 bar in pure H_2 flow; 2. reaction: feed of CO_2 : H_2 : He = 1.25 : 7.5 : 1 (mL min^{-1}) at 300 °C (temperature showing the highest performance from the catalytic test) and 15 bar pressure.

Incident X-ray energy at both Zr and Zn K-edges was scanned by two quick-XAS monochromators, each mounted on a cam-driven tilt table that oscillates periodically around a fixed Bragg angle. A Si(111) monochromator was used to measure the Zn K-edge (9659 eV) while Si(220) was employed for the Zr K-edge (17 998 eV). Time-resolved data throughout the applied protocol were initially obtained as the average of 50 scans for an exposure time of 12.5 s and a total time/scan of 25 seconds. The reported XAS spectra representative of the as-prepared and activated catalysts, as well as of the catalysts under reaction conditions, are obtained upon further averaging of the time-resolved spectra obtained in the last 10 min of acquisition for each protocol step, after checking for the complete stabilization of the spectral features. Incident (I_0) and transmitted (I_1) beams were measured by two sets of ionization chambers. An energy step of 2 eV was used for the two edges. The energy sampling was intensified using a step of 0.2 eV in the main edge region for Zn (range: 9530–9780 eV) and of 0.4 eV for Zr (range: 17 970–18 120 eV). A third set of ionization chambers (I_2) was employed to measure simultaneously the transmitted intensity after Zr and Zn metal foils, for energy calibration purposes. Pure hexagonal ZnO and tetragonal ZrO_2 powders, used as reference compounds, were measured at the same beamline, in the form of self-supporting pellets with optimized mass for transmission XAS at Zn and Zr K-edge, respectively. For the sake of comparison, a reference monoclinic ZrO_2 was also measured in the form of an optimized self-supporting pellet at the BM23 beamline of the European Synchrotron Radiation Facility (ESRF).[54]

The Athena software from the Demeter package[55] was used to align in energy and normalize the XAS spectra to unity edge jump, as well as to extract the $\chi(k)$ EXAFS function and calculate its Fourier transform.

2.2.6. Transmission electron microscopy characterization. High-angle annular dark-field imaging (HAADF) in conjunction with energy-dispersive X-ray spectroscopy (EDXS) was carried out with a Cs-corrected Titan G^2 80-300 ST Mono (Thermo-Fisher Scientific). The microscope was equipped with a GIF Quantum (Gatan Inc.) and a Super-X EDXS detector (Thermo-Fisher Scientific). STEM-EDXS analysis was performed with an accelerating voltage of 300 kV, a beam current of 0.10 nA and a dwell time of ~1 second per picture with a total acquisition time of 10 minutes per elemental map. Acquisition and processing of the obtained data were performed with the Velox (Thermo-Fisher Scientific) software package. Dry sample preparation was used for all of the samples.

2.2.7. X-ray photoelectron spectroscopy (XPS) characterization. XPS studies were carried out using a Kratos Axis Ultra DLD spectrometer (Kratos Analytical Ltd) equipped with a monochromatic AlKα X-ray source ($h\nu$ = 1486.6 eV) operating at 150 W; acquisition of spectra was performed under ultra-high vacuum conditions (10^{-8}–10^{-9} mbar). Measurements were carried out in hybrid mode using electrostatic and magnetic lenses. The high-resolution spectra were collected at a fixed analyzer pass energy of 20 eV. Charge neutralization with low energy electrons was applied for all the samples. The spectrum line of C1s (284.8 eV for adventitious carbon) was used for binding energy correction. The Zn LMM Auger peak was used for zinc chemical state identification ($KE_{(Zn(0))}$ ~ 988 eV). Typically, powder samples were immobilized on Cu conductive tape (SPI supplies, Structure Probe, Inc.), placed on the sample holder and evacuated overnight until ultra-high vacuum was reached.

3. Results and discussion

3.1. Chemical, textural and structural characterization of the ZrZn-*X* catalysts

As for zirconium and zinc contents in the ZrZn-*X* samples determined by ICP-AES analysis, the approximate compositions were calculated as weight percentage of Zn and reported in Table 1 along with specific surface areas (SSA) and pore volumes. As already mentioned in the Experimental section, the samples were named ZrZn-*X*, where *X* is the Zn loading.

The SSAs of ZrZn-5 and ZrZn-15 are approximatively the same, whereas that of ZrZn-30 is about 20% lower. The adsorption/desorption isotherms[56,57] and the pore size distributions (PSDs) of the as-prepared ZrZn-*X* catalysts are displayed in the ESI,† Fig. S1 and S2,† respectively.

All the samples exhibit the hysteresis loop characteristic of mesoporous materials with similar PSDs with a maximum at about 3 nm. However, all these samples show a broad PSD

covering a wide range of pore widths from 3 to 12 nm. Moreover, the pore volumes are comparable for ZrZn-5 and ZrZn-15, whereas it is twice as high for ZrZn-30.

The PXRD patterns of the as-prepared ZrZn-*X* samples are reported in Fig. 1. Intensities were not rescaled but only offset-shifted. All the three samples show a diffraction pattern typical of crystalline zirconia, but the diffractograms of cubic and tetragonal ZrO_2 are not distinguishable between each other. However, XAS measurements discussed in the following (see section 3.5) evidenced features characteristic of tetragonal zirconia. Moreover, reflections of monoclinic ZrO_2 are absent, also at $2\theta < 20°$ as shown in Fig. S3.†

The inset in Fig. 1 underlines a shift to higher 2θ values of the (101) reflection with respect to a pure ZrO_2 reference. This shift was previously observed by Wang *et al.*[51] and explained considering a shrinking of the ZrO_2 unit cell when the largest Zr^{4+} (0.82 Å)[58] is substituted by Zn^{2+} (0.74 Å).

The peak shift trend is consistent with the Zn concentration found from ICP analysis (*i.e.*, the higher the Zn loading, the more pronounced the shift results). Moreover, comparison of the diffractograms highlights a peak broadening effect, slightly enhanced as the Zn loading increases. The three samples were measured with the same instrumental parameters and the background position was the same for the three diffractograms (Fig. S3†). Hence, we can safely verify that the amorphous fraction is the same. The crystallite size obtained from Rietveld refinement decreases as the loading of Zn increases.

However, the SSA value does not reflect this trend (Table 1). The SEM images of the catalysts (Fig. S17†) show that they consist of particles with small aggregated crystallites. Therefore, the area exposed is correlated to the dimensions of these aggregates rather than to the crystallite size.

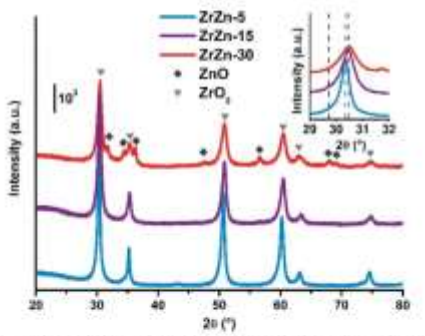

Fig. 1 PXRD patterns of the as-prepared ZrZn-*X* samples. Triangles and diamonds indicate respectively peak positions of cubic/tetragonal ZrO_2 and hexagonal ZnO. Inset: Magnification of the ZrO_2 (101) reflection with the peak position for a pure ZrO_2 (ref. 60) (dashed black line) compared to that observed for the ZrZn-*X* samples (dashed coloured lines).

Extra reflections are present only in sample ZrZn-30 (diamond symbols in Fig. 1). They are indexed considering an additional ZnO (ref. 59) wurtzite phase. The ZrO_2 : ZnO phase ratio was extracted by Rietveld refinement. Using hexagonal ZnO ($P6_3mc$) and tetragonal ZrO_2 ($P4_2/nmc$[60]) as input parameters, we found that ZrZn-30 is composed of 85 wt% of ZrO_2 and 15 wt% of ZnO (Table S1†). Consequently, part of Zn is not incorporated in the host lattice but is segregated as a second phase, justifying also why the (101) reflection for ZrZn-30 is very close to the one for ZrZn-15. Nonetheless, as evidenced by EXAFS results presented in section 3.5, a slightly higher amount of Zn is expected to enter the ZrO_2 lattice in ZrZn-30 with respect to ZrZn-15. With our co-precipitation technique, we could therefore achieve a maximum Zn doping of ZrO_2 of about 15 wt%. Finally, the decreased area and the increased pore volume observed for ZrZn-30 could be also correlated to the presence of segregated ZnO.

3.2. Spectroscopic characterization of the ZrZn-*X* catalysts

3.2.1. H_2 interaction with the oxidized samples at 400 °C. The activity of these catalysts in CO_2 hydrogenation can be related to the peculiar property of ZnO to form oxygen vacancies under reducing conditions.[17] Moreover, the presence of Zn in the ZrO_2 lattice can induce the formation of oxygen vacancies for the ZrZn-*X* catalysts. IR spectroscopy is suitable for revealing features characteristic of the presence of oxygen vacancies.

Fig. S4† compares the spectra recorded in oxygen and in hydrogen at 400 °C for the three catalysts. For all the samples under both conditions, absorption bands in the regions 4000–3000 cm^{-1}, 2500–2000 cm^{-1} and 1700–1000 cm^{-1} are present. These bands are related to surface hydroxyls, CO_2 encapsulated in closed pores and carbonate/nitrate species, respectively. Encapsulated CO_2 and carbonates/nitrates stem directly from the precursors used for the synthesis. More detailed discussion about these species is reported in the ESI.†

Focusing on the effect of the interaction with H_2, in Fig. S4† an increase of the sample absorbance in a large spectroscopic region passing from oxygen to hydrogen is evident, in particular for ZrZn-15 and ZrZn-30. This is due to the increase of a very broad absorption band, whose shape is discernable by subtracting the spectrum recorded in oxygen from the spectrum recorded in hydrogen. The result of this subtraction for the different samples is reported in Fig. 2. The very broad bands evidenced by the grey dotted lines are related to the photo-ionization of mono-ionized oxygen vacancies.[61–63] On these electronic absorption bands, negative vibrational peaks that complicate the shape of the spectra are superimposed.

Before discussing the origin of the negative peaks, we focus on the broad electronic absorption. It is well known that ZnO is a semiconducting material due to the presence of lattice defects, *i.e.* oxygen vacancies (V_O).[61,62] The two

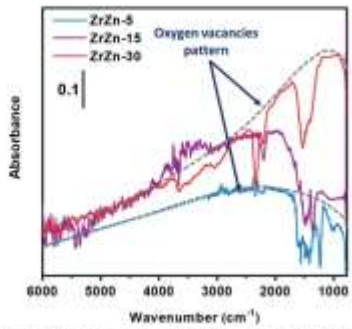

Fig. 2 FT-IR difference spectra of ZrZn-*X* catalysts at 400 °C in H_2 (subtrahend spectrum is that recorded in oxygen at 400 °C). The ZrZn-5 spectrum is cut at 3155 cm^{-1} because, beyond that frequency, data are affected by the low signal-to-noise ratio; the cut part has been substituted with a dotted blue line, which aims to reproduce the trend.

electronic levels at 0.05 and 0.18 eV below the conduction band (C.B.) are associated with the V_O of ZnO. Neutral vacancies show two trapped electrons that occupy the above-mentioned levels. The first ionization energy is so low that the major part of V_O are mono-ionized ($V_O^{\cdot}$), being the excited electrons in the C.B. The second ionization of V_O can be promoted by IR radiation (photo-ionization of mono-ionized oxygen vacancies): in the spectrum of pure ZnO, a broad absorption band appears centered at the energy corresponding to 0.18 eV, *i.e.* at about 1450 cm^{-1}, after reduction treatments. Interaction with hydrogen can create $V_O^{\cdot}$ following two routes: i) the filling with an electron of the pre-existing bi-ionized V_O ($V_O^{2\cdot}$) by consuming adsorbed oxygen species, such as O_2^-, O^-, and O_2^{2-}; ii) the creation of new $V_O^{\cdot}$ extracting lattice oxygen ions from the surface. This last pathway occurs only at high temperature, with the temperature threshold depending on the specific material. The IR technique is not able to distinguish the two routes to $V_O^{\cdot}$ formation.

Concerning our case, the $V_O^{\cdot}$ absorption bands reported in Fig. 2 for ZrZn-30 and ZrZn-5 show a maximum centered at about 1100 and 2200 cm^{-1}, respectively, which can be associated with mono-ionized oxygen vacancies at 0.14 and 0.27 eV under the C.B.[63–64] This result evidences the influence of the different Zn loadings on the associated energy level of the mono-ionized oxygen vacancies with respect to the C.B. In particular, ZrZn-30 shows a $V_O^{\cdot}$ ionization energy (0.14 eV) very close to that of pure ZnO (0.18 eV), being the sample with the highest Zn content in the ZrO_2 lattice, as evidenced by the EXAFS results presented in section 3.5.

We cannot exclude that the presence of a segregated ZnO extra-phase, as shown by PXRD (Fig. 1), could also slightly influence the position of the oxygen vacancy band. As for ZrZn-5, the $V_O^{\cdot}$ ionization energy (0.27 eV) is higher than that of pure ZnO: the effect of the ZrO_2 lattice and the low amount of Zn induce the formation of $V_O^{\cdot}$ with electronic levels deeper in the band gap.

The identification of the correct position of the maximum absorption related to $V_O^{\cdot}$ for ZrZn-15 is complicated by the superimposed, above mentioned "negative vibrational peaks". These peaks are well visible for all the samples, but only for ZrZn-15 their presence hamper the identification of the actual shape of the $V_O^{\cdot}$ absorption. The negative peaks are related to the vibrational modes of encapsulated CO_2 and carbonate/nitrate species and they arose from the subtraction operation, since these vibrational bands show lower intensity in hydrogen than in oxygen. It is important to underline that their intensities return to the original ones when the samples were exposed to oxygen after interaction with hydrogen. So, carbonates/nitrates and, even more reasonably, encapsulated CO_2 are not partially removed from the samples by the interaction with H_2, but their intensity loss has another origin. In particular, it is possible to consider a coupling process occurring between the electronic absorption of $V_O^{\cdot}$ and the surface species vibrations. Genzel and Martin,[64] using a continuum model made up of a phonon term and a free electron term, provided an explanation for a similar phenomenon when plasmon absorptions occurred in small particles of conducting and semiconducting materials. When the concentration of the free carriers is high enough to cause the plasmon frequency to overcome the phonon frequency, a plasmon–phonon coupling process occurs leading to the decrease/disappearance of any band of a purely vibrational nature. In our case, the coupling process occurs between vibrational modes of surface species and IR absorption of electrons trapped in mono-ionized oxygen vacancies, as already observed and reported in the literature for semiconducting oxides, such as SnO_2, ZnO, WO_3, and MoO_3.[65,66]

As for the intensity of the electronic band, ZrZn-30 and ZrZn-15 show a significant absorption related to $V_O^{\cdot}$, whereas ZrZn-5 does not, due to the different amount of $V_O^{\cdot}$ generated. As demonstrated by quantitative analysis, the Zn loading decreases in the order: ZrZn-30 > ZrZn-15 > ZrZn-5, so that the infrared absorption shown in Fig. 2 is in line with the chemical composition and with the Zn content in the ZrO_2 lattice shown by PXRD and EXAFS results. These results are corroborated by modelling calculations (see section 3.3). Moreover, the highest amount of $V_O^{\cdot}$ observed for ZrZn-30 can be correlated to the best catalytic performances of this catalyst among all the samples (see section 3.4). Finally, these IR results highlight the importance of pre-reducing the samples before the catalytic run in order to create a high concentration of reactive oxygen vacancies.

3.2.2. CO adsorption at LNT. CO dosage was performed at liquid-nitrogen temperature (LNT) because of its weak adsorption on Zr^{4+} and Zn^{2+} cations. Fig. 3 reports the spectra collected at increasing CO coverage (θ_{CO}) on oxidized and reduced ZrZn-*X* catalysts.

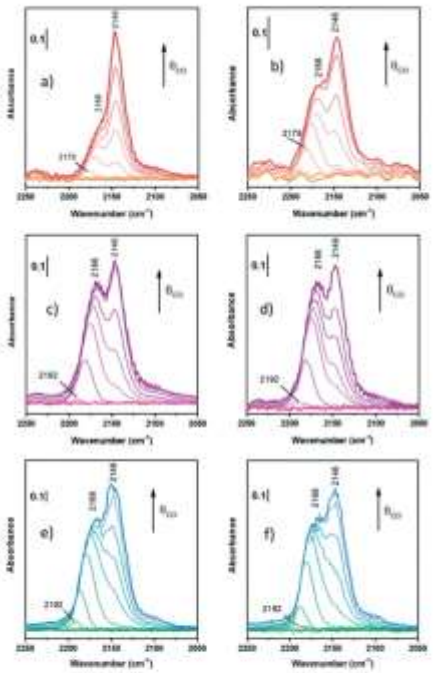

Fig. 3 FT-IR spectra of CO adsorption at LNT on oxidized ZrZn-30 (a), ZrZn-15 (c), and ZrZn-5 (e) and reduced ZrZn-30 (b), ZrZn-15 (d), and ZrZn-5 (f) at increasing doses up to 20 mbar.

Starting from the oxidized samples (Fig. 3a, c and e), two main peaks are highlighted between 2200 and 2100 cm^{-1}. The first peak at 2166 cm^{-1} can be related to coordinatively unsaturated Zr^{4+} carbonyls[67] (*cus*-Zr^{4+}–CO), *i.e.* Zr atoms located on edges or steps. Zr^{4+} carbonyls on regular facets should show absorption bands between 2148 and 2142 cm^{-1}.[67] However, when CO is adsorbed on metal cations with a dominant σ-donation, the higher the unsaturation of the adsorption site, the higher the ν(C≡O). In particular, Zr^{4+} is a $4d^0$ cation, thus it lacks π-backdonation and σ-bonding is the only contribution to the bond with CO.

The peak related to *cus*-Zr^{4+}–CO also features a red-shift from 2179–2192 cm^{-1} (according to the sample) to 2166 cm^{-1}. Different explanations can be proposed for the frequency shift *vs.* θ_{CO}, but the most observed are usually four: i) "through space" dipole–dipole interaction between parallel vibrating molecules;[68] ii) "through solid" *via* the vibrational coupling mechanism across binding electrons;[69] iii) the "*chemical effect*", another "through solid" phenomenon due to adsorbed molecules;[66,70] and iv) the "electrostatic" or "solvent" effect caused by adsorbed molecules perturbing each other.[71] The first and the second effect are dynamic, whereas the third and the fourth ones are static. Typically, among dynamic effects, the second one is negligible when adsorption is characterized by small adsorption enthalpy, or in general when ν(C≡O) is very close to that of free CO (2143 cm^{-1}). Among the static effects, the fourth one is often small or negligible[72] and it usually appears at higher pressures or for densely packed CO, where it assumes a solvent-like behavior, hence not in this case, since we observed this effect at low pressures.

Among the remaining effects, in our case we can exclude the dipole–dipole coupling since it is the dominant factor for CO adsorbed on sites on extended regular facets (dipolar coupling occurs between "equal" oscillators, *i.e.* CO molecules, and defects interrupt dipole–dipole coupling) and it causes in all cases a blue-shift on increasing coverage. Hence, the observed red-shift is due to the "*chemical effect*", as a result of the reduction of CO σ-donation on increasing coverage. As a matter of fact, for metal cations with dominant σ-donation, the higher the θ_{CO}, the higher the electron density on the binding sites. As a consequence, on increasing coverage the σ-donation contribution of all adsorbed CO molecules becomes smaller and smaller and thereby a decrease of ν(C≡O) is observed.[73]

The second peak at 2146 cm^{-1} is assigned to CO adsorbed on Zr^{4+} with a lower coordinative unsaturation.[67,74] This band does not show any shift on increasing CO coverage: this is reasonably due to the compensation between the dipole–dipole coupling effect (blue shift) and the chemical one (red-shift). As a consequence, the peak remains stationary and this observation confirms its assignment to CO on Zr^{4+} sites of regular facets.

Differently from Zr^{4+} sites, Zn^{2+} sites are not visible. Zinc is in a lower amount and, reasonably, its carbonyl band can be totally hidden by Zr^{4+}–CO bands. Indeed, according to some authors,[74,75] Zn^{2+}–CO is characterized by peaks between 2190 and 2160 cm^{-1}, where the absorption frequency changes according to the chemical environment. For the sake of clarity, it is possible that all peaks at 2192 (Fig. 3c and e) and 2179 cm^{-1} (Fig. 3a) observed as first peaks during CO adsorption can be associated with Zn^{2+}–CO, but there is neither evidence nor references to prove it in systems like the ZrZn-*X* samples studied in this work.

On the reduced samples (Fig. 3b, d and f), all peaks can be assigned as reported for the oxidized ones.

Nevertheless, comparing the spectra of all the samples, normalized for the specific surface area and pellet thickness, many features are evident (Fig. 4). First of all, for the oxidized samples, the markedly lower intensity of the band at 2166 cm^{-1}, related to coordinatively unsaturated Zr^{4+}, is well evident for ZrZn-30 with respect to the other samples. The lower amount of defect sites for ZrZn-30 can be related to the BET results: the lower surface area of this sample with respect to ZrZn-5 and ZrZn-15 is reasonably reflected in a minor amount of *cus*-Zr^{4+} sites. Moreover, by comparing the

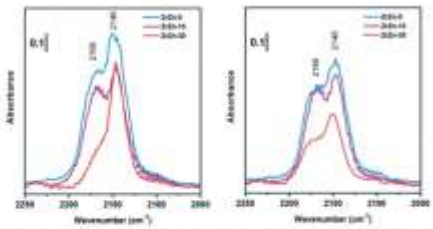

Fig. 4 Comparison between FT-IR spectra collected at the highest CO coverage for oxidized (left) and reduced (right) ZrZn-*X* catalysts.

total integrated intensity of the bands in the region 2200–2100 cm^{-1}, it decreases in the order: ZrZn-5 > ZrZn-15 > ZrZn-30. This is in agreement with the chemical analysis and the EXAFS results (*vide infra*) on the Zn content in the ZrO_2 lattice: on increasing the Zn loading, the amount of surface Zr^{0} sites decreases.

After reduction, there is not a significant variation in spectra except for ν(C≡O) at 2166 cm^{-1} on ZrZn-30. Comparing CO adsorption on oxidized and reduced ZrZn-30, the intensity of the band at 2166 cm^{-1} appears significantly increased after reduction. This phenomenon can be ascribed to oxygen vacancy formation: after reduction at 400 °C in H_2 the presence of oxygen vacancies is responsible for an increased surface disorder, which causes a growth of *cus*-Zr^{4+} concentration (2166 cm^{-1}) and thereby a correlated reduction in the amount of Zr^{4+} on facets (2146 cm^{-1}).

3.3. Molecular modelling of the ZrZn-*X* catalysts

We performed DFT calculations to characterize the catalyst structure and the involved reaction mechanism for CO_2 hydrogenation on a $ZnZrO_y$ solid solution. For the sake of simplicity, we model the system as a five layered ZrO_2 slab presenting variable ZnO–ZrO_2 composition on the surface. Beginning with a tetragonal unit cell of ZrO_2, we constructed low index facets (100), (101), and (111). The surface energies of the slabs were computed as $\gamma = \frac{\Delta E[\text{surface}]}{2A}$, with ΔE[surface] defined in eqn (5):

$$\Delta E[\text{surface}] = E[\text{slab}] - N_{ZrO_2} \times E[\text{bulk}] \quad (5)$$

where E[slab] is the DFT calculated energy of the whole slab, E[unit] is the energy per formula unit of bulk ZrO_2, N_{ZrO_2} is the number of ZrO_2 formula units in the slab, and A is the area of the slab surface.

According to calculations, the (101) surface has the lowest surface energy, 0.1 J m^{-2}, followed by the (100) and (111) surfaces, 0.7 and 2.8 J m^{-2} (see Fig. S5†). We thus focused on the (101) surface to investigate the formation energy of O vacancies in the presence of H_2, as thermal O vacancies are highly unlikely on ZrO_2, on $ZnZrO_y$ solid solutions using eqn (6):

$$E[\text{vac}] = E[\text{pristine}] - E[\text{system with O vacancy}] + E_{H_2O} - E_{H_2} \quad (6)$$

where E[pristine], E[system with O vacancy], E_{H_2O} and E_{H_2} are the DFT calculated energies of the pristine slab, the slab with oxygen vacancies, and isolated water and hydrogen molecules, respectively.

Using eqn (6), we first calculated the energy required to form an O vacancy on a pristine ZrO_2 (101) surface, 3.28 eV. In line with earlier reports,[76,77] this indicates that no O vacancy can be expected at thermodynamic equilibrium on the pristine (101) facets of ZrO_2 under the reactivity conditions used in this work. To include the effect of Zn doping, we replaced one ZrO_2 unit on the surface with one ZnO unit and a "stoichiometric" O vacancy, which is a vacancy introduced to balance the charge difference created by replacing one Zr^{4+} with one Zn^{2+} in the lattice. To quantify the formation energy of stoichiometric O vacancies, we computed the substitution energy of ZrO_2 units by ZnO units, E[sub], using eqn (7):

$$E[\text{sub}] = E_{\text{slab}}[x\text{ZnO}/\text{ZrO}_2] - E_{\text{slab}}[\text{ZrO}_2] - xE_{\text{bulk}}[\text{ZnO}] + \frac{1}{2}E_{O_2} \quad (7)$$

where x is the number of Zn atoms doped on the surface, and $E_{\text{slab}}[x\text{ZnO}/\text{ZrO}_2]$, $E_{\text{slab}}[\text{ZrO}_2]$, $E_{\text{bulk}}[\text{ZnO}]$ and E_{O_2} are the DFT calculated energies of a ZrO_2 (101) slab doped with x ZnO units, a pristine ZrO_2 (101) slab, a bulk ZnO unit, and an isolated oxygen molecule, respectively. Once a ZnO doped surface with a stoichiometric number of O vacancies is generated, the formation energy of additional O vacancies,

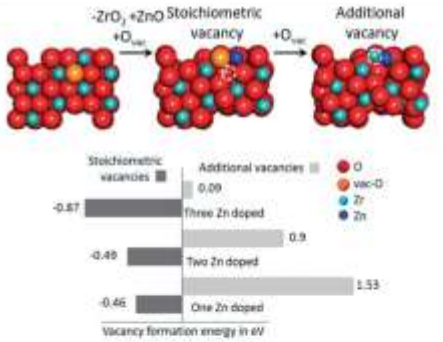

Fig. 5 The O vacancy formation energy trend with increasing number of Zn atoms on the surface of ZrO_2 (101). The schematic illustrates the way "stoichiometric" and additional vacancies are modeled. The red, blue and dark blue colors represent oxygen, zirconium and zinc atoms, respectively. The orange atom and dashed circle show the O atom to be removed and the O vacancy formed, respectively.

with the assistance of H_2, can be calculated using an approach similar to that of eqn (6).

Fig. 5 summarizes the formation energies of stoichiometric and additional O vacancies for x ranging from 1 to 3. Considering that the ZrO_2 supercell we used has 8 Zr atoms, the doping we considered corresponds to 12.5, 25.0 and 37.5% Zn atoms on the surface. Calculations indicate that substitution of a single ZrO_2 unit by ZnO, with creation of a vacancy, is thermodynamically favored by −0.46 eV, a value that reduces slightly to −0.29 eV per ZnO unit and −0.87 eV when 3 ZrO_2 units are replaced with 3 ZnO. This indicates that ZrO_2 can tolerate high amounts of Zn substitution at the surface. As for the formation of O vacancies, in addition to the stoichiometric ones, our calculations indicate that the system with just one Zn doped on the surface is not prone to further O vacancy formation, with an E[vac] = 1.53 eV, although this value is remarkably lower than that calculated on a pristine ZrO_2 surface, 3.28 eV. However, the chances of formation of additional O vacancies increase with increasing number of Zn atoms on the surface, with an E[vac] ~ 0.9 eV only, when 3 out of the 8 ZrO_2 units on the surface are replaced with ZnO. Overall, this is in qualitative agreement with the experimental evidence that increasing amounts of O vacancies are experimentally observed at increasing Zn content.

To investigate the catalytic behavior, we used the model composed of one ZnO unit replacing a surface ZrO_2 unit, with generation of a stoichiometric O vacancy. We first calculated CO_2 adsorption on the O vacancy near the Zn atom, which resulted in an adsorption energy of −0.50 eV. Dissociation of the adsorbed CO_2 molecule with release of a CO molecule is thermodynamically unfavored by 0.71 eV, indicating that these surface O vacancies cannot be CO_2 traps generating CO (Fig. S6†).

We were not able to locate any other energetically favored CO_2 adsorption geometry. Adsorption of molecular hydrogen occurs at the Zn atom, with an adsorption energy of −0.20 eV. However, dissociation of molecular hydrogen into 2H* is favored, with an energy gain of 0.39 eV. The dissociated hydrogen is present as $H^{\delta+}$ and $H^{\delta-}$ species on the O and Zn sites, respectively. Simultaneous adsorption of CO_2 and 2H* is favored by −0.73 eV, which is slightly less than the sum of the adsorption energies of isolated CO_2 and 2H*, −1.09 eV. The completely optimized geometries of the Zn-doped ZrO_2 (101) with CO_2, H_2, 2H* and CO_2 + 2H* are shown in Fig. S7.†

Possible thermodynamic profiles for the conversion of adsorbed CO_2 and dissociated H_2 on the ZnO/ZrO_2 surface are reported in Fig. 6. Considering that the formate and CO pathways have been proposed to be involved in methanol formation,[17] we evaluated the free energies of the most important intermediates involved in the two pathways. The starting point is CO_2 adsorbed on the O vacancy near the Zn site, and dissociated H_2 adsorbed on the Zn site and on a nearby O atom.

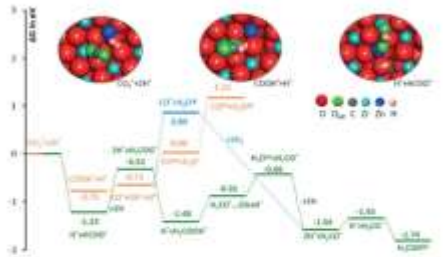

Fig. 6 Free energy diagram for comparing the intermediates involved in CO_2 hydrogenation to methanol via the formate and CO pathway. The three insets represent the completely optimized structures of reactants and intermediates with HCOO* and COOH*, respectively. The red, grey, pink, blue, green and dark blue colors represent oxygen, carbon, hydrogen, zirconium, O atom of the adsorbate and zinc atoms, respectively.

The first possibility we examined is the transfer of the H* on Zn to the C atom of *CO_2 along the formate pathway, leading to formation of HCOO* through a highly exergonic step, by −1.23 eV. Subsequent hydrogenation of HCOO* leads first to an adsorbed formaldehyde molecule with liberation of a water molecule, H_2CO^* + H_2O(gas), and finally to adsorbed methoxide, CH_3O^*. All intermediates along the formate pathway are at free energies below the starting CO† + 2H* species, and the overall energy span between the

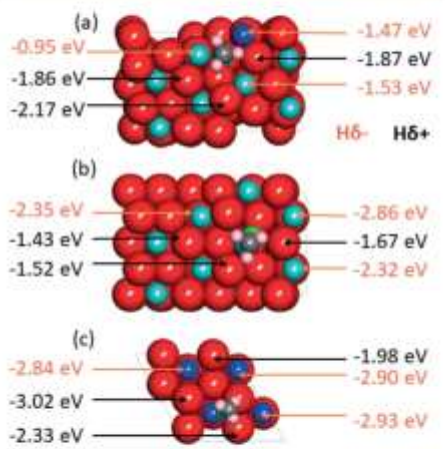

Fig. 7 A top view of the space filling atom model, with adsorbed CH_3O^*, of (a) Zn doped ZrO_2 (101), (b) ZrO_2 (101), and (c) ZnO (111) surface comparing the adsorption energies of $H^{\delta+}$ and $H^{\delta-}$ species. The red, grey, pink, blue, green and dark blue colors represent oxygen, carbon, hydrogen, zirconium, O atom of the adsorbate and zinc atoms, respectively.

highest and the lowest energy intermediates is smaller than 1.22 eV, indicating a viable reaction pathway under the reaction conditions used in this work. The second possibility we examined is reactivity along the carbon monoxide pathway, which starts with conversion of CO_2^* to CO*, followed by its hydrogenation to form methanol.[31] As shown in Fig. 7, the first intermediate along this pathway, COOH*, at −0.75 eV, is less stable than the first intermediate along the formate pathway, HCOO*, resting at −1.23 eV.

Evolution of this intermediate to CO* + H_2O* first, followed by CO dissociation to CO(gas) + H_2O*, is an endergonic sequence, with CO(gas) + H_2O* above the starting CO_2^* + 2H• species. Similarly, H_2O dissociation leaving CO*, from which hydrogenation to CH_3O* can occur, is even more expensive, with CO* + H_2O(gas) at 0.89 eV above the starting CO_2^* + 2H* species.

Furthermore, all intermediates involved in dissociation of CO_2 to CO are less stable than the intermediates formed by subsequent hydrogenation of formate species. This is consistent with the experimental CH_3OH selectivity (*vide infra*) and it suggests that the formate reaction pathway is operative.

Having clarified the pathway leading to CH_3O*, we investigate methanol *versus* methane selectivity, which has been shown to depend on a competition between the transfer of a $H^{\delta+}$ to the O atom of CH_3O*, liberating methanol, and the transfer of a $H^{\delta-}$ species to the C atom of CH_3O*, dissociating the C–O bond and liberating methane.[78,79] To shed light on this point, we explored the relative stabilities of $H^{\delta+}$ and $H^{\delta-}$ species on Zn doped ZrO_2, and pristine ZrO_2 and ZnO (Fig. 7). According to calculations, in the presence of CH_3O* on Zn doped ZrO_2, $H^{\delta+}$ species have stronger binding energies compared to $H^{\delta-}$ species, which can explain the catalyst selectivity towards methanol production.[78] On the other hand, on pristine ZrO_2 (101) and ZnO (111), $H^{\delta-}$ species have stronger binding energies than $H^{\delta+}$ species, which should imply that Zn doped ZrO_2 has better selectivity towards methanol formation than both its pristine counterparts.

3.4. Catalytic tests on the ZrZn-*X* catalysts and the combined ZrZn-*X*/zeolite systems

We first studied the stand-alone ZrZn-*X* catalysts with different Zn-loadings (ZrZn-5, ZrZn-15 and ZrZn-30) in the CO_2 conversion to methanol (MeOH), the initial step in the CO_2 'cascade' conversion over the bifunctional catalysts. In particular, we screened the effect of reaction pressure (20, 30 and 40 bar), temperature (250 °C, 300 °C and 350 °C) and CO addition (10% in the feed), as this gas is likely to be recycled with the unreacted CO_2 and H_2 in a perspective process.[80,81] The results are summarized in Fig. 8.

We can observe that increasing the pressure results in higher conversion and methanol selectivity for the three catalysts, in good agreement with the process thermodynamics.[79,82] The main byproduct in all cases is CO

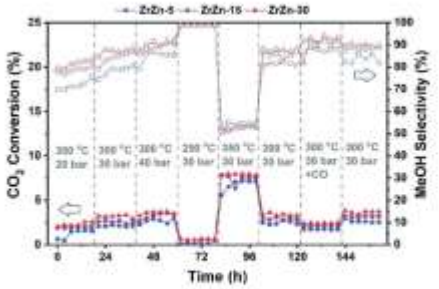

Fig. 8 Catalytic performance of all ZrZn-*X* stand-alone samples for the CO_2 conversion to MeOH. CO_2 : H_2 1 : 3, 12 000 mL h^{-1} g^{-1}.

with small traces of CH_4 (selectivity <1%) being as well detected. Similarly, decreasing the temperature increases the methanol selectivity to almost 100% with the CO_2 conversion being drastically reduced. On the other hand, increasing the temperature to 350 °C significantly increases the conversion with the MeOH selectivity being reduced to *ca.* 50%. CO addition slightly increases MeOH selectivity, again in line with previous observations.[82] Interestingly, despite the multiple conditions tested, no deactivation was observed for any of the samples after more than 150 hours under reaction conditions. From the reported results, ZrZn-30 appears as the optimal catalyst composition, displaying the highest activity and selectivity regardless of the reaction conditions. We attribute this superior performance of the ZrZn-30 sample to the already discussed higher amount of oxygen vacancies in the sample.[17,83]

Afterwards, we studied the combination of ZrZn-*X* catalysts with the two most common zeolites for the CO_2 cascade conversion:[84,85] ZSM-5 and H-SAPO-34. Similar to the above tests, we evaluated the effect of reaction pressure,

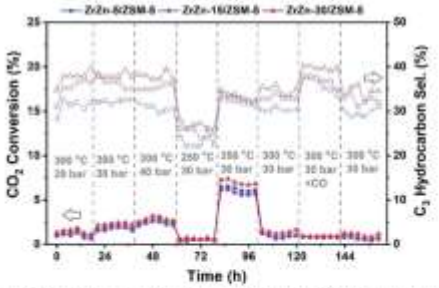

Fig. 9 Catalytic performance of the combined ZrZn-*X*/ZSM-5 systems for CO_2 conversion to hydrocarbons. CO_2 : H_2 1 : 3, 12 000 mL h^{-1} g^{-1}. Please note that the secondary *Y* axis refers to the C_1 selectivity among hydrocarbons (CO free).

temperature and CO addition. The results are summarized in Fig. 9 for ZSM-5 and in Fig. S8† for H-SAPO-34. We can observe that the CO_2 conversion for these bifunctional catalysts goes in line with the one observed for the stand-alone ZrZn-*X* samples, increasing with both pressure and temperature. Similar conversion values and CO selectivity are also obtained regardless of the reaction conditions or zeolite component (see Fig. S9† for a detailed comparison). However, when looking at the hydrocarbon distribution, we can observe that the zeolite component plays a critical role. In particular, the H-SAPO-34 based catalyst displayed a higher C_3 selectivity among hydrocarbons (up to 60%) but it is rapidly deactivated, especially at 350 °C where it lost almost all activity in less than 20 hours and unreacted methanol became the main reaction product (see Fig. S8 and S9†). Moreover, it seems that an operation temperature of 250 °C is too low for MeOH conversion to occur in H-SAPO-34.[87,88] This catalytic behavior is consistent with the fast deactivation and higher selectivity observed for H-SAPO-34 in the MTH reaction.[87,88] On the other hand, the ZSM-5 based catalyst displayed a more stable performance, with a C_3 selectivity of *ca.* 40%. However, we need to point out that a slight deactivation is also observed at 350 °C for the ZSM-5 based catalysts. Finally, CO addition seems to slightly enhance the C_3 selectivity, in line with the recent results by Tan *et al.*[89] who observed an increase in the hydrocarbon selectivity by CO co-feeding. Altogether, we can consider the ZrZn-30/ZSM-5 combined system, tested at 350 °C and 30 bar, as the most promising candidate/reaction conditions, displaying the highest conversion and stability with a C_3 selectivity close to 35% among hydrocarbons.

Further catalyst studies were performed under these optimal reaction conditions (350 °C, 30 bar), using two other ZSM-5 samples with Si/Al = 25 and 360 (ESI,† section 5.3). When testing the ZrZn-30 catalyst alone, methanol and CO were the only carbon-containing products (Fig. S10†). Product selectivity favored methanol at the shortest contact times, suggesting that the rate of CO_2 conversion to methanol (eqn (2)) is faster than the reverse water gas shift reaction (eqn (1)), in agreement with the results of the computational study (section 3.3). The methanol yield reached equilibrium after 0.4 s g^{-1} ml^{-1} contact time. The CO_2 conversion and hence, CO selectivity increased with a further increase in contact time. Due to water formed in the reverse water gas shift reaction, the methanol equilibrium yield decreased with increasing contact time.

When mixing ZrZn-30 with the two H-ZSM-5 catalysts in a 1 : 1 ratio, a range of hydrocarbon products, as well as dimethyl ether (DME) were observed, in addition to CO and methanol (Fig. S11†). The methanol yield was low, substantially below equilibrium, and decreased with increasing acid site density in H-ZSM-5. This result suggests that CO_2 hydrogenation to methanol is the rate-limiting step of hydrocarbon formation in the bifunctional ZrZn-30 : H-ZSM-5 = 1 : 1 mixed catalysts.

Considering next CO_2 conversion *versus* contact time, it did not change significantly with the addition of H-ZSM-5, as already observed in Fig. 8 and 9. However, the CO selectivity decreased with the addition of H-ZSM-5, and decreased further with an increase in the acid site density of H-ZSM-5 (Fig. S12†). This result may suggest that CO, like the hydrocarbons, is a (competing) secondary product from methanol, or that CO, like methanol, is converted to hydrocarbons over H-ZSM-5. The recent literature suggests that both hypotheses are plausible.[90,91]

Surprisingly, when considering next the hydrocarbon distribution over mixed catalysts, the aromatics selectivity is typically below 10% and only at 6000 ml h^{-1} g^{-1} is a significant fraction observed for the main ZSM-5 catalyst tested here (Fig. 10).

We attribute these results to the high space time employed in this work that suppresses the aromatization cycle, in line with the results by Cui *et al.* who observed an increase of aromatics selectivity from *ca.* 20% to 75% by reducing the space time by one order of magnitude.[92] These results are supported by testing other ZSM-5 catalysts mixed with ZrZn-30 (section S5.3). A higher acid site density in H-ZSM-5 led to more saturated aliphatic products, and less aromatic products, compared to a lower acid site density (Fig. S13 and S14†). These results suggest an intricate, joint behavior of the two catalyst functions that warrants further investigations in future contributions.

Additionally, if we look in detail at the CO free hydrocarbon distribution (Table S4† and Fig. 11), we can observe that, apart from the above-mentioned aromatics influence, the space time also affects the olefin/paraffin ratio. At high space times, paraffins are the predominant fraction, while at lower space times the olefins start to increase. These trends can be counter-intuitive and the opposite trend should be expected since olefins are the primary products of the HC pool reaction and the thermodynamic equilibrium of alkane

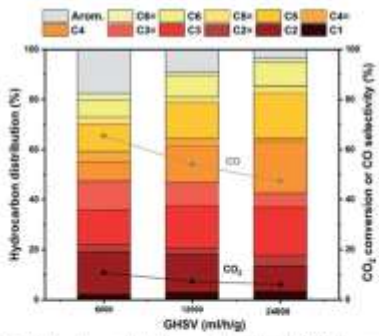

Fig. 10 Hydrocarbon distribution of the ZrZn-30/ZSM-5 combined system for CO_2 conversion to hydrocarbons at different space times. CO_2 : H_2 1 : 3, 350 °C, 30 bar.

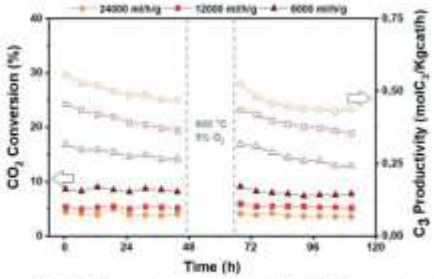

Fig. 11 Catalytic performance of the ZrZn-30/ZSM-5 combined system before and after regeneration for CO_2 conversion to hydrocarbons at different space times. CO_2 : H_2 1 : 3, 350 °C, 30 bar.

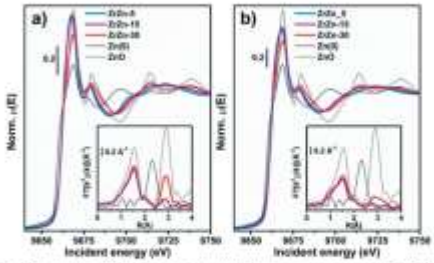

Fig. 12 K-edge XANES (main panel) and phase-uncorrected FT-EXAFS (bottom inset) spectra of the three samples and of Zn metal and ZnO model compounds, collected at (a) RT under He flux and (b) after the activation process (400 °C, H_2). The EXAFS spectra reported in the bottom insets have been obtained transforming the corresponding $k^2\chi(k)$ EXAFS function in the 2.5–13.0 $Å^{-1}$ range.

dehydrogenation reactions lies far to the alkane side for C_2 and C_3. However, if we look in detail at the reaction kinetics over ZSM-5,[93,94] we can observe that at very high space times (like the ones in our study) the slope of olefin increase is higher than the ones for paraffins plus C_{5+} hydrocarbons, therefore in line with our experimental observations. Last but not least, the productivities displayed here are among the highest reported for state-of-the-art catalysts[84] despite the low conversion, probably owing to the high space times employed in our study and the associated absence of aromatics.

Finally, since deactivation can play a role especially in view of industrial implementation of the investigated bifunctional catalysts, we studied the effect of *in situ* regeneration at 600 °C with a 5% O_2 in N_2 stream for the ZrZn-30/ZSM-5 combined system at different space times. The results are summarized in Fig. 11. We can observe that the *in situ* regeneration worked for all the samples and the initial activity was regained after the regeneration cycle at 600 °C. Moreover, increasing the space time drastically increases the C_3 productivity despite the CO_2 conversion decrease, achieving a maximum of 1.5 mol kg^{-1} h^{-1} at 24 000 ml h^{-1} g^{-1}.

3.5. XAS measurements on the combined ZrZn-*X*/ZSM-5 systems

Focusing on ZrZn-*X*/ZSM-5 combined systems, we finally applied *in situ* and *operando* XAS to monitor the average electronic properties and local structure of Zr and Zn metal centres, in the presence of the zeolite functionality and under realistic activation and process conditions. This becomes especially relevant, in view of recent findings highlighting inter-phase ion exchange phenomena in combined systems obtained by physically mixing acid zeolites and Zn-containing hydrogenation catalysts.[10] To obtain fully comparable information at Zr and Zn K-edges, we measured the two absorption edges quasi-simultaneously during the same experiment, exploiting the unique capability of the ROCK beamline[53] of the SOLEIL synchrotron (see section 2.2.5 for details).

Considering the Zn K-edge XAS spectra in Fig. 12a, we observe how the as-prepared samples exclusively contain Zn^{2+} species. Indeed, the edge energy position is substantially equivalent for the three ZrZn-*X*/ZSM-5 combined systems and overlapped with that of the ZnO model compound. Notably, ZrZn-30/ZSM-5 shows an overall XANES line-shape and specific post-edge features characteristic of ZnO (*e.g.* peaks at 9714 and 9738 eV), which are instead not detected in the other samples. This is explained considering the presence of the ZnO extra phase unveiled by PXRD in the ZrZn-30 catalyst. The inset of Fig. 12a shows the FT-EXAFS spectra of the two combined systems featuring the higher Zn-loadings, whereas for the lowest-loading ZrZn-5/ZSM-5 system, the low S/N ratio in the EXAFS region unfortunately prevented a reliable data interpretation. Both the samples show a very similar first coordination shell peak stemming from O nearest neighbours (NNs). The first-shell peaks are comparable with that of the reference ZnO in terms of the *R*-space position, while they display slightly lower intensity, consistent with distortions in the local coordination environment of substitutional Zn ions in the ZrO_2 lattice. The two samples show more pronounced differences in the second-shell region of the EXAFS spectra. In particular, for ZrZn-30/ZSM-5 we recognize a well-defined peak matching the position of the second-shell feature in ZnO, arising from Zn next nearest neighbour (NNN) atoms. The lower peak intensity with respect to what is observed for the model compound can be connected with the simultaneous presence of substitutional Zn ions in the ZrO_2 lattice, as well as with possible defectiveness of the segregated ZnO particles. Conversely, only a broad and much weaker peak is observed for ZrZn-15/ZSM-5 in the second-shell region, pointing to rather high structural disorder in the NNN distribution for substitutional Zn ions in ZrO_2.

During activation (Fig. 12b) the Zn K-edge XANES features are substantially unchanged, underpinning two important facts: i) the average oxidation state of Zn does not change (no edge-shift is observed nor any evidence for the formation of Zn^0 phases) and ii) Zn^{2+} does not diffuse in the zeolite (typical spectral features of Zn-exchanged zeolites[85] are not observed). Considering the corresponding FT-EXAFS spectra (Fig. 12b, inset), the first-shell peak undergoes a slight intensity decrease, consistent with the increased thermal contribution to Debye–Waller factors at 400 °C. The second shell peaks, connected with NNN contributions, appear more strongly affected. The two samples maintain the same intensity trend as in their as-prepared state, with ZrZn-30/ZSM-5 showing the highest intensity; however, in both cases an important dampening/broadening effect is observed. Also in this case, increased Debye–Waller factors at 400 °C contribute to EXAFS signal dampening. However, it is clear that activation also triggered an increase in the local disorder around Zn^{2+} sites – both those hosted in the ZrO_2 lattice and those segregated as ZnO extra-phases, in agreement with IR results demonstrating oxygen vacancy formation during thermal treatment in H_2 up to 400 °C.

Under quasi-simultaneous acquisition conditions, Zr K-edge XAS (Fig. 13a) allowed us to obtain structural insights on the ZrO_2 matrix complementary to the ones accessed by PXRD analysis (see section 3.1). In particular, we were able to discriminate tetragonal from cubic and monoclinic structures, as the XANES features for the two configurations are strongly influenced by the ZrO_8 polyhedron distortion. Li *et al.*[86] reported three important features in the spectra ascribable to tetragonal ZrO_2: i) the pre-edge peak associated with the 1s → 4d transition, ii) white-line peak splitting, absent in the monoclinic ZrO_2 and iii) broad post-edge resonance around 35 eV after the edge. All these spectroscopic fingerprints, further corroborated by the Zr K-edge XAS spectra of reference monoclinic and tetragonal ZrO_2 reported in Fig. 13, are observable in the XANES of the three investigated ZrZn-*X*/ZSM-5 combined systems, pointing to the presence of a tetragonal ZrO_2 phase. In particular the 1s → 4d pre-edge feature, which is very evident in the XANES first derivative (Fig. S15†), is a fingerprint of t-ZrO_2 where Zr is eight-fold coordinated. In the perfect ZrO_8 pyrochlore-like structure, this s-d transition would not be detectable, as it is dipole forbidden.

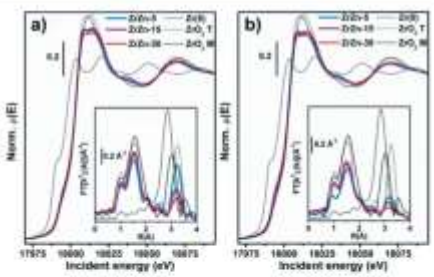

Fig. 13 K-edge XANES (main panel) and phase-uncorrected FT-EXAFS (bottom inset) spectra of the three samples and of Zr metal and ZrO_2 model compounds, collected at (a) RT under He flux and (b) after the activation process (400 °C, H_2). The EXAFS spectra reported in the bottom insets have been obtained transforming the corresponding $k^2\chi(k)$ EXAFS function in the 2.5–13.0 Å^{-1} range.

However, it is well documented[87,88] that in t-ZrO_2 four oxygens are closer while four are farther from the Zr cation. This leads to visualization of the Zr atom as coordinated with two different tetrahedra of oxygen atoms.[86,89] Since the centrosymmetricity is broken, the dipole forbidden 1s → 4d transition gains in intensity being observable in the Zr K pre-edge.[86,101] Moreover, two features in the FT-EXAFS, highlighted by dashed lines in Fig. S15,† can be ascribed to t-ZrO_2: i) the Zr–Zr second shell position and ii) the relatively intense high-*R* peak in the 6–7 Å range in the phase-uncorrected spectra. As shown by Li *et al.*[86,100] with careful EXAFS fit of various ZrO_2 polymorphs, in c-ZrO_2 the average Zr–Zr distance is almost 0.1 Å shorter than that in t-ZrO_2. Therefore, the Zr–Zr second feature of c-ZrO_2 should be located at a lower *R* value than that of the reference t-ZrO_2. Besides, the intense feature around 6.7 Å (Fig. S15† inset) is related to collinear multiple scattering between Zr atoms which is present in t-ZrO_2 but absent in c-ZrO_2.[86,101]

Previous works explained the stabilization of tetragonal ZrO_2 considering the substitution of the Zr atom with either Zn (ref. 31) or Hf.[102] For clarity, we outline that a trace of Hf L_2-edge (9561 eV) was observed during the Zn K-edge XAS measurements, in line with chemical analysis results: the small amount of Hf present in the investigated samples plausibly also contributes to promoting the tetragonal ZrO_2 structure. Phase-uncorrected FT-EXAFS, reported in the inset of Fig. 13a, show a first-shell peak stemming from O NN, consistent for all the three samples with the one observed for the ZrO_2 model compound.

Conversely, with the increase of Zn content (ZrZn-30 > ZrZn-15 > ZrZn-5) the intensity of the second-shell peak is progressively attenuated, while its position is substantially unaltered, always closely resembling the one observed for the tetragonal ZrO_2 model compound. In agreement with PXRD results, this intensity trend stems from Zn entering the ZrO_2 lattice, causing destructive interference among scattering paths involving Zr and Zn NNNs. We note a pronounced intensity decrease while moving from ZrZn-5 to ZrZn-15, while a further increase of Zn-loading in ZrZn-30 only results in a slight additional attenuation of the second-shell peak. This observation further supports that in ZrZn-15 we are close to the upper threshold for the incorporation of Zn in the ZrO_2 lattice.

However, in ZrZn-30, a slightly higher amount of Zn still enters the ZrO_2 matrix, as proven by the additional weakening of the second-shell peak. Afterwards, excess Zn segregates as hexagonal ZnO, silent in Zr K-edge XAS but detectable in Zn K-edge XAS and PXRD. Activation (Fig. 13b)

does not cause substantial modifications in the ZrO_2 structure, nor detectable reduction phenomena involving Zr atoms. Tetragonal features of ZrO_2 are still evident, while the structural disorder in the NNN distribution around Zr centres further increases, translating into an abatement of the second-shell peaks, as observed under the same conditions in Zn K-edge FT-EXAFS.

Under reaction conditions (Fig. S16†), XAS data collected at both absorption edges showed that the catalyst structural stability is preserved. In particular: i) the ZrO_2 matrix maintains the tetragonal structure; ii) Zn does not exchange in the zeolite; iii) both Zr^{4+} and Zn^{2+} do not undergo detectable reduction phenomena. The absence of structural changes after the reaction was also observed from the PXRD measurement of the tested catalysts, reported in the following section. Structural modifications possibly involving surface metal sites upon interaction with the CO_2/H_2 feed are not detectable, as the measured XAS signal includes mainly bulk information.

3.6. Structural characterization of the fresh/tested ZrZn-30/ZSM-5 combined system

In order to investigate possible structural modification induced by the physical mixing and the reaction conditions, we measured the PXRD pattern of the ZrZn-30/ZSM-5 physical mixture before and after 120 hours of catalytic test. Each reflection was ascribed to the corresponding crystalline phase by measuring the PXRD for the single components: i) ZrZn-30 catalyst alone after a reaction cycle and ii) commercial ZSM-5. The diffraction pattern of the ZrZn-30/ZSM-5 combined system in Fig. 14, measured before and after the catalytic test, does not present any differences related to potential structural changes, *i.e.* crystallite defects such as dimensions, stress or strain related to peak broadening. We can clearly distinguish the reflections from each crystal phase, *i.e.* orthorhombic zeolite, tetragonal zirconia and hexagonal zinc oxide. Rietveld refinement was conducted only on the diffraction pattern of the ZrZn-30 catalyst measured after the reaction (Fig. 14 inset). The same refinement strategy used for the fresh catalyst was applied. Taking into account the error of the technique, the results in Fig. 14 and Table S2† evidence structural features very similar to those observed for the fresh sample, while the zeolite crystallinity is preserved as the peaks show similar FWHM (Fig. 14 inset). The increase of the intensity between ZrZn-30 alone and its physical mixture with the zeolite is related to the decrease of the total absorption coefficient as in the second case, half of the capillary contains the zeolite.

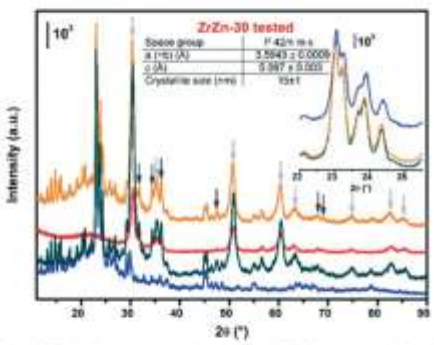

Fig. 14 Stacked representation of the PXRD measured for i) commercial ZSM-5 zeolite alone, in blue; ii) fresh physical mixture ZrZn-30/ZSM-5, in dark-green; iii) ZrZn-30 catalyst after 120 hours of catalytic test, in red; iv) physical mixture of ZrZn-30/ZSM-5 after 120 hours of catalytic test, in orange. For the sake of clarity in the latter pattern, the reflections corresponding to tetragonal ZrO_2 and hexagonal ZnO are indicated by light and dark grey arrows, respectively. Structure results obtained from Rietveld refinement of the tested ZrZn-30 catalyst alone are reported in the table. A detail of the zeolite Bragg peaks is reported in the inset.

We further investigated the possible surface composition changes before and after the reaction by performing XPS analysis on both fresh and tested samples (Fig. S18 and S19†). We can observe that there are no appreciable shifts in the binding energies of both Zn and Zr after 48 hours of catalytic test. Furthermore, the binding energy of Zr at the $Zr3p_{3/2}$ level is 182.37 eV, lower than the 182.7 eV assigned to the pure ZrO_2.[103] This shift has already been reported in the presence of oxygen vacancies due to the substitution of Zn^{2+} by Zn^{1+},[104] in line with our FT-IR observations. We also need to remark that, similar to the PXRD in Fig. 14, the intensity difference between ZrZn-30 alone and its physical mixture with the zeolite is related to the decrease of loading.

We next investigated the possible morphological changes in our system *via* high-angle annular dark-field transmission microscopy (HAADF) in conjunction with energy-dispersive X-ray spectroscopy (EDXS). We can observe that in the fresh

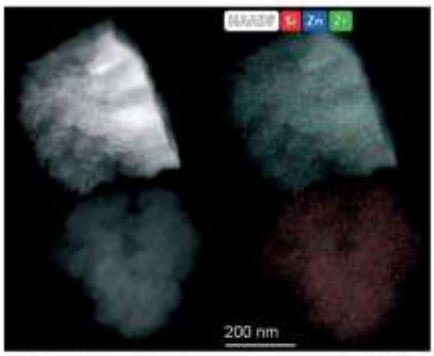

Fig. 15 HAADF STEM-EDXS images of the tested ZrZn-30/ZSM-5 catalyst after 48 hours of catalytic test.

ZrZn-30 sample both Zn and Zr elements are closely incorporated and that an excess of Zn segregates as ZnO_x in line again with the above XANES and PXRD characterization. (Fig. S20†). Similarly, imaging of the tested sample (Fig. 15) shows no structural changes after the reaction with an intimate mixture of both ZrZn-30 and ZSM-5 components in the final bifunctional system. However, we need to point out that a small migration of Zn was observed in some of the zeolite particles (~0.2 wt%, Fig. S21†).

Conclusions

In this work we have synergized catalytic tests under different conditions, multi-technique characterization and computational modelling to advance the understanding of bifunctional Zn-doped-ZrO_2/zeolite catalysts for CO_2 hydrogenation to methanol and conversion to value-added hydrocarbons.

Three Zn-containing ZrO_2 samples were prepared by co-precipitation (ZrZn-*X*, *X* = Zn wt%, *i.e.* 5, 15, 30). The formation of the expected $ZrZnO_x$ solid solution was confirmed by both XAS characteristic features and powder diffractograms. In particular, the crystalline structure of tetragonal zirconia was recognized with diffraction peak shifts consistent with the Zn loading in the structure. A ZnO extra phase is present for the ZrZn-30 sample, evidencing that the co-precipitation technique employed allows achievement of a maximum Zn doping of ZrO_2 of about 15 wt%, even though EXAFS results show that a slightly higher amount of Zn enters the ZrO_2 lattice in ZrZn-30 with respect to ZrZn-15. CO adsorption (at LNT) followed by FT-IR spectroscopy shows that the amount of Zr^{4+} sites at the surface decreases coherently with the increase of Zn loading found from chemical composition and X-ray results.

Interaction with hydrogen at increasing temperature causes the formation of mono-ionized oxygen vacancies, as evidenced by FT-IR spectroscopy. In agreement with FT-IR results, DFT calculations show that chances of oxygen vacancy formation with the assistance of hydrogen increase with increasing Zn content. In particular, DFT modelling points out that once a stoichiometric oxygen vacancy is induced by the presence of Zn, the formation of extra oxygen vacancies during activation is thermodynamically favored. Moreover, DFT modelling points out that i) the oxygen vacancies play an active role in CO_2 hydrogenation, ii) the presence of neighboring Zn and Zr sites enhances methanol selectivity thanks to the proximity of CH_3O^* and $H^{\delta+}$, strongly bonded than $H^{\delta-}$, and iii) methanol is most likely formed *via* the formate pathway.

Coherently, the catalytic performances of the stand-alone ZrZn-*X* samples showed the same trend shown by the oxygen vacancy amount, *i.e.* CO_2 conversion and CH_3OH selectivity increases with the Zn loading. While we cannot exclude that segregated ZnO in the most active catalyst (ZrZn-30) also plays a role, the reported characterization, modelling and testing results consistently suggest that the main contribution to the catalyst activity comes from the $ZrZnO_x$ solid solution. Combined systems were obtained by mechanical mixing of the ZrZn-*X* catalysts with a commercial zeolite (H-ZSM-5 and H-SAPO-34) with a mass ratio of 1 : 1. Comparing ZrZn-30/ZSM-5 and ZrZn-30/H-SAPO-34 combined systems, we pointed out that the ZSM-5-containing system is more promising than the one with H-SAPO-34. Indeed, the highest conversion and stability with *circa* 30% C_5^+ selectivity among hydrocarbons were found testing ZrZn-30/ZSM-5 at 350 °C and 30 bar. At $T < 350$ °C, alkylbenzene dealkylation is unlikely to occur.[45,46] However, in this work we highlight an unusual aliphatics selectivity (and stability) at lower temperature and shorter contact time, more favored with H-ZSM-5 than H-SAPO-34 as the zeotype has lower activity/stability at low temperature.

Finally, the structure of the catalysts is not affected by the reaction conditions as shown by the *operando* XAS and the structural/textural characterization of the tested samples; indeed a final catalytic test carried out on the regenerated catalyst shows that the initial performances are completely restored.

In conclusion, in the light of our findings, we can affirm that, for a bifunctional catalyst, both chemical (oxidic phase composition, Brønsted acid site density, and pore dimensions) and kinetic factors (temperature, pressure and space time velocity) must be considered in order to drive the reaction towards the desired products and, therefore, to achieve a good reaction yield.

Conflicts of interest

There are no conflicts to declare.

Acknowledgements

This project has received funding from the European Union's Horizon 2020 Research and Innovation Programme under grant agreement No. 837733. This work was supported by a public grant overseen by the French National Research Agency (ANR) as part of the "Investissements d'Avenir" program (reference: ANR-10-EQPX-45). The authors are grateful to C. La Fontaine, V. Briois, A. L. Bugaev and A. Lazzarini for the help with the XAS experiment at ROCK, Soleil.

References

1 J. Rockström, W. Steffen, K. Noone, Å. Persson, F. S. Chapin, E. F. Lambin, T. M. Lenton, M. Scheffer, C. Folke, H. J. Schellnhuber, B. Nykvist, C. A. de Wit, T. Hughes, S. van der Leeuw, H. Rodhe, S. Sörlin, P. K. Snyder, R. Costanza, U. Svedin, M. Falkenmark, L. Karlberg, R. W. Corell, V. J. Fabry, J. Hansen, B. Walker, D. Liverman, K. Richardson, P. Crutzen and J. A. Foley, *Nature*, 2009, **461**, 472–475.

2 M. Aresta, A. Dibenedetto and A. Angelini, *J. CO2 Util.*, 2013, **3–4**, 65–73.

3 T. Sakakura, J. C. Choi and H. Yasuda, *Chem. Rev.*, 2007, **107**, 2365–2387.
4 S. Saeidi, N. A. S. Amin and M. R. Rahimpour, *J. CO2 Util.*, 2014, **5**, 66–81.
5 Z. Jiang, T. Xiao, V. L. Kuznetsov and P. P. Edwards, *Philos. Trans. R. Soc., A*, 2010, **368**, 3343–3364.
6 S. Kattel, P. Liu and J. G. Chen, *J. Am. Chem. Soc.*, 2017, **139**, 9739–9754.
7 W. Wang, S. Wang, X. Ma and J. Gong, *Chem. Soc. Rev.*, 2011, **40**, 3703–3727.
8 J. B. Hansen and P. E. Højlund Nielsen, Methanol Synthesis, in *Handbook of Heterogeneous Catalysis*, ed. G. Ertl, H. Knözinger, F. Schüth and J. Weitkamp, Wiley, Germany, 2008.
9 J. R. Gallagher, D. J. Childers, H. Zhao, R. E. Winans, R. J. Meyer and J. T. Miller, *Phys. Chem. Chem. Phys.*, 2015, **17**, 28144–28153.
10 C. Ahoba-Sam, E. Borfecchia, A. Lazzarini, A. Bugaev, A. A. Isah, M. Taoufik, S. Bordiga and U. Olsbye, *Catal. Sci. Technol.*, 2020, **10**, 4373–4385.
11 M. Gentzen, D. E. Doronkin, T. L. Sheppard, A. Zimina, H. Li, J. Jelic, F. Studt, J. D. Grunwaldt, J. Sauer and S. Behrens, *Angew. Chem., Int. Ed.*, 2019, **58**, 15655–15659.
12 M. W. Tew, H. Emerich and J. A. Van Bokhoven, *J. Phys. Chem. C*, 2011, **115**, 8457–8465.
13 K. Cheng, B. Gu, X. Liu, J. Kang, Q. Zhang and Y. Wang, *Angew. Chem., Int. Ed.*, 2016, **55**, 4725–4728.
14 Z. Li, J. Wang, Y. Qu, H. Liu, C. Tang, S. Miao, Z. Feng, H. An and C. Li, *ACS Catal.*, 2017, **7**, 8544–8548.
15 G. Bonura, M. Migliori, L. Frusteri, C. Cannilla, E. Catizzone, G. Giordano and F. Frusteri, *J. CO2 Util.*, 2018, **24**, 398–406.
16 W. J. Thomas and S. Portalski, *Ind. Eng. Chem.*, 1958, **50**, 967–970.
17 J. Ye, C. Liu, D. Mei and Q. Ge, *ACS Catal.*, 2013, **3**, 1296–1306.
18 A. S. Malik, S. F. Zaman, A. A. Al-Zahrani, M. A. Daous, H. Driss and L. A. Petrov, *Appl. Catal., A*, 2018, **560**, 42–53.
19 A. S. Malik, S. F. Zaman, A. A. Al-Zahrani, M. A. Daous, H. Driss and L. A. Petrov, *Catal. Today*, 2020, **357**, 573–582.
20 H. Bahruji, M. Bowker, W. Jones, J. Hayward, J. Ruiz Esquius, D. J. Morgan and G. J. Hutchings, *Faraday Discuss.*, 2017, **197**, 309–324.
21 K. Li and J. G. Chen, *ACS Catal.*, 2019, **9**, 7840–7861.
22 S. Kattel, P. J. Ramírez, J. G. Chen, J. A. Rodriguez and P. Liu, *Science*, 2017, **355**, 1296–1299.
23 Y. Amenomiya, *Appl. Catal., A*, 1987, **30**, 57–68.
24 X. Dong, F. Li, N. Zhao, F. Xiao, J. Wang and Y. Tan, *Appl. Catal., B*, 2016, **191**, 8–17.
25 H. Gu, J. Ding, Q. Zhong, Y. Zeng and F. Song, *Int. J. Hydrogen Energy*, 2019, **44**, 11808–11816.
26 I. A. Fisher and A. T. Bell, *J. Catal.*, 1999, **184**, 144–156.
27 G. Wang, D. Mao, X. Guo and J. Yu, *Int. J. Hydrogen Energy*, 2019, **44**, 4197–4207.
28 F. Arena, G. Italiano, K. Barbera, S. Bordiga, G. Bonura, L. Spadaro and F. Frusteri, *Appl. Catal., A*, 2008, **350**, 16–23.
29 W. Li, K. Wang, J. Huang, X. Liu, D. Fu, J. Huang, Q. Li and G. Zhan, *ACS Appl. Mater. Interfaces*, 2019, **11**, 33263–33272.
30 K. Pokrovski, K. T. Jung and A. T. Bell, *Langmuir*, 2001, **17**, 4297–4303.
31 J. Wang, G. Li, Z. Li, C. Tang, Z. Feng, H. An, H. Liu, T. Liu and C. Li, *Sci. Adv.*, 2017, **3**, 1–11.
32 A. Wokaun, *Phys. Chem. Chem. Phys.*, 1999, **1**, 5071–5080.
33 H. Li, C. Rameshan, A. V. Bukhtiyarov, I. P. Prosvirin, V. I. Bukhtiyarov and G. Rupprechter, *Surf. Sci.*, 2019, **679**, 139–146.
34 L. H. Chagas, P. C. Zonetti, C. R. V. Matheus, C. R. K. Rabello, O. C. Alves and L. G. Appel, *ChemCatChem*, 2019, **11**, 5625–5632.
35 O. E. Everett, P. C. Zonetti, O. C. Alves, R. R. de Avillez and L. G. Appel, *Int. J. Hydrogen Energy*, 2020, **45**, 6352–6359.
36 X. Liu, W. Zhou, Y. Yang, K. Cheng, J. Kang, L. Zhang, G. Zhang, X. Min, Q. Zhang and Y. Wang, *Chem. Sci.*, 2018, **9**, 4708–4718.
37 A. V. Kirilin, J. F. Dewilde, V. Santos, A. Chojecki, K. Scieranka and A. Malek, *Ind. Eng. Chem. Res.*, 2017, **56**, 13392–13401.
38 M. D. Rhodes, K. A. Pokrovski and A. T. Bell, *J. Catal.*, 2005, **233**, 210–220.
39 F. Jiao, J. Li, X. Pan, J. Xiao, H. Li, H. Ma, M. Wei, Y. Pan, Z. Zhou, M. Li, S. Miao, J. Li, Y. Zhu, D. Xiao, T. He, J. Yang, F. Qi, Q. Fu and X. Bao, *Science*, 2016, **351**, 1065–1068.
40 S. Wang, P. Wang, Z. Qin, Y. Chen, M. Dong, J. Li, K. Zhang, P. Liu, J. Wang and W. Fan, *ACS Catal.*, 2018, **8**, 5485–5505.
41 T. Liang, J. Chen, Z. Qin, J. Li, P. Wang, S. Wang, G. Wang, M. Dong, W. Fan and J. Wang, *ACS Catal.*, 2016, **6**, 7311–7325.
42 K. Cheng, J. Kang, Q. Zhang and Y. Wang, *Sci. China Chem.*, 2017, **60**, 1382–1385.
43 C. Zhou, J. Shi, W. Zhou, K. Cheng, Q. Zhang, J. Kang and Y. Wang, *ACS Catal.*, 2020, **10**, 302–310.
44 Y. K. Park, K. C. Park and S. K. Ihm, *Catal. Today*, 1998, **44**, 165–173.
45 H. Schulz, *Catal. Today*, 2010, **154**, 183–194.
46 F. Bleken, M. Bjørgen, L. Palumbo, S. Bordiga, S. Svelle, K. P. Lillerud and U. Olsbye, *Top. Catal.*, 2009, **52**, 218–228.
47 J. Rodriguez-Carvajal, *Newsl. Comm. Powder Diffr. IUCr*, 2001, vol. 26, pp. 12–19.
48 P. Hohenberg and W. Kohn, *Phys. Rev.*, 1964, **136**, B864–B871.
49 W. Kohn and L. J. Sham, *Phys. Rev.*, 1965, **140**, A1133–A1138.
50 P. E. Blöchl, *Phys. Rev. B: Condens. Matter Mater. Phys.*, 1994, **50**, 17953–17979.
51 J. Klimeš, D. R. Bowler and A. Michaelides, *Phys. Rev. B: Condens. Matter Mater. Phys.*, 2011, **83**, 1–13.
52 S. Grimme, S. Ehrlich and L. Goerigk, *J. Comput. Chem.*, 2011, **32**, 1456–1465.
53 C. La Fontaine, S. Belin, L. Barthe, O. Roudenko and V. Briois, *Synchrotron Radiat. News*, 2020, **33**, 20–25.
54 O. Mathon, A. Beteva, J. Borrel, D. Bugnazet, S. Gatla, R. Hino, I. Kantor, T. Mairs, M. Munoz, S. Pasternak, F. Perrin and S. Pascarelli, *J. Synchrotron Radiat.*, 2015, **22**, 1548–1554.

55 B. Ravel and M. Newville, *J. Synchrotron Radiat.*, 2005, **12**, 537–541.
56 K. S. W. Sing and R. T. Williams, *Adsorpt. Sci. Technol.*, 2004, **22**, 773–782.
57 K. S. W. Sing, D. H. Everett, R. A. W. Haul, L. Moscou, R. A. Pierotti, J. Rouquerol and T. Siemieniewska, *Pure Appl. Chem.*, 1985, **57**, 603–619.
58 B. Y. R. D. Shannon, M. H. N. H. Baur, O. H. Gibbs, M. Eu and V. Cu, *Acta Crystallogr., Sect. A: Cryst. Phys., Diffr., Theor. Gen. Crystallogr.*, 1976, **32**, 751–767.
59 S. C. Abrahams and J. L. Bernstein, *Acta Crystallogr., Sect. B: Struct. Crystallogr. Cryst. Chem.*, 1969, **25**, 1233–1236.
60 G. Teufer, *Acta Crystallogr.*, 1962, **15**, 1187.
61 Ü. Özgür, Y. I. Alivov, C. Liu, A. Teke, M. A. Reshchikov, S. Doğan, V. Avrutin, S. J. Cho and H. Morkoç, *J. Appl. Phys.*, 2005, **98**, 1–103.
62 W. Göpel and U. Lampe, *Phys. Rev. B: Condens. Matter Mater. Phys.*, 1980, **22**, 6447–6462.
63 S. Morandi, A. Fioravanti, G. Cerrato, S. Lettieri, M. Sacerdoti and M. C. Carotta, *Sens. Actuators, B*, 2017, **249**, 581–589.
64 L. Genzel and T. P. Martin, *Surf. Sci.*, 1973, **34**, 33–49.
65 G. Ghiotti, A. Chiorino and F. Prinetto, *Sens. Actuators, B*, 1995, **25**, 564–567.
66 S. Morandi, M. C. Paganini, E. Giamello, M. Bini, D. Capsoni, V. Massarotti and G. Ghiotti, *J. Solid State Chem.*, 2009, **182**, 3342–3352.
67 C. Morterra, E. Giamello, L. Orio and M. Volante, *J. Phys. Chem.*, 1990, **94**, 3111–3116.
68 B. N. J. Persson and R. Ryberg, *Phys. Rev. B: Condens. Matter Mater. Phys.*, 1981, **24**, 6954–6970.
69 M. Moskovits and J. E. Hulse, *Surf. Sci.*, 1978, **78**, 397–418.
70 G. D. Mahan and A. A. Lucas, *J. Chem. Phys.*, 1978, **68**, 1344–1348.
71 G. L. Griffin and J. T. Yates, *J. Chem. Phys.*, 1982, **77**, 3744–3750.
72 D. Scarano and A. Zecchina, *J. Chem. Soc., Faraday Trans. 1*, 1986, **82**, 3611–3624.
73 C. Morterra, V. Bolis, B. Fubini, L. Orio and T. B. Williams, *Surf. Sci.*, 1991, **251–252**, 540–545.
74 K. I. Hadjiivanov and G. N. Vayssilov, *Adv. Catal.*, 2002, **47**, 307–511.
75 D. Scarano, S. Bertarione, G. Spoto, A. Zecchina and C. Otero Areán, *Thin Solid Films*, 2001, **400**, 50–55.
76 L. R. del Silva-Calpa, P. C. Zonetti, C. P. Rodrigues, O. C. Alves, L. G. Appel and R. R. de Avillez, *J. Mol. Catal. A: Chem.*, 2016, **425**, 166–173.
77 A. A. Safonov, A. A. Bagatur'yants and A. A. Korkin, *Microelectron. Eng.*, 2003, **69**, 629–632.
78 A. Bavykina, I. Yarulina, A. J. Al Abdulghani, L. Gevers, M. N. Hedhili, X. H. Miao, A. R. Galilea, A. Pustovarenko, A. Dikhtiarenko, A. Cadiau, A. Aguilar-Tapia, J. L. Hazemann, S. M. Kozlov, S. Oud-Chikh, L. Cavallo and J. Gascon, *ACS Catal.*, 2019, **9**, 6910–6918.
79 J. L. Snider, V. Streibel, M. A. Hubert, T. S. Choksi, E. Valle, D. C. Upham, J. Schumann, M. S. Duyar, A. Gallo, F. Abild-Pedersen and T. F. Jaramillo, *ACS Catal.*, 2019, **9**, 3399–3412.
80 E. S. Van-Dal and C. Bouallou, *J. Cleaner Prod.*, 2013, **57**, 38–45.
81 D. Milani, R. Khalilpour, G. Zahedi and A. Abbas, *J. CO2 Util.*, 2015, **10**, 12–22.
82 Y. Slotboom, M. J. Bos, J. Pieper, V. Vrieswijk, B. Likozar, S. R. A. Kersten and D. W. F. Brilman, *Chem. Eng. J.*, 2020, **389**, 124181.
83 N. Rui, Z. Wang, K. Sun, J. Ye, Q. Ge and C. J. Liu, *Appl. Catal., B*, 2017, **218**, 488–497.
84 A. Dokania, A. Ramirez, A. Bavykina and J. Gascon, *ACS Energy Lett.*, 2019, **4**, 167–176.
85 Z. Q. Ma and M. D. Porosoff, *ACS Catal.*, 2019, **9**, 2639–2656.
86 H. Schulz, *Catal. Lett.*, 2018, **148**, 1263–1280.
87 I. Yarulina, A. D. Chowdhury, F. Meirer, B. M. Weckhuysen and J. Gascon, *Nat. Catal.*, 2018, **1**, 398–411.
88 U. Olsbye, S. Svelle, M. Bjorgen, P. Beato, T. V. W. Janssens, F. Joensen, S. Bordiga and K. P. Lillerud, *Angew. Chem., Int. Ed.*, 2012, **51**, 5810–5831.
89 L. Tan, P. P. Zhang, Y. Cui, Y. Suzuki, H. J. Li, L. S. Guo, G. H. Yang and N. Tsubaki, *Fuel Process. Technol.*, 2019, **196**, 106174.
90 K. Cheng, W. Zhou, J. Kang, S. He, S. Shi, Q. Zhang, Y. Pan, W. Wen and Y. Wang, *Chem*, 2017, **3**, 334–347.
91 Q. Song, Y. Men, J. Wang, S. Liu, S. Chai, W. An, K. Wang, Y. Li and Y. Tang, *Int. J. Hydrogen Energy*, 2020, **45**, 9592–9602.
92 X. Cui, P. Gao, S. G. Li, C. G. Yang, Z. Y. Liu, H. Wang, L. S. Zhong and Y. H. Sun, *ACS Catal.*, 2019, **9**, 3866–3876.
93 J. S. Martinez-Espin, M. Mortén, T. V. W. Janssens, S. Svelle, P. Beato and U. Olsbye, *Catal. Sci. Technol.*, 2017, **7**, 2700–2716.
94 T. Cordero-Lanzac, A. Ateka, P. Pérez-Uriarte, P. Castaño, A. T. Aguayo and J. Bilbao, *Ind. Eng. Chem. Res.*, 2018, **57**, 13689–13702.
95 I. Pinilla-herrero, E. Borfecchia, J. Holzinger, U. V. Mentzel, F. Joensen, K. A. Lomachenko, S. Bordiga, C. Lamberti, G. Berlier, U. Olsbye, S. Svelle, J. Skibsted and P. Beato, *J. Catal.*, 2018, **362**, 146–163.
96 P. Li, I. W. Chen and J. E. Penner-Hahn, *Phys. Rev. B: Condens. Matter Mater. Phys.*, 1993, **48**, 10063–10073.
97 P. Li, I. W. Chen and J. E. Penner-Hahn, *Phys. Rev. B: Condens. Matter Mater. Phys.*, 1993, **48**, 10082–10089.
98 C. J. Howard, R. J. Hill and B. E. Reichert, *Acta Crystallogr., Sect. B: Struct. Sci.*, 1988, **44**, 116–120.
99 P. Li, I.-W. Chen and J. E. Penner-Hahn, *J. Am. Ceram. Soc.*, 1994, **77**, 1281–1288.
100 P. Li, I. W. Chen and J. E. Penner-Hahn, *Phys. Rev. B: Condens. Matter Mater. Phys.*, 1993, **48**, 10074–10081.
101 B. W. Veal, A. G. McKale, A. P. Paulikas, S. J. Rothman and L. J. Nowicki, *Physica B+C*, 1988, **150**, 234–240.
102 D. Y. Cho, H. S. Jung and C. S. Hwang, *Phys. Rev. B: Condens. Matter Mater. Phys.*, 2010, **82**, 1–7.

103 Y. Liu, C. Xia, Q. Wang, L. Zhang, A. Huang, M. Ke and Z. Song, *Catal. Sci. Technol.*, 2018, **8**, 4916–4924.

104 C. Wang, G. Garbarino, L. F. Allard, F. Wilson, G. Busca and M. Flytzani-Stephanopoulos, *ACS Catal.*, 2016, **6**, 210–218.

6.2 B : Salusso et al., J. Phys. Chem. C 2021, 125, 40, 22249–22261

THE JOURNAL OF PHYSICAL CHEMISTRY C

pubs.acs.org/JPCC

Article

Combining X-ray Diffraction and X-ray Absorption Spectroscopy to Unveil Zn Local Environment in Zn-Doped ZrO_2 Catalysts

Davide Salusso, Elisa Borfecchia,* and Silvia Bordiga

Cite This: J. Phys. Chem. C 2021, 125, 22249−22261

Read Online

ACCESS | Metrics & More | Article Recommendations | Supporting Information

ABSTRACT: Zinc-doped zirconia catalytic properties, promising toward CO_2 and CO hydrogenation, are commonly ascribed to the synergic interaction between Zn and Zr, yet an atomic-scale perspective on how this synergy is structurally realized remains elusive. In this work, to address this ongoing challenge, we deeply investigated the structure of three Zn-doped ZrO_2 catalysts by combining powder X-ray diffraction (PXRD) and X-ray absorption spectroscopy (XAS). PXRD showed the complete formation of a tetragonal solid solution, undistinguishable by Rietveld refinement from the cubic polymorph. Fit of extended X-ray absorption fine structure (EXAFS) spectra at the Zr and Zn K-edges unveiled the presence of hexagonal/cubic ZnO nanoclusters embedded and chemically bonded to the tetragonal ZrO_2 matrix. The concentration of Zn dopant was evaluated via both PXRD and EXAFS analysis. *In situ* EXAFS study of the catalyst during activation further confirmed the presence of a chemical interaction at ZnO/ZrO_2 interface, most probably the active site toward CO_2 hydrogenation. The ZnO cluster radius was found to be in the 11−13 Å range, using the Greegor and Lytle spherical model. Taken together, the results demonstrate how the combination of X-ray techniques probing both long-range and local structural properties could unlock an unprecedented level of understanding in mixed metal oxide catalysts.

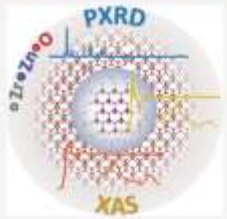

1. INTRODUCTION

Zirconium oxide, commonly prepared in the monoclinic (m-), tetragonal (t-), and cubic (c-) polymorphs, is the only metal oxide potentially displaying acidic or basic, as well as oxidizing or reducing, properties at its surface.[1] For this reason it is widely used as a catalyst[1,2] or catalyst support.[3] ZrO_2 surface can be generally described as formed by coordinatively unsaturated (CUS) cationic sites (Lewis acid sites, such as Zr^{4+} and Zr^{3+}), CUS Zr^{4+}−O pairs, oxygen vacancies (V_O), and terminal and multicoordinated hydroxyls.[4] This wide variety of acid/basic sites makes ZrO_2 a versatile catalyst able to promote many different reactions. Due to the drastic increase of CO_2 anthropogenic emissions,[5] catalytic reactions of major interest involve CO and CO_2.[6] Carbon monoxide and dioxide are activated on the ZrO_2 surface throughout carbonates formation.[4] Doping with aliovalent cations can tune the surface physicochemical properties, i.e., inducing formation of V_O (Zn^{2+}, Cu^{2+}, and Y^{3+})[7,8] neighboring a CUS Zr^{4+}, which acts as strong basic and acid sites, respectively.[9]

Among all the dopants, Zn has been recently investigated for several reactions.[8,10−16] Its ionic radius, comparable to the Zr^{4+} one (0.60 vs 0.84 Å),[10] permits Zn ions to easily dissolve in the ZrO_2 lattice. The addition of Zn^{2+} likely creates oxygen vacancies, modifying oxygen mobility and tuning the surface physicochemical properties. In the past decade, Zn-doped ZrO_2 (ZZR) has been studied for its properties in CO/CO_2 hydrogenation[13,15,16,21] and ethanol/propene dehydrogenation.[11,12,17] As H_2 can be activated through an heterolytic dissociation on ZnO, the presence of Zn−O pairs or ZnO clusters enhances the hydrogenation/dehydrogenation properties of the catalyst. In the last years, ZZR was also investigated for its catalytic activity and selectivity when used as the oxidic component forming bifunctional catalysts for the direct conversion of CO or CO_2 with H_2 to olefins and aromatics.[16,18,20,21] Particularly, a balanced Zn/Zr ratio allows to strongly activate CO_2 and CO forming carbonates which are selectively hydrogenated to methanol by H_2 activated over Zn−O.[8,20,21]

However, if much is known about ZZR catalytic properties, then detailed information about its structure is still largely lacking. According to DFT calculations, substitution of ZrO_2 units with ZnO induced V_O formation which favored the simultaneous CO_2 adsorption and H_2 dissociation,[20] suggesting that the catalyst becomes active when Zn maintains a ZnO-like coordination. In case of Zn-impregnated ZrO_2, its structure was unchanged,[10,12] but t-ZrO_2 has been mostly observed in ZZR obtained by coprecipitation,[10−13] showing that the presence of V_O stabilizes the tetragonal polymorph. The effective presence of ZnO−ZrO_2 solid solutions was observed by several laboratory techniques, based on the

Received: July 12, 2021
Revised: September 11, 2021
Published: September 29, 2021

following lines of evidence: (i) The substitution of Zr by Zn causes a shrink of the tetragonal lattice, observable by PXRD from the (101) Bragg reflection systematic shift.[20,21] (ii) UV–vis spectra of ZrO_2 is modified by the dopant, indicating the probable presence of isolated Zn^{2+}.[11] (iii) FTIR bands around 500 and 600–700 cm^{-1} were associated with the Zn–O–Zn and Zn–O–Zr vibrations.[14] By EXAFS fitting, Han et al.[12] showed that in Zn-impregnated ZrO_2, ZnO aggregates are formed. Nevertheless, when the two oxides are coprecipitated, the chemical environment surrounding Zn in the ZrO_2 lattice is unclear. Due to the indirect effects on the ZrO_2 lattice, Zn^{2+} has been considered as bonded to it, forming a solid solution with the host matrix.[21] However, it is still not clear whether it is present as single isolated Zn sites or as small ZnO_x clusters invisible to PXRD.

We recently investigated CO_2 hydrogenation over the oxidic catalyst for ZrO_2 doped with 5, 15, and 30 wt % of Zn showing 7, 7.5, and 8% of CO_2 conversion, respectively, at 300 °C/15 bar.[20] Even if these performances are lower than those of the conventional Cu-based catalysts,[24] ZZR showed excellent properties when combined with a zeolite/zeotype (SAPO-34 and H-ZSM-5) for the direct conversion of CO_2 to light olefins.[20] We investigated catalytic properties for olefins production in a previous work where we also reported the stability of ZZR/zeolite physical mixture under reaction conditions.[20]

The XAS data, measured during a catalysis-oriented *in situ* experiment, are hereafter critically compared with the complementary results from PXRD and thoroughly analyzed to unveil the Zr and Zn local structure. ZnO nanoclusters chemically bonded and embedded in the ZrO_2 matrix are unambiguously identified, leading to a consistent structural picture further on validated by Zr and Zn K-edge EXAFS fits carried out on the data collected at both room temperature and during the activation protocol, i.e., heating up to 400 °C under H_2 flow. The ZnO cluster dimension is evaluated using the Greegor and Lytle spherical model,[25] and hypotheses on V_O location and reaction active site are made.

2. EXPERIMENTAL AND THEORETICAL METHODS

2.1. Sample Preparation. The three ZrZn-*X* samples were prepared by colloidal impregnation from Zr and Zn inorganic salts solutions. The *-X* suffix represents the Zn loading quantified by ICP analysis. The complete synthesis procedure together with detailed elemental analysis results can be found elsewhere.[20]

2.2. Powder X-ray Diffraction. All the powder X-ray diffraction patterns (PXRD) here reported were measured with a PW3050/60 X'Pert PRO MPD Diffractometer from PANalytical working in Bragg–Brentano geometry, equipped with a Cu $K\alpha_{1,2}$ X-ray source. The three samples were measured in the as-prepared form in transmission mode using a glass capillary (Ø = 0.5 mm) in the 10–90° 2θ range. The as-prepared ZrZn-5 sample was further measured at room temperature in reflectance mode with a flat sample holder in the 10–140° 2θ range using 1/4 in. slits and a 0.008 s time/step in order to minimize peaks overlaps. Lattice parameters, phases composition (ZrO_2/ZnO), and peak profile were refined using the Rietveld method implemented in the FullProf software.[26] Thompson–Cox–Hastings approximation[27] was used to describe the peak shape following the procedure reported in a previous work.[20]

2.3. X-ray Absorption Spectroscopy. Zr and Zn K-edges were collected quasi-simultaneously in transmission mode at the Quick-XAS ROCK (Rocking Optics for Chemical Kinetics) Beamline[28] of the French Synchrotron SOLEIL using two quick-XAS monochromators, i.e., Si(111) for Zn K-edge (9659 eV) and Si(220) for Zr K-edge (17998 eV). The two monochromators were mounted on a cam-driven tilt table oscillating periodically around a fixed Bragg angle. Ionization chambers were employed to measure incident (I_0) and transmitted (I_1) beam. Zn and Zr metal foils were measured simultaneously with all the acquired spectra by a third ionization chamber (I_2) in order to achieve a precise energy calibration. The sample thickness was optimized in order to compromise absorption length at both edges. As the measurement was part of a previous catalytic experiment under *in situ* conditions (high pressure/high temperature) the three catalysts were ground in a mortar with H-ZSM-5 zeolite and loaded in a quartz capillary reactor (ø = 1 mm). The full catalytic experimental procedure was already described in the same work.[20] We hereby report a deeper structural data analysis concerning the XAS spectra measured: (i) at room temperature for the three samples in He atmosphere, (ii) under activation, i.e., heating (room temperature to 400 °C, 5 °C min^{-1}) at 1 bar in pure H_2 flow, and a qualitative interpretation of spectra collected (iii) under reaction conditions, i.e., feed of CO_2/H_2/He = 1.25:7.5:1 (mL min^{-1}) at 300 °C and 15 bar pressure. As previously discussed, the presence of the zeolite did not alter the structure of the ZrZn-*X* phase, so therein it will be safely considered as a spectroscopically silent spectator. The room-temperature data set was obtained as the average of 190 scans for an exposure time of 47.5 s and a total time/scan of 95 s, while the time-resolved data set throughout activation and reaction was obtained as average of 50 scans for an exposure time of 12.5 s and a total time/scan of 25 s. Energy sampling of 2 eV was used for the two edges, and it was intensified in the main edge region to 0.2 eV for Zn (9530–9780 eV) and 0.4 eV for Zr (17971–18120 eV). Pure hexagonal ZnO and tetragonal ZrO_2 powdered reference compounds were measured at the same beamline, in the form of self-supporting pellets. XAS spectra were aligned in energy, background-subtracted, and normalized to unity edge jump using the Athena software from the Demeter Package.[29] All the structures and pictorial representation of scattering paths provided in this work were prepared using the Vesta software.[30]

2.3.1. EXAFS Analysis Details. The $\chi(k)$ EXAFS function and its Fourier transform (FT) were extracted and calculated, respectively, using the Athena software from the Demeter package.[29] EXAFS fitting was carried out using the Artemis code within the same package, according to the strategy separately detailed in the following for each investigated absorption edge. EXAFS fitting procedure of room temperature-spectra was applied to the average of two sequentially measured data sets (each consisting of the average of 190 scans), merged after checking reproducibility among the two acquisitions. For clarity, the original k-space spectra for the three samples are reported in Figure S1.

2.3.1.1. Zr K-Edge at Room Temperature under He. Fits were carried out in *R* space in the ΔR = 1.15–4.00 Å range, on the FT of the k^2-weighted $\chi(k)$ EXAFS spectra transformed in the 2.5–12.0 $Å^{-1}$ range. FEFF6[31,32] code implemented in the Artemis software was used to calculate theoretical amplitudes and phases. As input for all the FEFF6 calculation we

https://doi.org/10.1021/acs.jpcc.1c06203
J. Phys. Chem. C 2021, 125, 22249–22261

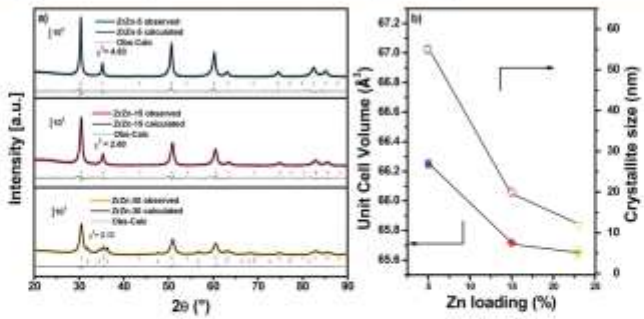

Figure 1. (a) PXRD patterns measured for the three ZrZn-*X* samples in transmission mode using glass capillary sample holder (Ø = 0.5 mm). Diffractograms for ZrZn-5 (blue curve), ZrZn-15 (red curve), and ZrZn-30 (yellow curve) are reported together with the corresponding refined curves (dark gray) and difference functions (light gray) between observed and calculated curves. t-ZrO_2 was used as input structure for the refinement. t-ZrO_2 and h-ZnO Bragg reflections are indicated by red and blue vertical sticks, respectively. (b) Unit cell volume (full symbols) and crystallite size (empty symbols) obtained from refined lattice parameters and peak shape, respectively, for ZrZn-5 (blue square), ZrZn-15 (red diamond), and ZrZn-30 (yellow triangles).

employed a tetragonal ZrO_2 crystallographic information file (CIF) available in the literature.[33] ZnZr-*X* lattice parameters were taken from PXRD Rietveld refinement (Table S1).

Zr K-edge EXAFS spectra for the ZrZn-*X* series were fit considering all the single scattering (SS) paths contributing to the analyzed *R*-space range. A triangular multiple scattering (MS) path between Zr−O(1)−O(2), where O(1) and O(2) are the two oxygens in the Zr first coordination shell (Figure S4b) was also included. We attributed independent radial shifts (ΔR) and Debye−Waller factors (σ^2) to O(1), O(2), and Zr, while the same energy shift parameter (ΔE) was used to optimize all the scattering paths. To reduce the number of optimized variables and evaluate a physically meaningful Zr−Zr coordination number (CN), we considered chemical transferability to import the amplitude reduction factor as S_0^2 (0.97 ± 0.13) from the optimized EXAFS fit of a reference tetragonal ZrO_2 (see Figure S5 and Table S2). As underlined by the Kröger−Vink notation[34] in eq 1 below, in ZrZn-*X* the Zr neighborhood is modified by an oxygen vacancy (V_O) by the dopant Zn_{Zr}.

$$(1-x)Zr_{Zr}^{x}\langle x\rangle Zn_{Zr}^{''}(2-x)O_{O}^{x}(x)V_{O}^{\cdot\cdot} \quad (1)$$

Zn doping was then considered by including an extra Zr−Zn SS path at the same distance of the Zr−Zr one (3.587 Å) and by describing the associated coordination number with an extra variable "Zn". This variable was also used to describe Zr nearest neighbor (NN) V_O (i.e., expressing oxygen degeneracy of the first coordination shell as 4-Zn/2 for O(1) and 4-Zn/2 for O(2)) and next nearest neighbor (NNN) Zn (i.e., changing Zr coordination to 12-Zn).

2.3.1.2. Zn K-Edge at Room Temperature under He. Fits were carried out in the *R*-space in the ΔR = 1.0−3.3/1.0−3.5 Å range, on the FT of the k^3-weighted $\chi(k)$ EXAFS spectra transformed in the 2.5−13.0 $Å^{-1}$ range. FEEF6 code implemented in the Artemis software from the Demeter package was used to calculate amplitudes and phases. As input for FEFF6 calculation we employed standard geometries available in the literature[35,36] and an *ad hoc* Zn-doped tetragonal ZrO_2 CIF file described in Table S4.

At the Zn K-edge, the most informative sample was ZrZn-15. It presented the best balance between Zn loading (best signal-to-noise ratio) and phase purity (absence of segregated bulk ZnO_x as described in section 3.1). FT-EXAFS extraction and fitting were therefore conducted only for this sample. S_0^2 (0.86 ± 0.10) optimized for reference h-ZnO (see Supporting Information section 3, Figure S8, and Table S3) was exported to the fit, while different geometries were considered as input structures for theoretical paths calculations: (i) t-ZrO_2 ($P4_2/nmc$) with the Zr^{4+} substituted by Zn^{2+} (t-$ZnZrO_2$) (Table S4), (ii) ZnO in the hexagonal ($P6_3mc$) wurtzite polymorph (h-ZnO),[35] (iii) ZnO in the cubic ($F\bar{4}3m$) zinc blende polymorph (b-ZnO),[36] and (iv) in the most advanced fitting model (h-ZnO/ZrO_2), ZnO nanoclusters chemically bonded to the ZrO_2 matrix. Structures and fit procedures are described in the Supporting Information section 5.

2.3.1.3. Cluster Size Evaluation. Considering the uncertainties intrinsically affecting our XAS measurements (i.e., Debye−Waller (DW) thermal contribution, edge jump optimized for both Zr and Zn edges), ZnO nanocluster shape has been approximated to a sphere. Greegor and Lytle formula, eq 2,[25] was used to evaluate average nanoparticle dimension from the Zn−Zn coordination number resulting by EXAFS fit.

$$\mathrm{CN}(R) = \frac{1}{R^3}\left|(R-R_1)^3\cdot N_1 + \sum_{n}(3\Delta R_n^2 + 3\Delta^2 R_n + \Delta^3)FN_n\right| \quad (2)$$

where CN is the coordination number, evaluated as a function of the radius *R* of the particle (assumed to be spherical) by summing unterminated coordination spheres in the inner regions $R-R_1$ with a summation over successive terminated coordination spheres of radius R_k in the outer regions $(R-R_1) < R_K \leq R$.

For a more detailed description of eq 2 and of the related parameters employed in this work, the reader is referred to Supporting Information section 6 (eq S1).

https://doi.org/10.1021/acs.jpcc.1c06203
J. Phys. Chem. C 2021, 125, 22249−22261

2.3.1.4. Fit of In Situ EXAFS Data during Catalyst Activation under H_2. During catalyst activation, 100 spectra (each consisting of an average of 50 scans) were collected at the Zr and Zn K-edges. EXAFS analysis was carried out on 10 spectra selected at constantly spaced temperatures from 310 to 673 K. For clarity, the original *k*-space spectra are reported in Figure S2. To find the structure describing the whole temperature evolution, the 10 spectra for the same absorption edge were collectively fit. To reduce the number of fitting variables, DW factors were described with the Einstein model introduced by Sevillano et al.[57] and already applied in literature for describing catalysts during thermal treatments.[58,59] Briefly, the model allows us to describe a single scattering path with three parameters: (i) a fixed temperature factor, defined as the sample experimental temperature, (ii) the reduced mass of the absorber-scatterer pair, calculated by IFEFFIT (implemented in the Artemis software), and (iii) the Einstein temperature. As the latter one is temperature independent, it does not change between data sets but only among scattering paths, allowing a drastic reduction in the number of fitting variables. High values of Einstein temperature are associated with a lower DW value. For the sake of clarity, considering the complexity of the Einstein model, and the presence of intrinsic temperature measurements errors, we considered out of the scope of this work the evaluation of the errors affecting the so found DW factors.[60] Since the Einstein model cannot describe a possible structural phase evolution during the analyzed spectral series, as hereafter described, we assumed the absence of phase transitions during the in situ experiment, as supported by the overall limited variations observed in both XANES and EXAFS regions at both Zr and Zn K-edges.

3. RESULTS AND DISCUSSION

3.1. Powder X-ray Diffraction (PXRD). As already discussed in a previous work,[20] PXRD diffractograms for the ZrZn-*X* series, shown in Figure 1, contain the same Bragg reflections, despite a series of extra peaks in the ZrZn-30 sample associated with a hexagonal ZnO extra phase. The common Bragg reflections were initially ascribed to both cubic ($Fm\bar{3}m$) and tetragonal ($P4_2/nmc$) ZrO_2 polymorphs. The two structures are simply not discernible from their diffractograms, especially in the case of nanosized crystallites, as evidenced by Rietveld refinement (Figure 1b, Table S1). Indeed, in this case, peak broadening causes a substantial overlap of reflections (e.g., the $(110)_t$ and $(002)_t$ Bragg peaks which occur at 35.18 and 35.28°, respectively, are convoluted in a single peak not distinguishable from the $(002)_c$ potentially occurring at 35.12°).

As shown elsewhere,[20] in view of the presence of XANES features at the Zr K-edge (Figure 3) related to the tetragonal ZrO_2 polymorph (t-ZrO_2), this structure was used to evaluate lattice parameters, phase composition and crystallite size for the three catalysts by Rietveld refinement of PXRD patterns measured in transmission mode (Figure 1a). The h-ZnO ($P6_3mc$) phase[15] was added to refine the extra reflections in the ZrZn-30 pattern. The obtained results, published in a previous work,[20] are reported in Table S1 for clarity. The effective Zn doping in the ZrO_2 structure can be simply verified from the interplanar spacing $d_{t\text{-}101}/d_{c\text{-}111}$ (where t- and c- stand for tetragonal and cubic, respectively) and the refined lattice parameters. As the Zn^{2+} ionic radius (0.60 Å) is smaller than the Zr^{4+} one (0.84 Å),[19] higher Zn loading consistently translates into a larger shift of the reflection to higher 2θ value (Figure S3) and a smaller unit cell volume (Figure 1b). The amount of Zn effectively doping ZrO_2 lattice, also reported in Table S1, was obtained combining the Zn wt % from ICP (dopant and segregated) with the ZnO wt % (segregated) refined with Rietveld method.

In this work we focused on the laboratory PXRD strengths/limits when investigating cubic/tetragonal ZrO_2 polymorphs, in combination with the Zn influence on lattice parameters. As it presented the most intense/less broadened peaks, the ZrZn-5 diffractogram was remeasured in reflection mode to avoid self-absorption phenomena and to enhance the detectability of weak reflections (Figure 2). Both cubic ($Fm\bar{3}m$)[61] and

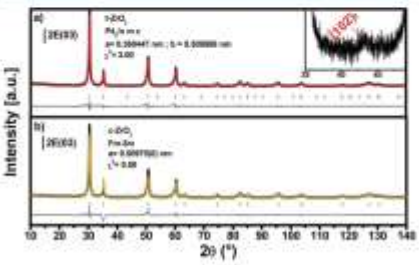

Figure 2. PXRD pattern of ZrZn-5 measured in reflection mode using a glass flat holder collected in the 10−140° 2θ range. Experimental data (black curve) and calculated curve for (a) tetragonal (red curve) and (b) cubic (yellow curve) structures are compared. Difference function between observed and calculated curves is reported below each diffractogram (thin gray curve). Tetragonal (102) reflection is showed in the inset. t-ZrO_2 and c-ZrO_2 Bragg reflections are indicated by green vertical sticks.

tetragonal ($P4_2/nmc$)[33] ZrO_2 were used as input geometries to refine the pattern by Rietveld method. Starting values for the lattice parameters were simply calculated from the $(002)_{t/c}$ and $(200)_c$ Bragg reflections at 34 and 50°, respectively. Refined curve in Figure 2 shows a good data/fit agreement factor for both the input geometries. Nevertheless, the diffractogram displays a weak peak at 43° (Figure 2 inset), which is not expected in the cubic structure while it is indexed as (102) using the tetragonal polymorph. Nevertheless, the aforementioned fingerpeint is intrinsically weak and close to the noise level. A more careful analysis of the XAS data previously reported was necessary to complementary solve the catalyst structure.

3.2. X-ray Absorption Spectroscopy (XAS). *3.2.1. Zr K-Edge XAS. 3.2.1.1. XANES.* The XAS spectra of the three samples measured at room temperature in He atmosphere are reported in Figure 3, together with those of monoclinic and tetragonal ZrO_2 polymorphs, as references. Edge position, giving important information on the absorber atom oxidation state, is observed at energy typical of Zr^{4+} for all the samples. The white-line peak is split into B and B′ features, while the multiple-scattering feature C occurs in the postedge region. These two latter fingerpeints allow us to safely distinguish between tetragonal and monoclinic polymorphs, confirming the PXRD results. Moreover, based on previous literature reports,[62,63] it is possible to distinguish tetragonal/cubic polymorphs from the presence/absence of a pre-edge shoulder

https://doi.org/10.1021/acs.jpcc.1c06203
J. Phys. Chem. C 2021, 125, 22249−22261

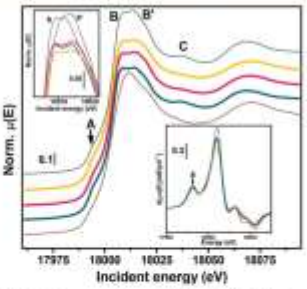

Figure 3. Stacked representation of Zr K-edge XANES measured at room temperature (He atmosphere) for the three ZrZn-*X* samples. ZrZn-5 (blue), ZrZn-15 (red), and ZrZn-30 (yellow) are represented together with reference tetragonal (gray) and monoclinic (brown) ZrO_2 polymorphs. Top left inset: nonstacked detail of the white-line peak. Bottom right inset: XANES first derivative enhancing the pre-edge feature related to the 1s → 4d transition.

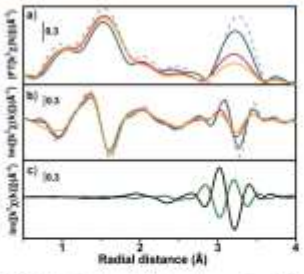

Figure 4. (a) Magnitude and (b) imaginary parts of k^2-weighted phase-uncorrected FT-EXAFS extracted in the k range of 2.5−12.0 $Å^{-1}$ for ZrZn-5 (blue), ZrZn-15 (red), ZrZn-30 (yellow), and reference t-ZrO_2 (dashed gray). (c) Imaginary part of the individual Zr−Zr (black) and Zr−Zn (green) scattering paths generated by FEFF6 optimized after the fit of ZrZn-30.

(labeled as A in Figure 3), more visible considering the XANES first derivative (Figure 3, bottom inset). This feature was initially attributed from electron-energy loss spectroscopy[42] and subsequently confirmed from the Zr K-edge XANES studies by Li et al.[43] to stem from a 1s → 4d transition, characteristic of t-ZrO_2. In the latter polymorph, Zr coordination changes from ZrO_7 centrosymmetric unit, typical of pyrochlore-like structures (i.e., c-ZrO_2), to a distorted ZrO_8 one. To incorporate the extra oxygen, Zr−O forms two nonequivalent tetrahedra, where four oxygens are closer ⟨O(1)⟩ to the Zr atom and four are farther ⟨O(2)⟩ (Figure S4a). As shown in the inset in Figure 3, the pre-edge peak is observed for all the ZrZn-*X* catalysts, confirming throughout the series of samples the tetragonality of the ZrO_2 matrix. Notably, these indications from Zr K-edge XANES corroborate those from PXRD, with respect to the weak (102) reflection observed in the higher-quality pattern of ZrZn-5 (Figure 2, inset).

The main edge width in the Zr K-edge (Figure 3, top inset) spectra could be also indirectly associated with the presence of Zn as Zr NNN, as confirmed later on by the Zr and Zn K-edge EXAFS fit (sections 3.2.1.2 and 3.2.2.2). The main edge width, also described as the fwhm of the first derivative main peak (Figure 3, bottom inset), is an indicator of the absorber symmetry. In particular, a higher coordination symmetry is expected to reflect into a smaller first derivative main peak fwhm. In Figures 3 inset and S6 (Supporting Information section 2), we observed a fwhm increase at higher Zn loading, showing that the presence of Zn distorts Zr NNN environment.

3.2.1.2. EXAFS. Phase-uncorrected Zr K-edge FT-EXAFS are reported in Figure 4a,b. Similar features for the spectra of the three ZrZn-*X* catalysts are observed. The two main peaks located at 1.5 and 3.2 Å can be safely connected to the NN Zr−O and NNN Zr−Zr SS contributions. As already reported,[44] at room temperature the Zr−O peak subshell structure characteristic of t-ZrO_2 is not evident from qualitative observation of the EXAFS data. The first-shell peak intensity is comparable between all the samples and substantially equivalent to that observed for the t-ZrO_2 model compound. Conversely, the second-shell peak displays a lower intensity than that observed for the reference t-ZrO_2, unveiling an enhanced structural disorder in the Zr local coordination environment. Most importantly, the peak intensity is progressively abated as Zn doping increases (Figure 4a). A comparison of the imaginary parts of the Zr−Zr and Zr−Zn scattering contributions (Figure 4c) extracted after EXAFS fitting in the representative case of ZrZn-30 (vide infra) shows that they cancel each other out perfectly, linking the chemical Zn doping in the ZrO_2 structure with the observed intensity decrease of the second-shell peak in Zr K-edge EXAFS.

EXAFS fits started from a tetragonal ZrO_2 model, used as initial geometry input for the refinement. The whole procedure, described in detail in section 2.3.1.1 and in Supporting Information section 2, led to the best-fit curves reported in Figure 5. A good agreement was observed for both magnitude and imaginary part of the FT-EXAFS spectra when comparing experimental and calculated curves. Physically meaningful values for energy shifts, radial shifts, and DW factors (σ^2) were found in all cases. Notably, a higher σ^2 value for NN O(2) was observed in all the samples, as well as in the reference t-ZrO_2 (Table S2). This result, already documented in previous literature for t-ZrO_2,[43,44] is ascribable to the farther spatial position of this oxygen from the Zr absorber. In fact, even if O(1) and O(2) positions are crystallographically equivalent and indistinguishable from PXRD, then the Zr−O(2) distance is higher ⟨2.37 versus 2.06 Å of Zr−O(1)⟩[43] lowering the bond strength and thus leading to a slight increase in the corresponding σ^2 value.[43] Zr−Zr and Zr−Zn SS paths starting with the same distance were considered for the second-shell fitting. It is worth noting the higher value for the Zn σ^2 factor in ZrZn-5, in line with the low Zn concentration in this sample, which complicates the optimization of the Zr−Zn scattering contribution in the corresponding EXAFS spectrum. The contribution of each path was modulated by refining the Zr coordination number (CN) with NNN Zr/Zn using the "Zn" variable as described above. Even if EXAFS CNs have a limited accuracy (≈20%), then the obtained EXAFS results yielded amounts of Zn chemically doping zirconia in substantial agreement with those obtained by combining elemental analysis and complementary insights from PXRD (Table 1). However, a general underestimation of

https://doi.org/10.1021/acs.jpcc.1c06203
J. Phys. Chem. C 2021, 125, 22249−22261

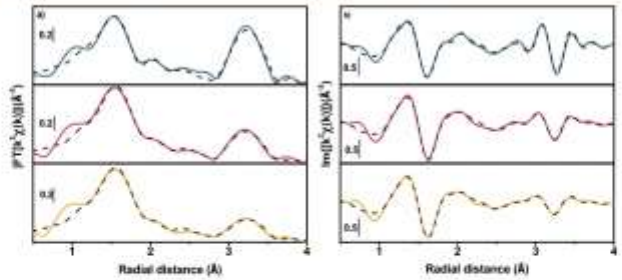

Figure 5. Experimental (colored lines) and best fit (dashed gray lines) (a) magnitude and (b) imaginary parts of the k^2-weighted, phase-uncorrected FT-EXAFS spectra for ZrZn-5 (blue), ZrZn-15 (red), and ZrZn-30 (yellow).

Table 1. Results from EXAFS Fit of the ZrZn−X Samples Using Tetragonal (t-ZrZn-*X*) and Cubic (c-ZrZn-5) Structures as Input Geometries[a]

sample	t-ZrZn5	t-ZrZn15	t-ZrZn30	c-ZrZn5
fit *R*-factor	0.017	0.013	0.0086	0.055
N_{par} (N_{ind})	10(16)	10(16)	10(16)	8(16)
ΔE (eV)	−3.5 ± 1.3	−2.9 ± 1.2	−3.4 ± 1.1	−5.8 ± 1.5
R_{Zr-O} (Å)	2.100 ± 0.011 2.28 ± 0.03	2.100 ± 0.014 2.25 ± 0.02	2.094 ± 0.013 2.240 ± 0.019	2.135 ± 0.015
σ^2_O (Å^2)	0.004 ± 0.002 0.011 ± 0.005	0.0023 ± 0.0017 0.005 ± 0.005	0.0023 ± 0.0015 0.006 ± 0.003	0.009 ± 0.002
R_{Zr-O}(Å)	3.62 ± 0.02	3.61 ± 0.02	3.60 ± 0.03	3.62 ± 0.03
σ^2_{Zr} (Å^2)	0.008 ± 0.003	0.007 ± 0.004	0.010 ± 0.004	0.004 ± 0.003
R_{Zr-Zn} (Å)	3.56 ± 0.10	3.58 ± 0.03	3.57 ± 0.04	3.58 ± 0.04
σ^2_{Zn} (Å^2)	0.0017 ± 0.0019	0.003 ± 0.005	0.005 ± 0.004	−0.0007 ± 0.004
Zn	1.9 ± 1.1	2.6 ± 0.6	3.0 ± 0.5	2.5 ± 0.7
Zn-loading (wt %) EXAFS	8 ± 9	12 ± 5	15 ± 4	
Zn loading (wt %) ICP/PXRD	5	15	30 (22)	

[a]Fit was carried out in *R*-space, in the range of 1.15−4.00 Å, on FT-EXAFS spectra transformed in the 2.5−12 Å^{-1} k range, resulting in a number of independent parameters $\pi\Delta R\Delta k/2 > 16$. Amplitude reduction factor ($S_0^2 = 0.97 \pm 0.13$) imported from reference t-ZrO_2 was fixed in all cases. The *R*-factor, number of parameters, Zn−O/Zr/Zn radial distance are reported. Zr−O radial distance and σ^2 contains two values for t-ZrZn-*X* and a single one for c-ZrZn5 as in the cubic polymorph Zr is surrounded by eight equidistant oxygens while in the tetragonal one four oxygen are closer, O(1), and four farther, O(2). The optimized average number of Zn atoms occurring as Zr NNN is reported though the "Zn" parameter, while the related Zn weight percentage for each ZrZn-*X* catalyst is calculated from this value.

Zn-loading is observed, which will be rationalized in section 3.2.3, in the view of EXAFS analysis at Zn K-edge.

The Zr−O(1)/O(2) bond lengths are ca. 2.10 Å and 2.24−2.28 Å, respectively, with each subshell including 4 ⟨Zn/2⟩ O atomic neighbors. Considering that the obtained values for Zr−O(1) and Zr−O(2) significantly differ within their fitting errors, we can consider the distances information obtained by EXAFS as reliable.

We also attempted a test fit of the ZrZn-5 EXAFS spectrum using as starting input the c-ZrO_2 model. Even if the calculated curve satisfactorily matched the experimental one (Figure S9), fit results also reported in Table 1 (last column) show a substantially higher *R*-factor and a negative value for σ^2_{Zn} making the fit unphysical. Additionally, from a structural point of view, we can observe that the Zr−Zr distance resulted from this test fit is significantly elongated with respect to the starting input value, underlying that the cubic structure is distorted to approach the tetragonal one. In fact, in stabilized cubic ZrO_2, Zr−Zr distance evaluated by EXAFS was reported by Li et al.[43] to be ca. 3.55 Å, while 3.62 Å is a value more usual for t-ZrO_2.

3.2.2. Zn K-Edge. 3.2.2.1. XANES. In order to deeply understand the local coordination and structure of Zn atoms doping the ZrO_2 lattice, we initially focused on the XANES region of Zn K-edge XAS spectra, measured quasi-simultaneously with the Zr K-edge ones. The spectra of the three ZrZn-*X* samples are reported in Figure 6, together with Zn K-edge XANES spectra of h-ZnO and Zn metal foil references. The edge position, reflecting the oxidation state of the absorber, highlights the presence of Zn^{2+} in all the samples. Typical h-ZnO spectral features, such as the main absorption peak B and postedge resonance C, are recognized in the XANES spectra of all the ZrZn-*X* samples. However, shoulder-like features (A, D, and E in Figure 6) present in h-ZnO are substantially dampened in the ZrZn-*X* catalysts, pointing out a higher defectivity. While for ZrZn-30 the presence of bulk h-ZnO was observed by PXRD (Figure 1a), in the case of ZrZn-5/15, we cannot specifically connect the ZnO phase to wurtzite or zinc blende, since their XANES spectra are very similar to each other.[45]

https://doi.org/10.1021/acs.jpcc.1c06203
J. Phys. Chem. C 2021, 125, 22249−22261

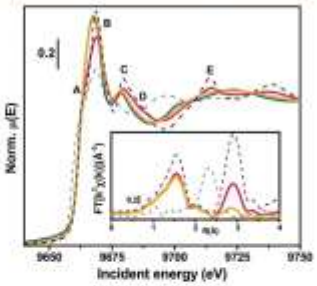

Figure 6. Zn K-edge XANES (main panel) and phase-uncorrected k^3-weighted FT-EXAFS (inset) transformed in the 2−12 $Å^{-1}$ k range measured at room temperature (He atmosphere) for the three ZrZn-*X* samples. Spectra of ZrZn-5 (blue), ZrZn-15 (yellow), and ZrZn-30 (red) are shown together with those of reference h-ZnO (dashed-black) and Zn metal foil (dashed-gray). FT-EXAFS of ZrZn-5 is missing due to the low absorber concentration as observable from Figure S1b.

3.2.2.2. EXAFS. Detailed information on the Zn local environment can be retrieved by a careful analysis of the EXAFS region. As mentioned above, within the limitations dictated by quasi-simultaneous data collection at Zr and Zn K-edges, analyzable FT-EXAFS spectra were obtained for the ZrZn-15/30 samples (Figure 6, inset). In the specific case of ZrZn-30, the contribution from segregated bulk ZnO, highlighted by PXRD (Figure 1), cannot be easily excluded. Notably, as reported in the Introduction, the catalytic properties of the three samples are not drastically different.[20] Hence, considering the k-space data quality (Figure S1b) and absence of segregated phases, for quantitative EXAFS refinement we focused on the ZrZn-15 sample in order to selectively access information on Zn atoms effectively doping the ZrO_2 matrix.

As observed from the Zr K-edge FT-EXAFS (Figures 4 and 5), the unit cell volume decrease (Figure 1b), and the (101) Bragg peak shift (Figure S3), Zn^{2+} effectively dopes ZrO_2 while locally maintaining a ZnO-like geometry. In order to describe Zn local coordination environment, two main scenarios have to be considered: (i) Zn^{2+} substitutes Zr^{4+} located in position (1/4 3/4 1/4) in t-ZrO_2 ($P4_2nmc$) adapting its interatomic distances to the host lattice, thus forming an ideal t-$ZnZrO_2$ solid solution (Figure 7a) and (ii) Zn^{2+} does not adapt its interatomic distances and forms a ZnO cluster embedded and chemically bonded to the t-ZrO_2 matrix (Figure 7b,c).

The first case seems unreasonable as, to enter in the t-ZrO_2 lattice, Zn should dramatically enlarge its interatomic distance (R_{Zn-O_1} = 3.20 Å and R_{O_1-Zr} = 3.59 Å). From the qualitative analysis of the relevant FT-EXAFS spectra, we note that Zn−Zr interatomic distance does not reflect the value obtained from the Zr K-edge fit ($R_{Zr-Zr} \approx 3.5$ Å). Indeed, the Zn K-edge phase-uncorrected EXAFS second-shell peak position (Figure 6, inset) occurs 0.3 Å below the one at the Zr K-edge (Figure 5). Furthermore, an EXAFS fit carried out using the t-$ZnZrO_2$ structure to reproduce the EXAFS of ZrZn-15 (Table S5) led to meaningless results, including excessively high radial shifts and a negative $\sigma^2_{O_1}$ value. Taken together, these lines of evidence allowed us to safely rule out the ideal solid solution scenario.

In the second case, we should assume that the cluster dimension consists of only few ZnO unit cells, smaller than the PXRD detection limit. We initially described the cluster structure using (i) hexagonal (wurtzite) ZnO ($P6_3mc$), h-ZnO, and (ii) cubic (zinc blende) ZnO ($F\bar{4}3m$), c-ZnO_c where in both cases Zn maintains ZnO_4 tetrahedral coordination (Figure 7b,c).

EXAFS fit in this case yielded physically meaningful results (Figure S11, Table S5). While the oxygen tetrahedra in the first shell of the two structures are very similar (h-R_{Zn-O} = 1.99 Å and c-R_{Zn-O} = 2.00 Å), the main difference arises from the scattering contributions in the second shell. Indeed, in h-ZnO the 12 NNN Zn are located at two different distances (h-$R_{Zn-Zn(1)}$ = 3.20 Å and h-$R_{Zn-Zn(1)}$ = 3.24 Å), while they are equidistant in c-ZnO (c-R_{Zn-Zn_c} = 3.27 Å, see also Figure S7 and Table S3). Anyhow, based on previous reports,[60] in the case of nanostructured h-ZnO only one Zn−Zn SS path with CN = 12 could be safely considered. Fit results in Figure S11 and Table S5 show an almost identical fitting quality using both the h- and c-ZnO structures. Best-fit σ^2_{Zn} values are

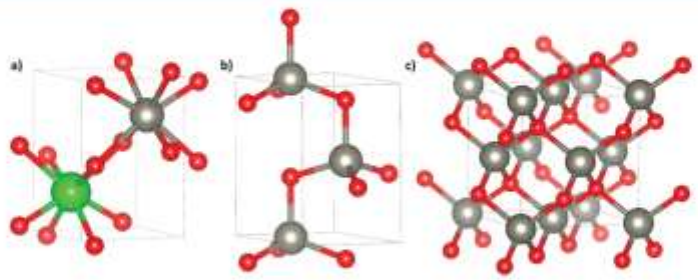

Figure 7. Structures used as input geometries in Zn K-edge EXAFS fits for ZrZn-15. Unit cells of (a) tetragonal ZrO_2 (space group $P4_2nmc$; lattice parameters a = 3.60 Å and c = 5.10 Å[53] from Table S1) substituted with Zn; (b) h-ZnO ($P6_3mc$; a = 3.25 Å and c = 5.21 Å)[59] and (c) c-ZnO ($F\bar{4}3m$, a = 4.63 Å).[58] Zinc (gray), zirconium (green), and oxygen (red) atoms are represented by colored spheres. Oxygen partial occupancy in model (a) is represented by nonfilled colors.

https://doi.org/10.1021/acs.jpcc.1c06203
J. Phys. Chem. C 2021, 125, 22249−22261

acceptable, yet rather high, in both cases. This is not surprising considering the inherently disordered nature of the proposed ZnO nanoclusters chemically bonded in the ZrO_2 matrix. Zn−Zn CN was refined to 4 ± 3, a value far from the ideal bulk condition, corresponding to CN = 12, consistently with the surface-to-bulk ratio increase in nanosized clusters. As previously reported, presence of ZnO nanoparticles on the surface of the ZrZn-*X* samples investigated here, as well as in other works adopting equivalent synthesis methods, was not observed, neither from Raman spectra nor from STEM-EDX analysis.[30,47] We then considered the ZnO clusters as embedded in the ZrO_2 matrix with only part of the surface potentially exposed. Dimensions of ZnO clusters with a given shape can be estimated based on Zn−Zn CNs measured by EXAFS. According to Agostini et al.,[69] only by extending the EXAFS fit at least to the third coordination shell we could obtain a reliable three-dimensional information. In our case, within the available data quality, typical of a catalysis-oriented *in situ* experiment, we preferred to limit the EXAFS fit to the second-shell region. Thus, for the following analysis, we approximated the cluster shape to a sphere. As reported in several previous works,[48−51] under this plausible assumption for the cluster shape, EXAFS CN is unequivocally correlated to the cluster size. As illustrated in Figure 8, using the Greegor and Lytle[35] equation, eq 2, we determined an average cluster radius of 13 ± 7 Å for the ZrZn-15 catalyst, consistent with a PXRD-silent nanosized phase.

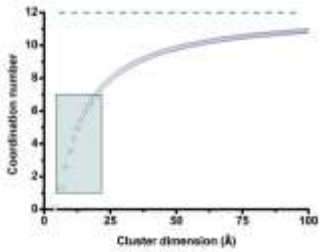

Figure 8. Relation between coordination number and cluster radius evaluated using the Greegor and Lytle equation within the spherical approximation (Supporting Information section 6). Zn−Zn distance found by EXAFS fit was used as shortest atomic distance. The box indicates the area where our experimental data are located (CN = 4 ± 3). Dashed line indicates the coordination number bulk limit (12).

As observed in Figure S11, even if h-ZnO gave the best fit for the experimental spectra, then it does not fully describe the scattering features located in the 3−3.4 Å range in the phase-uncorrected FT-EXAFS spectrum. Having assessed the presence of h-ZnO clusters embedded in a ZrO_2 matrix, a more careful fit of Zn K-edge EXAFS spectra implies to consider the interface between ZnO cluster and ZrO_2 matrix. Since the Zr−Zn scattering path was consistently observed from the Zr K-edge EXAFS fit (section 3.2.1.2), it is also straightforward to consider the presence of this path in the Zn EXAFS fit. As pictorially represented in Figure S10 (h-ZnO/ZrO_2 model), we then described the Zn K-edge second-shell region considering one contribution at shorter distance from (i) a Zn scatterer located in the ZnO cluster core ($Zn-Zn_I$) and two contributions at longer distance from (ii) a Zn scatterer on the surface of the cluster and chemically connected to Zr ($Zn-Zn_{II}$) and (iii) a Zr scatterer (Zn−Zr). As showed in Figure 9 and Table S7, considering these two paths globally improved the fit quality, while the relevant fit variables are comparable with those previously obtained using the simpler h-ZnO model. The h-ZnO cluster dimension was again evaluated from $Zn-Zn_I$ CN (Table S7), resulting in 11 ± 5 Å, which is in line with the 13 ± 7 Å value previously obtained (Table S5). At the same time, the so-obtained radial distances, coordination numbers, and DW factors have physically reliable values, i.e., Zn−Zr and $Zn-Zn_{II}$ paths are longer than the $Zn-Zn_I$ one, confirming the presence of a h-ZnO/ZrO_2 interface, the catalytic role of which will be discussed in the following sections.

3.2.3. In Situ EXAFS during Activation in H_2. Zr and Zn K-edge EXAFS analysis of data obtained at room temperature in He enabled a thorough description of the as prepared catalyst, yet in a catalysis-oriented perspective, it would be of paramount interest also understanding the material structure right before the reaction, i.e., after an activation treatment at high temperature under H_2. As aforementioned, the ZrZn-15 catalyst showed the best compromise between signal quality (Figures S1b and S2b) and catalysis properties. We then extended our analysis focusing on the *in situ* XAS spectra obtained at the Zr and Zn K-edges during activation for this sample. Despite subtle intensity losses, the XANES regions of Zr and Zn K-edges of ZrZn-15 catalyst did not change upon the activation procedure (Figure S12), indicating that oxidation state of both Zn and Zr was not modified by the activation protocol. In the following, we then describe the results and additional insights obtained from the analysis of the EXAFS region of Zr and Zn K-edges.

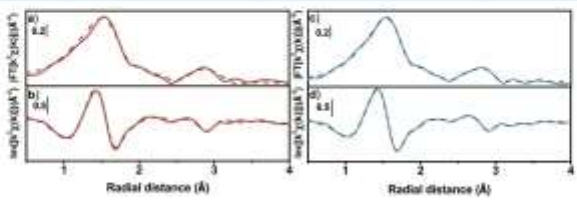

Figure 9. Experimental (solid colored line) and best fit (dashed gray line) (a, c) magnitude and (b, d) imaginary parts for k^3-weighted FT-EXAFS of ZrZn-15 using (a, b) h-ZnO and (c, d) h-ZnO/ZrO_2 (Figure S10) as the input structure.

https://doi.org/10.1021/acs.jpcc.1c06203
J. Phys. Chem. C 2021, 125, 22249−22261

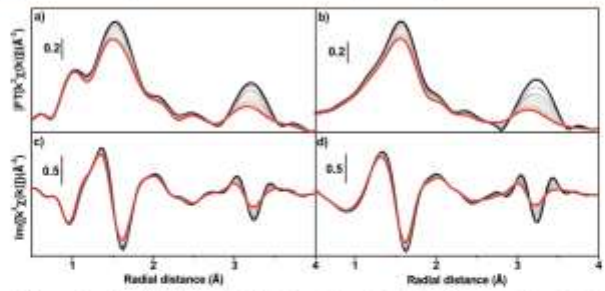

Figure 10. Zr K-edge (a, c) experimental and (b, d) best fit. (a, b) Magnitude and (c, d) imaginary parts of k^3-weighted phase uncorrected FT-EXAFS of ZrZn-15 measured at increasing temperatures (black to red lines) in the room temperature to 400 °C range under H_2 gas flow. Fits are carried out in the k range of 2.5−13 Å^{-1} and R range of 1.0−4.0 Å. Details on the fit results are reported in Figure S13, S14 and Table S6.

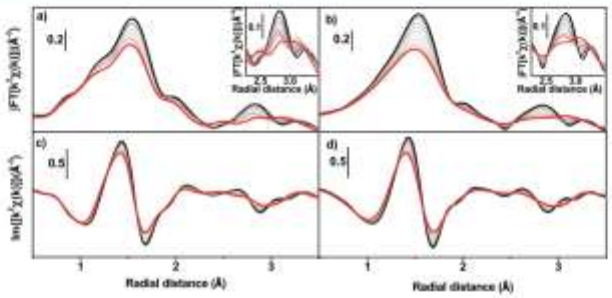

Figure 11. Zn K-edge (a, c) Experimental and (b, d) best fit of (a, b) magnitude and (c, d) imaginary parts of k^3-weighted FT-EXAFS of ZrZn-15 measured at increasing temperatures (black to red lines) in the room temperature to 400 °C range under H_2 gas flow. Magnification of the second-shell region is reported in the insets. Fits are carried out in the k range of 2−12 Å^{-1} and the R range of 1.0−4.0 Å. Details on the fit results are reported in Figure S15 and S16 and Tables S7 and S8.

3.2.3.1. Zr K-Edge. During activation, the phase-uncorrected FT-EXAFS spectra at Zr K-edge in Figure 10a,c showed a constant intensity decrease, consistent with the increase of the thermal contributions to DW factors. The same t-ZrO_2 structural model described in section 3.2.1.2 and Supporting Information section 2 (considering Zr−$O_{I/II}$ and Zr−Zr/Zn scattering paths), was applied to each data set at the ten different temperatures. Complete details on the fit parameters can be found in Supporting Information section 7. The best-fit spectra in Figures 10b,d and S13a,b are in good agreement with the experimental data, well describing the Zr−$O_{I/II}$ and Zr−Zr/Zn shells' intensity loss and shift. DW factors (Figure S14a) showed a linear trend rising with temperature, while the Zr−$O_{I/II}$ radial distances (Figure S14b) remained constant. Considering the antiphase effect involving the Zr−Zr and Zr−Zn scattering paths (Figure 4c) and the increase of their mean square displacement, directly related to the DW factor, we can justify that their radial distances slightly increase up to reaching the same value, showing that at high temperature we cannot safely distinguish between their relative position. The evaluated Einstein temperatures for Zr−O confirmed the presence of stronger Zr−O_I and weaker Zr−O_{II} bonds, in line with the results discussed in section 3.2.1.2. Consistently with the graphical comparison between experimental and best-fit curves (Figures 10 and S13), the corresponding R-factor values (Figure S14c) confirm the reliability of the adopted fitting model.

3.2.3.2. Zn K-edge. Phase-uncorrected FT-EXAFS at Zn K-edge recorded during thermal activation in Figure 11a,c showed a constant decrease of the first- and second-shell intensity related to the increase in DW factors. However, the second shell presents a nontrivial dynamic involving two distinct features. The feature at a lower radial distance (≈ 2.8 Å, phase-uncorrected), previously associated with Zn−Zn_I scattering path, slightly loses intensity. Conversely, the one at higher distance (≈ 3.2 Å), stemming from Zn−Zr and Zn−Zn_{II} scattering paths according to the h-ZnO/ZrO_2 model described in the previous section, shifts to lower values until it convolutes with the former one at high temperature. As shown in Figures S17 and S18, considering the simpler h-ZnO model for fitting the spectra during activation, the second-shell temperature evolution would not be described, leading to unphysically high DW factors, larger errors for the radial distances, and unreliable R-factors. The presence of Zn−Zr/Zn-Zn_{II} scattering paths originating from the h-ZnO/ZrO_2 interface must then be considered to describe the temperature-

https://doi.org/10.1021/acs.jpcc.1c06203
J. Phys. Chem. C 2021, 125, 22249−22261

dependent evolution of EXAFS signal in the second-shell region. Assuming a constant dimension of the ZnO cluster during the activation, a single CN for each path was fit for all the data set, while radial distances were left independent for all the paths in the data set. The fit in Figures 11c,d and S15 shows a good agreement with the experimental data, especially in reproducing the second-shell dynamics. Here, despite a little mismatch in the reproduction of the final intensity, the three contributions of Zn−Zn_I, Zn−Zn_{II}, and Zn−Zr described well the intensity variation of the two features during heating, up to their convolution at high temperatures. The so-obtained DW factors (Figure S16a) showed a linear increase with temperature leading, in the case of Zn−$Zn_{I/II}$, to quite high values but still comparable with those obtained at room temperature. Notably, during heating there is not net radial distance variation in the first coordination shell. Conversely, at high temperature the Zn−Zn_{II}/Zr scattering paths in the second shell are optimized to almost the same interatomic distance (Figure S16b), while a distinction is maintained between scattering paths originating from the core of the ZnO cluster (Zn−Zn_I) and from its surface (Zr−Zn_{II}/Zr). As showed for the Zr K-edge (see section 3.2.1.2), the so-introduced Zn−Zr scattering path is in antiphase with the Zn−Zn_{II}, which would have led to a strong correlation between their CN, DW factors, and radial distances if the Einstein model would have not been applied. The evaluated Zn−Zn_I CN (5.6 ± 1) (Tables S7 and S8) is associated with a ZnO cluster radius of 13 ± 3 Å, in good agreement with values obtained from the EXAFS analysis of room-temperature data. Reliability of the fit is furthermore confirmed by comparable Einstein temperatures for Zr−Zn (269 ± 24 K) and Zn−Zr (226 ± 26 K) and for Zn−Zn_I (174 ± 25 K) and Zn−Zn_{II}(174 ± 26 K) scattering paths (Table S8). The latter also matches literature values.[77] As showed in Table S7, fit reliability is additionally confirmed as values obtained at 312 K/H_2 and 300 K/He from fits carried out with and without the Einstein model, respectively, are entirely comparable.

Noteworthy, the same Zn K-edge second-shell dynamic was observed in the FT-EXAFS of ZrZn-30 catalyst reported in Figure S19. The spectra, collected under the same conditions as for ZrZn-15, showed a thermal DW factor-induced intensity loss for the first- and second-shell peaks. In the latter, even if a stronger Zn−Zn contribution originating from the segregated ZnO phase is present, it is clear that at high temperatures the signal structure follows the same dynamic discussed for ZrZn-15. In the ZrZn-30 case, we could not safely fit the EXAFS spectra, since segregated bulk h-ZnO was observed by PXRD (Figure 1). However, the quantitative results obtained using ZrZn-15 allowed us to qualitatively interpret the EXAFS spectral evolution for ZrZn-30, the most active catalyst, as originating from the interplay between scattering paths involving the core (Zn−Zn_I) and the surface (Zn−Zn_{II}/Zr) of the ZrO_2-embedded ZnO nanoclusters.

3.2.4. Implications for ZnO Clusters and V_O Location. By combining ICP analysis and Rietveld refinement of PXRD data, we quantitatively evaluated the amount of Zn loaded in the ZrO_2 structure excluding the bulk ZnO contribution (Table S1). In parallel, via Zr K-edge FT-EXAFS we obtained indirect information on Zn doping from the second-shell intensity loss (Table 1). The Zn coordination number extracted from Zr−Zn second shell fit is associated with its weight percentage (Table 1), which despite a slight underestimation falls in line with the values in Table S1. The information found by coupling ICP and PXRD refinement is easily accessible by widespread laboratory methods, but it does not provide chemical insights on the Zn dopant nature. Conversely, the Zn-loading-dependent intensity variations in Zr K-edge second-shell peak shows that EXAFS is sensitive to the guest−host structural/chemical proximity, proving that the Zn atom is not simply segregated or impregnated on zirconia but is chemically bonded to the oxidic matrix.

The presence of embedded ZnO nanoclusters (Section 3.2.2.2) explains the underestimation in the Zn wt % obtained from the Zr K-edge FT-EXAFS fit (Table 1) with respect to what was found by ICP and PXRD Rietveld refinement. In fact, the shell intensity can be influenced only by those Zn atoms which are located on the ZnO cluster surface: the bigger the ZnO cluster, the higher the underestimation of the wt % Zn by FT-EXAFS.

As mentioned in section 3.2.1.2, in our Zr K-edge EXAFS analysis, the variable "Zn" used to describe Zr−Zn and Zr−Zr CNs was also simultaneously used for Zr−O CN (i.e., 8 − Zn). CN and DW factors strongly correlate in the EXAFS equation; however, the simultaneous fit of Zr−O and Zr−Zr/Zn with the same variable Zn increases the latter reliability. The nature of the catalysis-oriented *in situ* XAS experiment does not allow us to quantify V_O. Nevertheless, as shown in eq 1, each Zn generates a V_O, leading to an average Zr−O coordination of ZrO_{8-2x} (where Zn is the same variable refined in the EXAFS fit), which would unlikely form a stable t-ZrO_2 phase. We should then consider that the average ZrO_{8-2x} configuration detected by EXAFS must be realized by combinations of ZrO_8 and ZrO_{8-x} (where x = 1, 2, 3, and 4) polyhedra which host the V_O, most likely localized at the periphery of ZrO_2-embedded ZnO clusters. The fwhm of the XANES feature A (Figure 3), sensitive to the Zr local geometry, shows that a higher concentration of Zn distorts the ZrO_8 double tetrahedra, supporting this hypothesis.

EXAFS spectra at Zr and Zn K-edges of the catalyst are described considering the presence of Zr−Zn and Zn−Zr scattering paths, respectively, for both measurements at room temperature in He and *in situ* temperature-dependent data collected during activation in H_2. These results confirm that Zn doping occurs with formation of ZnO clusters, the surface of which is chemically bonded to the ZrO_2 matrix. This finally led us to critically observe the variations in Zn K-edge EXAFS spectra of the activated catalysts after exposure to the reaction mixture (CO_2/H_2) under catalysis-relevant conditions. In this respect, some inherent limitations should be considered, mainly related to the following facts: (i) The catalysts presented a relatively low surface area (46 m^2/g).[79] (ii) CO_2/H_2 interactions are limited to the material surface, and (iii) XAS is a mainly bulk-sensitive technique. Nonetheless, as shown in Figure S20, subtle modifications can be noted in the Zn K-edge EXAFS spectra collected before and after the reaction, carried by sending a CO_2/H_2 feed at 300 °C/15 bar over activated ZrZn-15 and ZrZn-30. Notably, the scattering features previously assigned to the Zn−Zn_I shell, originating from the ZnO cluster core, is unaltered under reaction conditions. Conversely, the EXAFS feature stemming from the Zn−Zn_{II}/Zr contributions varies after the reaction, suggesting that these scattering paths are those influenced by the coordination of adsorbed reactants and products. These observations, guided by the quantitative analysis of *in situ* EXAFS data presented in section 3.2.3, consistently suggest that the interface between the ZnO cluster and the ZrO_2

https://doi.org/10.1021/acs.jpcc.1c06203
J. Phys. Chem. C 2021, 125, 22249−22261

matrix represent the active site toward CO_2 hydrogenation, where molecular events involving CO_2 adsorption/activation, H_2 splitting, and CH_3OH production ultimately take place.

4. CONCLUSIONS

In the present work, we combined PXRD and XAS to take a step further in the fundamental understanding of Zn-doped ZrO_2 catalysts, active toward CO and CO_2 hydrogenation. The XAS data set, even if measured in a catalysis-oriented experiment (i.e., on pressed and sieved catalyst powders hosted in a capillary reactor, at room temperature or higher temperatures), showed a great potential for clarifying the Zn-doped ZrO_2 atomic-scale structure through parallel analysis of data at Zr and Zn K-edges. While the ZrO_2 $d_{(101)}$ Bragg reflection shift was related to the presence of Zn in the ZrO_2 lattice, the t-ZrO_2 fingerprint peak identified by PXRD, close to the data set noise, cannot unambiguously identify the ZrO_2 polymorph. However, by coupling analysis of Zr K-edge XANES pre-edge features with EXAFS fitting, we safely confirmed the presence of t-ZrO_2. In addition, Zr K-edge EXAFS fit revealed Zn atoms chemically bonded to Zr, while Zn K-edge EXAFS unveiled the presence of h/c-ZnO clusters. Since previous measurements[20,21] did not show the presence of ZnO nanoparticles on ZrO_2 surface, we assumed the ZnO cluster to be largely embedded in the ZrO_2 matrix, with only a minor fraction exposed at the catalyst surface. Broadening of the size distribution cannot be accessed by EXAFS, while details on the cluster shape could be only accessed considering a fit extended to the third and fourth coordination shell, which would be unreliable within the available data quality. However, under the spherical shape approximation, we were able to estimate the average radius of ZrO_2-embedded ZnO clusters. In particular, a Zn−Zn CN value far from the ideal bulk condition, was refined from Zn K-edge EXAFS analysis of ZrZn-15 (15 wt % of Zn doping). The relation between the EXAFS-determined CN and cluster dimension was calculated by the Greegor and Lytle equation, showing an average radius of 11 ± 5 Å (or 13 ± 3 Å, evaluated from the analysis of *in situ* XAS data), small enough to escape detection by PXRD. Careful analysis of the *in situ* EXAFS data shows the presence of Zn−O−Zr interaction from both Zr and Zn K-edges, supporting the hypothesis that Zn-doped ZrO_2 catalysts consist of ZnO clusters chemically bonded to the ZrO_2 matrix. It is then the ZnO/ZrO_2 interface, where V_O are mostly located, the active phase toward CO_2 hydrogenation. More than increasing the Zn content, improving ZnO/ZrO_2 interface area is then envisaged as an effective way to maximize the catalyst activity. Taken together, this evidence provides, to the best of our knowledge, the deepest structural picture available so far on Zn-doped ZrO_2 catalysts. While highlighting the richness of information accessible from a wise combination of X-ray methods probing long range order and local structure in mixed-metal oxides, the obtained insights pave the way to the rational design of improved catalysts for CO_2 valorization.

■ ASSOCIATED CONTENT

Supporting Information

The Supporting Information is available free of charge at https://pubs.acs.org/doi/10.1021/acs.jpcc.1c06202.

K-space EXAFS spectra; additional PXRD results; EXAFS fitting for reference t-ZrO_2; fwhm analysis of first derivative of the Zr K-edge XANES main edge; EXAFS fitting for reference h-ZnO; test Zr K-edge EXAFS fitting of ZrZn-5 using a c-ZrO_2 model; additional details on input structures employed in Zn K-edge EXAFS fitting; additional details on cluster size evaluation; additional details on *in situ* XAS data during activation in H_2 and related EXAFS analysis using the Einstein model; *in situ* XAS data under reaction conditions (CO_2/H_2, 300 °C, 15 bar) (PDF)

■ AUTHOR INFORMATION

Corresponding Author

Elisa Borfecchia − *Department of Chemistry, NIS Center and INSTM Reference Center, University of Turin, 10125 Turin, Italy;* orcid.org/0000-0001-8374-8329; Email: elisa.borfecchia@unito.it

Authors

Davide Salusso − *Department of Chemistry, NIS Center and INSTM Reference Center, University of Turin, 10125 Turin, Italy;* orcid.org/0000-0001-7927-4001

Silvia Bordiga − *Department of Chemistry, NIS Center and INSTM Reference Center, University of Turin, 10125 Turin, Italy;* orcid.org/0000-0003-2371-4156

Complete contact information is available at: https://pubs.acs.org/10.1021/acs.jpcc.1c06202

Notes

The authors declare no competing financial interest.

■ ACKNOWLEDGMENTS

This project received funding from the European Union's Horizon 2020 research and innovation program under grant agreement no. 837733 (COZMOS project). XAS measurements on ROCK were supported by a public grant overseen by the French National Research Agency (ANR) as part of the "Investissements d'Avenir" program (reference: ANR-10-EQPX-45). We are grateful to the beamline staff (C. La Fontaine, V. Briois) and to K. A. Lomachenko, A. L. Bugaev, C. Ahoba-Sam, and A. Lazzarini for the help with the XAS measurements at ROCK, Soleil. We are also grateful to P. Ticali and S. Morandi (University of Turin) as well as to the other colleagues involved in the COZMOS project for insightful discussions and support, especially to C. Ahoba-Sam (University of Oslo) and A. Ramirez (King Abdullah University of Science and Technology) for catalyst synthesis and catalytic tests, respectively. We also thank G. Fiore for precious advice on Rietveld Refinement method. We are grateful to the reviewers for critically reading the manuscript and helping us in substantially improving this work with their constructive comments.

■ REFERENCES

(1) Tanabe, K. Surface and Catalytic Properties of ZrO_2. *Mater. Chem. Phys.* **1985**, *13*, 347−364.

(2) Yamaguchi, T. Application of ZrO_2 as a Catalyst and a Catalyst Support. *Catal. Today* **1994**, *20*, 199−217.

(3) Dong, X.; Li, F.; Zhao, N.; Xiao, F.; Wang, J.; Tan, Y. CO_2 Hydrogenation to Methanol over Cu/ZnO/ZrO_2 Catalysts Prepared by Precipitation-Reduction Method. *Appl. Catal., B* **2016**, *191*, 8−17.

(4) Pokrovski, K.; Jung, K. T.; Bell, A. T. Investigation of CO and CO_2 Adsorption on Tetragonal and Monoclinic Zirconia. *Langmuir* **2001**, *17*, 4297−4303.

(5) Rockström, J.; Steffen, W.; Noone, K.; Persson, Å.; Chapin, F. S.; Lambin, E. F.; Lenton, T. M.; Scheffer, M.; Folke, C.; Schellnhuber, H. J.; Nykvist, B.; de Wit, C. A.; Hughes, T.; van der Leeuw, S.; Rodhe, H.; Sörlin, S.; Snyder, P. K.; Costanza, R.; Svedin, U.; Falkenmark, M.; Karlberg, L.; Corell, R. W.; Fabry, V. J.; Hansen, J.; Walker, B.; Liverman, D.; Richardson, K.; Crutzen, P.; Foley, J. A. A Safe Operation Space for Humanity. *Nature* **2009**, *461*, 472−475.
(6) Zhou, W.; Cheng, K.; Kang, J.; Zhou, C.; Subramanian, V.; Zhang, Q.; Wang, Y. New Horizon in C1 Chemistry: Breaking the Selectivity Limitation in Transformation of Syngas and Hydrogenation of CO_2 into Hydrocarbon Chemicals and Fuels. *Chem. Soc. Rev.* **2019**, *48*, 3193−3228.
(7) Cole, M.; Catlow, C. R. A.; Dragun, J. P. EXAFS Studies of Doped-ZrO_2 Systems. *J. Phys. Chem. Solids* **1990**, *51*, 507−513.
(8) Huang, J.; Li, W.; Wang, K.; Huang, J.; Liu, X.; Fu, D.; Li, Q.; Zhan, G. M XO Y-ZrO_2 (M = = Zn, Co, Cu) Solid Solutions Derived from Schiff Base-Bridged UiO-66 Composites as High-Performance Catalysts for CO_2 Hydrogenation. *ACS Appl. Mater. Interfaces* **2019**, *11*, 33263−33272.
(9) Chagas, L. H.; Zonetti, P. C.; Matheus, C. R. V.; Rabello, C. R. K.; Alves, O. C.; Appel, L. G. The Role of the Oxygen Vacancies in the Synthesis of 1, 3-Butadiene from Ethanol. *ChemCatChem* **2019**, *11*, 5625−5632.
(10) Silva-Calpa, L. del R.; Zonetti, P. C.; Rodrigues, C. P.; Alves, O. C.; Appel, L. G.; de Avillez, R. R. The $Zn_xZr_{1-x}O_{2-y}$ Solid Solution on m-ZrO_2: Creating O Vacancies and Improving the m-ZrO_2 Redox Properties. *J. Mol. Catal. A: Chem.* **2016**, *425*, 166−173.
(11) Wang, C.; Garbarino, G.; Allard, L. F.; Wilson, F.; Busca, G.; Flytzani-Stephanopoulos, M. Low-Temperature Dehydrogenation of Ethanol on Atomically Dispersed Gold Supported on ZnZrOx. *ACS Catal.* **2016**, *6*, 210−218.
(12) Han, S.; Zhao, D.; Otroshchenko, T.; Lund, H.; Bentrup, U.; Kondratenko, V. A.; Rockstroh, N.; Bartling, S.; Doronkin, D. E.; Grunwaldt, J. D.; Rodemerck, U.; Linke, D.; Gao, M.; Jiang, G.; Kondratenko, E. V. Elucidating the Nature of Active Sites and Fundamentals for Their Creation in Zn-Containing ZrO_2-Based Catalysts for Nonoxidative Propane Dehydrogenation. *ACS Catal.* **2020**, *10*, 8933−8949.
(13) Zhou, S.; Li, S. Insights into the High Activity and Methanol Selectivity of the Zn/ZrO_2 Solid Solution Catalyst for CO_2 Hydrogenation. *J. Phys. Chem. C* **2020**, *124*, 27467−27478.
(14) Aghabeygi, S.; Khadomi-Shamami, M. ZnO/ZrO_2 Nanocomposite: Sonosynthesis, Characterization and Its Application for Wastewater Treatment. *Ultrason. Sonochem.* **2018**, *41*, 458−465.
(15) Wu, X.; Tan, M.; Tian, S.; Song, F.; Ma, Q.; He, Y.; Yang, G.; Tsubaki, N.; Tan, Y. Designing ZrO_2-Based Catalysts for the Direct Synthesis of Isobutene from Syngas: The Studies on Zn Promoter Role. *Fuel* **2019**, *243*, 34−40.
(16) Liu, X.; Zhou, W.; Yang, Y.; Cheng, K.; Kang, J.; Zhang, L.; Zhang, G.; Min, X.; Zhang, Q.; Wang, Y. Design of Efficient Bifunctional Catalysts for Direct Conversion of Syngas into Lower Olefins: Via Methanol/Dimethyl Ether Intermediates. *Chem. Sci.* **2018**, *9*, 4708−4718.
(17) Liu, Y.; Xia, C.; Wang, Q.; Zhang, L.; Huang, A.; Ke, M.; Song, Z. Direct Dehydrogenation of Isobutane to Isobutene over Zn-Doped ZrO_2 Metal Oxide Heterogeneous Catalysts. *Catal. Sci. Technol.* **2018**, *8*, 4916−4924.
(18) Cheng, K.; Zhou, W.; Kang, J.; He, S.; Shi, S.; Zhang, Q.; Pan, Y.; Wen, W.; Wang, Y. Bifunctional Catalysts for One-Step Conversion of Syngas into Aromatics with Excellent Selectivity and Stability. *Chem.* **2017**, *3*, 334−347.
(19) Shannon, B. Y. R. D.; H, M.; Baur, N. H.; Gibbs, O. H.; Eu, M.; Cu, V. Revised Effective Ionic Radii and Systematic Studies of Interatomic Distances in Halides and Chalcogenides. *Acta Crystallogr., Sect. A: Cryst. Phys., Diffr., Theor. Gen. Crystallogr.* **1976**, *32*, 751−767.
(20) Ticali, P.; Salusso, D.; Ahmad, R.; Ahoba-Sam, C.; Ramirez, A.; Shterk, G.; Lomachenko, K. A.; Bordiga, S.; Morandi, S.; Cavallo, L.; Gascon, J.; Bordiga, S.; Olsbye, U. CO_2 Hydrogenation to Methanol and Hydrocarbons over Bifunctional Zn-Doped ZrO_2/Zeolite Catalysts. *Catal. Sci. Technol.* **2021**, *11*, 1249−1268.
(21) Wang, G.; Zeng, L.; Cao, J.; Liu, F.; Lin, Q.; Yi, Y.; Pan, H. Highly Selective Conversion of CO_2 to Hydrocarbons over Composite Catalysts of ZnO-ZrO_2 and SAPO-34. *Microporous Mesoporous Mater.* **2019**, *284*, 133−140.
(22) Li, Z.; Qu, Y.; Wang, J.; Liu, H.; Li, M.; Miao, S.; Li, C. Highly Selective Conversion of Carbon Dioxide to Aromatics over Tandem Catalysts. *Joule* **2019**, *3*, 570−583.
(23) Zhang, T. ZnO-ZrO_2 Solid Solution Catalyst for Highly Selective Hydrogenation of CO_2 to Methanol. *Caihua Xuebao/Chin. J. Catal.* **2017**, *38*, 1781−1783.
(24) Murthy, P. S.; Liang, W.; Jiang, Y.; Huang, J. Cu-Based Nanocatalysts for CO_2 Hydrogenation to Methanol. *Energy Fuels* **2021**, *35*, 8558−8584.
(25) Greegor, R. B.; Lytle, F. W. Morphology of Supported Metal Clusters: Determination by EXAFS and Chemisorption. *J. Catal.* **1980**, *63*, 476−486.
(26) Rodríguez-Carvajal, J. Recent Developments of the Program Fullprof. *Newsl. Comm. Powder Diffr. IUCr* **2001**, *26*, 12−19.
(27) Thompson, P.; Cox, D. E.; Hastings, J. B. Rietveld Refinement of Debye-Scherrer Synchrotron X-Ray Data from Al_2O_3. *J. Appl. Crystallogr.* **1987**, *20*, 79−83.
(28) La Fontaine, C.; Belin, S.; Barthe, L.; Roudenko, O.; Briois, V. ROCK: A Beamline Tailored for Catalysis and Energy-Related Materials from ms Time Resolution to mm Spatial Resolution. *Synchrotron Radiat. News* **2020**, *33*, 20−25.
(29) Ravel, B.; Newville, M. ATHENA, ARTEMIS, HEPHAESTUS: Data Analysis for X-Ray Absorption Spectroscopy Using IFEFFIT. *J. Synchrotron Radiat.* **2005**, *12*, 537−541.
(30) Momma, K.; Izumi, F. VESTA 3 for Three-Dimensional Visualization of Crystal, Volumetric and Morphology Data. *J. Appl. Crystallogr.* **2011**, *44*, 1272−1276.
(31) Rehr, J. J.; Albers, R. C. Theoretical Approaches to X-Ray Absorption Fine Structure. *Rev. Mod. Phys.* **2000**, *72*, 621−654.
(32) Zabinsky, S. I.; Rehr, J. J.; Ankudinov, A.; Albers, R. C.; Eller, M. J. Multiple-Scattering Calculations of x-Ray-Absorption Spectra. *Phys. Rev. B: Condens. Matter Mater. Phys.* **1995**, *52*, 2995−3009.
(33) Teufer, G. The Crystal Structure of Tetragonal ZrO_2. *Acta Crystallogr.* **1962**, *15*, 1187.
(34) Kröger, F. A.; Vink, H. J. Relations between the Concentrations of Imperfections in Crystalline Solids. *Solid State Phys.* **1956**, *3*, 307−435.
(35) Abrahams, S. C.; Bernstein, J. L. Remeasurement of the Structure of Hexagonal ZnO. *Acta Crystallogr., Sect. B: Struct. Crystallogr. Cryst. Chem.* **1969**, *25*, 1233−1236.
(36) Bragg, W. L.; Darbyshire, J. A. The Structure of Thin Films of Certain Metallic Oxides. *Trans. Faraday Soc.* **1932**, *28*, 522−529.
(37) Sevillano, E.; Meuth, H.; Rehr, J. J. Extended X-Ray Absorption Fine Structure Debye-Waller Factors. I. Monatomic Crystals. *Phys. Rev. B: Condens. Matter Mater. Phys.* **1979**, *20*, 4908−4911.
(38) Braglia, L.; Borfecchia, E.; Martini, A.; Bugaev, A. L.; Soldatov, A. V.; Øien-ØDegaard, S.; Lønstad-Bleken, B. T.; Olsbye, U.; Lillerud, K. P.; Lomachenko, K. A.; Agostini, G.; Manzoli, M.; Lamberti, C. The Duality of UiO-67-Pt MOFs: Connecting Treatment Conditions and Encapsulated Pt Species by: Operando XAS. *Phys. Chem. Chem. Phys.* **2017**, *19*, 27489−27507.
(39) Øien, S.; Agostini, G.; Svelle, S.; Borfecchia, E.; Lomachenko, K. A.; Mino, L.; Gallo, E.; Bordiga, S.; Olsbye, U.; Lillerud, K. P.; Lamberti, C. Probing Reactive Platinum Sites in Uio-67 Zirconium Metal-Organic Frameworks. *Chem. Mater.* **2015**, *27*, 1042−1056.
(40) Fornasini, P.; Grisenti, R. On EXAFS Debye-Waller Factor and Recent Advances. *J. Synchrotron Radiat.* **2015**, *22*, 1242−1257.
(41) Martin, U.; Boysen, H.; Frey, F. Neutron Powder Investigation of Tetragonal and Cubic Stabilized Zirconia, TZP and CSZ, at Temperatures up to 1400 K. Acta Crystallogr. *Acta Crystallogr., Sect. B: Struct. Sci.* **1993**, *49*, 403−413.

(42) Frandon, J.; Brousseau, B.; Pradal, F. Electronic Excitations in Some Transition Metals and Their Oxides. *Phys. Status Solidi B* **1980**, *98*, 379−385.
(43) Li, P.; Chen, I. W.; Penner-Hahn, J. E. X-Ray-Absorption Studies of Zirconia Polymorphs. I. Characteristic Local Structures. *Phys. Rev. B: Condens. Matter Mater. Phys.* **1993**, *48*, 10063−10073.
(44) Li, P.; Chen, I. W.; Penner-Hahn, J. E. X-Ray-Absorption Studies of Zirconia Polymorphs. III. Static Distortion and Thermal Distortion. *Phys. Rev. B: Condens. Matter Mater. Phys.* **1993**, *48*, 10082−10089.
(45) Gilbert, B.; Frazer, B. H.; Zhang, H.; Huang, F.; Banfield, J. F.; Haskel, D.; Lang, J. C.; Srajer, G.; De Stasio, G. X-Ray Absorption Spectroscopy of the Cubic and Hexagonal Polytypes of Zinc Sulfide. *Phys. Rev. B: Condens. Matter Mater. Phys.* **2002**, *66*, 1−6.
(46) Wilmer, H.; Kurtz, M.; Klementiev, K. V.; Tkachenko, O. P.; Grünert, W.; Hinrichsen, O.; Birkner, A.; Rabe, S.; Merz, K.; Driess, M.; Wöll, C.; Muhler, M. Methanol Synthesis over ZnO: A Structure-Sensitive Reaction? *Phys. Chem. Chem. Phys.* **2003**, *5*, 4736−4742.
(47) Wang, J.; Li, G.; Li, Z.; Tang, C.; Feng, Z.; An, H.; Liu, H.; Liu, T.; Li, C. A Highly Selective and Stable ZnO-ZrO_2 Solid Solution Catalyst for CO_2 Hydrogenation to Methanol. *Sci. Adv.* **2017**, *3*, e1701290.
(48) Agostini, G.; Piovano, A.; Bertinetti, L.; Pellegrini, R.; Leofanti, G.; Groppo, E.; Lamberti, C. Effect of Different Face Centered Cubic Nanoparticle Distributions on Particle Size and Surface Area Determination: A Theoretical Study. *J. Phys. Chem. C* **2014**, *118*, 4085−4094.
(49) Frenkel, A. I.; Yevick, A.; Cooper, C.; Vasic, R. Modeling the Structure and Composition of Nanoparticles by Extended X-Ray Absorption Fine-Structure Spectroscopy. *Annu. Rev. Anal. Chem.* **2011**, *4*, 23−39.
(50) Frenkel, A. I. Applications of Extended X-Ray Absorption Fine-Structure Spectroscopy to Studies of Bimetallic Nanoparticle Catalysts. *Chem. Soc. Rev.* **2012**, *41*, 8163−8178.
(51) Kuzmin, A.; Chaboy, J. EXAFS and XANES Analysis of Oxides at the Nanoscale. *IUCrJ* **2014**, *1*, 571−589.
(52) Tchuigoua, B. H.; Sendja, B. T.; Mane, J. M.; Aquilanti, G.; Plaisier, J. R. EXAFS Study of the Temperature Dependence of the Debye-Waller Factor in ZnSe Zincblende Compound. *Phys. Scr.* **2020**, *95*, 045704.

https://doi.org/10.1021/acs.jpcc.1c06203
J. Phys. Chem. C 2021, 125, 22249−22261

6.3 C : Ramirez A., et al., JACS Au 2021, 1, 10, 1719–1732

JACS Au

Multifunctional Catalyst Combination for the Direct Conversion of CO_2 to Propane

Adrian Ramirez, Pierfrancesco Ticali, Davide Salusso, Tomas Cordero-Lanzac, Samy Ould-Chikh, Christian Ahoba-Sam, Aram L. Bugaev, Elisa Borfecchia, Sara Morandi, Matteo Signorile, Silvia Bordiga,* Jorge Gascon,* and Unni Olsbye*

Cite This: JACS Au 2021, 1, 1719−1732 Read Online

ACCESS | Metrics & More | Article Recommendations | Supporting Information

ABSTRACT: The production of carbon-rich hydrocarbons via CO_2 valorization is essential for the transition to renewable, non-fossil-fuel-based energy sources. However, most of the recent works in the state of the art are devoted to the formation of olefins and aromatics, ignoring the rest of the hydrocarbon commodities that, like propane, are essential to our economy. Hence, in this work, we have developed a highly active and selective PdZn/ZrO_2+SAPO-34 multifunctional catalyst for the direct conversion of CO_2 to propane. Our multifunctional system displays a total selectivity to propane higher than 50% (with 20% CO, 6% C_1, 13% C_2, 10% C_4, and 1% C_5) and a CO_2 conversion close to 40% at 350 °C, 50 bar, and 1500 mL g^{-1} h^{-1}. We attribute these results to the synergy between the intimately mixed PdZn/ZrO_2 and SAPO-34 components that shifts the overall reaction equilibrium, boosting CO_2 conversion and minimizing CO selectivity. Comparison to a PdZn/ZrO_2+ZSM-5 system showed that propane selectivity is further boosted by the topology of SAPO-34. The presence of Pd in the catalyst drives paraffin production via hydrogenation, with more than 99.9% of the products being saturated hydrocarbons, offering very important advantages for the purification of the products.

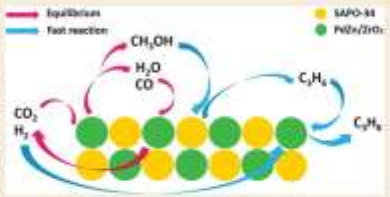

KEYWORDS: CO_2 conversion, hydrogenation, propane, tandem catalysts, zeolites, kinetics, reaction mechanism

1. INTRODUCTION

Carbon capture and utilization (CCU) is critical to reducing CO_2 emissions and mitigating global warming.[1] Through the production of carbon-rich hydrocarbons via CO_2 valorization,[2,3] CCU is expected to pave the route for the transition to renewable, non-fossil-fuel-based energy sources.[4]

One of the most promising approaches toward CO_2 valorization consists of the combination of conventional metallic catalysts with acidic zeolites.[5] This combination can directly transform CO_2 to a great variety of chemicals with a selectivity above the limitation of the Anderson−Schulz−Flory distribution (ASF).[6] However, most of the work to date has been limited to the production of either olefins or aromatics, with the rest of essential hydrocarbons being barely studied.[7] This is of particular importance as, for a real circular carbon economy (CCE), other common hydrocarbons and fuels should be as well produced via CO_2.[8] One example of essential hydrocarbon with high demand is propane.

Propane is nowadays produced as a byproduct in two other processes, natural gas processing and petroleum refining. The propane market is expected to grow at 5% per year, adding up to 350 million metric tons per year in 2025[9] (with the potential therefore to account for 1050 million metric tons of CO_2), being the industrial and residential sectors the two most relevant actors. In industrial processes, propane is used for large-scale applications such as furnaces and heaters. And in the residential sector, propane is widely used for air conditioning, heating, refrigeration, production of textiles, lighting, and other uses. However, despite the obvious importance of this hydrocarbon, propane formation from CO_2 has been barely touched in the available literature,[10,11] and only a few prior papers targeted paraffin formation, mostly from syngas.[12−17]

Hence, with propane production in mind, in this work we have developed a highly active and selective PdZn/ZrO_2+SAPO-34 multifunctional catalyst. In particular, we took advantage of the hydrogenation function of the Pd component and the high C_3 selectivity of the SAPO-34 to

Received: July 6, 2021
Published: September 2, 2021

develop a catalytic system with high selectivity toward propane. Zn and ZrO_2 were also included in the formulation because of the well-known ability of these elements to efficiently convert CO_2 to methanol,[16] the first step in the overall multifunctional mechanism.[6]

The resulting PdZn/ZrO_2+SAPO-34 catalytic system displays a total selectivity to propane higher than 50% with a CO_2 conversion close to 40% and only 20% of CO selectivity at 350 °C, 50 bar, and 1500 mL g^{-1} h^{-1}. To the best of our knowledge, this is the highest total selectivity per pass ever reported for a single C_{2+} hydrocarbon during CO_2 valorization.[1,2] We attribute these results to the intimate contact between the PdZn/ZrO_2 and SAPO-34 components that shifts the overall reaction equilibrium, ultimately boosting CO_2 conversion and minimizing CO selectivity. Kinetic modeling of the catalytic data alongside with thermodynamic equilibrium calculations fully support this hypothesis. Lastly, the presence of Pd in the catalyst drives paraffin production via hydrogenation, with more than 99.9% of the products being saturated hydrocarbons, offering very important advantages for the purification of the products.

2. EXPERIMENTAL SECTION

2.1. Catalyst Preparation

$Pd(CH_3COO)_2$ (>99.9%), $Zn(CH_3COO)_2$ (99.99%), $Zr(OH)_4$, PVP (Mwt 10000), DMF (99.8%), and ethylene glycol (99.8%) were purchased from Sigma-Aldrich and used as received. ZSM-5 (SiO_2/Al_2O_3 = 23) was purchased from Zeolyst. SAPO-34 (SiO_2/Al_2O_3 = 0.5) was purchased from ACS materials. All the zeolites were dried at 120 °C for 12 h and calcined at 550 °C for 2 h prior to testing.

The PdZn/ZrO_2 catalyst was obtained by a colloidal impregnation method. Briefly, 5 g L^{-1} of $Pd(CH_3COO)_2$ was dissolved in DMF and 20 g L^{-1} $Zn(CH_3COO)_2$ dissolved in ethylene glycol were prepared. Eight grams of PVP was added to 80 mL of the Zn precursor solution and heated to 80 °C to obtain a clear yellow solution. Fifty milliliters of the Pd precursor solution was added to the clear yellow zinc/PVP solution amidst stirring and heated to 100 °C under reflux for 2 h. The colloidal mixture was cooled, centrifuged, and washed with acetone and then dispersed in ethanol. The dispersed colloidal mixture in ethanol was added to 6 g of $Zr(OH)_4$ powder and stirred for 20 h at room temperature. The resulting mixture was oven-dried and calcined at 500 °C for 3 h. The multifunctional PdZn/ZrO_2+zeolite catalysts were prepared by mortar mixing of both components with a 1:1 mass ratio.

2.2. Catalytic Tests and Kinetic Modeling

Catalytic tests were executed in a 16 channel Flowrence from Avantium. Fifty milligrams of the stand-alone PdZn/ZrO_2 catalyst and 100 mg of composite catalyst with PdZn/ZrO_2+zeolite with a mass ratio of 1/1 in a mixed bed configuration were typically used. Both functions were pelletized together in a 1/1 ratio, and then sieved to a particle size 150−250 μm. The mixed feed had 22.5 vol % of CO_2, 72.5 vol % of H_2, and 5% of He as internal standard. For the catalyst activity evaluation, we aimed at a gas hourly space velocity (GHSV) value of 12000 mL g^{-1} h^{-1} per channel. One of the 16 channels was always used without catalyst as blank. The reaction temperature was typically set at 350 °C. Prior to feeding the reaction mixture all samples were pretreated in situ with a pure H_2 atmosphere for 4 h at 400 °C. The tubes were then pressurized to 30 bar using a membrane-based pressure controller. Extra runs were also performed in order to evaluate the kinetics of the reactions using the stand-alone PdZn/ZrO_2 catalyst and the multifunctional catalytic system. For this purpose, operation conditions were ranged between 250 and 350 °C, 30−50 bar and 1500−30 000 mL g^{-1} h^{-1}.

Reaction products were analyzed online in a gas chromatograph. The GC is an Agilent 7890B with three detectors, a TCD and 2 FIDs. TCD is equipped with 2 Haysep precolumn and a MSSA, where He, H_2, CH_4, CO_2, and CO are separated. FIDs are equipped with Gaspro and an Innowax columns. Gaspro separates C_1−C_5 hydrocarbons and DME. Innowax separates oxygenates and aromatics.

Conversion (X, %) and selectivity ($S_{C_nH_m}$ %) are defined as follow:

$$X_{CO_2} = \left(1 - \frac{C_{He,blk} C_{CO_2,R}}{C_{He,R} C_{CO_2,blk}}\right) 100 \quad (1)$$

$$S_{C_nH_m} = \frac{\frac{nC_{C_nH_m}}{C_{He,R}}}{\left(\frac{C_{CO_2,blk}}{C_{He,blk}} - \frac{C_{CO_2,R}}{C_{He,R}}\right)} \cdot 100 \quad (2)$$

where $C_{He,blk}$, $C_{He,R}$, $C_{CO2,blk}$, and $C_{CO2,R}$ are the concentrations determined by GC analysis of He in the blank, He in the reactor effluent, CO_2 in the blank, and CO_2 in the reactor effluent, respectively, and $C_{Cn,R}$ is the concentration of the reactor effluent determined be GC analysis of a product with n carbon atoms. The error in carbon balance was better than 2.5% in all cases.

Experimental results collected with both the stand-alone PdZn/ZrO_2 catalyst and the multifunctional PdZn/ZrO_2+SAPO-34 catalytic system were fitted by means of kinetic modeling in order to estimate and compare the rates of the reactions. Because of the characteristics of the experimental setup, some assumptions can be made, thereby simplifying the system. More details can be found in the Supporting Information. Briefly, a steady-state plug flow model, working at isothermal and isobaric conditions, is assumed for the reactor. To avoid mathematical uncertainty and strictly compare reaction rates, we considered two equilibrium reactions: CO_2 hydrogenation to methanol and the reverse water−gas shift reaction. Equilibrium constants were considered with empirical correlations, and the results were contrasted with those obtained from the *FactSage* equilibrium database. For the multifunctional system where methanol is further transformed to hydrocarbons, a fast conversion of methanol to propane is assumed, with both methanol-to-propene and propene hydrogenation considered to be quite faster than CO_2/CO/MeOH equilibria.

2.3. Characterization of Catalysts

The powder X-ray diffraction (XRD) measurements were performed by using a Bruker D8 Discover, with a Cu Kα source and a Lynx Eye silicon detector. The diffractograms were scanned with step size of 0.02° in the 2θ range of 10−90°. The crystalline phase was identified by comparison with data from the inorganic crystal structure database, *ICSD*.

Nitrogen adsorption-desorption isotherms were recorded using a Micromeritics ASAP 2040 at −196 °C. Samples were previously evacuated at 100 °C for 16 h. The Brunauer−Emmett−Teller (BET) method was used to calculate the surface area. The p/p_0 range for BET analysis was $0.067 < p/p_0 < 0.249$.

The temperature-programmed desorption (TPD) experiments were carried out in a Micromeritics ASAP 2020. The catalyst samples were first heated in helium flow at 350 °C for 4 h, followed by cooling to 50 °C. After cooling, the zeolites were saturated in ammonia and the temperature of the samples was increased linearly at a rate of 10 °C/min. Ammonia was fed at atmospheric pressure with a 5% vol. NH_3 concentration was diluted in Helium. The ammonia desorption was continuously monitored by a thermal conductivity detector.

Thermogravimetric analyses (TGA) of catalysts were carried out in a TGA/DSC1 STAR·e system apparatus (Mettler Toledo). Before TPO experiments, the catalyst was submitted to stripping under a N_2 stream (50 mL min^{-1}) up to the reaction temperature using a heating ramp of 10 °C min^{-1}. After that, the sample was cooled and stabilized at 100 °C. The temperature was then increased up to 850 °C using a heating ramp of 5 °C min^{-1} under an air flow of 50 mL min^{-1} to ensure the total combustion of coke.

XAS measurements were performed at the Quick-XAS ROCK[19] beamline of the French synchrotron SOLEIL. K-edges of Pd and Zn were separately collected in transmission mode. Si(220) and Si(111) monochromators were employed to scan Pd and Zn absorption edges,

https://doi.org/10.1021/jacsau.1c00303
JACS Au 2021, 1, 1719−1732

in the range 23.8–25.7 and 9.3–10.7 keV, respectively. The PdZn/ZrO_2 catalyst was physically mixed with zeolite ZSM-5 (1:1 weight ratio) and packed in a quartz capillary reactor. To optimize the signal quality in transmission mode, we chose a capillary of Ø 1 mm for the Zn K edge and 2.5 mm for the Pd K edge. The capillary was connected to a gas flow system while heating was provided by a heat gun. The measurement followed the catalyst activation protocol used for the catalytic tests, i.e. XAS spectra were recorded during a heating ramp (RT-400 °C) under H_2 gas flow (10 mL/min). The reported XAS spectra resulted from the *average* of 500 and 120 quick-EXAFS spectra (0.5 s/scan). Two ionization chambers were used to measure I_0 and I_T while a third one measured a reference metal foil used for energy alignment. ZnO and PdO were also measured as reference compounds in the form of self-supporting pellets. XAS data analysis (XANES normalization and energy calibration, $\chi(k)$ EXAFS extraction, and Fourier transform (FT)-EXAFS calculation) were carried out using the *Athena* software from the *Demeter* package.[20] The EXAFS fitting of PdZn active phase was performed using the *ARTEMIS* code of the *Demeter* package.[20] Pd–Pd and Pd–Zn scattering paths were generated by the FEFF6 code implemented in *ARTEMIS* using starting interatomic distances taken from literature.[21] The passive amplitude reduction factor was obtained from EXAFS analysis of aPd reference foil. Pd–Pd and Pd–Zn coordination numbers were fixed to the bulk values (4 and 8, respectively), whereas the energy shift (E_0), radial distances (ΔR), and Debye–Waller factors (σ^2) were fit as free variables.

Absorption IR spectra were run using a PerkinElmer FTIR 2000 spectrophotometer equipped with a Hg–Cd–Te cryo-detector, in the range of wavenumbers 7200–580 cm^{-1} at a resolution of 2 cm^{-1}. The powder of PdZn/ZrO_2 was compressed in self-supporting discs (~20 mg cm^{-2}) and placed in quartz IR cells suitable for thermal treatments in controlled atmosphere and spectra recording at room temperature (RT). Moreover, a commercial stainless-steel cell (Aabspec), allowing thermal treatments in situ under vacuum or controlled atmosphere and the simultaneous registration of spectra at temperatures up to 600 °C, was employed. Before IR measurements, catalyst underwent oxidizing or reducing pretreatment: in both cases, it was outgassed at 400 °C for 30 min and then oxidized in dry oxygen (40 mbar) or reduced in hydrogen (40 mbar) at 400 °C for 30 min. Reduction treatment simulates the reduction step performed prior to the catalytic tests. Prereduced catalyst will be named activated catalyst. First of all, interaction with the reagents involved in the CO_2-to-methanol process, i.e., H_2 and CO_2, was investigated. In particular, interaction with H_2 (10 mbar) was performed in situ at increasing temperature on the preoxidized catalyst to study the effect of the activation step used for the catalytic tests. Interaction with CO_2 (20 mbar) was studied at RT on both preoxidized and activated catalyst. To characterize the supported metal phase, we carried out CO adsorption for increasing pressure up to 20 mbar at RT on the activated catalyst.

Transmission electron microscopy (TEM) of the samples was performed with a Cs-probe corrected Titan microscope from Thermo Fisher Scientific by operating it at an accelerating voltage of 300 kV and with a beam current of 0.5–0.8 nA. Dark-field imaging was performed by scanning TEM (STEM) coupled to a high-angle annular dark-field (HAADF) detector. The STEM-HAADF data were acquired with a convergence angle of 17.1 mrad and a HAADF inner angle of 50 mrad. Furthermore, a X-ray energy-dispersive spectrometer (FEI SuperX, ~0.7 sR collection angle) was also utilized in conjunction with DF-STEM imaging to acquire STEM-EDS spectrum-imaging data sets (image size: 512 × 512 pixels, dwell time 4 μs). During the acquisition of these data sets, at every image-pixel, a corresponding EDS spectrum was also acquired for generating simultaneously the elemental maps of Si, Al, Pd, Zn, Zr, and O atoms. It is also pertinent to note herein that spectrum-imaging data sets were acquired in the so-called frame mode, in which the electron beam was allowed to dwell at each pixel for only a time of few microseconds in order to keep a total frame time to 2 s or less. Both imaging and spectroscopy data sets for each sample were acquired as well as analyzed with a newly developed software package called *Velox* from Thermo Fisher Scientific. The elemental maps for Si, Al, Pd, Zn, Zr, and O atoms were computed using the extracted intensity of their respective Kα lines after background subtraction. The generated maps were slightly postfiltered by applying a Gaussian filter (sigma = 0.5). Because of the possible air sensitivity of the PdZn/ZnO solid after H_2 activation and CO_2 hydrogenation, the sample was handled inside an Ar-filled glovebox. The specimen was prepared by simply shaking a small amount of dry powder and the TEM grid inside a 2 mL sample vial. The TEM grid was retrieved and mounted in a Gatan double-tilt vacuum transfer TEM holder, model 648 that was used for the transfer into the microscope.

UV-Raman spectra were collected with a Renishaw inVia Raman spectrometer, adopting a Coherent MotoFred 300C frequency doubled Ar^+ laser emitting at 244 nm as excitation source. The spectrometer is equipped with a 15× objective, a 3600 lines/mm grating and a Peltier cooled CCD detector. To prevent sample decomposition, we kept samples under movement during the measurements with a specifically designed setup.[22]

3. RESULTS AND DISCUSSION

3.1. Catalytic Tests for the CO_2 Hydrogenation to Propane

We first performed a catalytic screening over the stand-alone PdZn/ZrO_2 catalysts and their combination with SAPO-34 and ZSM-5, the two most common zeolites employed in multifunctional catalysts for CO_2 conversion.[7] These control experiments were focused on monitoring MeOH selectivity for the stand-alone PdZn/ZrO_2 catalysts and that of propane for the multifunctional systems. In particular, the effect of reaction pressure (20, 30, and 40 bar) and temperature (250 °C, 300 and 350 °C) was evaluated. The results are summarized in Figure 1a. CO_2 conversion is similar for the three systems (filled symbols, left axis) and it increases with pressure and temperature, in agreement with the process thermodynamics.[11] On the other hand, selectivity follows a completely different trend (empty symbols, right axis). For the stand-alone PdZn/ZrO_2 catalysts, MeOH selectivity also follows the process thermodynamics, increasing with pressure and decreasing with temperature. A full picture of the allowed equilibrium selectivities (lines) and the obtained experimental data (dots) can be observed in Figure S1. Note that the orange lines indicate the maximum allowed methanol selectivity considering the CO_2 to methanol equilibrium. For the multifunctional systems, however, no propane is observed for temperatures lower than 350 °C, and SAPO-34 displays higher selectivity than ZSM-5 (16% vs 3%), in line with the typical methanol-to-hydrocarbons (MTH) mechanism.[23] Looking in detail at the PdZn/ZrO_2+SAPO-34 system, the achieved propane selectivity is higher than the MeOH one of the stand-alone PdZn/ZrO_2 catalysts at 350 °C (16% vs 7%). Interestingly, MeOH selectivity is overlapped with the equilibrium line, indicating that at these conditions the reaction is limited by the reaction thermodynamics (Figure S2a). Conversely, propane selectivity is substantially higher than MeOH equilibrium, suggesting an equilibrium displacement when the multifunctional system is assembled. Therefore, we can conclude that SAPO-34 seems to be a more promising candidate to produce propane than ZSM-5. Moreover, although there are thermodynamics restrictions at high temperature, it seems that an operation temperature of 350 °C is needed for the MeOH conversion to occur in both SAPO-34 and ZSM-5.

Next, the more promising PdZn/ZrO_2+SAPO-34 system was studied at 350 °C using different space velocity values (1500, 3000, 6000, and 12000 mL g^{-1} h^{-1}) and pressures (30,

https://doi.org/10.1021/jacsau.1c00303
JACS Au 2021, 1, 1719–1732

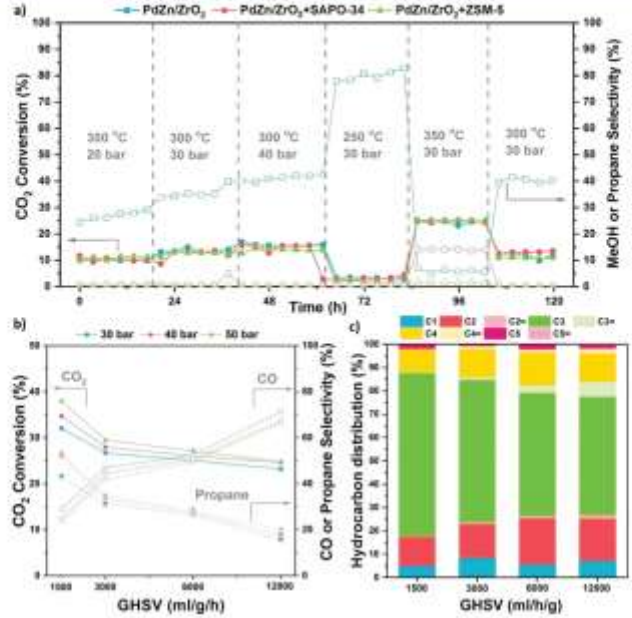

Figure 1. (a) CO_2 conversion (filled symbols) and MeOH (for $PdZn/ZrO_2$) or propane (for $PdZn/ZrO_2$+SAPO-34 and $PdZn/ZrO_2$+ZSM-5) selectivity (empty symbols) at several screening conditions. $H_2/CO_2 = 3$, 12 000 mL g^{-1} h^{-1}. (b) CO_2 conversion (filled symbols) and CO (empty symbols) or propane (half empty symbols) selectivity for the $PdZn/ZrO_2$+SAPO-34 system at different space velocities and pressures. 350 °C, $H_2/CO_2 = 3$. MeOH selectivity was lower than 1% at all conditions. (c) Detailed hydrocarbon distribution (CO free) of the $PdZn/ZrO_2$+SAPO-34 combined system for the CO_2 conversion to hydrocarbons at different space velocities. CO_2:H_2 1:3, 350 °C, 50 bar.

40, and 50 bar). The results are summarized in Figure 1b. As expected, CO_2 conversion increases with decreasing space velocity and increasing pressure. However, CO selectivity also decreases with space velocity, reaching a minimum value of 25% at 50 bar and 1500 mL g^{-1} h^{-1}. This behavior is unexpected as, for most of the state-of-the-art CO_2 to MeOH catalysts, the opposite trend is observed and higher MeOH selectivity is usually obtained at higher space velocity value.[51] Hence, these data may suggest that CO-involving reactions play a key role using the $PdZn/ZrO_2$+SAPO-34 system, because of a limitation in its formation or a consumption of the formed CO to produce more methanol. Moreover, from the data at 50 bar and 1500 mL g^{-1} h^{-1}, a total selectivity to propane higher than 50% can be observed, with a CO_2 conversion close to 40% and only 2.5% of CO selectivity. To the best of our knowledge, this is the highest total selectivity reported for a single C_3 hydrocarbon during CO_2 hydrogenation at meaningful conversion levels.[11] Additionally, thanks to the Pd hydrogenating effect and as intended, the paraffins account for more than 99.9% of the products, greatly facilitating the product separation in a potential industrial process. This later can be better observed if we look in detail at the CO free hydrocarbon distribution (Figure 1c). Figure S2 shows conversion/selectivity plots with these experiments being compared with the above-discussed CO_2-to-methanol equilibrium. The presence of acid sites in SAPO-34, in close proximity to the methanol-forming $PdZn/ZrO_2$ catalyst, leads to rapid conversion of methanol into hydrocarbons (mainly propene). Consequently, the methanol concentration remains below the equilibrium limit, and the selectivity to propane (formed from the fast hydrogenation of propene) is significantly above the equilibrium line at 350 °C and 30 (Figure S2a), 40 (Figure S2b), and 50 bar (Figure S2c). Otherwise, the selectivity to methanol was clearly restricted by equilibrium under these conditions (Figure S2a, orange dot).

To shed light on the strikingly low CO selectivity and the CO role, additional experiments with both CO_2 and CO feeds were performed comparing the original $PdZn/ZrO_2$+SAPO-34 mixed system with the stand-alone $PdZn/ZrO_2$ catalyst and the multifunctional system in dual bed configuration. The results are summarized in Figure 2. Considering first the CO_2 feed (Figure 2a), the rather stable CO_2 conversion, and the huge decrease in CO selectivity (from 95% to 35%), only observed when mixing $PdZn/ZrO_2$ with SAPO-34, a lower CO formation rate in the presence of SAPO-34 is suggested. The similar CO selectivity with similar CO_2 conversion in the dual bed setup confirms that, indeed, the intimate mixture of both components is needed to displace equilibrium. Here, the CO-

https://doi.org/10.1021/jacsau.1c00303
JACS Au 2021, 1, 1719−1732

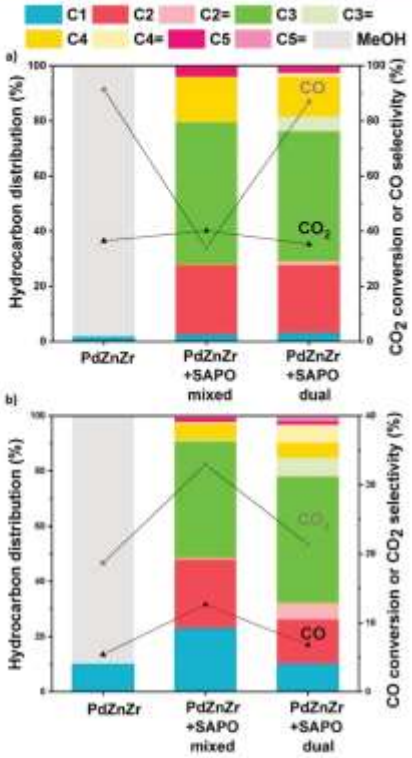

Figure 2. Catalytic performance of the $PdZn/ZrO_2$ catalyst and the $PdZn/ZrO_2$+SAPO-34 combined system: (a) CO_2 and (b) CO conversion to hydrocarbons. CO_2:H_2 1:3, 350 °C, 30 bar, 3000 mL g^{-1} h^{-1}.

forming $PdZn/ZrO_2$ will compete with the hydrocarbon-forming SAPO-34 for methanol and, due to the rapid transformation of methanol to hydrocarbons over SAPO-34, the CO_2/MeOH/CO equilibrium system would be shifted to minimize CO formation in the mixed bed case. The higher olefin-to-paraffin ratios in the dual bed configuration are the result of the higher hydrogenation ability of $PdZn/ZrO_2$ compared to SAPO-34 as we initially intended. At the same time, the dual bed data demonstrate that SAPO-34 has substantial hydrogenation activity in the presence of surplus H_2. This is well in line with prior literature over SAPO-34 in the presence of H_2.[25]

Considering the CO feed (Figure 2b), CO conversion is substantially lower than that of CO_2, but with higher methanol selectivity compared to CO_2 over the $PdZn/ZrO_2$ alone. This is in line with process thermodynamics (the lower the conversion, the higher the MeOH selectivity) but also suggests that CO limits the rate of the reaction. Surprisingly, here the CO_2 selectivity shows a different trend and it is maximized in the mixed bed $PdZn/ZrO_2$+SAPO-34 configuration. CO conversion is also increased in this mixed bed configuration. We attribute this result to another equilibrium displacement. This time, the water−gas shift (WGS) is promoted because of the water presence. Converting the MeOH generated on the $PdZn/ZrO_2$ to hydrocarbons on the SAPO-34 generates great amounts of water that can favor the WGS on the hydrogenating catalyst, thus increasing the CO conversion and selectivity to CO_2. Summing up, from these results, we can confirm the clear effect of CO and WGS in the mixed bed configuration when both catalytic functions are intimately mixed together and the equilibrium can be shifted.

3.2. Kinetic Modeling of the $PdZn/ZrO_2$+SAPO-34 System

Because of the relevant role of equilibrium and thermodynamics in the overall process and the observed advantages of intimate mixing both functions, a kinetic modeling study was carried out comparing the performances of the stand-alone $PdZn/ZrO_2$ catalyst and the $PdZn/ZrO_2$+SAPO-34 system. More details on the reaction network and kinetic equations can be found in the Supporting Information. Experimental data fitting at selected conditions can be observed in Figure 3a, b for both catalysts at the optimal conditions for the production of methanol and propane, respectively. Moreover, the fitting of all experimental data can be found in Figure S3. A clearly differentiated trend is observed. CO_2 is converted to CO and MeOH over the stand-alone catalyst, with the concentration of MeOH decreasing with space time and that of CO reaching a saturating trend at 350 °C (Figure S3c). Otherwise, in line with our previous claims, CO shows a maximum when both functions are mixed, accentuated at 50 bar (Figure 3b). As expected, the concentration of propane increases with space time. As propane is formed only from MeOH, this can only be explained by shifts on CO_2/CO/MeOH equilibria caused by the presence of SAPO-34. This can be more clearly understood when the estimated reaction rates for the CO_2-to-MeOH and rWGS reactions are compared (Figure 3c, d). The evolution with space time of the individual reactions rates at all tested temperatures and pressures are shown in Figures S4 and S5.

At low temperature and low CO_2 conversions (250 °C, Figure 3c), reactions are not limited by equilibrium, as was well-predicted by thermodynamics studies (Figure S4). Forward reactions are remarkably promoted but with low rate values. When temperature is increased, rate values increase but forward/reverse rates for CO_2/MeOH equilibrium are, in practice, the same, confirming the above-discussed thermodynamics constraint at this high temperature. A comparison of these rates with those calculated for the $PdZn/ZrO_2$+SAPO-34 multifunctional system at the same conditions and half GHSV (same CO_2-to-$PdZn/ZrO_2$ ratio, Figure 3d) shows a ten-times increase in MeOH formation (in equilibrium) because of its consumption to form propane, but also a significant increase in the reverse rate of CO formation (ca. 18 mol kg^{-1} h^{-1}, the forward reaction, ca. 4 vs ca. 14 mol kg^{-1} h^{-1}, the reverse reaction). The better performance at 50 bar is explained by the minimum formation of CO due to the CO_2/CO reaction being also in equilibrium, which is caused by the promotion of the propane formation rate. This result suggests a substantial modification of the CO_2/CO/MeOH equilibrium but also, as expected, a limitation in propane production due to the system thermodynamics.

https://doi.org/10.1021/jacsau.1c00303
JACS Au 2021, 1, 1719−1732

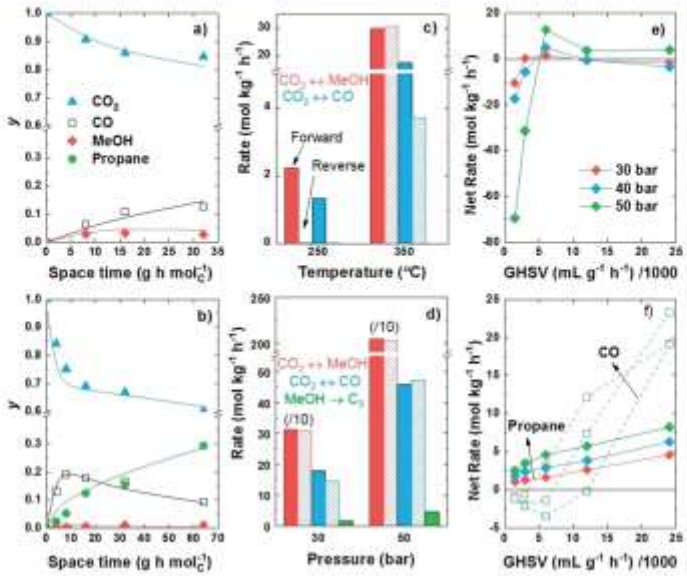

Figure 3. Experimental data fitting of (a) CO_2 to methanol over the PdZn/ZrO_2 catalyst at 300 °C and 30 bar and (b) CO_2 to propane over the PdZn/ZrO_2+SAPO-34 system at 350 °C and 50 bar. (c) Comparison of reaction rates for methanol and CO formation over the PdZn/ZrO_2 catalyst at 250 and 350 °C and 30 bar (12000 mL g^{-1} h^{-1}), and (d) influence of propane formation on these rates over the PdZn/ZrO_2+SAPO-34 system at 350 °C and 30 and 50 bar (6000 mL g^{-1} h^{-1}). Evolution with GHSV of the net formation rate of (e) methanol and (f) CO and propane over the PdZn/ZrO_2+SAPO-34 system at 350 °C.

The selective methanol conversion can be better observed in the evolution with GHSV of MeOH (Figure 3e), CO, and propane (Figure 3f) net formation rates. Those corresponding to the stand-alone PdZn/ZrO_2 catalyst can be found in Figure S6. At high GHSV values, MeOH formation rate tends to zero, with maximum rates for CO and propane formation. This coincides with the lowest CO_2 conversion values shown in Figure 1b. At conditions of optimized CO_2 conversion with low GHSV values, the net rate of MeOH decreases to negative values, also leading to a significant decrease in CO net formation rate. As a consequence, the propane rate is selectively higher, explaining the highest selectivity to this product at these conditions (Figures 1b and 3f). Moreover, all these trends are maximized when the pressure is increased, with 50 bar being the optimal pressure to enhance propane selective formation.

As previously discussed, the conversion of MeOH into propane takes place through the dual-cycle mechanism and a fast hydrogenation of the formed olefins. This industrial process over SAPO-34 suffers a well-known fast deactivation due to the formation of coke within the zeotype cages. For this reason, deactivation can also play a role in the view of the industrial implementation of the tandem process presented herein. Therefore, the effect of in situ regeneration at 600 °C was studied with a 5% O_2 in N_2 stream for 5 h (Figure S7). The catalytic system is rather stable for at least 48 h and only at very high space velocity values (24000 mL g^{-1} h^{-1}), deactivation is significant. In particular, after deactivation at 24000 mL g^{-1} h^{-1}, the products selectivity is mainly a mix of MeOH and DME with CO (73% MeOH, 26% DME and 1% CH_4), whereas the CO_2 conversion remains invariable, further corroborating that the SAPO-34 component is the one being deactivated. However, the in situ regeneration worked for all samples and the initial activity was regained after the regeneration cycle at 600 °C.

3.3. Characterization of the Multifunctional Catalysts

The powder X-ray diffraction (PXRD) pattern of the as prepared PdZn/ZrO_2 sample is shown in Figure S8. The sample shows a diffraction pattern of zincite (ZnO), PdO, and tetragonal/cubic ZrO_2. Concerning the ZrO_2 structure, even if cubic and tetragonal polymorphs are not discernible because of crystallite-induced peak broadening, their distinction is out of the scope of the present work. Indeed, as shown hereafter, ZrO_2's major role is to be an active support of PdZn alloy for CO_2 adsorption through carbonates formation, making the identification of a single phase/mixture of monoclinic/tetragonal (cubic) polymorphs the most relevant detail.[26] Energy-dispersive X-ray spectroscopy (EDS) shows a molar composition of 2% Pd, 13% Zn, and 85% Zr, close to the theoretical synthesis value (Table S2).

Nitrogen adsorption-desorption isotherms of both SAPO-34 and ZSM-5 zeolites are depicted in Figure S9. The detailed

https://doi.org/10.1021/jacsau.1c00303
JACS Au 2021, 1, 1719−1732

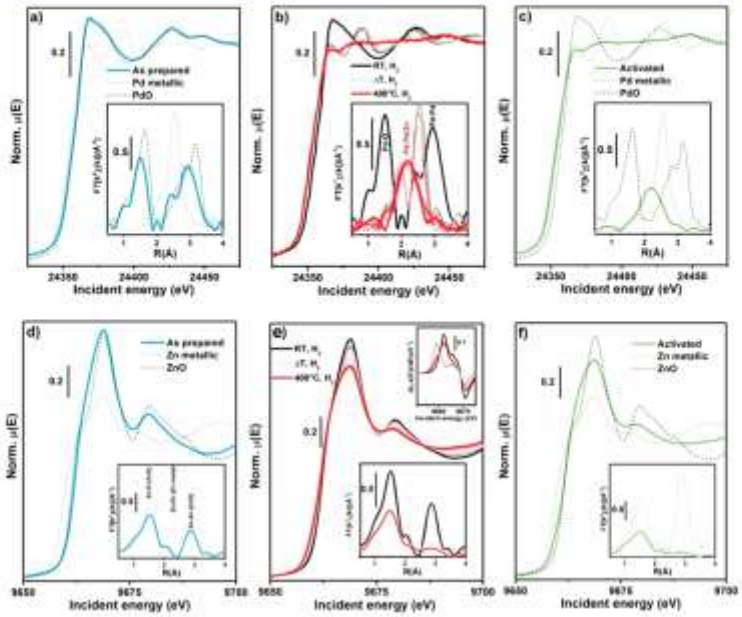

Figure 4. Pd K-edge, Zn K-edge XANES (main panels), and EXAFS (insets) spectra of PdZn/ZrO_2+ZSM-5 catalyst. XAS spectra for relevant reference compounds are also reported as dashed lines. (a) Pd K-edge for as prepared catalyst. (b) Pd K-edge for catalyst during activation (RT-400 °C) under H_2 gas flow. (c) Pd K-edge for catalyst after activation at 400 °C under H_2 atmosphere. (d) Zn K-edge for as prepared catalyst. (e) Zn K-edge for catalyst during activation (RT-400 °C) under a H_2 gas flow. Top right inset: first derivative of the XANES spectra for as prepared catalyst (black), activated catalyst (red), reference Zn(0) metal foil (light gray). (f) Zn K-edge for catalyst after activation at 400 °C under a H_2 gas flow. For clarity of comparison, the Pd metallic foil EXAFS signal was rescaled by a factor of 1/2. The EXAFS spectra reported in the bottom insets have been obtained by transforming the corresponding $k^2\chi(k)$ EXAFS function in the 2.5−11.0 $Å^{-1}$ range.

textural properties are summarized in Table S3. SAPO-34 displays a microporous type I isotherm and ZSM-5 a micro-mesoporous type IV isotherm. The BET surface of SAPO-34 is estimated to be 770 m^2/g with 762 m^2/g of micropores, whereas for ZSM-5, it is estimated to be 417 m^2/g with 296 m^2/g of micropores. NH_3-TPD profiles of both zeolites are depicted in Figure S10. SAPO-34 displays only one peak at ca. 400 °C, whereas ZSM-5 displays the two characteristic peaks of weak (Lewis) and strong (Brønsted) acid sites at 225 and 425 °C, respectively.[27]

3.3.1. Local Structure and Electronic Properties of Pd and Zn Species. X-ray absorption spectroscopy (XAS) was initially performed on the PdZn/ZrO_2 catalyst physically mixed with ZSM-5 aiming to characterize, in an element-selective way, Pd- and Zn-containing species formed in a model multifunctional system, in its as-prepared state and upon activation. The XAS spectra reported in Figure 4 show how electronic and structural features of both Pd and Zn change considerably when the catalyst is subjected to the activation treatment. Indeed, both XANES (main panels) and EXAFS spectra (insets) show substantial modifications at high temperature in the presence of H_2.

Considering the Pd K-edge, the as-prepared catalyst (Figure 4a) presents the typical XANES (edge position, postedge resonances) and EXAFS (Pd−O bond in first coordination shell) features of the reference PdO, consistently with PXRD results (section 3.1). During activation (Figure 4b, from ca. 50 °C up to ca. 200 °C) Pd(II)-to-Pd(0) reduction is underlined by (i) shift of the absorption edge position to lower energy, (ii) rapid change of the oscillation in the XANES from PdO-like to those resembling metallic Pd (Figure 4a, b light gray line), and (iii) intensity loss of the Pd−O first coordination shell in the phase-uncorrected EXAFS (inset Figure 4b) and shift to lower R values of the Pd−Pd second coordination shell. As the temperature rises (300 °C), the oscillations in the XANES get flatter and EXAFS evolves into a single broad peak around 2.15 Å in the phase-uncorrected spectrum (Figure 4b red curve). These features were already observed and well reported in the case of other PdZn systems and ascribed to the formation of β_1-PdZn alloy.[23,28−35] The EXAFS fit on the activated catalyst spectrum, reported in Figure S11, further confirmed the alloy formation. The fit obtained considering the simultaneous presence of Pd−Zn and Pd−Pd scattering paths well reproduced the experimental data. The magnitude and the

https://doi.org/10.1021/jacsau.1c00303
JACS Au 2021, 1, 1719−1732

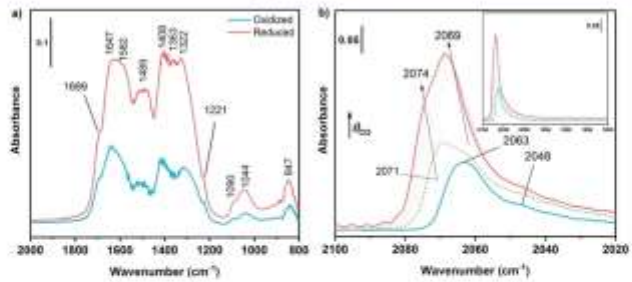

Figure 5. (a) FT-IR spectra of CO_2 adsorbed at RT on oxidized and activated $PdZn/ZrO_2$ at equilibrium pressure of 20 mbar. (b) FT-IR spectra of CO adsorbed at RT on activated $PdZn/ZrO_2$. Spectra were acquired at increasing dosage of CO up to 20 mbar (from blue to red line) and after outgassing (green dashed line).

imaginary parts of the FT-EXAFS spectra (Figure S11a,b) presented a broad peak and a single oscillation, respectively. Analysis of the imaginary parts of the Pd−Pd and Pd−Zn scattering paths optimized in the fit (Figure S11c) highlighted a wide overlap of the two contributions, justifying the observed broadening in the experimental spectra (Figure S11a, b). Despite their overlap, Pd−Zn and Pd−Pd paths have a stronger contribution at lower and higher radial distances, respectively, leading to evaluation of a shorter Pd−Zn and a longer Pd−Pd path, the values of which are reported in Table S4 and confirmed the PdZn alloy formation.[21,28] σ_2 values are consistent with the thermal contribution at 400 °C and are comparable with literature results obtained at similar temperatures.[31,38]

Moving to the Zn K-edge, the as-prepared catalyst (Figure 4d) essentially presents the same XANES and EXAFS features of the reference ZnO, also in line with PXRD analysis of the as-prepared $PdZn/ZrO_2$ phase. A careful observation of the EXAFS data unveils a lower intensity of the second shell peak in the catalyst with respect to the reference oxide (inset Figure 4d), indicating a higher concentration of defects in the former. From the Zn perspective, the activation protocol causes (i) a pronounced decrease of the signal intensity in both the XANES and EXAFS region and (ii) a subtle red-shift of the edge energy position, better observed from the growth of a shoulder at low energy values in the XANES first derivative, matching the first maximum for Zn(0) metal foil (top right inset Figure 4e). Zn species are present in the activated sample (Figure 4f), and therefore they dominantly occur as a highly defective ZnO phase with a minor Zn(0) contribution ascribable to the fraction of Zn taking part to the formation of PdZn alloy. Despite its nature as a bulk-sensitive technique, in the case of ion-exchanged zeolite/zeotype systems, XAS becomes extremely sensitive to the absorber atom local environment.[30−32] In the case of other PdZn/zeolite combined systems, Zn was observed to diffuse within the zeolite,[29] modifying the Zn local environment and leading to characteristic Zn K-edge spectra well reported in the literature.[30] In the case of the system here investigated, i.e., $PdZn/ZrO_2$+zeolite, fingerprints of Zn-exchanged zeolite were not observed,[30] suggesting that impregnating Pd and Zn over ZrO_2 stabilizes the former atoms, avoiding their further diffusion into the zeolitic component.

3.3.2. Surface Interactions with Key Reactants and Molecular Probes. Differently from XAS, which provided an element-selective view on Pd- and Zn-containing species in a representative combined system, FT-IR analysis was focused on the stand-alone $PdZn/ZrO_2$ system. Exploring its interaction with key reactants/molecular probes (H_2, CO_2, and CO), we aimed at confirming and further deepening two major issues related to the CO_2-hydrogenation functionality, namely activation-driven oxygen vacancies formation and nature of the PdZn phase.

Zinc oxide phase plays a key role for both intermediate stabilization and H_2 heterolytic splitting thanks to its propensity to form stoichiometric defects (such as oxygen vacancies).[40−42] In our case, the presence of a ZnO phase is shown by XAS and XRD results. Specifically, according to XAS, after the activation a highly defective ZnO phase is formed, together with the PdZn alloy. Hence, CO_2 hydrogenation can be due to the oxygen-vacancy formation in the defective ZnO phase. To investigate the formation of oxygen vacancies, different IR measurements were performed in H_2 at different temperatures, as well as under oxidizing conditions for comparison purposes.

To understand the IR results, it is important to underline that lattice defects, such as oxygen vacancies (V_O), make ZnO a semiconducting material.[43−45] Neutral V_O shows two trapped electrons located in levels at 0.05 and 0.18 eV below the conduction band (C.B.). The first electronic level is very near to the bottom of the C.B., so that the majority of electrons can be moved to the C.B. at room temperature to produce monoionized oxygen vacancies ($V_O^{\cdot}$). The second ionization of V_O can be promoted by IR, and thus it is possible to observe the photoionization of monoionized oxygen vacancies. Typically, pure ZnO shows a broad absorption band centered at about 1450 cm^{-1}, i.e. 0.18 eV, after reduction treatments.[45] Interaction with H_2 can create $V_O^{\cdot}$ following two main pathways: (i) the filling with an electron of pre-existing bi-ionized V_O ($V_O^{2\cdot}$) by consuming adsorbed oxygen species, such as O_2^-, O^-, O_2^{2-}; (ii) the generation of new $V_O^{\cdot}$ extracting lattice oxygen ions from the surface, but this route occurs only at high temperature. The IR method is not able to discriminate the two routes for $V_O^{\cdot}$ formation.

Figure S12 displays different spectra obtained in H_2 at different temperature from 50 to 400 °C. The broad absorption band related to monoionized oxygen vacancies is

https://doi.org/10.1021/jacsau.1c00303
JACS Au 2021, 1, 1719−1732

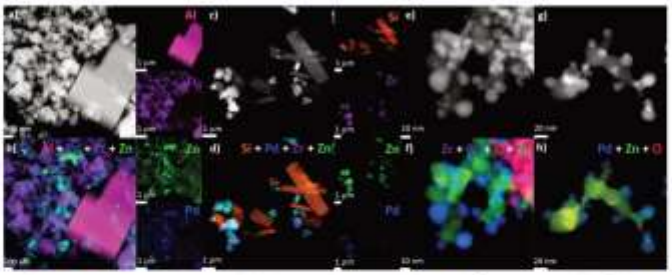

Figure 6. Low-magnification HAADF-STEM imaging of $PdZn/ZrO_2$ catalysts mixed either with (a) SAPO-34 and with (c) ZSM-5 crystals and (b, d) related elemental maps built with Kα emission lines provided by Al, Si, Pd, Zr, and Zn atoms. Magnification of the PdZn/ZnO nanoparticles observed at the edge of the ZrO_2 support when mixed either with (e) SAPO-34 and with (g) ZSM-5 crystals. (f, h) Associated overlaps of elemental maps.

well evident. The band increases in intensity up to 150 °C, losing intensity at higher temperature. The intensity loss can be ascribed to the PdZn alloy formation evidenced by XAS measurements (reduction of Zn^{2+} to Zn^0 occurs at the expense of electrons trapped in V_O^{+1}). As a matter of fact, the formation of metallic Zn at this temperature is not expected, but it could be favored by Pd presence and alloy formation. The band is centered at about 1250 cm^{-1}, which corresponds to monoionized oxygen vacancies at about 0.15 eV under the $C.B._s$ very near to the ionization energy observed for pure ZnO. The obtained results, in agreement with XAS findings, demonstrate the presence of a highly defective ZnO-like phase.

To explore the interaction/adsorption of CO_2 with the catalyst surface, we followed adsorption at room temperature on both oxidized and H_2-activated $PdZn/ZrO_2$ by FT-IR spectroscopy and spectra, reported in Figure 5a. All the shown bands can be assigned to different carbonate species. These species could be formed on both the ZnO and ZrO_2 phase; however, CO_2 adsorption on ZnO[46,47] and tetragonal ZrO_2[48] gives carbonates with spectral features different from those shown in Figure 5a. In particular, tetragonal zirconia gives an appreciable amount of polydentate bridging carbonates that are not present in our case. Bare ZnO gives an appreciable amount of bicarbonates that are present in very small amounts in our case. None of them forms the bridged and monodentate species that are present for the $PdZn/ZrO_2$ catalyst. More specifically, the following adsorbed species can be identified:[47−53] (i) bicarbonates, weak bands at 1689 and 1221 cm^{-1}, assigned to ν(C=O) and δ(C−O−H) modes, respectively; (ii) bridged carbonates, bands at 1647, 1322, and 1044 cm^{-1}, assigned to ν(C=O), ν_{asym}(O−C−O), and ν_{sym}(O−C−O) modes, respectively; (iii) bidentate carbonates, bands at 1582, 1363, and 1044 cm^{-1}, assigned to ν(C=O), ν_{asym}(O−C−O), and ν_{sym}(O−C−O) modes, respectively; (iv) monodentate carbonates, bands at 1489, 1408, and 1090 cm^{-1}, assigned to ν_{asym}(O−C−O), ν_{sym}(O−C−O), and ν(C−O), respectively. The band at 847 cm^{-1} can be related to the δ(O−C−O) mode of both monodentate and bidentate carbonates, as mentioned by some works on different oxides.[54,55]

Spectral features obtained for the oxidized sample are the same obtained for the activated one, but the overall intensity of the bands in Figure 5a shows that there are much more carbonates on the activated sample when compared with the oxidized one. The reason could reside in the stoichiometric defect formation: reduction generates oxygen vacancies on the surface of ZnO, giving a highly defective phase more suitable for carbonate formation. In light of this result, we reasonably ascribe the formation of carbonate species mainly to CO_2 adsorption on this phase. Different spectral features with respect to bare ZnO carbonates[47,56] can be related to the fact that ZnO is a supported phase in our system. This causes the presence of huge amount of surface defects, such as edges, corners and kinks, beside stoichiometric defectiveness, which is characteristic of ZnO itself. Surface defects are able to create high heterogeneity of surface-adsorbed species. Moreover, the interaction with both ZrO_2 and Pd reasonably contributes to carbonate species heterogeneity.

CO adsorption at room temperature was also performed to characterize metallic Pd and explore its interaction to CO. The adsorption was carried out on activated $PdZn/ZrO_2$, i.e., after reduction in H_2 at 400 °C. Figure 5b reports several spectra obtained at increasing CO coverage (θ_{CO}) corresponding to increasing CO pressure up to 20 mbar: an asymmetric band in the region between 2080 and 2020 cm^{-1} appears and increases in intensity upon increasing pressure. The band lies in the region of Pd^0 linear carbonyls[46,57] and more specifically, it appears constituted by different components: the main peak at 2063 cm^{-1} that shifts to 2069 cm^{-1} at the maximum CO coverage and two shoulders at 2071 cm^{-1} (2074 cm^{-1} for the maximum θ_{CO}) and 2048 cm^{-1}. As a matter of fact, the frequencies reached at the maximum coverage are quite lower with respect to the characteristic ones of Pd^0 linear carbonyls. According to literature,[58−60] the lower frequencies can be ascribed to CO on Pd sites in the PdZn alloy. Indeed, the dilution of Pd in the alloy deletes the dipolar coupling and changes in the electronic properties of Pd, induced by the alloying, can slightly increase π-backdonation.

To assign the different components, it is worth remembering that the Pd^0−CO bond shows strong π-backdonation character; as a consequence, the lower the band frequency the more coordinatively unsaturated the site.[61] Hence, the shoulder at 2048 cm^{-1} is assigned to CO adsorbed on highly defective Pd^0 sites, such as corners, the main band at 2063−2069 cm^{-1} to less defective sites, such as edges, whereas the shoulder at the higher frequency can be related to terrace sites.

https://doi.org/10.1021/jacsau.1c00303
JACS Au 2021, 1, 1719−1732

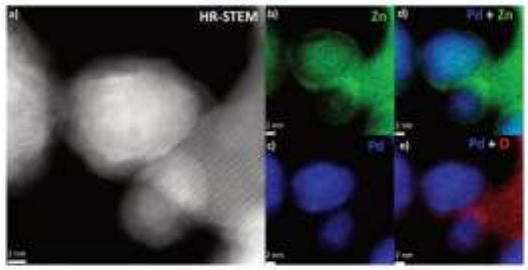

Figure 7. (a) High-resolution HAADF-STEM imaging of a PdZn alloy nanoparticle after CO_2 hydrogenation. Elemental maps of the same area built with Kα emission lines: (b) Zn, (c) Pd, (d) overlap of Pd and Zn maps, and (e) overlap of Pd and O maps.

As for the blue shift observed by increasing coverage, it can be explained by two phenomena: the dipolar coupling and the "chemical effect". The first one is predominant for terrace sites on regular facets but, in our case, it can be neglected due to the presence of Pd dilution by alloying with Zn, as evidenced by XAS measurements. The second one is caused by the decrease in π-backdonation as the number of adsorbed CO molecules increases, so that the higher the θ_{CO}, the lower the donated electron density per each adsorbed molecule. Therefore, upon increasing coverage, the π-backdonation contribution to all adsorbed CO molecules becomes weaker and weaker, and then an increase in $\nu(C{\equiv}O)$ is observed.

After outgassing (dashed-green line in Figure 5b), the intensity of the peak is drastically reduced but not totally brought down, showing a certain stability of Pd^0−CO at room temperature. It is important to note that the outgassing cancels out all of the effect due to the θ_{CO}. Hence, the peaks are shifted back to their original frequency, with slightly different relative intensities of the three main absorptions. Pd is also known to form a considerable amount of bridged carbonyls on different supports when reduced to metallic Pd.[45,62] In our case, it is worth noting the absence of bridged Pd−carbonyls in the region between 2000 and 1800 cm^{-1} (inset Figure 5b). This highlights the absence of neighboring Pd atoms, confirming the PdZn alloy formation, in agreement with XAS results.

3.3.3. Morphological/Chemical Insights on Used Multifunctional Catalysts. Imaging by high-angle annular dark-field scanning transmission electron microscopy (HAADF-STEM) was performed to investigate the morphological properties of the $PdZn/ZrO_2$ catalyst mixed either with SAPO-34 or with ZSM-5, recovered after catalytic testing for 24 h at 350 °C, 30 bar, and 12000 mL g^{-1} h^{-1}. The low-magnification micrograph presented in Figure 6a shows a typical juxtaposition of large cubic SAPO-34 crystals with the $PdZn/ZrO_2$ function showing as nanoparticle agglomerates. Furthermore, Zr, Zn, and Pd elemental maps computed from X-ray fluorescence spectroscopy (STEM-EDX) reveal that most of the Pd and Zn atoms are distributed at the periphery of the ZrO_2 support (Figure 6b). Similar observations are also recorded when the $PdZn/ZrO_2$ catalyst is mixed with ZSM-5 (Figure 6c, d). Besides, there is no clear signal from the X-ray fluorescence spectra that would suggest a quantitative migration of Pd and Zr atoms over or into SAPO-34 and ZSM-5 crystals during CO_2 hydrogenation. However, a small X-ray emission from Zn atoms was detected in both case (<1 wt %). The nature of those Zn species was difficult to pinpoint given their low abundance and the thickness of the SAPO-34 and ZSM-5 crystals.

Magnification on the edge of the ZrO_2 support shows nanoparticles in 5−30 nm range (Figure 6e, g). Interestingly, some nanoparticles appear brighter, suggesting the presence of heavier atoms, e.g., Pd. The atomic composition shown on Figure 6f, h) reveals a mixture of ZnO and alloyed PdZn nanoparticles, as suggested by former HAADF imaging and consistently with the spectroscopy results presented in section 3.2. Quantification of the Pd and Zn atomic content at the core of the PdZn alloy by X-ray fluorescence provides a Pd/Zn molar ratio of 1.16 ± 0.15 and 1.27 ± 0.14 for SAPO-34 and ZSM-5, respectively (measurement performed on ca. 20 particles). All the observations described below are identical for both catalysts, mixed either with ZSM-5 or with SAPO-34.

High-resolution STEM images highlight a core−shell structure displaying clearly resolved lattice fringes (Figure 7a). The shell is polycrystalline as seen from the various orientation of lattice fringes and has a thickness of about 2 nm. In contrast, the core appears monocrystalline and composed of Pd and Zn atoms. Subsequent elemental mapping provides more details related to the shell composition, which is divided in two parts: (i) a main volume attached to the core where Zn is depleted and metallic Pd majorly remains (Figure 7b−d), (ii) an outer layer composed of zinc oxide (Figure 7b, d, and e). Those compositional characteristics were already reported by Armbrüster et al.[63−65] for PdZn/ZnO catalysts used with methanol steam reforming (i.e., the inverse reaction: $CH_3OH + H_2O \rightarrow 3\,H_2 + CO_2$). They have shown that the oxidation of the PdZn alloy by the CO_2 gas causes the Zn atoms to leave the intermetallic phase and rise to the surface, forming ZnO patches.

Since a reoxidation of the metallic particles with O_2 from the air prior to TEM imaging cannot be univocally ruled out,[66] those results were completed with a imaging study handled without air exposure both after H_2 activation and CO_2 hydrogenation. Initially, the sample in its as-synthesized state displays grapes of PdO nanoparticles with a size in the 1−3 nm which are distributed between the ZnO nanoparticles (Figure S14). During H_2 activation, the PdO nanoparticles within the grapes merges and reduces into 10 to 30 nm metallic nanoparticles (Figure S15). The elemental composition as revealed by STEM-EDS shows clearly the formation of a Pd−Zn alloy at that stage. CO_2 hydrogenation is also confirmed to

https://doi.org/10.1021/jacsau.1c00303
JACS Au 2021, 1, 1719−1732

induce the formation of the ZnO shell on the surface of the Pd−Zn alloy (Figures S16 and S17). The latter phenomenon was further established by multiple observations in several area of the sample (Figure S18).

To obtain deeper insight into deactivation pathways in bifunctional systems, UV-Raman spectroscopy was also used to characterize the multifunctional system. Figure S13 reports Raman spectra collected at RT on SAPO-34 alone and on the fresh and spent $PdZn/ZrO_2$+SAPO-34 combined catalyst. Spectra of the bare SAPO-34 and of fresh $PdZn/ZrO_2$+SAPO-34 are almost superimposable. The most intense signals are observed for the spent catalyst, i.e., two intense peaks at 1630 and 1384 cm^{-1}. The latter also presents an evident shoulder at higher Raman shifts, roughly centered at 1420 cm^{-1}. All these features relate to species trapped in the zeotype cages, identifiable as fingerprints of alkenes (1630 and 1420 cm^{-1} modes)[67−69] and polycyclic aromatic hydrocarbons (1383 cm^{-1} peak, typical for naphthalene).[70] TGA analysis was further employed on the spent hybrid system to quantify the amount of coke, showing a 2.96 wt % weight loss in the 300−600 °C region that can be attributed to coke (see Figure 7b). This is evidence for an incipient catalyst deactivation by coking due to the condensation of methanol-to-hydrocarbon reaction intermediates and can justify the decrease in propane production (over SAPO-34) while constant CO_2 conversion (over the $PdZn/ZrO_2$ function) is observed at high GHSV values in Figure S7a.

3.4. Reaction Mechanism for the CO_2 Conversion to Propane

On the basis of the above results, we propose a reaction mechanism for the CO_2 conversion to propane on the PdZn/ZrO_2+SAPO-34 multifunctional systems (see Figure 8). First, a

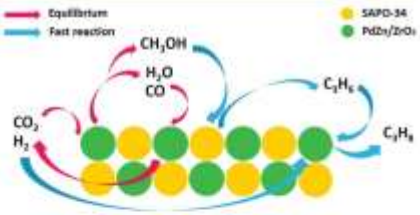

Figure 8. Reaction mechanism for the CO_2 conversion to propane over the $PdZn/ZrO_2$+SAPO-34 system.

PdZn alloy is formed during catalyst activation, in intimate contact with oxygen-vacancy rich ZnO particles over the ZrO_2 support, as demonstrated by XAS and FT-IR (see section 3.3). This alloy, once exposed to the CO_2-containing reaction feed, develops into a core−shell structure (see Figure 7) with a 2 nm polycrystalline ZnO shell and it is directly responsible of the MeOH formation in the $PdZn/ZrO_2$ component.[71−73] This MeOH formed in the alloy instantly reacts over the SAPO-34 following a classical MTO mechanism with propene as the main product.[76,77] The instant consumption of MeOH can be ascribed to the intimate mixture of both $PdZn/ZrO_2$ and SAPO-34 and ultimately causes a CO_2/CO/MeOH equilibria displacement, increasing the CO_2 conversion and reducing drastically the CO selectivity (from 95% to 35%, see Figure 2a). The rapid transformation of MeOH to hydrocarbons (mainly propene) over SAPO-34 tends to minimize the formation rate of CO as a side product over the $PdZn/ZrO_2$ catalyst, which can be explained by a shift in the reverse WGSR (Figure 3). Nevertheless, an avoided formation of CO via MeOH degradation in the $PdZn/ZrO_2$ due to its transformation to hydrocarbons cannot be discarded. This was suggested by the clear differences in the net formation rates of CO when SAPO-34 was added to the catalytic bed (Figure 3c, d). Moreover, the H_2O formed as byproduct over SAPO-34 can also displace the reverse WGS equilibrium (reaction 2 in Supporting Information, $CO_2 + H_2 \rightarrow CO + H_2O$),[74] further reducing the CO selectivity. Lastly, the again intimately mixed $PdZn/ZrO_2$ rapidly hydrogenates the propene produced over SAPO-34, forming the resulting propane.

CONCLUSIONS

In conclusion, we have developed a highly active and selective $PdZn/ZrO_2$+SAPO-34 multifunctional catalyst for the direct conversion of CO_2 to propane that displays a total selectivity to propane higher than 50% (with 20% CO, 6% C_1, 13% C_2, 10% C_4, and 1% C_5) and a CO_2 conversion close to 40% at 350 °C, 50 bar, and 1500 mL g^{-1} h^{-1}. These results can be rationalized as a consequence of the combined effects of each component of the multifunctional system. First, the alloy formed during catalyst activation is responsible for the formation of MeOH in the $PdZn/ZrO_2$ component. XAS and FT-IR, together with high-resolution HAADF-STEM imaging, demonstrate that this alloy is directly responsible for the initial high CO_2 conversion and evolves into a core−shell structure with a 2 nm polycrystalline ZnO shell. The MeOH formed in the $PdZn/ZrO_2$ component instantly reacts over the SAPO-34 forming propene as main product following a classic MTO mechanism. This rapid MeOH consumption triggers several reaction equilibrium shifts, ultimately boosting the initial CO_2 conversion and minimizing the CO selectivity. Lastly, the Pd component of the system hydrogenates all the propene formed over the intimately mixed SAPO-34, resulting in a paraffins hydrocarbon selectivity over 99.9%. Our results confirm the great importance of synergies in catalyst development for the production of individual hydrocarbons from CO_2 with the ultimate goal of facilitating the transition to renewable, non-fossil-fuel-based energy sources.

ASSOCIATED CONTENT

Supporting Information

The Supporting Information is available free of charge at https://pubs.acs.org/doi/10.1021/jacsau.1c00302.

CO_2 hydrogenation thermodynamics (Figures S1 and S2), kinetic model for CO_2 hydrogenation (Methodology, Table S1 and Figures S3−S6), regeneration of the $PdZn/ZrO_2$+SAPO-34 multifunctional catalyst (Figures S7), chemical and textural characterization of catalysts (Tables S2 and S3 and Figures S8−S10), spectroscopic characterization of the $PdZn/ZrO_2$ (Table S4 and Figures S11−S13), imaging of the $PdZn/ZrO_2$ and $PdZn/ZrO_2$+SAPO-34 catalysts (Figures S14−S18) (PDF)

https://doi.org/10.1021/jacsau.1c00302
JACS Au 2021, 1, 1719−1732

AUTHOR INFORMATION

Corresponding Authors

Unni Olsbye − *SMN Centre for Materials Science and Nanotechnology, Department of Chemistry, University of Oslo, Oslo N-0315, Norway*; orcid.org/0000-0003-3693-3857; Email: unni.olsbye@kjemi.uio.no

Jorge Gascon − *KAUST Catalysis Center (KCC), King Abdullah University of Science and Technology, Thuwal 23955, Saudi Arabia*; orcid.org/0000-0001-7558-7123; Email: jorge.gascon@kaust.edu.sa

Silvia Bordiga − *Department of Chemistry, NIS Center and INSTM Reference Center, University of Turin, Turin 10125, Italy*; orcid.org/0000-0003-2371-4156; Email: silvia.bordiga@unito.it

Authors

Adrian Ramirez − *KAUST Catalysis Center (KCC), King Abdullah University of Science and Technology, Thuwal 23955, Saudi Arabia*

Pierfrancesco Ticali − *Department of Chemistry, NIS Center and INSTM Reference Center, University of Turin, Turin 10125, Italy*; orcid.org/0000-0003-3514-0196

Davide Salusso − *Department of Chemistry, NIS Center and INSTM Reference Center, University of Turin, Turin 10125, Italy*; orcid.org/0000-0001-7927-4001

Tomas Cordero-Lanzac − *SMN Centre for Materials Science and Nanotechnology, Department of Chemistry, University of Oslo, Oslo N-0315, Norway*

Samy Ould-Chikh − *KAUST Catalysis Center (KCC), King Abdullah University of Science and Technology, Thuwal 23955, Saudi Arabia*; orcid.org/0000-0002-3486-0944

Christian Ahoba-Sam − *SMN Centre for Materials Science and Nanotechnology, Department of Chemistry, University of Oslo, Oslo N-0315, Norway*

Aram L. Bugaev − *The Smart Materials Research Institute, Southern Federal University, Rostov-on-Don 344090, Russian Federation*; orcid.org/0000-0001-8273-2560

Elisa Borfecchia − *Department of Chemistry, NIS Center and INSTM Reference Center, University of Turin, Turin 10125, Italy*; orcid.org/0000-0001-8374-8329

Sara Morandi − *Department of Chemistry, NIS Center and INSTM Reference Center, University of Turin, Turin 10125, Italy*; orcid.org/0000-0003-0577-7911

Matteo Signorile − *Department of Chemistry, NIS Center and INSTM Reference Center, University of Turin, Turin 10125, Italy*; orcid.org/0000-0003-0521-3702

Complete contact information is available at: https://pubs.acs.org/10.1021/jacsau.1c00302

Notes

The authors declare no competing financial interest.

ACKNOWLEDGMENTS

This project has received funding from the European Union's Horizon 2020 research and innovation programme under grant agreement 837733. The XAS measurements were supported by a public grant overseen by the French National Research Agency (ANR) as part of the "Investissements d'Avenir" program (reference: ANR-10-EQPX-45). The authors are grateful to C. La Fontaine and V. Briois, as well as to K. A. Lomachenko and A. Lazzarini for the help with the XAS experiment at ROCK, Soleil. Dr. Idoia Hita Del Olmo is acknowledged for her help with the TGA measurements. A.R., S.O.C., and J.G. acknowledge financial support from King Abdullah University of Science and Technology (KAUST). C.A.S. acknowledges the Norwegian Research Council for financial support through project no. 288331 (CO2LO). A.L.B. acknowledges the President's Grant of Russian Federation MK-5853.2021.1.2.

REFERENCES

(1) Markewitz, P.; Kuckshinrichs, W.; Leitner, W.; Linssen, J.; Zapp, P.; Bongartz, R.; Schreiber, A.; Müller, T. E. Worldwide Innovations in the Development of Carbon Capture Technologies and the Utilization of CO_2. *Energy Environ. Sci.* **2012**, *5* (6), 7281.

(2) Centi, G.; Quadrelli, E. A.; Perathoner, S. Catalysis for CO_2 Conversion: A Key Technology for Rapid Introduction of Renewable Energy in the Value Chain of Chemical Industries. *Energy Environ. Sci.* **2013**, *6* (6), 1711.

(3) Ojelade, O. A.; Zaman, S. F. A Review on CO_2 hydrogenation to Lower Olefins: Understanding the Structure-Property Relationships in Heterogeneous Catalytic Systems. *Journal of CO_2 Utilization* **2021**, *47*, 101506.

(4) Dittmeyer, R.; Klumpp, M.; Kant, P.; Ozin, G. Crowd Oil Not Crude Oil. *Nat. Commun.* **2019**, *10* (1), 1818.

(5) Zhou, W.; Cheng, K.; Kang, J.; Zhou, C.; Subramanian, V.; Zhang, Q.; Wang, Y. New Horizon in C1 Chemistry: Breaking the Selectivity Limitation in Transformation of Syngas and Hydrogenation of CO_2 into Hydrocarbon Chemicals and Fuels. *Chem. Soc. Rev.* **2019**, *48* (12), 3193−3228.

(6) Ramirez, A.; Dutta Chowdhury, A.; Dokania, A.; Cnudde, P.; Caglayan, M.; Yarulina, I.; Abou-Hamad, E.; Gevers, L.; Ould-Chikh, S.; de Wispelaere, K.; van Speybroeck, V.; Gascon, J. Effect of Zeolite Topology and Reactor Configuration on the Direct Conversion of CO_2 to Light Olefins and Aromatics. *ACS Catal.* **2019**, *9* (7), 6320−6334.

(7) Dokania, A.; Ramirez, A.; Bavykina, A.; Gascon, J. Heterogeneous Catalysis for the Valorization of CO_2: Role of Bifunctional Processes in the Production of Chemicals. *ACS Energy Letters* **2019**, *4* (1), 167−176.

(8) Shih, C. F.; Zhang, T.; Li, J.; Bai, C. Powering the Future with Liquid Sunshine. *Joule* **2018**, *2* (10), 1925−1949.

(9) *Propane Market−Growth, Trends, And Forecast (2020−2025)*; Report Linker, 2020.

(10) Liu, Z.; Ni, Y.; Sun, T.; Zhu, W.; Liu, Z. Conversion of CO_2 and H_2 into Propane over InZrO and SSZ-13 Composite Catalyst. *J. Energy Chem.* **2021**, *54*, 111−117.

(11) De, S.; Dokania, A.; Ramirez, A.; Gascon, J. Advances in the Design of Heterogeneous Catalysts and Thermocatalytic Processes for CO_2 Utilization. *ACS Catal.* **2020**, *10* (23), 14147−14185.

(12) Ge, Q.; Li, X.; Kaneko, H.; Fujimoto, K. Direct Synthesis of LPG from Synthesis Gas over Pd-Zn-Cr/Pd-β Hybrid Catalysts. *J. Mol. Catal. A: Chem.* **2007**, *278* (1−2), 215−219.

(13) Li, C.; Fujimoto, K. Selective Synthesis of Isobutane from CO2-Containing Synthesis Gas. *Energy Fuels* **2014**, *28* (2), 1331−1337.

(14) Li, G.; Jiao, F.; Miao, D.; Wang, Y.; Pan, X.; Yokoi, T.; Meng, X.; Xiao, F. S.; Parvulescu, A. N.; Müller, U.; Bao, X. Selective Conversion of Syngas to Propane over ZnCrOx-SSZ-39 OX-ZEO Catalysts. *J. Energy Chem.* **2019**, *36*, 141−147.

(15) Li, C.; Fujimoto, K. Synthesis Gas Conversion to Isobutane-Rich Hydrocarbons over a Hybrid Catalyst Containing Beta Zeolite − Role of Doped Palladium and Influence of the SiO_2/Al_2O_3 Ratio. *Catal. Sci. Technol.* **2015**, *5* (9), 4501−4510.

(16) Li, C.; Yuan, X.; Fujimoto, K. Direct Synthesis of LPG from Carbon Dioxide over Hybrid Catalysts Comprising Modified Methanol Synthesis Catalyst and β-Type Zeolite. *Appl. Catal., A* **2014**, *475*, 155−160.

(17) Ge, Q.; Tomonobu, T.; Fujimoto, K.; Li, X. Influence of Pd Ion-Exchange Temperature on the Catalytic Performance of Cu-

ZnO/Pd-β Zeolite Hybrid Catalyst for CO Hydrogenation to Light Hydrocarbons. *Catal. Commun.* **2008**, *9* (8), 1775−1778.
(18) Ticali, P.; Salusso, D.; Ahmad, R.; Ahoba-Sam, C.; Ramirez, A.; Shterk, G.; Lomachenko, K. A.; Borfecchia, E.; Morandi, S.; Cavallo, L.; Gascon, J.; Bordiga, S.; Olsbye, U. CO_2 Hydrogenation to Methanol and Hydrocarbons over Bifunctional Zn-Doped ZrO 2 /Zeolite Catalysts. *Catal. Sci. Technol.* **2021**, *11*, 1249.
(19) La Fontaine, C.; Belin, S.; Barthe, L.; Roudenko, O.; Briois, V. ROCK: A Beamline Tailored for Catalysis and Energy-Related Materials from Ms Time Resolution to Mm Spatial Resolution. *Synchrotron Radiation News* **2020**, *33* (1), 20−25.
(20) Ravel, B.; Newville, M. ATHENA, ARTEMIS, HEPHAESTUS: Data Analysis for X-Ray Absorption Spectroscopy Using IFEFFIT. *J. Synchrotron Radiat.* **2005**, *12*, 537−541.
(21) Tew, M. W.; Emerich, H.; Van Bokhoven, J. A. Formation and Characterization of PdZn Alloy: A Very Selective Catalyst for Alkyne Semihydrogenation. *J. Phys. Chem. C* **2011**, *115* (17), 8457−8465.
(22) Signorile, M.; Bonino, F.; Damin, A.; Bordiga, S. A Novel Raman Setup Based on Magnetic-Driven Rotation of Sample. *Top. Catal.* **2018**, *61* (14), 1491−1498.
(23) Yarulina, I.; Chowdhury, A. D.; Meirer, F.; Weckhuysen, B. M.; Gascon, J. Recent Trends and Fundamental Insights in the Methanol-to-Hydrocarbons Process. *Nature Catalysis* **2018**, *1* (6), 398−411.
(24) Bavykina, A.; Yarulina, I.; Al Abdulghani, A. J.; Gevers, L.; Hedhili, M. N.; Miao, X. H.; Galilea, A. R.; Pustovarenko, A.; Dikhtiarenko, A.; Cadiau, A.; Aguilar-Tapia, A.; Hazemann, J. L.; Kozlov, S. M.; Oud-Chikh, S.; Cavallo, L.; Gascon, J. Turning a Methanation Co Catalyst into an In-Co Methanol Producer. *ACS Catal.* **2019**, *9* (8), 6910−6918.
(25) Arora, S. S.; Shi, Z.; Bhan, A. Mechanistic Basis for Effects of High-Pressure H_2 Cofeeds on Methanol-to-Hydrocarbons Catalysis over Zeolites. *ACS Catal.* **2019**, *9* (7), 6407−6414.
(26) Bachiller-Baeza, B.; Rodriguez-Ramos, I.; Guerrero-Ruiz, A. Interaction of Carbon Dioxide with the Surface of Zirconia Polymorphs. *Langmuir* **1998**, *14* (13), 3556−3564.
(27) Lónyi, F.; Valyon, J. On the Interpretation of the NH_3-TPD Patterns of H-ZSM-5 and H-Mordenite. *Microporous Mesoporous Mater.* **2001**, *47* (2−3), 293−301.
(28) Gallagher, J. R.; Childers, D. J.; Zhao, H.; Winans, R. E.; Meyer, R. J.; Miller, J. T. Structural Evolution of an Intermetallic Pd-Zn Catalyst Selective for Propane Dehydrogenation. *Phys. Chem. Chem. Phys.* **2015**, *17* (42), 28144−28153.
(29) Ahoba-Sam, C.; Borfecchia, E.; Lazzarini, A.; Bugaev, A.; Isah, A. A.; Taoufik, M.; Bordiga, S.; Olsbye, U. On the Conversion of CO_2 to Value Added Products over Composite PdZn and H-ZSM-5 Catalysts: Excess Zn over Pd, a Compromise or a Penalty? *Catal. Sci. Technol.* **2020**, *10*, 4373−4385.
(30) Gentzen, M.; Doronkin, D. E.; Sheppard, T. L.; Zimina, A.; Li, H.; Jelic, J.; Studt, F.; Grunwaldt, J. D.; Sauer, J.; Behrens, S. Supported Intermetallic PdZn Nanoparticles as Bifunctional Catalysts for the Direct Synthesis of Dimethyl Ether from CO-Rich Synthesis Gas. *Angew. Chem., Int. Ed.* **2019**, *58* (44), 15655−15659.
(31) Kast, P.; Friedrich, M.; Girgsdies, F.; Kröhnert, J.; Teschner, D.; Lunkenbein, T.; Behrens, M.; Schlögl, R. Strong Metal-Support Interaction and Alloying in Pd/ZnO Catalysts for CO Oxidation. *Catal. Today* **2016**, *260*, 21−31.
(32) Jenros, E.; Lebarbier, V.; Datye, A.; Wang, Y.; Volux, J. M. Interaction of CO with Surface PdZn Alloys. *Surf. Sci.* **2007**, *601* (23), 5546−5554.
(33) Johnson, R. S.; DeLaRiva, A.; Ashbacher, V.; Halevi, B.; Villanueva, C. J.; Smith, G. K.; Lin, S.; Datye, A. K.; Guo, H. The CO Oxidation Mechanism and Reactivity on PdZn Alloys. *Phys. Chem. Chem. Phys.* **2013**, *15* (20), 7768−7776.
(34) Bollmann, L.; Ratts, J. L.; Joshi, A. M.; Williams, W. D.; Pazmino, J.; Joshi, Y. V.; Miller, J. T.; Kropf, A. J.; Delgass, W. N.; Ribeiro, F. H. Effect of Zn Addition on the Water-Gas Shift Reaction over Supported Palladium Catalysts. *J. Catal.* **2008**, *257* (1), 43−54.
(35) Kattel, S.; Ramirez, P. J.; Chen, J. G.; Rodriguez, J. A.; Liu, P. Active Sites for CO_2 Hydrogenation to Methanol on Cu/ZnO Catalysts. *Science* **2017**, *355* (6354), 1296−1299.
(36) Bordiga, S.; Groppo, E.; Agostini, G.; Van Bokhoven, J. A.; Lamberti, C. Reactivity of Surface Species in Heterogeneous Catalysts Probed by in Situ X-Ray Absorption Techniques. *Chem. Rev.* **2013**, *113* (3), 1736−1850.
(37) Martini, A.; Borfecchia, E.; Lomachenko, K. A.; Pankin, I. A.; Negri, C.; Berlier, G.; Beato, P.; Falsig, H.; Bordiga, S.; Lamberti, C. Composition-Driven Cu-Speciation and Reducibility in Cu-CHA Zeolite Catalysts: A Multivariate XAS/FTIR Approach to Complexity. *Chemical Science* **2017**, *8* (10), 6836−6851.
(38) Pinilla-herrero, I.; Borfecchia, E.; Holzinger, J.; Mentzel, U. V.; Joensen, F.; Lomachenko, K. A.; Bordiga, S.; Lamberti, C.; Berlier, G.; Olsbye, U.; Svelle, S.; Skibsted, J.; Beato, P. High Zn/Al Ratios Enhance Dehydrogenation vs Hydrogen Transfer Reactions of Zn-ZSM-5 Catalytic Systems in Methanol Conversion to Aromatics. *J. Catal.* **2018**, *362*, 146−163.
(39) Pinilla-herrero, I.; Borfecchia, E.; Cordero-Lanzac, T.; Mentzel, U. V.; Joensen, F.; Lomachenko, K. A.; Bordiga, S.; Olsbye, U.; Beato, P.; Svelle, S. Finding the Active Species : The Conversion of Methanol to Aromatics over Zn-ZSM-5/Alumina Shaped Catalysts. *J. Catal.* **2021**, *394*, 416−428.
(40) Rozanov, V. V.; Krylov, O. V. Hydrogen Spillover in Heterogeneous Catalysis. *Russ. Chem. Rev.* **1997**, *66* (2), 107−119.
(41) Conner, W. C.; Falconer, J. L. Spillover in Heterogeneous Catalysis. *Chem. Rev.* **1995**, *95* (3), 759.
(42) Ye, J.; Liu, C.; Mei, D.; Ge, Q. Active Oxygen Vacancy Site for Methanol Synthesis from CO_2 Hydrogenation on In_2O_3(110): A DFT Study. *ACS Catal.* **2013**, *3* (6), 1296−1306.
(43) Özgür, U.; Alivov, Y. I.; Liu, C.; Teke, A.; Reshchikov, M. A.; Dogan, S.; Avrutin, V.; Cho, S.-J.; Morkoc, H. A Comprehensive Review of ZnO Materials and Devices. *J. Appl. Phys.* **2005**, *98* (4), 041301.
(44) Göpel, W.; Lampe, U. Influence of Defects on the Electronic Structure of Zinc Oxide Surfaces. *Phys. Rev. B: Condens. Matter Mater. Phys.* **1980**, *22* (12), 6447−6462.
(45) Morandi, S.; Fioravanti, A.; Cerrato, G.; Lettieri, S.; Sacerdoti, M.; Carotta, M. C. Facile Synthesis of ZnO Nano-Structures: Morphology Influence on Electronic Properties. *Sens. Actuators, B* **2017**, *249* (3), 581−589.
(46) Esken, D.; Noei, H.; Wang, Y.; Wiktor, C.; Turner, S.; Van Tendeloo, G.; Fischer, R. A. ZnO@ZIF-8: Stabilization of Quantum Confined ZnO Nanoparticles by a Zinc Methylimidazolate Framework and Their Surface Structural Characterization Probed by CO_2 Adsorption. *J. Mater. Chem.* **2011**, *21* (16), 5907−5915.
(47) Busca, G.; Lorenzelli, V. Infrared Spectroscopic Identification of Species arising from Reactive Adsorption of Carbon Oxides on Metal Oxide Surfaces. *Mater. Chem.* **1982**, *7*, 89−126.
(48) Föttinger, K.; Emhofer, W.; Lennon, D.; Rupprechter, G. Adsorption and Reaction of CO on $PdAl_2O_3$ and $PdZrO_2$: Vibrational Spectroscopy of Carbonate Formation. *Top. Catal.* **2017**, *60* (19−20), 1722−1734.
(49) Lavalley, J. C. Infrared Spectrometric Studies of the Surface Basicity of Metal Oxides and Zeolites Using Adsorbed Probe Molecules. *Catal. Today* **1996**, *27* (3−4), 377−401.
(50) Köck, E.-M.; Kogler, M.; Bielz, T.; Klötzer, B.; Penner, S. In Situ FT-IR Spectroscopic Study of CO_2 and CO Adsorption on Y_2O_3, ZrO_2, and Yttria-Stabilized ZrO_2. *J. Phys. Chem. C* **2013**, *117* (34), 17666−17673.
(51) Pokrovski, K.; Jung, K. T.; Bell, A. T. Investigation of CO and CO_2 Adsorption on Tetragonal and Monoclinic Zirconia. *Langmuir* **2001**, *17*, 4297−4303.
(52) Akune, T.; Morita, Y.; Shirakawa, S.; Katagiri, K.; Inumaru, K. ZrO_2 Nanocrystals As Catalyst for Synthesis of Dimethylcarbonate from Methanol and Carbon Dioxide: Catalytic Activity and Elucidation of Active Sites. *Langmuir* **2018**, *34* (1), 23−29.

https://doi.org/10.1021/jacsau.1c00303
JACS Au 2021, 1, 1719−1732

(53) Bachiller-Baeza, B.; Rodriguez-Ramos, I.; Guerrero-Ruiz, A. Interaction of Carbon Dioxide with the Surface of Zirconia Polymorphs. *Langmuir* **1998**, *14* (13), 3556−3564.
(54) Freund, H.-J.; Roberts, M. W. Surface Chemistry of Carbon Dioxide. *Surf. Sci. Rep.* **1996**, *25*, 225−273.
(55) Ramis, G.; Busca, G.; Lorenzelli, V. Low-Temperature CO_2 Adsorption on Metal Oxides: Spectroscopic Characterization of Some Weakly Adsorbed Species. *Mater. Chem. Phys.* **1991**, *29* (1−4), 425−435.
(56) Esken, D.; Noei, H.; Wang, Y.; Wiktor, C.; Turner, S.; Van Tendeloo, G.; Fischer, R. A. $ZnO@ZIF$-8: Stabilization of Quantum Confined ZnO Nanoparticles by a Zinc Methylimidazolate Framework and Their Surface Structural Characterization Probed by CO_2 Adsorption. *J. Mater. Chem.* **2011**, *21* (16), 5907−5915.
(57) Groppo, E.; Bertarione, S.; Rotunno, F.; Agostini, G.; Scarano, D.; Pellegrini, R.; Leofanti, G.; Zecchina, A.; Lamberti, C. Role of the Support in Determining the Vibrational Properties of Carbonyls Formed on Pd Supported on SiO_2-Al_2O_3, Al_2O_3, and MgO. *J. Phys. Chem. C* **2007**, *111* (19), 7021−7028.
(58) Föttinger, K. The Effect of CO on Intermetallic PdZn/ZnO and Pd_2Ga/Ga_2O_3 Methanol Steam Reforming Catalysts: A Comparative Study. *Catal. Today* **2013**, *208*, 106−112.
(59) Conant, T.; Karim, A. M.; Lebarbier, V.; Wang, Y.; Girgsdies, F.; Schlögl, R.; Datye, A. Stability of Bimetallic Pd-Zn Catalysts for the Steam Reforming of Methanol. *J. Catal.* **2008**, *257* (1), 64−70.
(60) Rameshan, C.; Stadlmayr, W.; Weilach, C.; Penner, S.; Lorenz, H.; Hävecker, M.; Blume, R.; Rocha, T.; Teschner, D.; Knop-Gericke, A.; Schlögl, R.; Memmel, N.; Zemlyanov, D.; Rupprechter, G.; Klötzer, B. Subsurface-Controlled CO_2 Selectivity of PdZn near-Surface Alloys in H_2 Generation by Methanol Steam Reforming. *Angew. Chem., Int. Ed.* **2010**, *49* (18), 3224−3227.
(61) Hollins, P. The Influence of Surface Defects on the Infrared Spectra of Adsorbed Species. *Surf. Sci. Rep.* **1992**, *16* (2), 51−94.
(62) Khivantsev, K.; Jaegers, N. R.; Kovarik, L.; Hanson, J. C.; Tao, F.; Tang, Y.; Zhang, X.; Koleva, I. Z.; Aleksandrov, H. A.; Vayssilov, G. N.; Wang, Y.; Gao, F.; Szanyi, J. Achieving Atomic Dispersion of Highly Loaded Transition Metals in Small-Pore Zeolite SSZ-13: High-Capacity and High-Efficiency Low-Temperature CO and Passive NOx Adsorbers. *Angew. Chem., Int. Ed.* **2018**, *57* (51), 16672−16677.
(63) Nowicka, E.; Althahban, S. M.; Luo, Y.; Kriegel, R.; Shaw, G.; Morgan, D. J.; He, Q.; Watanabe, M.; Armbrüster, M.; Kiely, C. J.; Hutchings, G. J. Highly Selective PdZn/ZnO Catalysts for the Methanol Steam Reforming Reaction. *Catal. Sci. Technol.* **2018**, *8* (22), 5848−5857.
(64) Friedrich, M.; Penner, S.; Heggen, M.; Armbrüster, M. High CO_2 Selectivity in Methanol Steam Reforming through ZnPd/ZnO Teamwork. *Angew. Chem., Int. Ed.* **2013**, *52* (16), 4389−4392.
(65) Heggen, M.; Penner, S.; Friedrich, M.; Dunin-Borkowski, R. E.; Armbrüster, M. Formation of ZnO Patches on ZnPd/ZnO during Methanol Steam Reforming: A Strong Metal−Support Interaction Effect? *J. Phys. Chem. C* **2016**, *120* (19), 10460−10465.
(66) Föttinger, K.; Van Bokhoven, J. A.; Nachtegaal, M.; Rupprechter, G. Dynamic Structure of a Working Methanol Steam Reforming Catalyst: In Situ Quick-EXAFS on Pd/ZnO Nanoparticles. *J. Phys. Chem. Lett.* **2011**, *2* (5), 428−433.
(67) Signorile, M.; Rojo-Gama, D.; Bonino, F.; Svelle, S.; Beato, P.; Bordiga, S. Operando UV-Raman Study of the Methanol to Olefins Reaction over SAPO-34: Spatiotemporal Evolution Monitored by Different Reactor Approaches. *Catal. Today* **2019**, *336*, 203−209.
(68) Signorile, M.; Rojo-Gama, D.; Bonino, F.; Beato, P.; Svelle, S.; Bordiga, S. Topology-Dependent Hydrocarbon Transformations in the Methanol-to-Hydrocarbons Reaction Studied by Operando UV-Raman Spectroscopy. *Phys. Chem. Chem. Phys.* **2018**, *20* (41), 26580−26590.
(69) Sheppard, N.; Simpson, D. M. The Infra-Red and Raman Spectra of Hydrocarbons. Part I. Acetylenes and Olefins. *Q. Rev., Chem. Soc.* **1952**, *6* (1), 1−33.
(70) Signorile, M.; Bonino, F.; Damin, A.; Bordiga, S. In Situ Resonant UV-Raman Spectroscopy of Polycyclic Aromatic Hydrocarbons. *J. Phys. Chem. C* **2015**, *119* (21), 11694−11698.
(71) Bahruji, H.; Bowker, M.; Jones, W.; Hayward, J.; Ruiz Esquius, J.; Morgan, D. J.; Hutchings, G. J. PdZn Catalysts for CO_2 Hydrogenation to Methanol Using Chemical Vapour Impregnation (CVI). *Faraday Discuss.* **2017**, *197*, 309−324.
(72) Malik, A. S.; Zaman, S. F.; Al-Zahrani, A. A.; Daous, M. A.; Driss, H.; Petrov, L. A. Development of Highly Selective PdZn/CeO_2 and Ca-Doped PdZn/CeO_2 Catalysts for Methanol Synthesis from CO_2 Hydrogenation. *Appl. Catal., A* **2018**, *560* (April), 42−53.
(73) Malik, A. S.; Zaman, S. F.; Al-Zahrani, A. A.; Daous, M. A.; Driss, H.; Petrov, L. A. Selective Hydrogenation of CO_2 to CH_3OH and In-Depth DRIFT Analysis for PdZn/ZrO 2 and CaPdZn/ZrO 2 Catalysts. *Catal. Today* **2020**, *357*, 573.
(74) Ojelade, O. A.; Zaman, S. F.; Daous, M. A.; Al-Zahrani, A. A.; Malik, A. S.; Driss, H.; Shterk, G.; Gascon, J. Optimizing Pd:Zn Molar Ratio in PdZn/CeO_2 for CO_2 Hydrogenation to Methanol. *Appl. Catal., A* **2019**, *584* (May), 117185.
(75) Ojelade, O. A.; Zaman, S. F. A Review on Pd Based Catalysts for CO_2 Hydrogenation to Methanol: In-Depth Activity and DRIFTS Mechanistic Study. *Catal. Surv. Asia* **2020**, *24* (1), 11−37.
(76) Hereijgers, B. P. C.; Bleken, F.; Nilsen, M. H.; Svelle, S.; Lillerud, K.-P.; Bjørgen, M.; Weckhuysen, B. M.; Olsbye, U. Product Shape Selectivity Dominates the Methanol-to-Olefins (MTO) Reaction over H-SAPO-34 Catalysts. *J. Catal.* **2009**, *264* (1), 77−87.
(77) Dahl, I. M.; Kolboe, S. On the Reaction Mechanism for Propene Formation in the MTO Reaction over SAPO-34. *Catal. Lett.* **1993**, *20* (3−4), 329−336.
(78) Daza, Y. A.; Kuhn, J. N. CO_2 Conversion by Reverse Water Gas Shift Catalysis: Comparison of Catalysts, Mechanisms and Their Consequences for CO_2 Conversion to Liquid Fuels. *RSC Adv.* **2016**, *6* (55), 49675−49691.

https://doi.org/10.1021/jacsau.1c00303
JACS Au 2021, 1, 1719−1732

6.4 D : Ruzzi et al., Applied Catalysis A, General 635 (2022) 118568

Applied Catalysis A, General 635 (2022) 118568

Contents lists available at ScienceDirect

Applied Catalysis A, General

journal homepage: www.elsevier.com/locate/apcata

Supported PdZn nanoparticles for selective CO_2 conversion, through the grafting of a heterobimetallic complex on $CeZrO_x$

Paolo Ruzzi [a], Davide Salusso [b], Matilde Baravaglio [a,b], Kai C. Szeto [a], Aimery De Mallmann [a], Laia Gil Jiménez [c], Cyril Godard [c], Anass Benayad [d], Sara Morandi [b], Silvia Bordiga [b,*], Mostafa Taoufik [a,*]

[a] Université de Lyon 1, CPE Lyon, CNRS-UMR 5128 – Laboratoire Catalyse, Polymérisation, Procédés et Matériaux (CP2M), F-69616 Villeurbanne, France
[b] Department of Chemistry, NIS Center and INSTM Reference Center, University of Turin, 10125 Turin, Italy
[c] Departament de Química Física i Inorgànica, Universitat Rovira i Virgili, Marcel·lí Domingo s/n, Campus Sescelades, 43007 Tarragona, Spain
[d] Université Grenoble Alpes, CEA-LITEN, 17 rue des Martyrs, 38054 Grenoble Cedex 9, France

ARTICLE INFO

Keywords:
Surface organometallic chemistry
In-situ IR
Hydrocarbon production
Palladium
Light alkanes

ABSTRACT

Controlling the stoichiometry of supported bimetallic nanoparticles is essential in many catalytic reactions, notably selective CO_2 hydrogenation. Thus, a new strategy to ensure the preferred stoichiometry (1:1) of supported bimetallic PdZn nanoparticles is presented, involving the deposition of a heterobimetallic precursor, $[PdZn(\mu\text{-}OOCMe)_4]_2$ on a $CeZrO_x$ support. After calcination and reduction, the material contained mainly a PdZn alloy, as revealed by powder XRD and XAFS, and further supported by XPS, TEM-EDX, elemental analysis and in-situ IR at low temperature using CO as probe molecule. Moreover, a minor phase of oxidized Zn was determined by XAFS. This PdZn/CeZrOx reduced catalyst was combined with SAPO-34 to form a tandem catalytic system for CO_2 conversion to hydrocarbons. This system could readily convert CO_2 and H_2 at high temperature (380 °C) into hydrocarbons with a conversion of 24% and high relative selectivity in light hydrocarbons (C2–C5: 82%) with virtually no deactivation of the catalyst after 16 h on stream. Controlled experiments were performed with Pd/CeZrOx and Zn/CeZrOx in order to gain supplementary insights on this system: Pd/CeZrOx gave only methane and Zn/CeZrOx gave mainly CO under the same conditions. The latter clearly shows that the control of the formation of PdZn phase has great impact for the selective production of hydrocarbons.

1. Introduction

Constant increase of the CO_2 concentration in the atmosphere has resulted in environmental changes such as global warming and ocean acidification [1–5]. Any action to decrease the CO_2 emission or concentration in the atmosphere is of great interest. Among them are carbon capture and storage (CCS), and carbon capture and utilization (CCU) [6, 7]. CCU seems to be more valuable and sustainable than CCS [8,9]. Although CO_2 seems to be an undesired molecule, it can theoretically be served as an inexpensive, non-toxic, non-flammable and sustainable carbon source to produce high value products such as fuels and chemicals [10,11]. However, due to its high stability, CO_2 has to be activated by heat, light, or electricity (thermochemical, photochemical, electrochemical, or photo-electrochemical processes) [12–16], and more efficiently assisted by a catalyst. Nowadays, the processes based on thermo-catalytic conversion of CO_2 show suitable productivity at commercial scale. Indeed, these processes lead to a variety of carbon-based products, including carbon monoxide, formaldehyde, methanol, methane, or light hydrocarbons (e.g., ethylene, propylene) [17,18], depending on the nature of the catalyst. Chemical conversion of CO_2 to value-added chemicals and fuels potentially presents an important supply for the declining and non-renewable fossil fuels that are currently the major source of chemicals and energy being inevitable in current society [19,20].

Transformation of CO_2 into hydrocarbon-based fuels can be achieved via hydrogenation through two different ways: i) synthesis gas production by the reverse water-gas shift (RWGS) reaction followed by Fischer-Tropsch (FT) reaction to produce hydrocarbons [21]; ii) methanol synthesis [22] accompanied by methanol-to-olefin (MTO) process [23,24]. The second method is more selective and lead to C2-C4 olefins while FT

* Corresponding authors.
E-mail addresses: silvia.bordiga@unito.it (S. Bordiga), mostafa.taoufik@univ-lyon1.fr (M. Taoufik).

https://doi.org/10.1016/j.apcata.2022.118568
Received 30 November 2021; Received in revised form 1 March 2022; Accepted 2 March 2022
Available online 5 March 2022

synthesis leads to a Schultz-Flory-Anderson distribution of hydrocarbons that needs to be treated by cracking and separation in order to obtain the desired products [25]. Moreover, CO_2 hydrogenation via methanol requires lower energy and cost than the other route. Consequently, the cascade reaction to produce light hydrocarbons through methanol has motivated many research groups for extensive exploration. Obviously, this process requires two different catalysts, first for the conversion of CO_2 into methanol intermediate, supported metal nanoparticles or metal oxide or mixed oxide (e.g. In_2O_3, ZnO, ZrO_2/ZnO) catalysts can be used. Second, MTO reaction can be readily catalyzed by zeolites, such as ZSM-5 or SAPO-34 [26–28].

The main challenge of catalytic CO_2 hydrogenation into hydrocarbons over a single reactor is the presence of the RWGS reaction, which is kinetically favored leading to the production of CO. Particularly at high working temperatures required for MTO (over 350 °C), the selectivity of CO can be over 80%. Moreover, water formed during CO_2 hydrogenation to hydrocarbons using bifunctional catalysts can alter the activity and stability of the zeolite. Therefore, synthesis of light hydrocarbons with a high selectivity from CO_2 hydrogenation over a bifunctional catalyst is very challenging. Despite some promising results, the aforementioned issues, like high CO selectivity, frequently higher than 50% and the proper zeolite selection still have to be overcome. Furthermore, the hydrogenation of CO_2 is thermodynamically unfavorable, but the conversion of methanol to lower olefins is considerably favorable. Hence, a cascade process by coupling these two reactions gives an additional driving force to convert the formed methanol and thereby make the overall process (CO_2 to light hydrocarbons) feasible. However, this thermodynamic coupling is observed only when the two catalytic components are in intimate contact [29,30].

Several tandem catalytic systems are reported in the literature. For example, ZnO-ZrO_2 mixed with Zn-modified SAPO-34 shows high relative selectivity (among hydrocarbons) towards lower olefins (80–90%) but accompanied with a high selectivity in undesired CO (ca. around 50%). Surprisingly, the CO selectivity for the tandem catalysts is already significantly suppressed compared to the ZnO-ZrO_2 mixed oxide alone [31]. The reason is probably associated to the formation of water by the MTO reaction catalyzed by the zeolite that will trigger the water-gas shift reaction, resulting in the consumption of CO. Another aspect to limit the formation of CO is to select a proper active phase in order to minimize the RWGS reaction upon hydrogenation of CO_2 to hydrocarbons under the given working temperature (over 350 °C). Based on thermodynamic and kinetic analyses of this process (CO_2 to hydrocarbon via methanol) along with literature reports, the greatest challenge lies on the methanol synthesis catalyst. Several metals, metal alloys and metal oxides were used for CO_2 hydrogenation to MeOH, including catalysts based on other mixed oxides, for example In_2O_3/ZrO_2 [30,31] or ZnO/ZrO_2 [32–37] or noble metal such as supported Pd-NPs, PdZn-based catalysts have shown promising MeOH yield especially at medium temperatures (210–270 °C) [38–43]. Supplementary screening of different catalysts with various compositions revealed that the methanol production can be enhanced by increasing the Zn/Pd ratio [39,40]. The latter is attributed to increased $Zn^{(0)}$ incorporation in the Pd lattice, ensuring the formation of surface PdZn (1:1 ratio) alloy which is believed to be the most important phase for methanol production. Complementary experiments conducted on Pd (without Zn) supported on TiO_2 or Al_2O_3 showed that CO was the predominant product, indicating that Pd nanoparticles promote the RWGS reaction. A mechanistic study using DRIFT and DFT calculations proposed two possible intermediates in CO_2 hydrogenation over PdZn catalysts: (i) HCOO which directly hydrogenates to MeOH or (ii) trans-COOH, which isomerize to cis-COOH for RWGS reaction or MeOH [39–42]. Trans-COOH formation was found to be energetically favored on pure Pd (111) while it was highly unstable on Pd_1Zn_1 (111). These findings are in good agreement with experimental data, and highlight the importance of the PdZn (1:1) alloy for hydrogenation of CO_2 to methanol. Furthermore, different supports were also studied. Apart from the robust ZrO_2 support, the presence of Cerium seems to have a beneficial effect due to supplementary CO_2 uptake [44,45]. Since the ultimate goal is to produce light hydrocarbons from CO_2, additional circumstances, such as thermodynamic and the involvement of MTO catalyst, have to be considered. Methanol formation is generally favored at fairly low temperatures (around 250 °C). At higher temperature, production of CO becomes favorable. Unfortunately, the MTO reaction requires higher temperature (> 350 °C) to be efficient. Hence, an expected challenge will be to minimize the CO selectivity. In addition, a recent study of the PdZn system mechanically mixed with H-ZSM-5 and PdZn on meso-porous H-ZSM-5 (prepared through surface organometallic chemistry on metal) revealed that Zn has a tendency to exchange with Brønsted proton. During the catalytic process, this resulted in an inhibition of the hydrocarbon production [46].

Gathering information from the literature for Pd-based methanol synthesis catalysts, an enhanced system should contain PdZn alloy having the preferred stoichiometry (1:1). Moreover, employing a Ce-based support is favorable in order to maximize the CO_2 uptake. Hence, we hereby describe a methodology to access such system by applying surface organometallic chemistry with a heterobimetallic precursor based on Pd and Zn onto a commercial ceria-zirconia support. We also prepared PdZn alloy onto pure ZrO_2 to directly compare SOMC to the same catalyst prepared by colloidal impregnation recently applied to prepare PdZn/ZrO_2 catalyst [47]. Employing a heterobimetallic precursor will ensure the desired stoichiometry between Pd and Zn (1:1), which is essential for this system and has already shown to enhance the catalytic activity for partial acetylene hydrogenation [48]. Furthermore, the surface organometallic chemistry approach involves grafting of the selected precursor onto the support, offering a firmly bonded intermediate and thereby minimizing migration and leaching of the elements upon calcination and reduction. In addition, this synthesis strategy will avoid formation of local monometallic nanoparticles or clusters that may occur by using conventional preparation methods like wetness impregnation and sol-gel synthesis. In this paper, we report the synthesis of PdZn nanoparticles supported on ceria-zirconia and the characterization of the material by elemental analysis, Surface and porosity analyses, IR, PXRD, TEM and EDX, CO adsorption followed by IR, XPS, and EXAFS. The catalytic performance in the conversion of CO_2 of the different tandem catalysts composed of supported PdZn mechanically mixed with commercial SAPO-34 are reported. For comparison complementary catalysts containing PdZn supported on ceria and on zirconia and monometallic Pd and Zn supported ceria-zirconia were also prepared to gain further comprehension. Finally, the most promising system, being PdZn/CeZrOx was characterized by XAS and in-situ IR.

2. Experimental

2.1. Catalysts preparation

Commercial Ceria (Solvay ACTALYS HSA 5) and Ceria Zirconia (Solvay ACTALYS 922, CeZrOx with a CeO_2/ZrO_2 ratio of 58–42 wt%) were purchased from Solvay. Zirconia was synthetized from Zr(IV) hydroxide (Sigma-Aldrich, CAS no. 14475-63-9) by calcination in a dry oxygen flow at 500 °C for 16 h.

Ceria, Zirconia and Ceria Zirconia were calcined for 16 h at 500 °C under a flow of dry air, then cooled down under vacuum. After a rehydration under an inert atmosphere, the oxides were partially dehydroxylated at 200 °C under a high vacuum (10^{-5} mbar) for 2 h.

This supported catalyst was synthesized using surface organometallic chemistry (SOMC) grafting approach. The heterobimetallic precursor, PdZn(μ-$OOCCH_3$)$_4$, was obtained following the procedure reported by Kozitsyna et al. [49].

The catalysts were produced starting from PdZn(μ-$OOCCH_3$)$_4$ (1.54 mmol) and the oxide (CeO_2, ZrO_2 or CeZrOx, 3 g, 5 wt% Pd) in toluene for 4 h, stirred at 80 °C under an inert atmosphere. The titration of surface OH provided a concentration of 0.6 mmol/g for CeO_2, 0.21

mmol/g for CeZrOx and 0.15 mmol/g for ZrO_2. Then among the three studied supports, CeO_2 has sufficient surface OH groups to react with the amount of precursor (ca. 0.513 mmol Pd/g of oxide). However, the available surface OH groups of CeZrOx and ZrO_2 are in deficient with respect to the added precursor. Thus, part of the precursor is probably grafted and a quantity will be deposited for these two latter supports. Acetic acid was qualitatively observed by GC in the solution, testifying some grafting of the hetero bimetallic complex through protonolysis. However, due to the strong adsorbing nature of acetic acid on the basic supports, quantification was rather challenging. The solvent was evaporated and the sample was then calcined for 16 h at 500 °C under a flow of dry air, then cooled down under vacuum. Afterwards, the sample was reduced under a flow of H_2 at 400 °C for 3 h. Afterwards, the samples were stored in an inert atmosphere.

The same procedure was applied for the production of Pd@CeZrOx (5 wt% Pd) and Zn@CeZrOx (3 wt% Zn) using Pd(μ-$OOCCH_3$)$_2$ and Zn (μ-$OOCCH_3$)$_2$ as precursors.

SAPO-34 (CAS: 1318-02-1) was purchased from ACS materials. The sample was calcined for 16 h at 500 °C under a flow of dry air.

2.2. Elemental analysis

Elemental analyses were performed by the Pascher Microanalysis Laboratory in Remagen, via ICP. Samples were sent there sealed under vacuum.

2.3. Surface area and porosity analysis

BET surface area analysis was run via N_2 adsorption at 77,185 K on a Micromeritics ASAP 2020 Surface Area and Porosity Analyzer, interfaced with the ASAP 2020 V3.04 program. This analysis allowed to quantify BET and Langmuir surface area, as well as pore volume and size.

2.4. Powder X-Ray Diffraction

Powder X-Ray Diffraction (PXRD) patterns were collected on a Bruker D8 Advance diffractometer with Bragg-Brentano geometry goniometer in Theta-Theta mode and Cu Kα1,2 X-Ray source. Diffractograms were collected in 10–70° 2θ range by ethanol dispersion over Silicon support and treated using DIFFRAC.EVA Bruker software.

2.5. Infrared spectroscopy

Fourier Transform Infrared Spectroscopy (FTIR) in Attenuated Total Reflectance (ATR) mode was used to characterize the evolution of the samples during the synthesis procedure by measuring spectra under inert atmosphere, i.e. by using a Bruker-Alpha spectrophotometer with diamond crystal directly inside the glove-box. Spectra were collected in a 4000–600 cm^{-1} range with 2 cm^{-1} resolution using a Deuterated TriGlycine Sulfate (DTGS) detector.

FTIR spectroscopy in transmission mode was instead employed to characterize surface properties of the catalysts by following the adsorption of CO used as probe molecule. Absorption/transmission FTIR spectra were collected using a Bruker Vertex 70 spectrophotometer equipped with a Mercury Cadmium Telluride (MCT) cryo-detector in the 4000–600 cm^{-1} range with 2 cm^{-1} resolution. Powders were pressed in self-supporting discs (~ 10 mg/cm^2) and placed in quartz IR cells suitable for thermal treatments in controlled atmosphere and for spectra recording at room temperature (RT) and liquid nitrogen temperature (nominal LNT). Before IR measurements, catalysts underwent an activation procedure meant to simulate the catalyst calcination and reduction processes. In both cases the followed protocol started with: i) outgassing and heating of the catalyst from RT to 400 °C at 5 °C/min, ii) holding at 400 °C for 30', iii) treating under O2 (40 mbar) for 30' and iv) cooling down to RT under O_2. Reduction treatment was simulated prior treating the oxidised catalyst with H_2 (40 mbar) at 400 °C for 30' followed by cooling under vacuum. As presented the best conversion/selectivity results, FTIR spectra were collected only for PdZn alloy supported on CeZrOx. After the activation procedure, spectra of CO absorption at increasing pressure up to 40 mbar were collected at RT and 77 K. Spectra were treated using Bruker OPUS spectroscopy software.

2.6. X-ray photoelectron spectroscopy (XPS)

Chemical characterization by XPS was carried out using a Versaprobe II spectrometer from ULVAC-PHI. A monochromatic microfocused beam (X-ray source Al-Kα 1486.6 eV) of 100 μm of diameter and 250 W power was focused on the surface of the samples. The high-resolution and survey spectral analyses were performed using pass energy of 23.9 and 117 eV corresponding to a resolution of 0.6 and 1.6 eV, respectively. All XPS measurements were carried out in an ultra-high vacuum chamber ($7 \cdot 10^{-10}$ mbar). Each core level peak was recorded within a scan rate of 0.1 eV/s. The binding energy calibration was performed using Au4f7/2 (83.94 eV), Ag3d5/2 (368.2 eV) and Cu2p3/2 (932.6 eV). CasaXPS software was used for Ce 3d, Zn LMM and Pd 3d curve fitting. All were performed using pseudo-Voigt function and corrected Shirley background for the former and linear background for the Zn and Pd regions.

2.7. X-ray absorption spectroscopy (XAS)

EXAFS spectra were acquired at ESRF, Grenoble, France, using BM23 beam-line at the zinc K-edge in the transmission mode. For each sample, four scans were recorded, between 9.5 and 10.7 keV, at room temperature (295 K). Each data set was collected simultaneously with a Zn metal foil reference (9658.6 eV) [50], and was later aligned according to that reference (first maximum of the derivative of the Zn foil spectrum set at 9658.6 eV). The samples were packed in an argon-filled glovebox within an air-tight sample holder. The data analyses were carried out using the program "Athena" [51] and the EXAFS fitting program "RoundMidnight", from the "MAX" package [52], using spherical waves. The program FEFF8 was used to calculate theoretical files for phases and amplitudes based on model clusters of atoms [53]. The refinements were carried out by fitting the structural parameters N_i, R_i, σ_i and the energy shift, ΔE_0 (generally the same for all shells of a same phase). The S_0^2 parameter was set at the value proposed by FEFF8 program (0.92). For each fit, the quality factor, $(\Delta\nu)^2/\nu$, where ν is the number of degrees of freedom in the signal, was calculated and its minimization considered in order to control the number of variable parameters in the fits [54].

2.8. Electron microscopy: TEM, STEM and EDX

Scanning Transmission Electron Microscopy – High Angle Annular Dark Field (STEM-HAADF) images were obtained in a probe-corrected Titan Low Base (FEI) at a working voltage of 300 kV, coupled with a HAADF detector (Fischione) available at the "Advanced Microscopy Laboratory (LMA)" of the University of Zaragoza". X-ray Energy Dispersive Spectra (EDS) were obtained with an EDAX detector. The samples were dispersed in toluene and a small amount of solution was deposited on a Cu-carbon grid.

2.9. Catalytic tests

CO2 conversion was performed in Microreactivity (PID, Micromeritics) reactor equipped with a furnace (max. temperature = 700 °C), Bronkhorst massflow controllers and a back-pressure regulator. The ½'' stainless steel reactor was placed in the furnace inside a hot box (max. temperature = 150 °C) allowing pre-heating of the gas and avoiding condensation in the outlet lines. The catalytic bed is comprised of the catalyst in powder form (grain size of the catalyst powder: 15–20 nm, grain size of the SAPO-34: 3–5 μm). The reactor contains a 4-way valve,

the catalyst can then be charged in the glovebox and the gas lines can be extensively purged with the reactant gas before exposing to the catalyst. A certified gas cylinder (Mélange Crystal, Air Liquide) with H_2/CO_2 ratio of 3 was used. The reactor was first pressurized to the desired pressure (up to 30 bar) before the heating was started (10 °C/min). The post-reactor lines were heated to 150 °C to minimize condensation of the product and connected to an online GC (Agilent 7890A) equipped with two columns in series (PLOT Q and Carbon Plot, the latter in store column configuration). The products were detected by TCD and FID (equipped with JetanizerTM) connected in series. The conversion and selectivity values were obtained using the following formulas:

$$Conversion = \frac{\text{Total mol of } products}{\text{Total mol in } effluent} * 100$$

$$Selectivity\ to\ Cn = \frac{n * Total\ mol\ of\ Cn}{\Sigma(n * Total\ mol\ of\ Cn)} * 100$$

The carbon balance is close to 100% when taking into account instrumental errors (typically aroued 5% for GC).

3. Results and discussion

3.1. Supported PdZn nanoparticles through surface organometallic chemistry

3.1.1. From the complex to the supported PdZn nanoparticles

Successful deposition and reduction of $[PdZn(\mu\text{-}OOCMe)_4]_2$ was monitored by ATR spectroscopy using the acetate complex spectra reported in Fig. S1 as reference spectra. Whilst after grafting acetates vibration modes, discussed in detail in Table S1, are observed over catalysts surface, they are consumed after reduction process (Fig. S2). This result, combined with the multiple Pd and Zn signals in the XPS scans (vide infra) and the PdZn Bragg Reflection in the diffractogram (Fig. 2), confirms bimetallic alloy formation parallel to the acetate complex thermolysis. ATR-FTIR is based on the interaction between the evanescent wave and the sample. The former consists only of a little part of the incoming beam and penetrates few μm in the sample. Since the particle size is observed to be in the nm scale (Fig. S8) in this case ATR can be considered as a bulk technique reducing the surface-to-bulk signal. As clearly visible in Fig. S2, ATR-FTIR spectra shows only features of very intense band (i.e., abundant acetates) whilst it does not provide sufficient information on the OH stretching region. To deeply investigate molecule-to-support interactions we then characterized PdZn@CeZrOx, the most promising catalyst (vide infra) by FTIR spectroscopy in transmission mode.

Absorption/transmission FTIR spectra of the PdZn@CeZrOx synthesis steps unveiled a variation in the OH stretching region parallel to acetate band formation appeared between 1650 and 1300 cm^{-1} (Fig. 1, **a**) Absorption/transmission FTIR spectra of CeZrOx support after: i) hydroxyl groups normalization (grey), ii) $[PdZn(\mu\text{-}OOCMe)_4]_2$ grafting and deposition (yellow), iii) calcination under O_2 (purple) and iv) reduction under H_2 (blue). Spectra of reference CeZrOx reduced is reported in red for clarity. b) Detail of OH stretching region. Figs. 1**a** and 1**b** pinpointing as grafting occurs to the detriment of terminal and bi-bridged OH groups at 3687 and 3650 cm^{-1}, respectively [55]. Calcination process restored partly OH vibrations collateral to acetate consumption (purple spectra, Fig. 1), whilst reduction induced formation of $Ce^{+3}\ ^2F_{5/2} \rightarrow {}^2F_{7/2}$ electronic transition at 2127 cm^{-1} (blue spectra, Fig. 1**a**) indirectly unveiling presence of oxide-related bulk oxygen vacancies (V_O) [56]. In order to obtain deeper information on the catalytic sites available on the catalyst surface before and after PdZn alloy formation, i.e. metallic and Lewis sites, we then probed the surface by CO adsorption.

As supporting samples, $[PdZn(\mu\text{-}OOCMe)_4]_2$ grafting and calcination over pure CeO_2 and ZrO_2 were followed by ATR spectroscopy, showing the same behavior as PdZn@CeZrOx (Fig. S2).

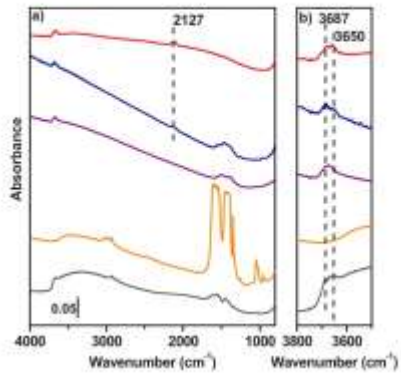

Fig. 1. a) Absorption/transmission FTIR spectra of CeZrOx support after: i) hydroxyl groups normalization (grey), ii) $[PdZn(\mu\text{-}OOCMe)_4]_2$ grafting and deposition (yellow), iii) calcination under O_2 (purple) and iv) reduction under H_2 (blue). Spectra of reference CeZrOx reduced is reported in red for clarity. b) Detail of OH stretching region.

3.1.2. Composition, structure, and texture of PdZn nanoparticles: basic characterization

CeO_2, ZrO_2 and CeZrOx presented good crystallinity after grafting and calcination, as evidenced by the PXRD patterns in Fig. S3. Due to crystallite dimension-induced peak broadening, we cannot safely distinguish between cubic and tetragonal polymorphs. Thus, the most common structures for the three supports were used for simulation: cubic (*Fm*-3*m*) for CeO_2 [57], tetragonal ($P4_2/nmc$) for CeZrOx [58] and tetragonal/monoclinic ($P4_2/nmc$ and $P2_1/c$) mixture for ZrO_2 [59,60]. For the latter tetragonal-to-monoclinic ratio was evaluated as 50:50 using the equation proposed by Evans et al. [61] reported for clarity in SI together with the peak fit in Fig. S4.

The characterization of the reduced bimetallic catalyst, PdZn/CeZrOx by X-ray diffraction revealed the presence of a Bragg reflection at ca. 41° in the diffractogram (Fig. 2) [62,63], confirming the formation of a

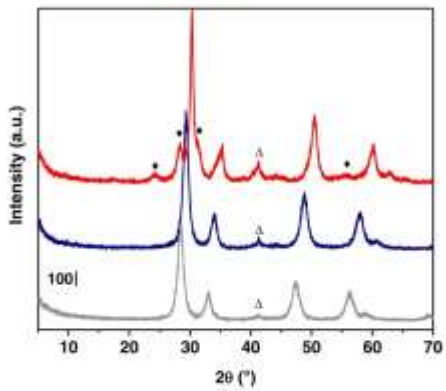

Fig. 2. PXRD patterns of $[PdZn(\mu\text{-}OOCMe)_4]_2$ grafted/deposited and reduced under H_2 on c-CeO_2 (gray), t-CeZrOx (blue) and m/t-ZrO_2 (red), diamonds indicate monoclinic reflections. Triangles indicate PdZn alloy Bragg reflection.

supported bimetallic $Pd_{1-x}Zn_x$ alloy after thermolysis under hydrogen [46]. Similar features were observed for PdZn supported on CeO_2 and ZrO_2 (Fig. S3). However, among the various existing PdZn alloy phases [64], several of them show a Bragg reflection in this 2θ range [65]. Due to low PXRD pattern resolution it is then not possible to specify the alloy phase, i.e. tetragonal β1 phase ($P4/nmm$ space group; $Pd_{1-x}Zn_x$ with $x = 0.36–0.51$), or palladium rich cubic β° phase or a mixture of different alloy phases [66]. The β1 phase should present two Bragg diffraction peaks in the 40–45° 2θ range for (101) type planes and (110) type planes in a 10/4 ratio at ca. 41.3 and 44.1° and a cubic structure only one. A less intense peak at ca. 44° may exist but is difficult to observe on the diffractograms (Fig. 2). The material was further characterized by XAS in order to try to specify the type of PdZn alloy present in the material (see below). Noteworthy, Bragg reflections from segregated ZnO, previously observed by preparing $PdZn/ZrO_2$ through colloidal impregnation synthesis [47], have not been observed, suggesting as SOMC techniques increased PdO/ZnO surface dispersion hence improving PdZn alloy formation.

The textural properties of the bare support and reduced sample are compared in Table 1. The adsorption/desorption isotherms are reported in the Supplementary information (Fig. S7) and show hysteresis loop characteristic of mesoporous materials. It is important to underline that the specific surface area and the pore volume of PdZn/CeZrOx somewhat decrease after immobilization of the bimetallic alloy (see Table S2). Similar features were observed for PdZn supported on CeO_2 and ZrO_2 (Table S2 and Figs. S5–S6).

TEM was used to characterize PdZn/CeZrOx. This technique normally allows to acquire information about the particle size distribution of the samples. In this case, as shown in picture Fig. S7, no sign of metallic particles or alloy was clearly observed due to the heavy support (notably the presence of Ce as well as Zr) which will absorb most of the electron beam and mask the lighter elements (Pd and Zn). No intuitive improvement was observed in the dark field mode (STEM HAADF). Nevertheless, the coupling of the microscopy with EDX analysis still provides insight about the elemental composition of the catalyst, though this method remains local and extremely selective dependent on the analyzed spot. The sampling of different points can in fact be used to verify the homogeneity in the composition of the bimetallic nanoparticles and its homogeneous distribution on the surface. Interestingly, all of the sampled points show correspondence between Pd and Zn. The technique also allows a quantification of these metals. EDX analyses on multiple zones revealed that the Zn/Pd ratio lies around 1, with an average value of 1.2 having a relatively high standard deviation (0.6). The inhomogeneity is most likely due to the presence of different metallic phases. The presence of PdZn alloy was confirmed by XRD. However, it was reported that monometallic Pd core can exist due to incomplete alloying [62]. Elemental analysis (ICP) is a far more reliable method to determine the bulk composition than TEM/EDX. ICP analysis of the sample proved that the bulk composition of the material (Pd = 5.07 wt%; Zn 3.10 wt%) maintain the desired 1:1 ratio between Zn/Pd (Table S3). The bulk composition of Zn/Pd is found to be 1. Nevertheless, the heterogeneity seems to be more pronounced for PdZn supported on CeO_2 and ZrO_2, suggested by TEM-EDX (Table S4).

Table 1
Superficial area, pore volume and pore diameter obtained for the treated support CeZrOx and for the reduced catalyst.

	CeZrOx	PdZn@CeZrOx
BET SA (m^2/g)	101.4	83.2
BJH pore volume (cm^3/g)	0.24	0.18
BJH poreo diameter (nm)	6.87	6.47

3.1.3. Advanced characterization: XPS, CO adsorption followed by IR and X-Ray absorption spectroscopy

3.1.3.1. X-ray photoelectron spectroscopy. A careful investigation of Ce and Pd 3d regions and Zn LMM Auger lines, reported in Fig. 3, gave a valuable information on the element's oxidation states and their chemical surroundings. Ce3d(5/2) region of $PdZn@CeZrO_x$ (Fig. 3a) presented an high surficial concentration of Ce^{3+}. Even if presence of Ce^{3+} in CeZrOx support was already observed by IR spectroscopy (Fig. 1), this technique probed both catalyst surface and bulk. On the contrary XPS signal is limited to the catalyst surface, unveiling that $CeZrO_x$ support possess a higher surface $Ce^{3+}(V_o)$ concentration than pure CeO_2. This is qualitative observable from the relative intensities difference between Ce^{3+} (v0 and v') and Ce^{4+} (v and v'') electronic transitions (Figs. 3a, S10) [67]. $CeZrO_x$ solid solutions are well known to present a considerable concentration of Ce^{+3} i.e., oxygen vacancies, due to the ionic radii difference between Zr and Ce atoms [68].

While Zr oxidation state (+4) was clearly identified from its 3d region (Fig. S11 b), metallic Zn and ionic ZnO cannot be distinguished from the Zn 2p spectra (Fig. S11 a) due to their low energy shift (≈ 0.3 eV) [69]. For this purpose, Zn LMM auger line reported in Figs. 3 **b** and S12 is more informative. Two components were observed at among 494 and 497 eV (Binding Energy) which can be associated to two chemical environments for Zn atoms. The associated Wagner parameters $\alpha' = E_K(LMM) + E_b(2p_{3/2})$, where E_K and E_b are kinetic and binding energies, respectively, are 2013 eV and 2010 eV, signatures of metallic and ionic Zn, respectively [70]. Presence of the alloy induces an inter atomic electron transfer and a Pd orbitals rehybridation, which shows as direct consequence a shift of Zn(2p) and Pd(3d) levels to lower and higher binding energies, respectively [71–77]. Moreover, Pd and Zn alloying induced electronic perturbation which is also clearly observed from CO adsorption discussed in the following section. The energy shift, respect to the usual metallic/oxidic position, observed for the Zn 2p bands (Fig. S11a) [69], is very clear in the Pd one 3d region. Pd 3d region (Fig. 3 **c**) seems to present a single intense doublet, i.e., Pd 3d 5/2 and 3/2. However, a careful consideration of the energy positions and a direct comparison with reference $PdZn@ZrO_2/CeO_2$ (Fig. S13 and Table S5) unveiled as a weak contribution from metallic Pd 3d(5/2) component can be identified at fixed BE of 334.8 eV while the intense band at 335.1 eV is associated to alloyed Pd, reported as $Pd^{\delta-}$ due to the charge transfer aforementioned. Noteworthy, a higher concentration of Ce^{+3}, Zn(0) and Pd^{PdZn} was observed in PdZn@CeZrOx respect to $PdZn@ZrO_2/CeO_2$ (Figs. S10, S12, S13), unveiling a higher concentration of oxygen vacancies and PdZn alloy.

3.1.3.2. CO adsorption followed by IR. Carbon monoxide is employed since decades as simple accessible probe molecule to investigate the chemical nature of surface sites. Once CO interacts with metal/ions sites on the catalyst surface, depending on the cation ionic potential, the predominant charge withdrawing direction can be divided into CO-to-metal or metal-to-CO, defining the interaction as σ-donation or π-backdonation, respectively [78,79]. The former depletes charge density from CO slightly antibonding level, increasing its bond strength and causing a hypsochromic shift from the ideal CO stretching vibration (2143 cm^{-1}), whilst the latter fills CO strongly antibonding levels, weakening the triple bond and inducing a bathochromic shift. Typically, for cationic sites σ-donation prevails, for metallic sites π-backdonation prevails, thus causing blueshift and redshift, respectively, of the stretching vibration of adsorbed CO. As a consequence, CO adsorption allows to determine whether: a) strong and weak Lewis acid sites (Ce^{4+} and Zr^{4+}), necessary for CO_2 adsorption as carbonates [80,81], are still present over the catalyst surface after grafting and reduction treatments (blueshifted bands) and b) if the metallic PdZn alloy was formed at the surficial scale (redshifted bands with peculiar features).

3.1.3.2.1. Room temperature CO adsorption. At RT CO is mainly

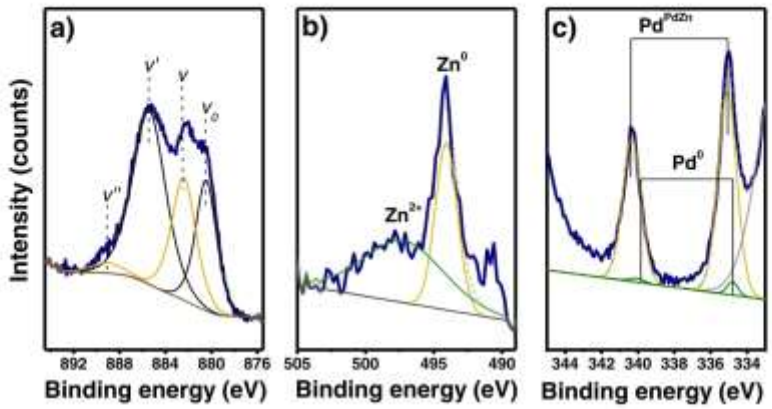

Fig. 3. High resolution XP spectra of PdZn/CeZrOx: a) Ce 3d(5/2), b) Zn 2p and c) Pd 3d regions. Experimental and best fit curves are represented by blue and dashed brown lines, respectively. Ce+3 (yellow line), Ce+4 (black line), metallic Zn/Pd alloy (yellow), ionic Zn (dark green) and Pd metal (green) components are reported.

adsorbed on strongly interacting sites i.e., $Pd^{0/2+}$. As calcination was conducted under O_2 atmosphere, from RT CO adsurption (Fig. 4a) we expected to observe presence of PdO. However, a sharp band pointed at 2090 cm^{-1} and a broader one at 1926 cm^{-1} were assigned to CO linearly and bridged coordinated, respectively, to Pd^0, where π-backdonation prevails [82]. As a matter of fact, it is well reported in literature that Pd^0 is frequently observed on oxidized samples when using CO as probe at RT as the latter can easily reduce Pd^{2+} [83]. Moreover, a weak band at 2048 cm^{-1} is observed at low CO coverages which assignment is not trivial. It could be related to CO interacting either with Pd^δ or with Pd^0 sites in preformed PdZn alloy. In the former case, the band could be located at such low wavenumber as related either to Pd defect sites, such as corners, edges and kinks, and/or to Pd^0 interacting with Ce^{3+}, which causes an electron transfer from Ce^{3-} to Pd^0, reinforcing the back-donation from Pd to CO, i.e. increasing the redshift [83]. As PdZn alloy is formed under strong reducing conditions [62,63,84], the presence of PdZn nanodomains under oxidizing conditions is hard to proof and to believe. On the contrary, due to the CeZrOx solid solution [85], Ce^{3+} is present on the catalyst surface (vide infra).

PdO reduction by CO was confirmed by measuring the evolution of CO interaction with calcined PdZn@CeZrOx with rising the temperature from liquid nitrogen temperature (nominal LNT) to RT, reported in

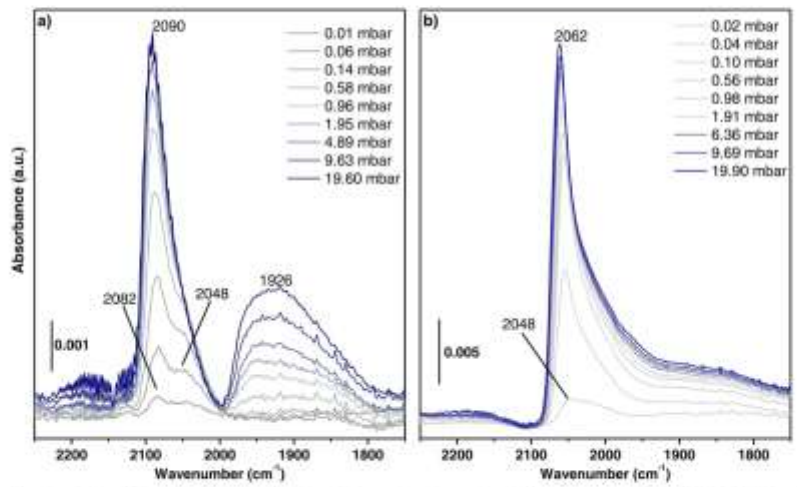

Fig. 4. Absorption/transmission FTIR spectra of CO adsorbed at Room Temperature at increasing partial pressures over: a) calcined PdZn@CeZrOx and b) reduced PdZn@CeZrOx. Increasing CO partial pressure (grey to blue lines) are reported in both panels.

Fig. S14. At nominal LNT, as also seen in the next session in Fig. 5a large band at 2155 cm^{-1} indicates a convoluted contributions of CO interacting with Zr^{4+}/Ce^{4+} and Pd^{2+} sites (Fig. S14a). While temperature rises, CO desorbs from Ce^{4+}/Zr^{4+} Lewis acid sites and selectively reduces PdO forming first Pd^{+} and Pd^{0} sites, unveiled by the presence of bands at 2131 and 2095 cm^{-1} related to CO linearly adsorbed over Pd^{+} and Pd^{0}, respectively [86]. Finally close to room temperature, only a band at 2095 cm^{-1} is observed, showing that all $Pd^{+/2+}$ sites have been reduced to Pd^{0}. Moreover, a large band occurs at lower wavenumbers with main contributions at 1970 and 1920 cm^{-1} assigned to bridged carbonyls on Pd(100) and Pd(111) faces, respectively [82]. PdO reduction is accompanied by CO-to-CO_2 oxidation as shown by presence of symmetric and asymmetric stretching modes of monodentate (1504 and 1345 cm^{-1}), bidentate (1575 and 1299 cm^{-1}) carbonates and bicarbonates (1619 and 1393 cm^{-1}, δ(OH) at 1219 cm^{-1}) in Fig. S14b [87].

CO adsorption at RT over reduced catalyst (Fig. 4**b**) showed a single asymmetric band at 2062 cm^{-1}, red-shifted ($\Delta\nu \simeq 30$ cm^{-1}) from the frequency of linear CO-Pd^{0} observed for the calcined sample (≈2090 cm^{-1}).[83] This phenomena, well reported in literature [72–77, 88], is a fingerprint of Pd in PdZn alloy since the Zn-to-Pd charge transfer, observed by XPS measurements, leads to a strengthening of the Pd(4d)-CO(2π) backdonation, shifting ν(CO-Pd) from 2090 to 2062 cm^{-1}.

Band asymmetry is due to a component at lower wavenumbers that can be reasonably assigned to carbonyls of Pd^{0} defect sites in the PdZn alloy nanoparticles and/or Pd^{0} in the alloy and interacting with Ce^{3+}. As a matter of fact, along with Ce^{3+} sites due to the $CeZrO_x$ solid solution (vide infra) and those formed by the reduction at 400 °C, small amount of additional Ce^{3+} sites are reasonably formed by CO interaction. This is demonstrated by the small amount of carbonates formed during interaction with CO. Even if their amount is much lower than that observed for the calcined sample (Fig. S18), their formation is not negligible. The small amount of carbonates on the reduced sample can be ascribed to CO oxidation by the lattice oxygen of $CeZrO_x$ catalysed by supported PdZn alloy [89,90]. This causes the formation of additional Ce^{3+} sites involved in an electron transfer to Pd^{0}. It is worth noting the presence of a broad band in the region 1950–1750 cm^{-1} related to bridged CO-$(Pd^{0})_2$ species. However, this species is not expected for Pd in the alloy, due to the lack of neighbouring Pd sites. The presence of this band indicates that nano-scaled Pd clusters, already observed by XPS (Fig. 3**c**), are present. Due to the lack of the corresponding band of linear carbonyls at 2090 cm^{-1}, it is reasonable that these Pd clusters occur on defect sites of the PdZn nanoparticles, such as the edges of the alloy, whose linear carbonyl absorption falls under the band at 2062 cm^{-1}. Noteworthy, CO is adsorbed selectively on Pd and not on Zn [91], therefore the blueshift of linear carbonyl band with respect to the calcined catalyst proved the alloy formation while the low amount of bridged carbonyls underlined the presence of low amount of Pd clusters and the prevalent Pd-Zn alternation on the catalyst surface.

In both spectra in Fig. 4, a blueshift of the main band was observed at increasing CO partial pressure: from 2082 to 2090 cm^{-1} for the calcined catalyst (panel a) and from 2048 to 2062 cm^{-1} for the reduced catalyst (panel b). This shift is explained considering the so called "chemical effect", i.e. when the surface coverage increases, CO σ-donation and π-backdonation contributions decrease, weakening the bond of CO with the site and shifting the CO vibration frequency at lower and higher frequencies, respectively, according to the dominating contribution [76, 92]. In the case of Pd, the dominating contribution is the π-backdonation and a blueshift is observed.

3.1.3.2.2. Liquid nitrogen temperature CO adsorption. Nominal LNT CO adsorption was carried out on calcined and reduced PdZn@CeZrOx, reported in Fig. 5**a** and **b**, respectively, showed presence of very different Lewis and metallic sites on the two samples. Calcined catalyst (Fig. 5**a**) presented a single sharp band at 2170 cm^{-1} which is redshifted to 2156 cm^{-1} by rising CO partial pressure. Band position, associated to CO interacting predominantly by σ-donation with Zr^{4+}/Ce^{4+} and Pd^{2+} defect sites [93,94], is in agreement with presence of PdO nanodomains over CeZrOx surface. As in these sites, the σ-donation is the prevalent contribution, at higher CO partial pressure, the redshift of the main band is explained considering the aforementioned "chemical effect" [78]. At low CO partial pressure is evident the presence of three extra bands (inset Fig. 5) at 2128, 2088 and 2048 cm^{-1}. While the former is associated to CO interacting with Ce^{3+}, the latter two are assigned to Pd^{0}

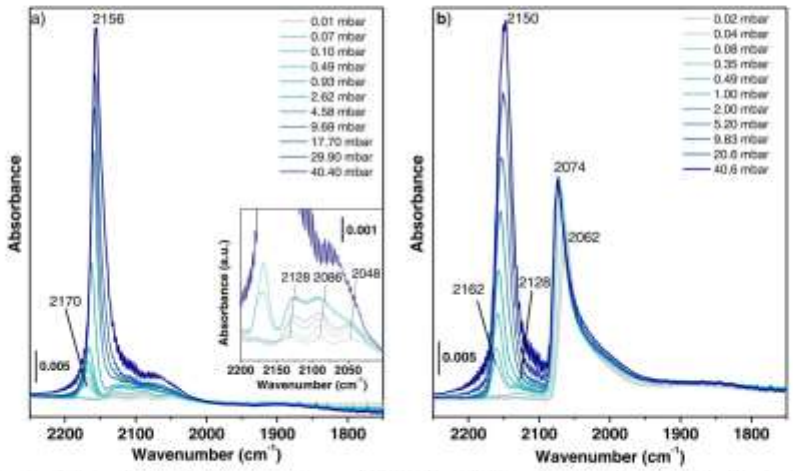

Fig. 5. FTIR spectra of CO adsorbed at Liquid Nitrogen Temperature over PdZn@CeZrOx: a) calcined and b) reduced. Main Panels: Increasing CO partial pressure (grey to blue line) are reported in both panels. Bottom inset in a) detail of Ce^{3+}/Pd^{0} region during stabilization at first pressure of 0.01 mbar.

more and less coordinated and not-or-in interaction with Ce^{3+}, respectively, as already observed in the RT spectra in Fig. 4b. Presence of Ce^{3+}, above confirmed by XPS spectroscopy, is justified as doping CeO_2 lattice with Zr^{4+} induces strain, compensated with the formation of oxygen vacancies associated to Ce^{3+} formation [85]. On the contrary, observing Pd^0 indicates that in this particular sample, i.e. PdO nanodomains originated from $[PdZn(\mu\text{-}OOCMe)_4]_2$ thermolysis, PdO is easily reduced during activation even under oxidising condition.

Two intense bands are observed from CO adsorption over reduced catalyst (Fig. 5**b**). The one located at higher wavenumbers is again associated to Ce^{4+}/Zr^{4+} sites whilst the second one, pointed at 2074 cm^{-1}, as discussed in the previous section, is associated to Pd^0 located in the intermetallic PdZn. As observed in the measurement at RT, the band asymmetricity is associated to Pd^0 defect sites in the PdZn alloy and/or Pd^0 in the alloy and interacting with Ce^{3+} (2062–1950 cm^{-1}); the weak band in the region 1950–1800 cm^{-1} is related to bridged carbonyls formed on metallic Pd nanodomains. As σ-donation contribution prevails in CO-Ce^{4+}/Zr^{4+}, "chemical effect" causes a band redshift from 2162 to 2150 cm^{-1} when increasing CO partial pressure, while π-backdonation dominates for CO-Pd^0/PdZn interaction, leading to a blueshift of the band from 2062 to 2074 cm^{-1}. Presence of bulk Ce^{3+} was already observed from the electronic transition at 2127 cm^{-1} in Fig. 3, while the band at 2128 cm^{-1} in Fig. 4**b** unveiled the presence of Ce^{3+} also on the surface.

3.1.3.3. X-Ray absorption spectroscopy. The PdZn/CeZrOx sample reduced under hydrogen was studied by X-ray absorption spectroscopy at the Zn-K edge in order to shed light on the structure of the supported species of zinc.

3.1.3.3.1. XANES analysis. From the XANES spectrum (Fig. 6), it can be observed that the sample PdZn/$CeZrO_x$ reduced present two inflexion points at 9658.0 and 9662.2 eV, energy values close to those observed respectively for Zn metal (Zn(0)), positioned at 9658.6 eV, and for ZnO (Zn(II)), at 9661.6 eV, thus suggesting strongly that zinc exists in two different phases with two different oxidation states in this sample. This agrees with a bimodal distribution of zinc, between a PdZn alloy and possibly single-sites grafted on the $CeZrO_x$ support or ZnO particles.

3.1.3.3.2. EXAFS analysis. The fit of the EXAFS signal of PdZn/CeZrOx reduced sample was carried out from the filter of the FT of the real extracted signal (k^3.Chi(k)) between 0.5 and 3.4 Å. The corresponding curves are shown in Fig. S15 and Fig. 7 and the parameters obtained from the fit are given in Table 2.

The first peak in the FT (below 2 Å in Fig. 7) could be fitted by light back-scatterers, ca. one oxygen atom at 1.96(2) Å which is in good agreement with values observed for ZnO wurtzite-type crystals (3 × 1.9738–1 × 1.9884 Å) [95], or for Zn-O distances observed from crystallographic data of molecular complexes which can be taken as model for isolated sites, in particular alkoxy types [96–101], in the 1.89–1.99 Å range. The highest peak in the FT (Fig. 7) could be fitted by palladium metal back-scatterers, ca. 5.3 Pd atoms at a distance of 2.598 (8) Å, which is slightly higher than the sum of the metallic radii of both Zn and Pd atoms (ca. 2.53 Å). In large crystals of $Pd_{1-x}Zn$ alloys, usually longer Zn-Pd distances are observed by XRD: 2.638 Å for the tetragonal PdZn β_1 phase [66], but an average Zn-Pd distance as short as 2.538 Å could be observed for a Pd_2Zn phase [102]. Besides, by EXAFS, short Pd-Zn distances of 2.56 Å [56] and 2.61 Å [65] were found for PdZn alloys prepared from $Pd(NO_3)_2$/ZnO or $(Pd(NO_3)_2 + Zn(NO_3)_2)/Al_2O_3$ materials after reduction by H_2. The fit was improved by adding two further layers of zinc, one corresponding to a PdZn alloy with 2.99(3) Å for Zn-Zn and the other corresponding to a ZnO phase at 3.22(3) Å, with a model considering PdZn and ZnO particles. It should be noted that these two scattering paths are in complete antiphase (lower part in Fig. 7**B**). Though the second distance is perfectly in line with a ZnO phase [82], the first distance is higher than the one found for a Pd-Zn β_1 phase (2.88–2.92 Å) but distances as long as 3.055 Å can be found for other Pd-Zn alloys as $Pd_{2.93}Zn_{0.97}$ [64]. This could indicate that the 1:1 stoichiometry is probably not uniform, as in PdZn β1 phase (P4/mmm space group; $Pd_{1-x}Zn_x$ with x = 0.36–0.51) [64]. Similar parameters were obtained when fitting k^3.Chi(k) extracted signal (Fig. S16 and Table S6). Since at least two different phases are present in the sample, the interpretation of the EXAFS is delicate. However, the results seem to agree with the presence of ca. 25% of Zn in a ZnO phase, with each zinc atom σ-bonded by four oxygen atoms at 1.96(2) Å and twelve zinc atom at 3.22(3) Å, and ca. 75% of the zinc present in bimetallic particles of a Pd_xZn alloy. This would thus confirm the observations made from the XANES spectrum of the sample with two oxidation states for Zn.

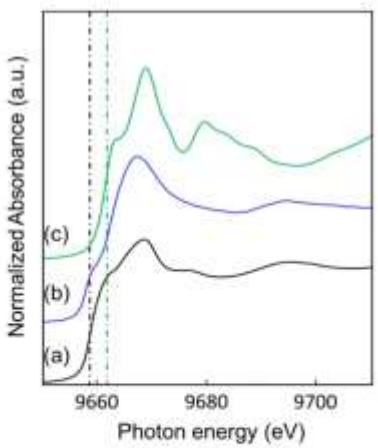

Fig. 6. Zinc K-edge XANES for (a) zinc metal foil (Zn(0)); (b) reduced PdZn/$CeZrO_x$; (c) ZnO (Zn(II)).

3.2. Catalytic tests

The catalytic bed comprises a mechanical mixture of different catalysts and SAPO-34 in a 1:1 ratio (in weight). The results of the tests are resumed in Table 3.

The reaction conditions of 380 °C, 30 bar and 2000 GHSV was adapted based on literature reports [103]. Hybrid catalysts exhibited fairly high conversion (Fig. 8**a**) and is about 24% in all PdZn supported systems (Table 3). A notable amount of CO is formed, originated from the RWGS reaction, which is endothermic and thus favored at higher temperatures. Thus, the different supports have apparently no effect on the conversion under the given conditions.

All the hydrocarbons found in the products are saturated. This is probably due to the hydrogenating activity of Pd, able to hydrogenate the olefins that are produced nearby in the zeolite framework. Importantly, the relative selectivity in C2+ among the hydrocarbons is over 99%. The systems are very stable in the reaction conditions and no substantial deactivation over 15 h of testing is observed (Fig. 8).

The PdZn@CeZrOx + SAPO34 system is identified to be the most promising catalyst among the series exhibiting more than 50% global selectivity in hydrocarbons. Moreover, this system also showed the lowest amount of CO, as reported in Table 3: the selectivity in CO reaches ca. 76% for PdZn/CeO_2, 68% for PdZn/ZrO_2 (see also Fig. S17) and only ca. 48% for PdZn/CeZrOx. Extensive studies were performed in order to further understand the role of each elements in the most promising system. First of all, the bare support is inactive under the given conditions. Furthermore, Pd/CeZrOx (5 wt%) and ZnOx/CeZrOx

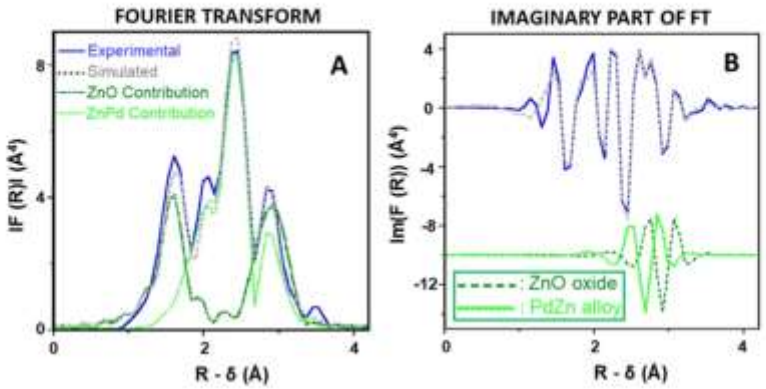

Fig. 7. (A): Modulus of the Fourier transform of the k^3-weighted Zn K-edge EXAFS of reduced PdZn/CeZrOx, with the contributions of ZnO (dark green) and ZnPd alloy (light green) phases; (B): imaginary part of the Fourier transform with the Zn–Zn contributions of the ZnO and ZnPd alloy phases. Solid lines: From experimental data; dashed lines: curve fit obtained with spherical wave theory.

Table 2
k^3.Chi(k) EXAFS curve fit parameters for PdZn@CeZrOx after reduction.[a]

Neighboring atom of Zn	Number of atoms N	Distance from Zn R(Å)	Debye-Waller factor σ^2(Å^2)
Zn-O[b]	1.0(2)	1.96(2)	0.0014(8)
Zn-Pd[c]	3.3(4)	2.598(8)	0.0103(10)
Zn–Zn[c]	2.7[d]	2.99(3)	0.0090(19)
Zn–Zn[b]	3.0[d]	3.22(3)	0.0094(20)

[a] The errors on the last digit, generated by the EXAFS fitting program "RoundMidnight" are indicated in parentheses; Δk: [1.9–14.7 Å^{-1}] – ΔR: [0.6–3.3 Å]; S_0^2 = 0.92; Fit residue: r = 5.2%; Quality factor: $(\Delta\chi)^2/\nu$ = 3.25, with ν = 12/24.
[b] From a ZnO phase, ΔE_{01} = 2.6 ± 1.9 eV (fitted).
[c] From a PdZn alloy phase, ΔE_{02} = 2.2 ± 1.2 eV (fitted).
[d] Shell constrained to a parameter above.

(3 wt%) were prepared and submitted for catalytic investigation under the same conditions. ZnOx/CeZrOx leads to CO as main product, while Pd/CeZrOx gives selectively methane. These results suggest that the PdZn alloy is successfully formed for PdZn/CeZrOx by using the current synthesis approach. Nevertheless, the substantial amount of CO produced may indicate that a fraction of Zn migrated to the support during the catalyst preparation, as indicated by XPS, TEM/EDX and EXAFS. The tandem effect was also investigated by excluding the SAPO-34 from the bed. Under the same conditions, PdZn/CeZrOx gave unexpectedly high selectivity to CO (95%) and only 4% methanol. The extremely high selectivity to CO compared to the hybrid catalyst prompted us to elucidate the GHSV. Increasing the space velocity led to increase in the CO selectivity and evidently lower the hydrocarbon selectivity (Fig. 9). Importantly, lower space velocity partly suppressed the CO production and increased the selectivity in the desired products. GHSV = 1000 presented the same conversion, but with a far lower selectivity in CO (28.3%) and high selectivity towards hydrocarbons (C2+ = 71.5%). The reason is probably associated to the formation of water by the MTO reaction catalyzed by the zeolite that will trigger the water-gas shift reaction, resulting in the consumption of CO. The latter can be justified by comparing the conversion of the PdZn/CeZrOx with and without SAPO-34. Higher CO_2 conversion was observed in the absence of SAPO-34, suggesting that the water-gas shift reaction occur in the presence of SAPO-34. Matching conclusions were drawn from the testing of a similar system [47], which was produced in fairly different conditions (synthetic method, metallic ratios and loading), but presented analogous catalytic features. The PdZn/ZrO_2 + SAPO-34 reported in the article produced mainly saturated hydrocarbons and the effect on the WGS equilibrium was observed. The authors performed additional studies and attributed the presence of saturated hydrocarbons to the strong hydrogenating nature of PdZn alloy, while the kinetic studies led to the same conclusions on the WGS equilibrium that are reported in this paper.

4. Conclusions

PdZn/CeZrOx was carefully prepared and characterized through the

Table 3
Summary of Conversion and product selectivity of the catalytic tests on the different systems mixed with SAPO-34. Reaction conditions: 380 °C 30 bar and 2000 ml/g/h. *: Space velocity is 1000 ml/g/h **: Space velocity is 6000 ml/g/h.

Catalysts	Conv. (%)	Global selectivity (%)					
		CO	CH_4	C2	C3	CH_3OH	C4
PdZn@CeO_2 SAPO-34	23.9	75.7	0	7.8	12.5	0.2	3.9
PdZn@ZrO_2 SAPO-34	23.8	68.5	0.2	9.4	15.3	0.2	6.3
PdZn@CeZrOx + SAPO-34	23.9	48.4	0.2	15.1	27	0.3	8.9
PdZn@CeZrOx	30.3	95.8	0	0	0	4.2	0
PdZn@CeZrOx + SAPO-34*	24.2	28.3	0.2	27.6	36.8	0	7.1
PdZn@CeZrOx + SAPO-34**	23.9	61	0	12.4	18.5	0.4	7.7
ZnOx@CeZrOx SAPO-34	40.5	89.6	0	4.4	5.1	0	0.9
Pd@CeZrOx SAPO-34	70	0.1	99.8	0	0	0.1	0

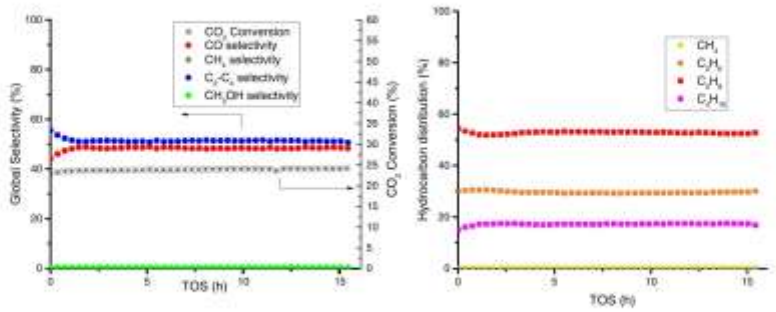

Fig. 8. Conversion and product selectivity (a) and hydrocarbon distribution (b) vs. time on stream (TOS) during the catalytic tests on PdZn@CeZrO$_x$ + SAPO-34. Reaction conditions: 380 °C, 30 bar and 2000 ml/g/h. A more detailed version of Fig. 9a is present in the Supplementary information (Fig. S17).

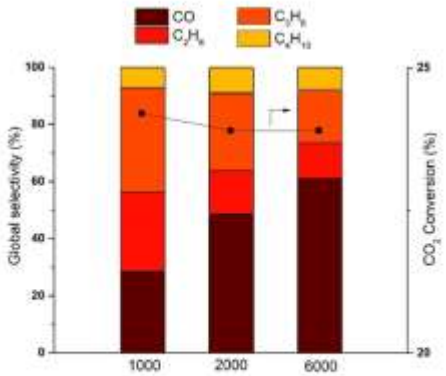

Fig. 9. Conversion and products selectivities at different space velocities (ml/g/h) for the PdZn@CeZrOx + SAPO-34. Reaction conditions: 380 °C, 30 bar (only traces of CH_3OH and CH_4 are formed, S < 0.4%).

loading of a heterobimetallic precursor, $[PdZn(\mu\text{-}OOCMe)_4]_2$, partly by grafting on the mixed oxide OH groups and by a simple deposition of the excess of complex on the support. It was followed by a calcination and a reduction of this material. This unique preparation method provides an ideal starting point to form the necessary PdZn alloy, reported to be the desired phase for the selective hydrogenation of CO_2 to methanol, intermediate for the production of light hydrocarbons in the presence of SAPO-34. The reduced catalyst PdZn/CeZrOx was extensively characterized by various techniques. The supported PdZn phase was revealed by XRD. Supplementary XPS and EXAFS experiments indicated that there are two phases of Zn, assigned to a PdZn alloy phase as the major component accompanied by minor amount of oxidized Zn, most probably ZnO. TEM-EDX analysis over several points showed that the Zn/Pd ratio was in average slightly below 1 with a fairly large standard deviation. The latter supports XPS and EXAFS data, suggesting that a minor, but notable amount of Zn escaped from the heterobimetallic precursor during the calcination and reduction, resulting in ZnO phase and PdZn alloy, with probably a core with monometallic Pd. Nevertheless, the bulk composition of Pd and Zn had the preferred ratio 1:1, as determined by elemental analysis. The presence of PdZn alloy is supported by in-situ FTIR at low temperature using CO as probe molecule. When combining PdZn/CeZrOx with SAPO-34, a tandem catalytic system for CO_2 conversion to hydrocarbons can be obtained. The latter system can readily transform CO_2 and H_2 to hydrocarbon with a conversion of 24% and high selectivity in light hydrocarbons (C2-C3: 82%). Virtually no deactivation of the catalyst was observed after 16 h on stream. Controlled experiments were performed with Pd/CeZrOx and Zn/CeZrOx in order to gain supplementary insights of this system. Importantly, Pd/CeZrOx gave only methane and Zn/CeZrOx gave mainly CO under the same conditions. The latter clearly shows that the PdZn phase has an important impact for the production of hydrocarbons.

CRediT authorship contribution statement

Paolo Ruzzi: Methodology, Validation, Investigation, Writing – original draft, Writing – review & editing. **Davide Salusso**: Formal analysis, Writing – original draft, Writing – review & editing. **Matilde Baravaglio**: Investigation, Validation. **Kai C. Szeto**: Methodology, Writing – original draft, Writing – review & editing. **Aimery De Mallmann**: Investigation, Writing – original draft. **Laia Gil Jiménez**: Investigation, Validation. **Cyril Goddard**: Supervision, Validation. **Anass Benayad**: Investigation, Writing – original draft. **Sara Morandi**: Supervision, Validation. **Silvia Bordiga**: Supervision, Conceptualization, Writing – original draft, Writing – review & editing. **Mostafa Taoufik**: Supervision, Conceptualization, Project administration, Writing – original draft, Writing – review & editing.

Declaration of Competing Interest

The authors declare that they have no known competing financial interests or personal relationships that could have appeared to influence the work reported in this paper.

Acknowledgments

This project COZMOS has received funding from the European Union's Horizon 2020 Research and Innovation Program under Grant agreement no. 837733. In particular PR and DS are grateful for their PhD grant. MB is grateful to EU for an Erasmus Grant and to CNRS for a complementary financial support during her Master internship at C2P2 Laboratory. LGJ (University of Tarragona, Spain) thanks BIZEOLCAT project (European Union's Horizon 2020 Research and Innovation Program, Grant agreement no. 814671) for a PhD grant. AdM (CNRS) thanks Olivier Mathon and Kirill Lomachenko for their help during the recording of the X-ray absorption spectra at ESRF, BM23.

Appendix A. Supporting information

Supplementary data associated with this article can be found in the online version at doi:10.1016/j.apcata.2022.118568.

References

[1] T.B. Brunson, B.E. Tuleya, J. Clim. 17 (2004) 3477–3495.
[2] J. Hansen, M. Sato, R. Ruedy, K. Lo, D.W. Lea, M. Medina-Elizade, Proc. Natl. Acad. Sci. USA 103 (2006) 14288–14293.
[3] J. Yang, W. Cai, M. Ma, L. Li, C. Liu, S. Ma, L. Li, S. Chen, Sci. Total Environ. 711 (2020), 134569.
[4] R. Ahmed, G. Liu, B. Yousaf, Q. Abbas, H. Ullah, M.U. Ali, J. Clean. Prod. 242 (2020), 118409.
[5] L. Amaducci, J. Subo-Guy, S. Ligi, M.D. Bacchetti, J. Membr. Sci. 522 (2017) 216–225.
[6] N. Mac Dowell, P.S. Fennell, N. Shah, G.C. Maitland, Nat. Clim. Change 7 (2017) 243–249.
[7] Z. Wang, H. Song, H. Liu, J. Ye, Angew. Chem. Int. Ed. 59 (2020) 8016–8035.
[8] R.M. Cuéllar-Franca, A. Azapagic, J. CO2 Util. 9 (2015) 82–102.
[9] E. Baig, T. Xiao, Y.L. Kuimova, P.P. Edwards, Philos. Trans. R. Soc. Math. Phys. Eng. Sci. 368 (2010) 3343–3364.
[10] Y.A. Daza, J.N. Kuhn, RSC Adv. 6 (2016) 49675–49691.
[11] N. Ali, M. Bilal, M.A. Nasir, A. Khan, F. Ali, H.M.N. Iqbal, Sci. Total Environ. 712 (2020), 136482.
[12] A. Galadima, O. Muraza, Renew. Sustain. Energy Rev. 115 (2019), 109335.
[13] M.D. Garba, M. Usman, S. Khan, F. Shehzad, A. Galadima, M.F. Ehsan, A. S. Ghanem, M. Humayun, J. Environ. Chem. Eng. 9 (2021), 104756.
[14] A.A. Olajire, J. CO2 Util. 3–4 (2013) 74–92.
[15] B. Grignard, S. Gennen, C. Jérôme, A.W. Kleij, C. Detrembleur, Chem. Soc. Rev. 48 (2019) 4466–4514.
[16] J. Huang, R. Buonsanti, Chem. Mater. 31 (2019) 13–25.
[17] L. Xu, Y. Shi, F. Liu, Y. Liang, S. Wang, Molecules 25 (2020) 3653.
[18] S. Das, J. Perez-Ramirez, J. Gong, N. Dewangan, K. Hidajat, B.C. Gates, S. Kawi, Chem. Soc. Rev. 49 (2020) 2937–3004.
[19] H. Yang, C. Zhang, P. Gao, H. Wang, X. Li, L. Zhong, W. Wei, Y. Sun, Catal. Sci. Technol. 7 (2017) 4580–4598.
[20] G.A. Floudas, P. Christodoulides, Environ. Int. 33 (2008) 395–401.
[21] A. Ramírez, L. Gevers, A. Bavykina, S. Ould-Chikh, J. Gascon, ACS Catal. 8 (2018) 9174–9182.
[22] S.C. Jadhav, P.D. Vaidya, B.M. Bhanage, J.B. Joshi, Chem. Eng. Res. Des. 92 (2014) 2557–2567.
[23] I. Yaroslava, A.D. Chowdhury, F. Meirer, B.M. Weckhuysen, J. Gascon, Nat. Catal. 1 (2018) 398–411.
[24] I. Yaroslava, E. De Wispelaere, S. Bailleul, J. Goetze, M. Radersma, E. Abou-Hamad, I. Vollmer, M. Goesten, B. Mezari, E.J.M. Hensen, J.S. Martinez-Espin, M. Morant-S. Mitchell, J. Perez-Ramirez, U. Olsbye, B.M. Weckhuysen, V. Van Speybroeck, F. Kapteijn, J. Gascon, Nat. Chem. 10 (2018) 804–812.
[25] R. Zhao, P. Zhai, P. Wang, J. Li, T. Li, M. Peng, M. Zhao, G. Hu, Y. Yang, Y.-W. Li, Q. Zhang, W. Fan, D. Ma, Chem 3 (2017) 323–333.
[26] M.D. Porosoff, B. Yan, J.G. Chen, Energy Environ. Sci. 9 (2016) 62–73.
[27] W. Li, H. Wang, X. Jiang, J. Zhu, Z. Liu, X. Guo, C. Song, RSC Adv. 8 (2018) 7651–7669.
[28] T.A. Atabi, T. Yoon, P. Seungho, C.-J. Lee, J. CO2 Util. 44 (2021), 101413.
[29] P. Sharma, J. Sebastian, S. Ghosh, D. Creaser, L. Olsson, Catal. Sci. Technol. 11 (2021) 1665–1697.
[30] P. Gao, S. Dang, S. Li, X. Bu, Z. Liu, M. Qiu, C. Yang, H. Wang, L. Zhong, Y. Han, Q. Liu, W. Wei, Y. Sun, ACS Catal. 8 (2018) 571–578.
[31] Z. Li, J. Wang, Y. Qu, H. Liu, C. Tang, S. Miao, Z. Feng, H. An, C. Li, ACS Catal. 7 (2017) 8544–8548.
[32] J. Wang, G. Li, Z. Li, C. Tang, Z. Feng, H. An, H. Liu, T. Liu, C. Li, Sci. Adv. 3 (2017), e1701290.
[33] R. Kudelski, M.V. Nielsen, R.L. Kerkli, Top. Catal. 45 (2007) 57–60.
[34] X.-M. Liu, G.Q. Lu, Z.-F. Yan, Appl. Catal. Gen. 279 (2005) 241–245.
[35] J. Hrozyński, R. Grabowski, A. Kozłowska, P. Olszewski, J. Stoch. J. Skrzypek, M. Lachowska, Appl. Catal. Gen. 278 (2004) 11–23.
[36] J. Hrozyński, R. Grabowski, P. Olszewski, A. Kozłowska, J. Stoch, M. Lachowska, J. Skrzypek, Appl. Catal. Gen. 310 (2006) 127–137.
[37] T. Phongamwong, U. Chantaprasertporn, T. Witoon, T. Numpilai, Y. Poo-arporn, W. Limphirat, W. Donphai, P. Dittanet, M. Chareonpanich, J. Limtrakul, Chem. Eng. J. 316 (2017) 692–703.
[38] F. Gao, X.-F. Wu, J. Zheng, M.-J. Li, Z. Zeng, X. Hong, A. Kroner, Y. Yuan, X.-Q. Gong, S.C. Edman Tsang, Catal. Sci. Technol. 6 (2016) 7698–7702.
[39] H. Bahruji, M. Bowker, W. Jones, J. Hayward, J. Ruiz Esquius, D.J. Morgan, G. J. Hutchings, Faraday Discuss. 197 (2017) 309–324.
[40] H. Bahruji, M. Bowker, G. Hutchings, N. Dimitratos, P. Wells, E. Gibson, W. Jones, C. Brookes, D. Morgan, G. Lalev, J. Catal. 343 (2016) 133–146.
[41] J. Xu, X. Su, X. Liu, X. Pan, G. Pei, Y. Huang, X. Wang, T. Zhang, H. Geng, Appl. Catal. Gen. 514 (2016) 51–58.
[42] F. Liao, K.-P. Wu, J. Zheng, M. Meng-Jung Li, A. Kroner, Z. Zeng, X. Hong, Y. Yuan, X.-Q. Gong, S.C. Edman Tsang, Green Chem. 19 (2017) 270–280.
[43] A.S. Malik, S.F. Zaman, A.A. Al-Zahrani, M.A. Daous, H. Driss, L.A. Petrov, Appl. Catal. Gen. 560 (2018) 42–53.
[44] O.A. Ojelade, S.F. Zaman, Catal. Surv. Asia 24 (2020) 11–37.
[45] O.A. Ojelade, S.F. Zaman, M.A. Daous, A.A. Al-Zahrani, A.S. Malik, H. Driss, G. Shimi, J. Gascon, Appl. Catal. Gen. 584 (2019), 117185.
[46] C. Abeba-Sass, S. Berkovicha, A. Lazaratid, A. Bagaev, A. Adamo-Ioli, M. Tsoufis, S. Doeffga, U. Olsbye, Catal. Sci. Technol. 10 (2020) 4373–4385.
[47] A. Ramírez, P. Ticali, D. Salomo, T. Gevers-Lanzar, S. Ould-Chikh, C. Abeba-Sass, A.L. Bagaev, E. Berkovicha, S. Morandi, M. Signoretto, S. Bordiga, J. Gascon, U. Olsbye, JACS Au 1 (2021) 1719–1732.
[48] I.S. Mashkovsky, Mendeleev Commun. 24 (2014) 355–357.
[49] N.F. Kozlitina, S.E. Nefedov, P.M. Dolgushin, N.V. Cherkashina, M.N. Yargaeva, I.I. Moiseev, Inorg. Chim. Acta 359 (2006) 2072–2086.
[50] J.S. Bradley, A.F. Butt, Rev. Mod. Phys. 39 (1967) 129–142.
[51] B. Ravel, M. Newville, J. Synchrotron Radiat. 12 (2005) 537–541.
[52] M. Alain, M. Jacques, M.-B. Illian, F. Karine, J. Phys. Conf. Ser. 190 (2009), 012034.
[53] A.L. Ankudinov, B. Ravel, J.J. Rehr, S.D. Conradson, Phys. Rev. B 58 (1998) 7565–7576.
[54] **D.E. Sayers. The IXS Standards and Criteria Committee.**
[55] A. Laachir, V. Perrichon, A. Badri, J. Lamotte, E. Catherine, J. Claude Lavalley, J. E. Fallah, L. Hilaire, F.L. Normand, E. Quéméré, G. Noël Sauvion, O. Touret, J. Chem. Soc. Faraday Trans. 87 (1991) 1601–1609.
[56] C. Binet, M. Daturi, J.-C. Lavalley, Catal. Today 50 (1999) 207–225.
[57] C. Arrigo, M. Ferri, M.M. Carnasciali, M.T. Buscaglia, J.R. Plaisier, G.A. Costa, Inorg. Chem. 54 (2015) 4126–4137.
[58] T. Wakita, M. Yoshima, Acta Crystallogr. B 63 (2007) 384–391.
[59] P. Li, I.W. Chen, J.E. Penner-Hahn, Phys. Rev. B 48 (1993) 10063–10073.
[60] Y. Kuzuba, H. Takeda, H. Asoshi, Phys. Chem. Miner. 13 (1986) 233–237.
[61] J.G.P. Evans, P.A. Stevens, R. Binner, Trans. J. Br. Ceram. Soc. 80 (1971) 39–43.
[62] M.W. Tew, H. Emerich, J.A. van Bokhoven, J. Phys. Chem. C 115 (2011) 8457–8465.
[63] J.B. Gallagher, D.J. Chleboun, H. Zhao, B.E. Winger, R.J. Meyer, J.T. Miller, Phys. Chem. Chem. Phys. 17 (2015) 28144–28153.
[64] H. Sowerny, E. Bauer, A. Steripff, Verwandte Tell. Anal. Wiss. 82 (1961) 1086–1093.
[65] **ICSD web database FIZ Karlsruhe.**
[66] K.J. Petersen, B. Halevi, R. Kiefer, M.N. Spilde, A.R. Dreye, J. Petersen, L. Daemen, A. Llobet, H. Nakotte, J. Alloy. Compd. 509 (2011) 1453–1455.
[67] E. Paparazzo, J. Phys. Condens. Matter 30 (2018), 343003.
[68] B. Liu, C. Li, G. Zhang, X. Yao, S.S.-Chuang, Z. Li, ACS Catal. 8 (2018) 10446–10456.
[69] M.C. Biesinger, L.W.M. Lau, A.R. Gerson, R.S.C. Smart, Appl. Surf. Sci. 257 (2010) 887–898.
[70] E. Lee, A. Benaouf, T. Shin, H. Lee, D.-E. Ko, T.S. Kim, K.S. Seo, M. Byu, S. Jeon, G.-S. Park, Sci. Rep. 4 (2014) 4948.
[71] J.A. Rodrigues, J. Phys. Chem. 98 (1994) 5758–5764.
[72] C. Weilach, S.M. Kozlov, H.H. Holzapfel, R. Zimmgor, K.M. Neyman, G. Rupprechter, J. Phys. Chem. C 116 (2012) 18768–18778.
[73] C. Rameshan, W. Stadlmayr, C. Weilach, S. Penner, H. Lorenz, M. Hävecker, R. Blume, T. Rocha, D. Teschner, A. Knop-Gericke, R. Schlögl, N. Memmel, D. Zemlyanov, G. Rupprechter, B. Klötzer, Angew. Chem. Int. Ed. 49 (2010) 3224–3227.
[74] K.M. Neyman, R. Inntam, C. Inntam, S. Hengrasmee, N. Rösch, J. Phys. Chem. B 108 (2004) 5424–5430.
[75] H.P. Koch, I. Balin, B. Schernach, Surf. Sci. 604 (2010) 596–608.
[76] A. Boyer, K. Fleischner, R. Denecke, H.-P. Steinrück, K.M. Neyman, N. Rösch, Surf. Sci. 600 (2006) 78–94.
[77] K.M. Neyman, K. Hwa Lim, Z.-X. Chen, L.V. Moskaleva, A. Boyer, A. Reindl, D. Borgmann, R. Denecke, H.-P. Steinrück, N. Rösch, Phys. Chem. Chem. Phys. 9 (2007) 3470–3482.
[78] A. Zecchina, D. Scarano, S. Bordiga, G. Ricchiardi, G. Spoto, F. Geobaldo, Catal. Today 27 (1996) 403–435.
[79] K.I. Hadjiivanov, G.N. Vayssilov, Adv. Catal. 47 (2002) 307–511.
[80] **K. Pokrovski, K.T. Jung, A.T. Bell, 2001, pp. 4297–305.**
[81] **C. Li, Y. Sakata, T. Arai, K. Domen, K. Maruya, vol. 85, 1989, pp. 929–43.**
[82] E. Groppo, S. Bertarione, F. Rotunno, G. Agostini, D. Scarano, R. Pellegrini, G. Leofanti, A. Zecchina, C. Lamberti, J. Phys. Chem. C 111 (2007) 7021–7028.
[83] A. Bensalem, J.C. Muller, D. Tessier, F. Bozon-Verduraz, J. Chem. Soc. - Faraday Trans. 92 (1996) 3233–3237.
[84] M. Gaetzen, D.E. Doronkin, T.L. Sheppard, A. Zimina, H. Li, J. Jelic, F. Studt, J.-D. Grunwaldt, J. Sauer, S. Behrens, Angew. Chem. 131 (2019) 15822–15826.
[85] B. Liu, C. Li, G. Zhang, X. Yao, S.S.C. Chuang, Z. Li, ACS Catal. 8 (2018) 10446–10456.
[86] D. Tessier, A. Rakai, F. Bozon-Verduraz, J. Chem. Soc. Faraday Trans. 88 (1992) 741–749.
[87] M. Daturi, C. Binet, J.C. Lavalley, G. Blanchard, Surf. Interface Anal. 30 (2000) 273–277.
[88] K. Hettinger, Catalysts 11 (2021) 77–117.
[89] A.A. Pawar, D. Lee, W.-J. Chung, H. Kim, Chem. Eng. J. 395 (2020), 124970.
[90] G.S. Zafiris, R.J. Gorte, J. Catal. 139 (1993) 561–567.
[91] J.A. Rodriguez, Surf. Sci. Rep. 24 (1996) 223–287.
[92] P. Hollins, J. Pritchard, Surf. Sci. 89 (1979) 486–495.
[93] C. Binet, M. Daturi, J.C. Lavalley, Catal. Today 50 (1999) 207–225.
[94] C. Martens, G. Cerrato, S. Di Cicco, Appl. Surf. Sci. 126 (1998) 107–126.
[95] H.F. McMurdie, M.C. Morris, E.H. Evans, B. Paretzkin, W. Wong-Ng, L. Ettlinger, C.R. Hubbard, Powder Diffr. 1 (1986) 64–77.
[96] K. Su, T.D. Tilley, M.J. Sailor, J. Am. Chem. Soc. 118 (1996) 3459–3468.

[97] M.G. Gardiner, S.M. Lawrence, C.L. Raston, B.W. Skelton, A.H. White, Chem. Commun. 0 (1996) 2491–2492.
[98] E. Bukhtiyarv, I. Goldberg, A. Vigalok, Organometallics 23 (2004) 4540–4543.
[99] E. Bukhtiyarv, I. Goldberg, A. Vigalok, Organometallics 24 (2005) 5732–5736.
[100] S. Jana, H.J.F. Berger, R. Fröhlich, T. Pape, N.W. Mitzel, Inorg. Chem. 46 (2007) 4293–4297.
[101] R. Petrus, P. Sobota, Acta Crystallogr. C 68 (2012) m275–m280.
[102] H.H. Stadelmaier, W.K. Hardy, Int. J. Mater. Res. 52 (1961) 391–396.
[103] K. Ring Tse, G. Zhao, D. Sun, J. Huang, Q. Li, J. Mater. Chem. A 9 (2021) 5197–5231.

6.5 E : Barreau M. et al., Materials Today Chemistry 26 (2022) 101011

Materials Today Chemistry 26 (2022) 101011

Contents lists available at ScienceDirect

Materials Today Chemistry

journal homepage: www.journals.elsevier.com/materials-today-chemistry/

Synthesis of Ni-doped ceria nanoparticles and their unusual surface reduction in hydrogen

M. Barreau [a], D. Chen [a], J. Zhang [a], V. Papaefthimiou [a], C. Petit [a], D. Salusso [b], E. Borfecchia [b], S. Turczyniak-Surdacka [c, d], K. Sobczak [c], S. Mauri [e, f], L. Braglia [e], P. Torelli [e], S. Zafeiratos [a, *]

[a] Institut de Chimie et Procédés pour L'Energie, L'Environnement et La Santé, UMR 7515 CNRS-UdS, 25 Rue Becquerel, 67087 Strasbourg, France
[b] Department of Chemistry, INSTM Reference Center and NIS Centers, University of Torino, 10125 Torino, Italy
[c] Faculty of Chemistry, Biological and Chemical Research Centre, University of Warsaw, Żwirki, Wigury 101, 02-089 Warsaw, Poland
[d] Faculty of Chemistry, University of Warsaw, Pasteura 1, 02-093 Warsaw, Poland
[e] IOM CNR Laboratorio TASC, AREA Science Park, Basovizza, Trieste, 34149, Italy
[f] Department of Physics, University of Trieste, Via Valerio 2, Trieste, 34127, Italy

ARTICLE INFO

Article history:
Received 26 March 2022
Received in revised form
25 April 2022
Accepted 24 May 2022
Available online xxx

Keywords:
X-ray absorption spectroscopy
Operando analysis
In situ DRIFT
Square-planar symmetry
NEXAFS

ABSTRACT

This work presents an original approach to preparing pure and Ni-doped CeO_2 nanoparticles (NPs) that can be directly drop-casted on a substrate or calcined to form powders. The reduction of the NPs in H_2 is very different than the one usually anticipated for supported Ni–CeO_2 catalysts. *In situ* soft X-ray absorption and infrared spectroscopies revealed that the reduction of Ce^{4+} into Ce^{3+} in H_2 proceeds via simultaneous oxidation of Ni^{2+} ions into $Ni^{\delta+}$ ($2<\delta<3$). Comparison with reference samples indicates that Ce^{4+} ions reduction is promoted over Ni-doped CeO_2 NPs, whereas that of Ni^{2+} is hindered. Theoretical simulation of Ni L-edge spectra suggested that Ni dopant into ceria is in a square planar four-coordinate environment, in contrast to the familiar octahedral symmetry of bulk nickel oxides. Our results reveal that the surface chemistry of Ni-doped CeO_2 is quite distinct as compared to that of the individual bulk oxides, which potentially can lead to a different performance of this material, notably in catalytic applications.

1. Introduction

Ceria (CeO_2) is a material commonly employed in various catalytic processes, including three-way-catalysis [1,2], NO_x reduction [3], solid oxide cells [4], CO oxidation [5], water-gas-shift reaction [6], CO_2 valorization [7,8] and many more [9]. A key characteristic of CeO_2 is the ease to exchange between Ce^{4+} and Ce^{3+} oxidation states while keeping a rather stable cubic fluorite crystal structure [10]. This property facilitates the creation of oxygen vacancies [11], which can serve both as reservoir of mobile oxygen in bulk and as adsorption sites for reactants on the surface [12]. There are two main strategies to facilitate the reduction of ceria and consequently the creation of vacant sites. The first is to manipulate the size and the surface planes of pure CeO_2 [13,14], and the second is to introduce dopant atoms into the crystal structure [15,16]. For this latter, several elements have been studied, including rare-earth (La, Zr, Gd), platinum group (Ru, Pt), and transition metals (Fe, Ni, Cu, denoted as TM) [6,17,18]. The properties of doped-ceria depend on the size, the valence, and the concentration of the dopant atom. Therefore, the choice of the dopant controls the oxygen storage capacity [19] and the redox behavior of ceria [18].

The synthesis of metal-doped ceria particles is challenging, especially when TM are used as dopants. The use of conventional synthesis methods, such as coprecipitation, sol-gel, or hydrothermal, often leads to a mixture of doped particles and segregated metallic particles [1,20–22]. Among the recent strategies devoted to the synthesis of TM-doped particles [1], the use of organic soft templates has been proven to be effective in obtaining pure-phase particles with small size and size distributions. Briefly, this type of synthesis consists of the self-assembly of isolated cerium and TM in an organic matrix, followed by its removal upon heat treatment. This technique has several advantages: (i) it efficiently impedes the phase separation in single oxides leading to atomic dispersion of

* Corresponding author.
E-mail address: spiros.zafeiratos@unistra.fr (S. Zafeiratos).

https://doi.org/10.1016/j.mtchem.2022.101011
2468-5194/

the dopant and potentially to single-atom catalysts [23]; (ii) the size of the resulting material is controlled and uniform; (iii) the removal of the organic template can provide high nanoporosity to the finite structure resulting in high-surface-area materials. Particularly, the use of coordination polymers [24] or metal-organic frameworks [15,25,26] turned out to be an efficient strategy for conceiving highly uniform and porous nanostructures. Among the methods proposed, Elias and coworkers prepared monodispersed $M_{0.1}Ce_{0.9}O_{2-\delta}$ particles (with M = Mn, Fe, Co, Ni, Cu) via pyrolysis of metallic Schiff-base complexes in an oleylamine medium [15]. Although this synthesis method ensures the remarkable production of a wide range of TM-doped ceria catalysts, it suffers from its complexity and low production yields. Recently we reported on the preparation of Ni-doped CeO_2 NPs from Schiff base complexes [25] using an approach with fewer synthesis steps than preceding reports [15]; however, the production yield was still relatively low. Herein, we simplify the synthesis method to produce pure CeO_2 and Ni-doped CeO_2 with small and uniform particle sizes while increasing its yield by a factor of 10. Furthermore, *in situ* surface spectroscopy is employed to examine the reduction of the nanoparticles in 1 bar H_2. It is demonstrated that the reduction of Ni^{2+} in H_2 is hindered, and that of Ce^{4+} is promoted on doped NPs as compared to pure reference samples. Contrary to the generally accepted notion that Ni^{2+} reduction precedes that of Ce^{4+}, we found that Ni^{2+} not only resists reduction but is oxidized further, likely due to electronic interaction with Ce ions. This is a radically different reactivity path than that reported on CeO_2–supported Ni particles [27].

2. Experimental section

2.1. Synthesis of CeO_2 and $Ni_xCe_{1-x}O_2$ NPs

Ni-doped CeO_2 nanoparticles (hereafter named $Ni_xCe_{1-x}O_2$) were prepared from a method recently developed in our group involving the use of Schiff-base metal complexes to produce pure-phase TM-doped ceria nanoparticles [25]. In this four-step method, one step is devoted to the preparation of the Ce^{III}-L, while a two-step reaction is dedicated to the preparation of the heteremetallic Ce^{III}–Ni^{II}-L (where L = N,N′-bis(3-methoxysalicylidene)-propylene-1,3-diamine). Finally, the last step consists in mixing the metallic complexes in oleylamine media and followed by pyrolysis at 180 °C under an inert atmosphere [25]. In the present paper, this method has been simplified in several ways: (i) the number of steps has been lowered to three, using only monometallic complexes for the synthesis (Ce^{III}-L and Ni^{II}-L). In other terms, the bimetallic complex preparation has been discarded since we observed that it is not a prerequisite for the preparation of monodisperse Ni-doped CeO_2 nanoparticles; (ii) the synthesis yield was improved by a factor of 10 while lowering the solvent/reactant ratio, allowing to produce more catalyst (from 50 to 100 mg to around 1 g with the new method) without using excessive amounts of solvent; (iii) after pyrolysis of the metallic Schiff-base complexes under oleylamine medium, the NPs were extracted using methanol instead of ethanol, which has been found to be more efficient to precipitate the NPs.

2.1.1. Preparation of Ce(III)-L

In a solution of 200 ml of methanol were added 3 g of 2-hydroxy-3-methoxybenzaldehyde (20 mmol), 0.7 g of 1,3-diaminopropane (10 mmol), and 4.06 g of $Ce(NO_3)_3.6H_2O$ (10 mmol), giving a yellow precipitate immediately. The yellow suspension was stirred at reflux for 3h before cooling down to room temperature. The crude product was filtered through a frit, washed several times with cold EtOH, and dried under vacuum to give Ce^{III}-L as a yellow powder.

2.1.2. Preparation of Ni (II)-L

In a three-necked flask were mixed 8 g of 2-hydroxy-3-methoxybenzaldehyde (52.6 mmol), 2.1 g of 1,3-diaminopropane (30 mmol), and 6.66 g $Ni(OCOCH_3)_2.4H_2O$ (27 mmol) in a solution of 100 ml of methanol. The green solution was refluxed at 80 °C for 4 h before cooling down to room temperature. The green crystals obtained after reducing the volume of the solution to 20 ml were then filtered and washed several times with methanol.

2.1.3. Preparation of $Ni_xCe_{1-x}O_2$ nanoparticles

The $Ni_xCe_{1-x}O_2$ nanoparticles were prepared by mixing 5.1 of Ce^{III}-L and 1.5 g of Ni^{II}-L in 200 ml of oleylamine. The mixture was refluxed at 180 °C under argon for 4 h, and the remaining dark brown product was isolated by centrifugation. Around 450 ml of methanol were added to the solution leading to the precipitation of the nanoparticles. Consequently, the brown flocculent was isolated by centrifugation. After recuperation of the NPs by centrifugation (4400 rpm for 10 min), the NPs were calcined under air at 450 °C for 1 h, leading to approximately 1 g of powder. A similar protocol was used for the preparation of undoped CeO_2 particles by pyrolysis of only Ce^{III}-L in oleylamine.

2.2. Characterization techniques

2.2.1. Standard characterization

Ex situ X-ray diffraction (XRD) patterns of the calcined samples were recorded on a Bruker D8 advance diffractometer operating at 40 kV and 40 mA using Cu Kα radiation (λ = 1.5418 Å). XRD patterns were recorded from 20 to 80° at a scan rate of 0.032° s^{-1}. The resulting patterns were processed using DIFFRAC.EVA for the crystallite size calculation according to the line broadening of the most intense reflection (i.e. the (111) plan for the fluorite-type CeO_2 phase) using the Scherrer equation, while the FullProf software [28] was used for the Rietveld refinement and the determination of the lattice parameters. Raman spectra were measured using a micro-Raman spectrometer (Horiba LabRam Aramis). A 10 × objective was used to focus the excitation laser with an excitation wavelength of 532 nm, giving approximately a 2.6 μm wide spot with a laser power of less than 1 mW in order to avoid damaging the sample. Temperature-Programmed Reduction of the catalysts by hydrogen (H_2-TPR) was carried out in an AutoChem II apparatus (Micromeritics) incorporating a thermal conductivity detector (TCD). The profiles were obtained after loading 50 mg of sample in a U-shaped fixed bed reactor and heating at 950 °C under 20 ml/min of 10% H_2/Ar with a 10 °C min^{-1} heating rate. Elemental analysis of the Ni-doped CeO_2 material was carried out by Inductively Coupled Plasma Optical Emission Spectroscopy (ICP-OES, Varian 720 ES) after the dissolution of the powdered sample in acidic medium (HNO_3) followed by filtration of residual particles.

The TEM investigations were carried out using an FEI Talos F200X microscope operating at 200 kV. Observations were performed in scanning transmission electron microscopy (STEM) mode using high-angle annular dark-field (HAADF) imaging. Energy-dispersive X-ray spectroscopy (EDX) using a Super-X system with four silicon drift detectors (SDDs) was applied to the detection of differences in local chemical composition.

2.2.2. In situ infrared experiments

In situ Diffuse Reflectance Infrared Fourier Transform Spectroscopy (DRIFTS) was used to investigate the behavior of different functional groups characterizing the samples under air or H_2 while heating. The experiments were performed on a Bruker Vertex 70

FTIR spectrometer equipped with a Praying Mantis diffuse reflectance accessory and a tailor-made reaction cell with ZnSe windows. A cold trap was placed at the inlet of the reaction cell in order to remove water traces from the gas feed. Prior to the tests, the powder samples were grounded with a mortar and diluted with KBr in order to avoid signal saturation (10 wt% in KBr). A background (64 scans, 4 cm^{-1}) was acquired by placing pure KBr in the reaction cell. Then, around 120 mg of diluted sample were loaded into the cup and deposited in the center of the reaction cell for the analysis. The sample was first subjected to an oxidative treatment under 10 ml/min of synthetic air to 400 °C with a 10 °C min^{-1} heating rate for 30 min. After cooling down to 120 °C, a reducing treatment was subsequently realized under 10 ml/min of H_2 at 400 °C for 30 min. Spectra were recorded continuously during the treatments via the execution of a macro with an accumulation of 32 scans at a resolution of 4 cm^{-1}.

2.2.3. In situ sXAS experiments

The soft X-ray absorption spectroscopy (sXAS) experiments were performed at the APE-HE beamline of the Elettra synchrotron radiation facility (Trieste, Italy), exploiting a dedicated setup based on a reaction cell with Si_3N_4 membranes, as described in detail elsewhere [29]. The sXAS signal was detected in TEY mode by probing the drain current from the sample with a picoammeter. The catalyst powder was loaded in the *in situ* cell, installed in the APE-HE instrument, and interfaced with gas delivery and temperature control systems. Gas flows were monitored by calibrated mass flow controllers. All reported experiments were performed at a gas pressure of 1 bar. The sample was initially pretreated in 10% O_2/He mixture at 340 °C for about 30 min and then cooled to room temperature under He gas flow. Then the gas atmosphere was switched to 10% H_2/He mixture, and the temperature was raised at a rate of 2.5 °C/min up to 360 °C, while *in situ* sXAS Ni L- and Ce M-edges spectra were recorded at selected temperatures. Finally, the sample remained for about 30 min at the maximum annealing temperature before cooling down in H_2/He. Spectra analysis was performed using the CasaXPS vs. 2.3.23 software. The background subtraction was done using a spline-linear function.

The shape of the Ce $M_{5,4}$ edge is distinguishably different between the Ce^{3+} and Ce^{4+} oxidation states; therefore, the differences in the oxidation state can be easily detected based on the overall peak shape. In particular, the Ce M_5-edge spectra were fitted by a linear combination of standard reference curves of Ce^{4+} and Ce^{3+} species recorded at the same spectrometer over a 10%Ni–CeO_2 sample prepared by the impregnation method. The Ce M_5-edge corresponding to Ce^{4+} was recorded after O_2 treatment at 360 °C, while the Ce^{3+} one after a long-time reduction in H_2 at 350 °C. Fitting was performed after linear background subtraction, while the full width at the half maximum and the energy difference among the two reference peaks were fixed. The reference peaks were allowed to vary until the difference between their sum and the experimental spectra (residual standard deviation, STD) was minimized (typical STD between 0.005 and 0.010).

In the case of Ni $L_{3,2}$ edge, the modifications between the various nickel oxidation states are less evident in the peak shape, and therefore, it is important to define the position of the peak. In order to be able to exclude artifacts in the peak position between different samples and conditions, we used the position of the most prominent feature of the Ce M_5-edge as an internal reference for all the samples and conditions. The position of this peak was fixed at 884 eV, and the position of the Ni L-edge was calculated according to this value. All the sXAS spectra shown in this paper have been calibrated using this method. The position of the reference Ni (metallic) and NiO peaks was collected *in situ* over a reference sample composed of 10%Ni on CeO_2, after reducing and oxidizing treatments.

2.2.4. Charge-transfer multiplet calculations

The Ni $L_{3,2}$-edge was simulated using the charge-transfer multiplet (CTM) approach using the CTM4XAS 5.23 program [30]. We attempted to fit the experimental Ni $L_{3,2}$-edge spectra with both octahedral and tetrahedral symmetries; however, only the latter symmetry gave theoretical curves in resemblance with the experimental ones. The crystal field value (10Dq) and the charge transfer energy value (Δ) were the main parameters adjusted in the simulation to obtain the best accordance with the experimental spectra. Other simulation parameters were as follows: (i) for Ni^{2+} slater integrals (F_{dd}, F_{pd}, G_{pd}) = 1, spin-orbit spitting parameter SO = 0.99, optical parameters Dt = 0.1, Ds = 0.05eV, core hole potential U_{pd} and the 3d-3d repulsion energy U_{dd}=0, U_{pd}nbsp;= −1.8, and the hopping parameters $e_g$nbsp;= 2 eV and t_{2g} = 1 eV, Temperature 600K; (ii) for Ni^{3+}, (F_{dd}, F_{pd}, G_{pd}) = 1, SO = 0.97, Dt = 0.13, Ds = 0.05eV, U_{dd}=0, U_{pd}nbsp;= −0.1, $e_g$nbsp;= 1 eV and t_{2g} = 1.5 eV, Temperature 600K.

3. Results and discussion

3.1. Synthesis and ex situ characterization

Ni-doped CeO_2 NPs (hereafter abbreviated as $Ni_xCe_{1-x}O_2$ with x = 0.036, determined by ICP-OES) were prepared from Schiff-base metal complexes as detailed in the experimental part. Briefly, the method involves the preparation of the monometallic Ce^{III}-L and Ni^{II}-L complexes followed by their pyrolysis at 180 °C in an inert atmosphere under oleylamine media. After cooling down to room temperature, the resulting nanoparticles are obtained by extraction with methanol and finally dispersed in hexane solution or calcined at 450 °C to form a powder (Fig. 1). A similar protocol was used for the preparation of undoped CeO_2 particles (hereafter abbreviated as CeO_2). The production yield was around 1g of NPs, which is around 10 higher than that of previous reports (50–100 mg) [25].

The XRD patterns of calcined nanoparticles (Fig. S1a) are characteristic of the cubic fluorite phase (JCPDS 34–0394). The absence of any Ni-containing crystal phases discards the presence of segregated Ni particles and confirms the high dispersion of Ni at $Ni_xCe_{1-x}O_2$. The analysis of the XRD results, presented in Table 1, shows similar crystallite sizes of the two NPs types (ca. 6.7 nm). The lattice parameters of both samples are lower than the theoretical value of bulk ceria (5.411 Å), which can be attributed to reduced surface relaxation in small nanoparticles [22]. A slight increase (0.13 ± 0.01%) of the $Ni_xCe_{1-x}O_2$ lattice parameter as compared to CeO_2 (Table 1) can be indicative of the Ni occupation sites in the ceria lattice. In particular, Ni ions may substitute lattice Ce^{4+} (substitutional sites) or alternatively occupy interstitial lattice positions (interstitial sites), while they may easily exchange between the two sites, depending on the conditions (e.g. temperature) [31,32]. Although in both cases, nickel is stabilized as Ni^{2+} [31], the ceria lattice parameters are distinct. Substitution of Ce^{4+} with the smaller Ni^{2+} cations (83 p.m. for Ni^{2+} *vs.* 101 p.m. for Ce^{4+}) would lead to lattice contraction, while lattice expansion is expected for Ni impurities at interstitial ceria sites [32]. The increase of the lattice parameter in Table 1 not only confirms the successful doping of Ni atoms but is also compatible with Ni^{2+} at interstitial ceria sites [32].

According to the theoretical study of Chafi et al. [33], when a nickel atom is located at interstitial sites of the cubic fluorite ceria lattice, an increase of the ceria lattice parameter is expected. This is due to the large repulsion between Ce atoms around the Ni-dopant, causing expansion of the CeO_2 lattice. As Ni concentration

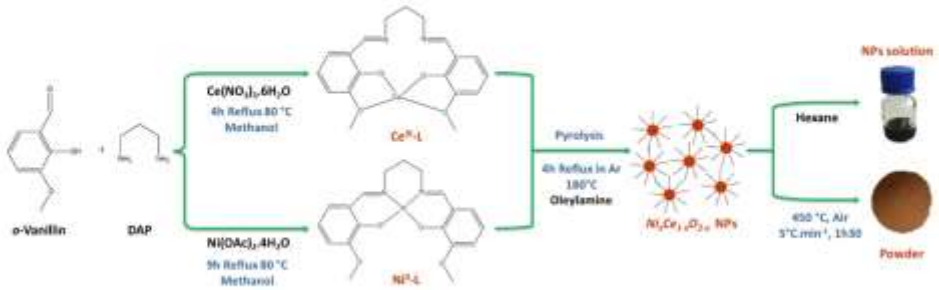

Fig. 1. Illustration of the Ni_xCeO_2 NPs preparation method. For the CeO_2 NPs synthesis, a similar protocol was used, with only Ce^{3+}-L Schiff-base complexes.

Table 1
Structural and textural parameters of calcined samples.

Catalyst	Crystallite size[a] (nm)	Lattice parameter[b] (±0.0005 Å)	Volume cell[b] (±0.03 Å^3)
CeO_2	6.8	5.4082	158.18
$Ni_xCe_{1-x}O_2$	6.6	5.4153	158.81

[a] Crystallite size estimated from the Scherrer's equation applied to the most intense (111) diffraction peak.
[b] Data obtained from Rietveld refinement using FullProf software.

increases, the insertion becomes more exothermic, allowing easier insertion of Ni atoms [33]. Of course, one should also mention here that the enhanced reducibility of $Ni_xCe_{1-x}O_2$ can be an additional cause of lattice expansion. Since the size of Ce^{3+} is larger than that of Ce^{4+} (rCe^{3+} = 1.143 Å, rCe^{4+} = 0.970 Å; both ions are 8-fold coordinated), reduction of ceria would also induce lattice expansion in order to retrieve the strain induced by the Ce^{3+} ions [34]. Although we cannot totally exclude the enhanced reducibility of $Ni_xCe_{1-x}O_2$ as the cause of the observed lattice expansion, we assume that this mechanism is quite unlikely since the XRD measurements were performed over calcined samples.

The Raman spectrum of ceria is dominated by a sharp peak attributed to the triply degenerate oxygen breathing mode of F2g symmetry, characteristic of cubic fluorite structure. As shown in Fig. S1b, in the case of CeO_2, the F2g peak is located at 464 cm^{-1}, while for $Ni_xCe_{1-x}O_2$, it shifts at 460 cm^{-1} and becomes broader. The shift of the F2g Raman peak to lower wavenumbers indicates an expansion of the average fluorine lattice parameter of ceria due to Ni doping, in full agreement with the XRD results [10,35,36]. In addition, new bands appear at 228, 558, and 625 cm^{-1} for the $Ni_xCe_{1-x}O_2$ sample. These peaks are attributed to the D band defects and the creation of O vacancies due to nickel solubility [37,38].

Fig. 2a and b show representative TEM and HR-TEM images combined with selected area electron diffraction (SAED) patterns. The TEM images of the calcined sample show aggregation of small and uniform nanoparticles. The particle size distribution histogram inserted in Fig. 2a, indicates a mean CeO_2 particle size around 7.7 nm, in fair agreement with the crystallite sizes found by XRD (6.8 nm, see Table 1). The HR-TEM image combined with the SAED pattern in Fig. 2a shows distinct diffraction spots and lattice fringes spacing corresponding to the planes of CeO_2 NPs. The microscopy analysis of $Ni_xCe_{1-x}O_2$ (Fig. 2b) shows similar particle morphology to CeO_2, but the mean particle size is somewhat smaller (5.5 nm). The diffraction patterns correspond to that of ceria; however in the EDX mapping (Fig. 2d and Fig. S2), the presence of nickel is evident and is quantified to 3.5% Ni atomic ratio, corroborating the $Ni_{0.036}Ce_{0.964}O_2$ stoichiometry determined separately by inductively coupled plasma atomic emission spectroscopy (ICP-OES). The Ni and Ce mappings indicate a rather homogenous mixture of the two elements, although some areas richer in Ni are visible (see also Fig. S2 showing higher EDX analysis area). Interesting structural information comes from the comparison of the high-resolution images and diffraction patterns between areas with high and lower nickel signals (Fig. 2c). From this, it is shown that Ni significantly increases the lattice planes of the ceria crystalline phase, corroborating the lattice parameter difference observed in XRD and confirming the integration of nickel in the ceria lattice. Consequently, diffraction and microscopy results of $Ni_xCe_{1-x}O_2$ NPs confirm Ni incorporation into CeO_2 lattice [39].

The reducibility in H_2 was initially investigated by H_2-TPR (Fig. S3). The H_2-TPR profile of CeO_2 exhibits two broad peaks with a maximum of around 500 °C and 850 °C, typically assigned to the reduction of the surface and bulk Ce^{4+} ions, respectively [40,41]. In the case of $Ni_xCe_{1-x}O_2$, an additional peak at 310 °C is evident, which was previously linked to NiO reduction [42]. However, the high H_2 uptake in our case (estimated to be 644 μmol/g), is incompatible with the low nickel amount of $Ni_xCe_{1-x}O_2$ NPs ($x = 0.036$), which would theoretically lead to three times lower H_2 consumption than the one observed (see Fig. S3). The origin of this peak is probably due to Ce^{4+} reduction, as will be explained below on the basis of *in situ* sXAS.

3.2. *In situ* DRIFTS analysis

The reduction of preoxidized CeO_2 and $Ni_xCe_{1-x}O_2$ samples was followed by *in situ* DRIFTS. Fig. 3 displays 2D maps recorded during heating in pure H_2, while DRIFT spectra are shown in Fig. S4. The stretching vibrations of OH groups can be followed in the 3900-3550 cm^{-1} region, while the 2250-1950 cm^{-1} region gives information about the cerium oxidation state. The H_2 treatment induces progressive dehydroxylation, characterized by several negative peaks in the 3900−3550 cm^{-1} region. An intense band is observed for both samples at 3658 cm^{-1} together with features in the 1800−1100 cm^{-1} region (not shown), assigned to desorption of

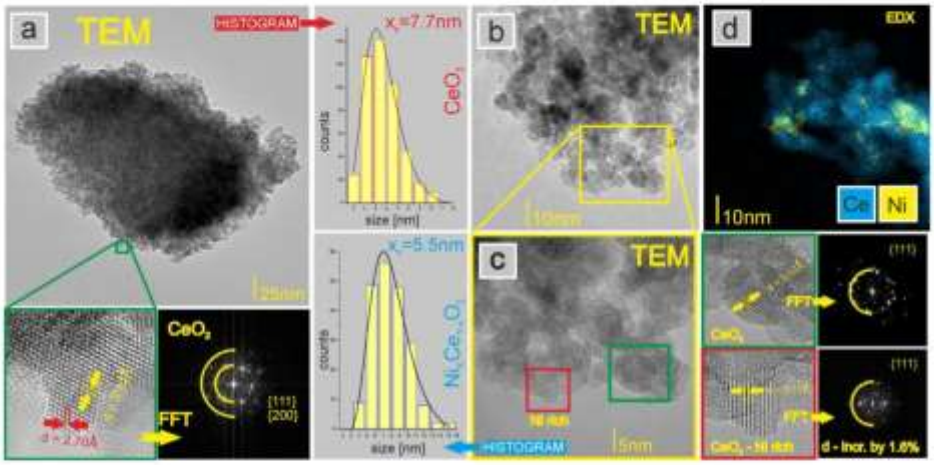

Fig. 2. HAADF-STEM images of calcined (a) CeO_2 and (b,c) $Ni_xCe_{1-x}O_2$ NPs samples. The particle size distribution histograms, HR images, and selected SAED patterns are inserted in the two figures. (d) EDX mapping of $Ni_xCe_{1-x}O_2$ sample indicating mixing of Ni and Ce elements.

bicarbonate compounds, probably remaining on the sample surface after calcination. Starting from 200 °C two additional peaks at 3709 cm^{-1} (terminal OH groups-Type I) and 3685 cm^{-1} (bridging OH groups-Type II) [43–45], are observed on $Ni_xCe_{1-x}O_2$. Therefore, $Ni_xCe_{1-x}O_2$ is differentiated from CeO_2 by desorption of poly-coordinated OH groups during heating in H_2. According to the literature [46], type I OH groups have a higher propensity to dissociate as OH^- anions, causing the creation of charge deficiency on the coordinated cerium atom upon their removal. Interestingly, at 300 °C a broad band at 2117 cm^{-1} appeared on $Ni_xCe_{1-x}O_2$, the intensity of which increases with temperature. This band has been attributed to the forbidden $^2F_{5/2} \rightarrow {}^2F_{7/2}$ electronic transition of Ce^{3+} [47]. This peak is much less evident for CeO_2 and appears only at the maximum annealing temperature (400 °C). According to these results, the reduction of Ce^{4+} to Ce^{3+} over $Ni_xCe_{1-x}O_2$ takes place between 300 and 400 °C simultaneously with surface dehydroxylation.

3.3. *In situ* sXAS analysis

It is important to note that the DRIFTS bands associated with Ce^{3+} ions come from a sampling depth of a few μm. The nickel and cerium oxidation states at the outer 5 nm [48] of the NPs are examined by *in situ* sXAS in 1 bar 10% H_2/He. Characteristic Ni $L_{3,2}$-edge spectra of $Ni_xCe_{1-x}O_2$ upon annealing in H_2 are shown in Fig. 4a. The position of the Ni $L_{3,2}$-edge (centroid of the peak) and its shape (multiplet structure) are sensitive to the nickel chemical environment (i.e. oxidation state, coordination symmetry, and interaction with ligand ions). In general, the Ni L_3-edge centroid shifts to higher energy for higher nickel oxidation [49,50], while the peak features around 855 and 872 eV are sensitive to Ni interaction with the ligand ion (O^{2-}) (e.g. transformation of nickel oxide to hydroxide) [51]. The Ni $L_{3,2}$-edge of calcined $Ni_xCe_{1-x}O_2$ (50 °C in Fig. 4a) has the same centroid position with reference bulk NiO (852.8 eV) but quite a different edge shape. This indicates bivalent nickel ions (Ni^{2+}) but in a different chemical environment as compared to the standard octahedral NiO. The Ni $L_{3,2}$-edge is stable up to 230 °C, but above this temperature, the peak becomes broader, and two distinct Ni L_3 features appear at 852.6 and 853.4 eV. The Ni $L_{3,2}$-edge measured above 230 °C does not resemble any of the standard nickel oxide or hydroxide spectra [51], while its complex peak shape suggests the possible overlapping of two, or more, nickel chemical states. Attempts to simulate the Ni $L_{3,2}$-edge by the linear combination of Ni, NiO, and oxidized $Ni_xCe_{1-x}O_2$ reference peaks were unsuccessful. The accuracy of the fitting was improved when one of the reference peaks ($Ni_xCe_{1-x}O_2$, up to 310 °C, and metallic Ni^0, from 325 to 360 °C) is combined with a spectrum composed by 4 Gaussian/Lorentzian peaks (Fig. 4a and Figs. S5 and S6) and shifted to a higher energy than Ni^{2+} by 0.6 eV. Since the multiplet structure of this spectrum does not resemble the trivalent Ni^{3+} ions [51,52], we attribute it to a nickel oxidation state between 2 and 3, denoted as δ ($Ni^{\delta+}$ with $2< \delta<3$). The appearance of $Ni^{\delta+}$ is a remarkable observation, which, contrary to the common consensus, indicates oxidation of Ni ions in 1 bar H_2. Notably, when the sample is cooled down in H_2 the Ni $L_{3,2}$-edge is modified, and Ni^{2+} reappears (Fig. S6), suggesting that the reported behavior can be observed only *in situ* and it is elusive to post-treatment analysis.

The Ce M_5-edge of the oxidized $Ni_xCe_{1-x}O_2$ corresponds to the Ce^{4+} state (Fig. 4b), while starting from 265 °C, the absorption edge is modified due to the formation of Ce^{3+} as indicated by the linear peak fitting analysis of Ce M_5-edge depicted in Fig. S7. Partial reduction of ceria is, of course, expected upon annealing in H_2; however, the ease of ceria reduction (e.g. the amount of Ce^{3+} species and the temperature they appear) in Ni-doped samples as compared to standard nanosized ceria with similar physico-structural properties is of major interest for the applications and will be analyzed below.

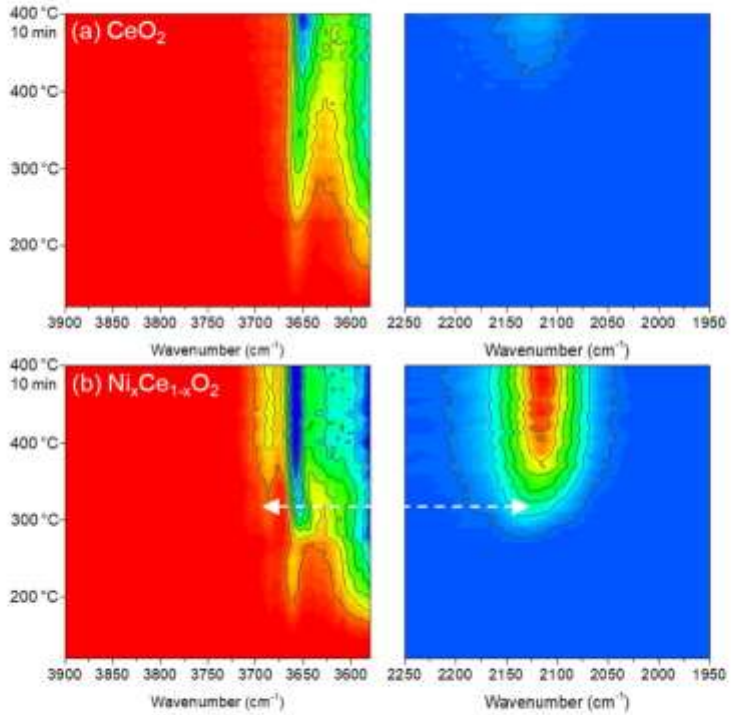

Fig. 3. 2D mapping of the DRIFTS spectra recorded in 1 bar H_2 during heat treatment up to 400 °C after background subtraction and applying Kubelka-Munk equation for a) CeO_2 and b) $Ni_xCe_{1-x}O_2$. In the 3900-3580 cm^{-1} range (left panels), the color scale goes from $f(r_\infty) > 0$ (red) to negative values (blue). In the 2250-1950 cm^{-1} range (right panels), the color scale goes from $f(r_\infty) = 0$ (blue) to positive values (red).

3.4. Charge-transfer multiplet calculations of Ni $L_{3,2}$-edge

The formation of Ni^{2+} ions in Ni-doped ceria is supported by previous experimental findings [31,32], and first-principle calculations [53,54]. To get more insights into the local electronic structure and the chemical bonding of Ni ions in $Ni_xCe_{1-x}O_2$ NPs, we perform charge-transfer multiplet (CTM) calculations of the Ni $L_{3,2}$-edge using the CTM4XAS 5.23 software [30,55]. Calculated and experimental Ni $L_{3,2}$-edges of Ni^{2+} and Ni^{0+} states are shown in Fig. 5. Please note that CTM calculations describe quite well the experimental atomic multiple splitting and therefore, the Ni L-edge shape; however, they cannot reproduce with accuracy the position of the Ni L-edge [56]. Therefore in Fig. 5 the centroid position of the theoretically simulated Ni L-edge is aligned to the centroid of the experimental peak. As shown in Fig. 5 the experimental spectra are accurately simulated assuming Ni^{2+} ions in square planar D_{4h} coordination symmetry (for brevity, $Ni^{2+}[D_{4h}]$). Attempts to reproduce them by octahedrally (O_h) coordinated Ni^{2+} ions failed since $Ni^{2+}[O_h]$ ions have a characteristic double-peak L_2-edge [57,58], very different from the spectra in Fig. 4a.

The $Ni^{2+}[D_{4h}]$ geometry has been verified for Ni–S compounds [49,57] and salen complexes [59] by sXAS. However, as far as we are aware, this is the first time that $Ni^{2+}[D_{4h}]$ sites have been observed in the case of doped oxide particles. This structure is in sharp contrast with Ni ions coordinated in the bulk NiO, which is known to crystallize in the O_h symmetry. Our experiments confirm the earlier theoretical studies predicted that when Ni substitutes lattice Ce atoms, instead of the conventional octahedral coordination, it is coordinated by four O atoms in a square-planar environment [32,54,60]. For example, in the case of the CeO_2(111) surface, two lattice oxygen atoms that were initially three-fold coordinated with Ce ions become two-fold coordinated Ni [60]. Similar predictions regarding four-fold coordinated Ni were also reported for Ni ions occupying interstitial lattice positions, at least for low Ni dopant concentrations [33]. In this case, Ni atoms are located at the center of the cube formed by the eight oxygen atoms in the fluorite unit cell [33].

Apart from the local geometry, the analysis of the 10Dq and Δ parameters, defined in the CTM calculations, provides information about the nickel-ligand (Ni–O) interactions. In particular, the 10Dq term increases when the Ni and O ions come closer, while an increased Δ parameter denotes weaker Ni–O interactions [61]. The simulation of the Ni^{0+} spectrum needs higher 10Dq and lower Δ values (10Dq = 0.9 and Δ = 3) as compared to the Ni^{2+} (10Dq = 0.5

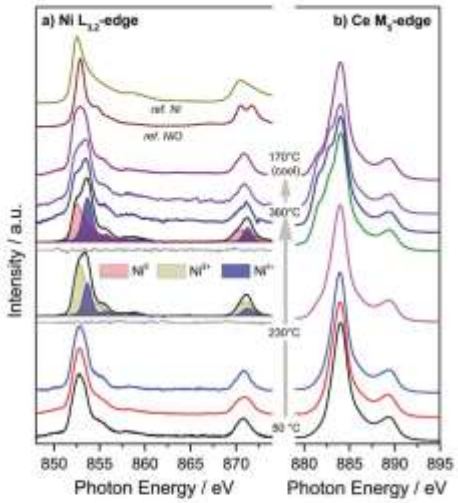

Fig. 4. (a) Ni $L_{3,2}$-edge sXAS spectra of pre-oxidized $Ni_xCe_{1-x}O_2$ NPs upon annealing in 1 bar 10% H_2/He mixture. Two characteristic cases of Ni $L_{3,2}$-edge fitting, as well as peaks of metallic and NiO reference samples, are included. (b) Ce M_5-edge sXAS recorded at the same conditions as described in (a).

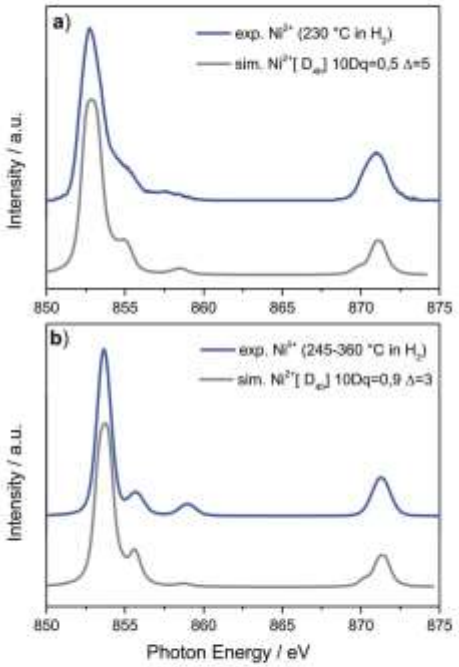

Fig. 5. *In situ* Ni $L_{3,2}$-edge sXAS spectra (blue lines) of (a) the Ni^{2+} state recorded at 230 °C and (b) the Ni^{2+} state composed of 4 G/L peaks and used to fit the experimental spectra between 245 and 360 °C in 1 bar 10% H_2/He. The theoretically simulated Ni $L_{3,2}$-edge (gray lines) for square-planar (D_{4h}) coordinated Ni^{2+} ions and the corresponding 10Dq and Δ values used in the simulations are included in the figure.

and Δ = 5) as shown in Fig. 5 and specified in experimental part. These differences indicate smaller square size, and larger attractive interactions, between Ni^{2+} and O^{2-} ions as compared to the $Ni^{2+}$of the fully oxidized sample. This means an increasing covalent character of the Ni^{2+}-O^{2-}, which can explain the stability of these species under severe reducing conditions.

3.5. The evolution of nickel and ceria oxidation states as compared to reference samples

The evolution of Ni^0 and Ni^{5+} states as a function of temperature, as derived from the Ni-$L_{3,2}$ edge deconvolution, is shown in Fig. 6a. The results collected over the NiO powder sample are included for comparison. The amount of Ni^{5+} enhances continuously at the expense of Ni^{2+}, up to the maximum annealing temperature. Metallic Ni^0 appears rather abruptly around 330 °C, which is 130 °C higher than the NiO reference. One should note here that the distributions of nickel and cerium states shown in Fig. 6 represent their contribution to the sXAS spectrum, as this is given by the peak fitting analysis. Eventual differences in the photoabsorption cross section (PCS) between different oxidation states are not considered since these values are practically unknown. However, metallic nickel is expected to have lower PCS than the oxidized one due to the lower number of empty 3d band states. Therefore, the Ni^0 concentration shown in Fig. 6a is most probably underestimated.

The results of linear peak fit analysis of the Ce M_5-edges shown in Fig. 6b reveal a sharp increase of Ce^{3+} contribution above 270 °C. When the CeO_2 NPs are exposed to the same conditions (the Ce M_5-edges are shown in Fig. S8), they are less reduced (Fig. 4b). This result can be used to associate the lower temperature peaks of the $Ni_xCe_{1-x}O_2$ NPs found in the TPR analysis (Fig. S3) with the ease of ceria reduction in this sample. Since Ni-doped and pure ceria nanoparticles have very similar size distribution (Fig. 2), one can exclude that their reducibility is affected by differences in their size. Therefore, the promotion effect of Ni-dopant remains the most plausible explanation of the improved ceria reducibility by H_2.

Very interesting findings regarding the mechanism of $Ni_xCe_{1-x}O_2$ reduction emerge by comparison of Fig. 6a and b. The first remarkable observation is that Ce^{4+} reduction is not preceded by the reduction of Ni^{2+}, as commonly assumed for supported nickel particles. On the contrary, Ni^{2+} is oxidized further to Ni^{5+}. Metallic Ni^0 is observed 70 °C higher than in Ce^{3+}, yet it coexists with a significant amount of Ni^{5+} species. In previous studies of the nickel-ceria system [62,63], it was proposed that electrons can transfer from Ce^{4+} towards nickel, generating Ni^{2+} and Ce^{3+}. Although, in our case, the geometry of the system is different (diluted, instead of supported, nickel ions), one can propose that a similar mechanism also takes place for $Ni_xCe_{1-x}O_2$, where Ce^{4+} is transformed to Ce^{3+} by transferring electrons toward Ni^{2+} to form Ni^{5+}. The charge exchange between Ni^{5+}/Ni^{2+} and Ce^{4+}/Ce^{3+} redox couple can be the reason for the enhanced Ce^{4+} reducibility on $Ni_xCe_{1-x}O_2$ as compared to the CeO_2 sample, at least at the initial stage of reduction. When metallic Ni^0 is formed, Ce^{4+} reduction can take place via the classical reduction mechanism related to adsorption

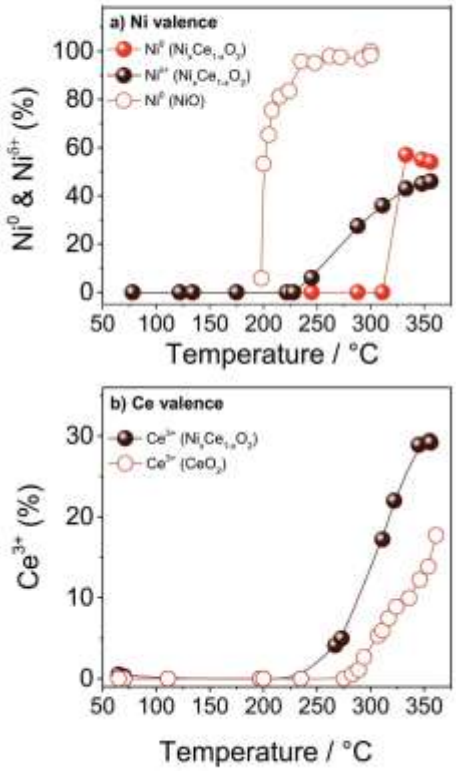

Fig. 6. (a) Evolution of Ni^0 and $Ni^{\delta+}$ valence states as a function of annealing temperature in H_2. The full circle symbols correspond to the $Ni_xCe_{1-x}O_2$ NPs sample, while the empty circles are from reference NiO powder samples treated under identical conditions. (b) Evolution of Ce^{3+} valence state as a function of annealing temperature in H_2. The full circle symbols correspond to the $Ni_xCe_{1-x}O_2$ NPs sample, while the empty circles are from undoped CeO_2 NPs treated under identical conditions. The amount of nickel and cerium species is derived from the deconvolution of Ni $L_{3,2}$ and Ce M_5-edge *sXAS* spectra, respectively, and does not take into account eventual differences in the photoabsorption cross section between various oxidation states.

and dissociation of H_2 on Ni^0 [8]. The infrared characterization showed that Ce^{3+} formation might also be linked with the loss of monocoordinated hydroxyls from the surface, probably desorbed as H_2O. The ease of ceria reduction observed for $Ni_xCe_{1-x}O_2$ is consistent with several previous ab initio studies, which show that the oxygen vacancy formation energy is reduced in the case of doped-ceria as compared to the undoped one, for both substitutional [53,54,60] and interstitial [64] Ni sites.

4. Conclusions

In summary, a relatively simple and efficient approach to synthesizing undoped and Ni-doped CeO_2 nanoparticles with small particle size and size distribution is proposed. *In situ*, sXAS and DRIFT spectroscopies were used to investigate in detail the adsorbed species and the reducibility of the NPs under H_2, an important process involved in several applications of doped ceria. Ni insertion into the ceria lattice enhances the Ce^{4+} reducibility, kinetically slow over pure CeO_2, via a proposed mechanism based on electronic interaction between cerium and nickel ions at an early stage of the reduction process. The findings in this work suggest that ionic nickel is stabilized in quite harsh reducing conditions, which is an intriguing discovery calling for further investigation of their reactivity, notably in hydrogenation reactions.

CRediT author statement

Mathias Barreau: Conceptualization, Methodology, Synthesis, Investigation, Formal analysis, Writing-Original draft preparation, **Dingkai Chen**: Investigation, **Jinming Zhang**: Investigation, Visualization, **Vasiliki Papaefthimiou**: Investigation, Writing-Original draft preparation, **Corinne Petit**: Resources, **Davide Salusso**: Investigation, **Elisa Borfecchia**: Resources, Investigation, **Sylwia Turczyniak-Surdacka**: Resources, Investigation, **Kamil Sobczak**: Investigation, **Silvia Mauri**: Investigation, **Luca Braglia**: Resources, Investigation, **Piero Torelli**: Resources, Validation, **Spyridon Zafeiratos**: Conceptualization, Methodology, Writing- Original draft preparation, Visualization, Formal analysis, Supervision, Writing- Reviewing and Editing, Project administration, Funding acquisition.

Declaration of competing interest

The authors declare the following financial interests/personal relationships, which may be considered as potential competing interests: M. BARREAU reports financial support was provided by French National Research Agency.

Acknowledgment

M.B. acknowledges financial support from Strasbourg University via the IdEX-018 ⟨Post-doctorate⟩ project. J.Z. would like to thank the China Scholarship Council (CSC) for supporting his stay at ICPEES. D.S. and E.B. acknowledge the support from project n. 2017KKP5Z PRIN-2017 MOSCATo (Cutting-edge X-ray methods and models for the understanding of surface site reactivity in heterogeneous catalysts and sensors). We thank Dr D. Tescher for the useful and constructive discussions and S. Sall for the support with DRIFTS. We acknowledge Elettra for the allocation of synchrotron radiation beamtime and the APE-HE beamline staff for the collaboration during the experiments. This work was partially performed in the framework of the Nanoscience Foundry and Fine Analysis (NFFA-MIUR Italy Progetti Internazionali) facility. Finally, D.C. and S.Z. acknowledge the support of the French Agence Nationale de la Recherche (ANR), under contract No 236294 (project DuCaCO2).

Appendix A. Supplementary data

Supplementary data to this article can be found online at https://doi.org/10.1016/j.mtchem.2022.101011.

References

[1] W. Yang, X. Wang, S. Song, H. Zhang, Syntheses and applications of noble-metal-free CeO2-based mixed-oxide nanocatalysts, Inside Chem. 5 (2019) 1743–1774, https://doi.org/10.1016/j.chempr.2019.04.009.
[2] J. Kaspar, P. Fornasiero, M. Graziani, Use of CeO2-based oxides in the three-way catalysts, Catal. Today 50 (1999) 285–298, https://doi.org/10.1016/S0920-5861(98)00510-0.

[3] F. Can, S. Berland, S. Royer, X. Courtois, D. Duprez, Composition-dependent performance of Ce0.2Zr1-x0 2 mixed-oxide-supported WO3 catalysts for the NO x storage reduction-selective catalytic reduction coupled process, ACS Catal. 3 (2013) 1120–1132. https://doi.org/10.1021/cs3008329.
[4] D. Chen, D.K. Niakolas, V. Papaefthimiou, E. Ioannidou, S.G. Neophytides, S. Zafeiratos, How the surface state of nickel/gadolinium-doped ceria cathodes influences the electrochemical performance in direct CO2 electrolysis, J. Catal. 404 (2021) 518–528. https://doi.org/10.1016/j.jcat.2021.10.027.
[5] H.J. Kim, M.G. Jang, D. Shin, J.W. Han, Design of ceria catalysts for low-temperature CO oxidation, ChemCatChem 12 (2020) 11–26. https://doi.org/10.1002/cctc.201901787.
[6] J. Paier, C. Penschke, J. Sauer, Oxygen defects and surface chemistry of ceria: quantum chemical studies compared to experiment, Chem. Rev. 113 (2013) 3949–3985. https://doi.org/10.1021/cr3004949.
[7] K. Chang, H. Zhang, M.J. Cheng, Q. Lu, Application of ceria in CO2 conversion catalysis, ACS Catal. 10 (2020) 613–631. https://doi.org/10.1021/acscatal.9b03935.
[8] M. Boaro, S. Colussi, A. Trovarelli, Ceria-based materials in hydrogenation and reforming reactions for CO2 valorization, Front. Chem. (2019) 28. https://doi.org/10.3389/FCHEM.2019.00028, 0.
[9] T. Montini, M. Melchionna, M. Monai, P. Fornasiero, Fundamentals and catalytic applications of CeO2 -based materials, Chem. Rev. 116 (2016) 5987–6041. https://doi.org/10.1021/acs.chemrev.5b00603.
[10] R. Schmitt, A. Nenning, O. Kraynis, R. Korobko, A.I. Frenkel, I. Lubomirsky, S.M. Haile, J.L.M. Rupp, A review of defect structure and chemistry in ceria and its solid solutions, Chem. Soc. Rev. 49 (2020) 554–592. https://doi.org/10.1039/C9CS00868A.
[11] D.R. Mullins, The surface chemistry of cerium oxide, Surf. Sci. Rep. 70 (2015) 42–85. https://doi.org/10.1016/j.surfrep.2014.12.001.
[12] T. Sakpal, L. Lefferts, Structure-dependent activity of CeO2 supported Ru catalysts for CO2 methanation, J. Catal. 367 (2018) 171–180. https://doi.org/10.1016/j.jcat.2018.09.027.
[13] X. Liu, K. Zhou, L. Wang, B. Wang, Y. Li, Oxygen vacancy clusters promoting reducibility and activity of ceria nanorods, J. Am. Chem. Soc. 131 (2009) 3140–3141. https://doi.org/10.1021/ja808453d.
[14] A. Trovarelli, J. Llorca, Ceria catalysts at nanoscale: how do crystal shapes shape catalysis? ACS Catal. 7 (2017) 4716–4735. https://doi.org/10.1021/acscatal.7b01246.
[15] J.S. Elias, M. Risch, L. Giordano, A.N. Mansour, Y. Shao-Horn, Structure, bonding, and catalytic activity of monodisperse, transition-metal-substituted CeO2 nanoparticles, J. Am. Chem. Soc. 136 (2014) 17193–17200. https://doi.org/10.1021/ja508214d.
[16] A. Figueroba, A. Bruix, G. Kovács, K.M. Neyman, Metal-doped ceria nanoparticles: stability and redox processes, Phys. Chem. Chem. Phys. 19 (2017) 21728–21738. https://doi.org/10.1039/C7CP02820B.
[17] S. Loridant, Raman spectroscopy as a powerful tool to characterize ceria-based catalysts, Catal. Today 373 (2021) 98–111. https://doi.org/10.1016/j.cattod.2020.03.044.
[18] A.B. Kehoe, D.O. Scanlon, G.W. Watson, Role of lattice distortions in the oxygen storage capacity of divalently doped CeO2, Chem. Mater. 23 (2011) 4464–4468. https://doi.org/10.1021/cm201673d.
[19] A. Gupta, U.V. Waghmare, M.S. Hegde, Correlation of oxygen storage capacity and structural distortion in transition-metal-, noble-metal-, and rare-earth-ion-substituted CeO2 from first principles calculation, Chem. Mater. 22 (2010) 5184–5198. https://doi.org/10.1021/CM101349D.
[20] W. Shan, M. Luo, P. Ying, W. Shen, C. Li, Reduction property and catalytic activity of Ce1−XNiX02 mixed oxide catalysts for CH4 oxidation, Appl. Catal. Gen. 246 (2003) 1–9. https://doi.org/10.1016/S0926-860X(02)00659-2.
[21] Y. Xiong, L. Li, L. Zhang, Y. Cao, S. Yu, C. Tang, L. Dong, Migration of copper species in CexCu1-xO2 catalyst driven by thermal treatment and the effect on CO oxidation, Phys. Chem. Chem. Phys. 19 (2017) 21840–21847. https://doi.org/10.1039/c7cp03715j.
[22] S. Kurajica, K. Muzina, G. Dražić, G. Matijašić, M. Duplančić, V. Mandić, M. Župančić, I.K. Munda, A comparative study of hydrothermally derived Mn, Fe, Co, Ni, Cu and Zn doped ceria nanocatalysts, Mater. Chem. Phys. 244 (2020) 122689. https://doi.org/10.1016/j.matchemphys.2020.122689.
[23] A. Figueroba, G. Kovács, A. Bruix, K.M. Neyman, Towards stable single-atom catalysts: strong binding of atomically dispersed transition metals on the surface of nanostructured ceria, Catal. Sci. Technol. 6 (2016) 6806–6813. https://doi.org/10.1039/C6CY00294C.
[24] K.J. Lee, J.H. Lee, S. Jeoung, H.R. Moon, Transformation of metal–organic frameworks/coordination polymers into functional nanostructured materials: experimental approaches based on mechanistic insights, Acc. Chem. Res. 50 (2017) 2684–2692. https://doi.org/10.1021/acs.accounts.7b00259.
[25] W. Desafa, F. Paloukis, B. Mewafy, W. Baaziz, O. Ersen, C. Petit, G. Corbel, S. Zafeiratos, Synthesis and Characterization of Nickel-Doped Ceria Nanoparticles with Improved Surface Reducibility, vol. 8, 2018, pp. 40712–40719. https://doi.org/10.1039/C8RA07905A.
[26] Y. Li, W. Han, R. Wang, L.T. Weng, A. Serrano-Lotina, M.A. Bañares, Q. Wang, K.L. Yeung, Performance of an aliovalent-substituted CoCeOx catalyst from bimetallic MOF for VOC oxidation in air, Appl. Catal. B Environ. 275 (2020) 119121. https://doi.org/10.1016/j.apcatb.2020.119121.
[27] A. Cárdenas-Arenas, A. Quindimil, A. Davó-Quiñonero, E. Bailón-García, D. Lozano-Castelló, U. De-La-Torre, B. Pereda-Ayo, J.A. González-Marcos, J.R. González-Velasco, A. Bueno-López, Design of active sites in Ni/CeO2 catalysts for the methanation of CO2: tailoring the Ni-CeO2 contact, Appl. Mater. Today 19 (2020) 100591. https://doi.org/10.1016/j.apmt.2020.100591.
[28] J. Rodríguez-Carvajal, Recent developments of the program fullprof, in: Newsl. Comm. Powder Diffr. IUCr, International Union of Crystallography, 2001, pp. 12–19.
[29] C. Castán-Guerrero, D. Krizmancic, V. Bonanni, R. Edla, A. Deluisa, F. Salvador, G. Rossi, G. Panaccione, P. Torelli, A reaction cell for ambient pressure soft x-ray absorption spectroscopy, Rev. Sci. Instrum. 89 (2018). https://doi.org/10.1063/1.5019333, 054101.
[30] E. Stavitski, F.M.F. de Groot, The CTM4XAS program for EELS and XAS spectral shape analysis of transition metal L edges, Micron 41 (2010) 687–694. https://doi.org/10.1016/j.micron.2010.06.009.
[31] S.K. Misra, S.I. Andronenko, M.H. Engelhard, A. Thurber, K.M. Reddy, A. Punnoose, Role of dopant incorporation on the magnetic properties of Ce1−xNixO2 nanoparticles: an electron paramagnetic resonance study, J. Appl. Phys. 103 (2008). https://doi.org/10.1063/1.2833291, 07D122.
[32] D.-K. Lim, N.W. Kwak, J.-S. Kim, H. Kim, B.-K. Kim, Y.-C. Kim, W. Jang, Ni diffusion in ceria lattice: a combined experimental and theoretical study, Acta Mater. 219 (2021) 117252. https://doi.org/10.1016/j.actamat.2021.117252.
[33] Z. Chafi, N. Keghouche, C. Minot, DFT study of Ni–CeO2 interaction: adsorption and insertion, Surf. Sci. 601 (2007) 2323–2329. https://doi.org/10.1016/j.susc.2007.03.041.
[34] D. Schweke, Y. Mordehovitz, M. Halabi, L. Shelly, S. Hayun, Defect chemistry of oxides for energy applications, Adv. Mater. 30 (2018) 1706300. https://doi.org/10.1002/adma.201706300.
[35] J.E. Spanier, R.D. Robinson, F. Zhang, S.-W. Chan, I.P. Herman, Size-dependent properties of CeO2-y nanoparticles as studied by Raman scattering, Phys. Rev. B 64 (2001) 245407. https://doi.org/10.1103/PhysRevB.64.245407.
[36] C. Schilling, A. Hofmann, C. Hess, M.V. Ganduglia-Pirovano, Raman spectra of polycrystalline CeO2: a density functional theory study, J. Phys. Chem. C 121 (2017) 20834–20849. https://doi.org/10.1021/acs.jpcc.7b06641.
[37] S. Mahammadunnisa, P. Manoj Kumar Reddy, N. Lingaiah, C. Subrahmanyam, NiO/Ce1−xNixO2-δ as an alternative to noble metal catalysts for CO oxidation, Catal. Sci. Technol. 3 (2013) 730–736. https://doi.org/10.1039/c2cy20641b.
[38] C.A. Chagas, E.F. de Souza, R.L. Manfro, S.M. Landi, M.M.V.M. Souza, M. Schmal, Copper as promoter of the NiO-CeO2 catalyst in the preferential CO oxidation, Appl. Catal. B Environ. 182 (2016) 257–265. https://doi.org/10.1016/j.apcatb.2015.09.033.
[39] G.M. Mullen, E.J. Evans, B.C. Siegert, N.R. Miller, B.K. Rosselet, I. Sahbaziari, A. Brush, Z. Duan, C. Buddie Mullins, The interplay between ceria particle size, reducibility, and ethanol oxidation activity of ceria-supported gold catalysts, React. Chem. Eng. 3 (2018) 75–85. https://doi.org/10.1039/C7RE00175D.
[40] J.P. Holgado, R. Alvarez, G. Munuera, Study of CeO2 XPS spectra by factor analysis: reduction of CeO2, Appl. Surf. Sci. 161 (2000) 301–315. https://doi.org/10.1016/S0169-4332(99)00577-2.
[41] F. Giordano, A. Trovarelli, C. De Leitenburg, M. Giona, A model for the temperature-programmed reduction of low and high surface area ceria, J. Catal. 193 (2000) 273–282. https://doi.org/10.1006/jcat.2000.2901.
[42] C.W. Hu, J. Yao, H.Q. Yang, Y. Chen, A.M. Tian, On the inhomogeneity of low nickel loading methanation catalyst, J. Catal. 166 (1997) 1–7. https://doi.org/10.1006/jcat.1997.1489.
[43] C. Binet, M. Daturi, J.C. Lavalley, IR study of polycrystalline ceria properties in oxidised and reduced states, Catal. Today 50 (1999) 207–225. https://doi.org/10.1016/S0920-5861(98)00504-3.
[44] O. Pozdnyakova, D. Teschner, A. Wootsch, J. Kröhnert, B. Steinhauer, H. Sauer, L. Toth, F.C. Jentoft, A. Knop-Gericke, Z. Paál, R. Schlögl, Preferential CO oxidation in hydrogen (PROX) on ceria-supported catalysts, part I: oxidation state and surface species on Pt/CeO2 under reaction conditions, J. Catal. 237 (2006) 1–16. https://doi.org/10.1016/j.jcat.2005.10.014.
[45] A. Badri, C. Binet, J.C. Lavalley, An FTIR study of surface ceria hydroxy groups during a redox process with H2, J. Chem. Soc. - Faraday Trans. 92 (1996) 4669–4673. https://doi.org/10.1039/ft9969204669.
[46] B. Sudduth, D. Yun, J. Sun, Y. Wang, Facet-Dependent selectivity of CeO2 nanoparticles in 2-Propanol conversion, J. Catal. 404 (2021) 96–108. https://doi.org/10.1016/j.jcat.2021.09.009.
[47] C. Binet, A. Badri, J.-C. Lavalley, A spectroscopic characterization of the reduction of ceria from electronic transitions of intrinsic point defects, J. Phys. Chem. 98 (1994) 6392–6398.
[48] A. Ruosi, C. Raisch, A. Verma, R. Werner, B.A. Davidson, J. Fujii, R. Kleiner, D. Koelle, Electron sampling depth and saturation effects in perovskite films investigated by soft x-ray absorption spectroscopy, Phys. Rev. B 90 (2014) 125120. https://doi.org/10.1103/PhysRevB.90.125120.
[49] W. Gu, H. Wang, K. Wang, Nickel L-edge and K-edge X-ray absorption spectroscopy of non-innocent Ni[S2C2(CF3)2]2n series (n = −2[,] −1[,] 0): direct probe of nickel fractional oxidation state changes, Dalt. Trans. 43 (2014) 6406–6413. https://doi.org/10.1039/C4DT00308J.
[50] H. Wang, D.S. Patil, W. Gu, L. Jacquamet, S. Friedrich, T. Funk, S.P. Cramer, L-edge X-ray absorption spectroscopy of some Ni enzymes: probe of Ni

electronic structure, J. Electron Spectros. Relat. Phenomena 114–116 (2001) 855–863, https://doi.org/10.1016/S0368-2048(00)00370-4.
[51] M. Al Samarai, A.W. Hahn, A. Beheshti Askari, Y.T. Cui, K. Yamazoe, J. Miyawaki, Y. Harada, O. Rüdiger, S. Debeer, Elucidation of structure-activity correlations in a nickel manganese oxide oxygen evolution reaction catalyst by operando Ni L-edge X-ray absorption spectroscopy and 2p3d resonant inelastic X-ray scattering, ACS Appl. Mater. Interfaces 11 (2019) 38595–38605, https://doi.org/10.1021/acsami.9b06752.
[52] H. Wang, S.M. Butorin, A.T. Young, J. Guo, Nickel oxidation states and spin states of bioinorganic complexes from nickel L-edge X-ray absorption and resonant inelastic X-ray scattering, J. Phys. Chem. C 117 (2013) 24767–24772, https://doi.org/10.1021/jp402404h.
[53] W. Zhang, M. Pu, M. Lei, Theoretical studies on the stability and reactivity of the metal-doped CeO2(100) surface: toward H2 dissociation and oxygen vacancy formation, Langmuir 36 (2020) 5891–5901, https://doi.org/10.1021/acs.langmuir.0c00644.
[54] W.Q. Li, S. Gowrapet Srinivasan, D.R. Salahub, T. Heine, Ni on the CeO2(110) and (100) surfaces: adsorption vs. substitution effects on the electronic and geometric structures and oxygen vacancies, Phys. Chem. Chem. Phys. 18 (2016) 11139–11149, https://doi.org/10.1039/C6CP00738D.
[55] F. De Groot, Multiplet effects in X-ray spectroscopy, Coord. Chem. Rev. 249 (2005) 31–63, https://doi.org/10.1016/j.ccr.2004.03.018.
[56] X. Zheng, B. Zhang, P. De Luna, Y. Liang, R. Comin, O. Voznyy, L. Han, F.P. García de Arquer, M. Liu, C.T. Dinh, T. Regier, J.J. Dynes, S. He, H.L. Xin, H. Peng, D. Prendergast, X. Du, E.H. Sargent, Theory-driven design of high-valence metal sites for water oxidation confirmed using in situ soft X-ray absorption, Nat. Chem. 10 (2018) 149–154, https://doi.org/10.1038/nchem.2886.
[57] G. van der Laan, B.T. Thole, G.A. Sawatzky, M. Verdaguer, Multiplet structure in the L2,3 X-ray-absorption spectra: a fingerprint for high- and low-spin Ni2+ compounds, Phys. Rev. B 37 (1988) 6587–6589, https://doi.org/10.1103/PhysRevB.37.6587.
[58] R.J.O. Mossanek, G. Domínguez-Cañizares, A. Gutiérrez, M. Abbate, D. Díaz-Fernández, L. Soriano, Effects of Ni vacancies and crystallite size on the O 1s and Ni 2p x-ray absorption spectra of nanocrystalline NiO, J. Phys. Condens. Matter 25 (2013) 495501, https://doi.org/10.1088/0953-8984/25/49/495501.
[59] G.I. Sviriskiy, A. V Generalov, N.A. Vinogradov, K.O. Brykalova, A. V Vereshchagin, O. V Levin, A.G. Lyalin, A.B. Preobrajenski, A.S. Vinogradov, Electronic structure of the [Ni(Salen)] complex studied by core-level spectroscopies, Phys. Chem. Chem. Phys. 23 (2021) 11015–11027, https://doi.org/10.1039/D1CP00011A.
[60] Y.-Q. Su, L. Zhang, V. Muravev, E.J.M. Hensen, Lattice oxygen activation in transition metal doped ceria, Chinese J. Catal. 41 (2020) 977–984, https://doi.org/10.1016/S1872-2067(19)63468-6.
[61] L. Zhong, M. Barreau, V. Caps, V. Papaefthimiou, M. Harvecker, D. Teschner, W. Baaziz, E. Borfecchia, L. Braglia, S. Zafeiratos, Improving the catalytic performance of cobalt for CO preferential oxidation by stabilizing the active phase through vanadium promotion, ACS Catal. 11 (2021) 5169–5185, https://doi.org/10.1021/acscatal.0c05482.
[62] Z. Mao, P.G. Lustemberg, J.R. Rumptz, M.V. Ganduglia-Pirovano, C.T. Campbell, Ni nanoparticles on CeO2(111): energetics, electron transfer, and structure by Ni adsorption calorimetry, spectroscopies, and density functional theory, ACS Catal. 10 (2020) 5101–5114, https://doi.org/10.1021/acscatal.0c00331.
[63] C. Lamonier, A. Ponchel, A. D'Huysser, L. Jalowiecki-Duhamel, Studies of the cerium–metal–oxygen–hydrogen system (metal=Cu, Ni), Catal. Today 50 (1999) 247–259, https://doi.org/10.1016/S0920-5861(98)00507-0.
[64] X. Wang, M. Shen, J. Wang, S. Fabris, Enhanced oxygen buffering by substitutional and interstitial Ni point defects in ceria: a first-principles DFT+U study, J. Phys. Chem. C 114 (2010) 10221–10228, https://doi.org/10.1021/jp101300f.

6.6 F : Surface species in direct liquid phase synthesis of dimethyl carbonate from methanol and CO2: an MCR-ALS augmented ATR-IR study. Signorile et al., 2022

This manuscript was recently submitted and is currently under peer review process. Most of the main results are reported within the thesis. However, I believe that for sake of clarity, some part of the manuscript needed to be reported hereafter.

Experimental

Materials

ZrO_2 was synthesized according to the literature.[1] This specific synthetic method provides a final material in a 83:17 mixture of the monoclinic and tetragonal polymorphs, respectively (see XRD pattern in Figure 71) with a BET specific surface area of 73 m2g-1 (N2 adsorption isotherm at 77 K in Figure 72). Cyclohexane (VWR, >99.8%) solvent was dried overnight over 4A molecular sieves prior to use. Methanol (VWR, >99.9% HPLC), dimethyl carbonate (DMC, Sigma-Aldrich, >99.0%), CO2 (PANGAS, 99.995%) were used as received, without further purification.

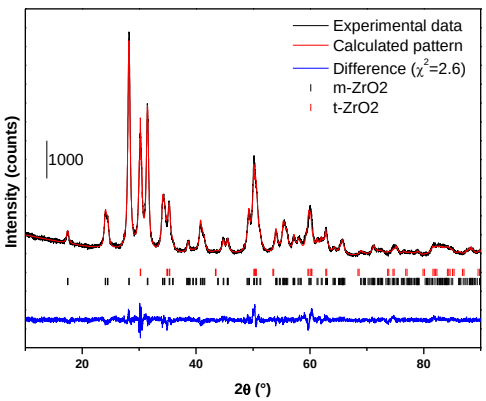

Figure 71 Experimental and refined PXRD patterns of the ZrO_2 catalyst. Bragg reflections of monoclinic (m-ZrO_2) and tetragonal (t-ZrO_2) phases are indicated.

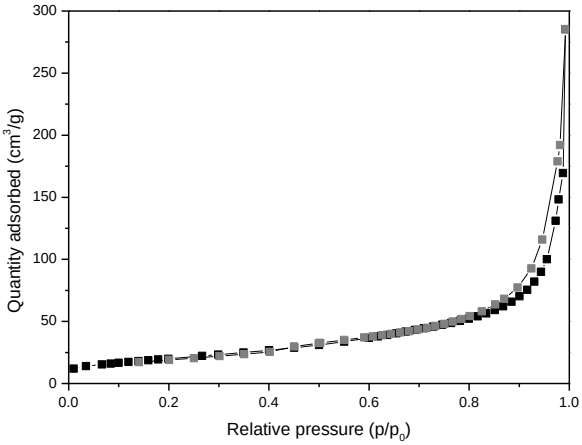

Figure 72 Adsorption (black) and desorption (gray) isotherms of N_2 at 77 K.

In situ IR experiments were conducted in multiple reflections ATR mode using a commercial horizontal ATR mirror unit and cell (Bruker), allowing circulation of a liquid phase over the internal reflection element. Circulation was controlled through a peristaltic pump operated at 0.5 ml/min constant flow (Figure 73). In a typical experiment, ZrO_2 was deposited from a water suspension (15 mg per 0.5 ml of MilliQ H_2O) on the prismatic ZnSe single crystal internal reflection element (72×10×6 mm, 45°, Specac) and allowed drying at room temperature overnight. A fresh deposition was performed prior to each experiment. The sample was pretreated at 70 °C under cyclohexane for 60 min to favor the removal of weakly interacting surface species. After cooling to the target temperature (if required), the background spectrum was collected and the experiment started. In a typical run, a 0.2 M solution of methanol in cyclohexane was mixed in a 1:1 volume ratio with CO_2-saturated cyclohexane. Such reactive mixture was dosed onto the sample for 60 min. Spectra were collected continuously (1 spectrum every 20 s, 4 cm^{-1} resolution): a typical dataset consisted of approximately 180 spectra. This procedure was repeated at four different temperatures: 10 °C, 30 °C, 50 °C and 70 °C.

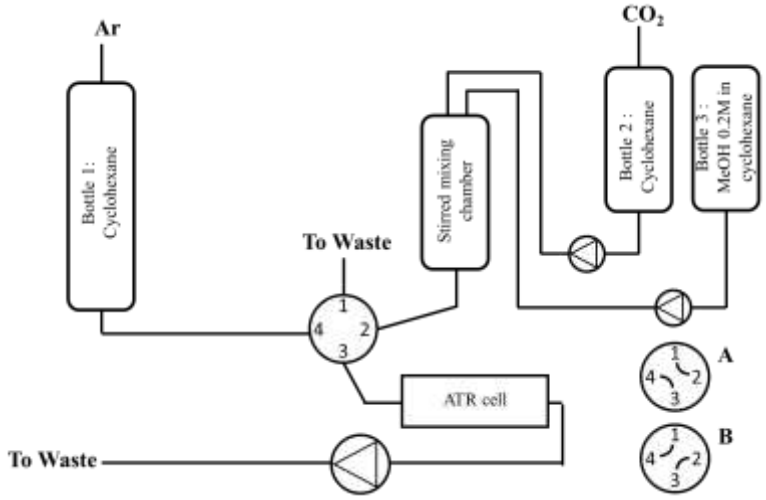

Figure 73 Schematic of the ATR-IR experimental set-up. The two possible positions for the 4-way valve (A and B) are indicated.

References

(1) Gionco, C.; Paganini, M. C.; Giamello, E.; Sacco, O.; Vaiano, V.; Sannino, D. Rare Earth Oxides in Zirconium Dioxide: How to Turn a Wide Band Gap Metal Oxide into a Visible Light Active Photocatalyst. J. Energy Chem. 2017, 26 (2), 270–276. https://doi.org/10.1016/j.jechem.2016.07.006.